Exploring the monooxygenase activity and selectivity of two related Cytochrome P450 enzymes

By Saurabh Kumar Ahirwar

Thesis submitted for the degree of Master of Philosophy

Supervisors:
Assoc. Prof. Stephen G. Bell
Prof. Simon Pyke

School of Physical Sciences

The University of Adelaide

March 2020

Contents

Abstract

The cytochrome P450 enzymes CYP101B1 and CYP101C1 from *Novosphingobium aromaticivorans* DSM12444 are homologues of the CYP101D1 and CYP101D2 enzymes from the same bacterium and CYP101A1 ($P450_{cam}$) from *Pseudomonas putida.* Both enzymes can efficiently hydroxylate norisoprenoids and related substrates in combination with the same ferredoxin reductase, ArR and a [2Fe-2S] ferredoxin, Arx, electron transfer partners. Even though the physiological substrates for both the enzymes are yet to be confirmed, the crystal structure of CYP101C1 bound to β-ionone and modelled structure of CYP101B1 has been generated. The Met82 residue of CYP101C1 aligns with the His85 residue of CYP101B1. In the crystallographic structure, this Met82 residue of CYP101C1, interacts with the carbonyl group of β-ionone, which makes it an interesting site for mutation as these could potentially alter the activity and hydroxylation of norisoprenoid substrates. CYP101B1 oxidised β-ionone with the highest product formation rate (1010 ± 60 min^{-1}). The CYP101C1 enzyme oxidised β-ionol with the highest product formation rate (1130 ± 30 min^{-1}), whereas, the M82L-CYP101C1 mutant enzyme had the highest product formation rate (790 ± 22 min^{-1}) with α-ionone. The selectivity for hydroxylation of norisoprenoids varies between CYP101B1 and CYP101C1. The M82L mutation however, did not change the selectivity for CYP101C1. For example, both β-damascone and β-ionone were hydroxylated at the C4 position by CYP101C1 and the M82L-CYP101C1 mutant. The CYP101B1 enzyme displayed an altered selectivity and hydroxylated these substrates predominantly at C3 position. When the substrate functional group was changed from a carbonyl to an alcohol (i.e. β-ionol), the hydroxylation occurred preferentially at the C3 position with all three enzymes. By comparing the oxidation of α-, β- and δ- substituted damascones, we found that the alkene moiety present inside the cyclohexyl ring did have an effect on the selectivity of oxidation. The α- substituted substrates are oxidised only at the C3 position by all three enzymes. The β- substituted substrates are oxidised at C3 position by CYP101B1 and at C4 position by CYP101C1 and M82L-CYP101C1. The δ- substituted substrate generates the 3,4-epoxide as the major product.

To further explore the substrate range of CYP101B1 and CYP101C1, various substrates including cyclic ketones and cyclic esters were assessed to see if they induce enzyme activity and binding to the enzyme. The combinations of the best enzyme / substrates were then chosen to generate the oxidation metabolites in a larger quantity using whole-cell oxidation system to enable characterisation. The oxidation of 1-decalone by CYP101B1 generated a single major metabolite along with two minor products. The major product was characterized as 6-hydroxy-1-decalone and the minor product as 7-hydroxy-1-decalone. Comparison of the 1-decalone substrate to damascones, highlight the relationship of the oxidation metabolites 6-hydroxy-1-decalone to 4-hydroxy-β-damascone and 7-hydroxy-1-decalone to 3-hydroxy-β-damascone. Oxacyclotridecan-2-one is oxidised by CYP101B1 on a carbon opposite to the carbonyl group. Along with these, muscone and cyclopentadecanone show a dissociation constant similar to β-ionone with CYP101B1. However, the spin-state shift and activity induced by both of these substrates to CYP101B1 are comparatively smaller than β-ionone. *p*-Tolyl acetate induced a large type-I spin-state shift and a weak binding to CYP101B1. It was oxidised at the benzylic methyl group, generating 7-hydroxy-*p*-tolyl acetate. Similarly, dihydroactinidiolide was also oxidised at the carbon opposite to the ester group generating 6-hydroxy-dihydroactinidiolide. However, this substrate induces a very small spin-state shift and was oxidised with low activity by CYP101B1. None of the tested substrate showed a spin-state shift larger than 10% HS or increased activity with CYP101C1.

Declaration

I certify that this work contains no material which has been accepted for the award of any other degree or diploma in my name, in any university or other tertiary institution and, to the best of my knowledge and belief, contains no material previously published or written by another person, except where due reference has been made in the text. In addition, I certify that no part of this work will, in the future, be used in a submission in my name, for any other degree or diploma in any university or other tertiary institution without the prior approval of the University of Adelaide and where applicable, any partner institution responsible for the joint-award of this degree.

I give permission for the digital version of my thesis to be made available on the web, via the University's digital research repository, the Library Search and also through web search engines, unless permission has been granted by the University to restrict access for a period time.

I acknowledge the support I have received for my research through the provision of an Australian Government Research Training Program Scholarship.

Saurabh Kumar Ahirwar

March 12, 2020

Acknowledgement

"*Part of the journey is the end*"!! – Tony stark, *Avengers Endgame*.

What a journey it has been to reach here. Being an international student, the last two years have been a life changing experience for me.

A big thanks and applaud goes to Assoc. Prof. Stephen Bell for countless insights, ideas and guidance without which this thesis would make no sense. It has been a pleasure learning under your guidance, thank you for choosing me to be a part of the Bell group and turning me into the scientist I am.

The same has to be extended to my co-supervisor Prof. Simon Pyke and The University of Adelaide and the graduate center, for providing me with this opportunity and for giving me a scholarship towards an M.Phil degree, without which it would be impossible for me to come and live in Australia.

Thank you to each and every member of the Bell group (past and present) for your support and friendship: Tom, Stella, Sherry, Raihan, Joel, Daniel, Matthew, Andrew, Heba and Amna. A big thanks to Andrew for helping me during the end of this work. All of you guys will be greatly missed.

Thank you to the Pukala group for all help and fun. Especially, Beejay, Katherine, Ruth and Henry. You guys have been an absolute delight.

A big thanks to Natasha, Katherine for proof reading and dealing with my terrible grammar. Thank you to the members of Chemistry department - in particular Michael for your friendship and showing me the good coffee shops in Adelaide.

A big shoutout to all friends in Adelaide: - in particular Gaurav, Jessie & Lori, Sugandha, Tanveen, Shivani, Akansha, Mansi, Parul, Anand, Nishanth, Ramu, Dave, James, Sarah, Soyena and many others whom I met as strangers and became family. Thank you to each and every one of you for all the wonderful memories, fun, support and encouragement, you guys will be missed a lot.

A big thanks to my old group in Spain (Paula Munin, Paula polo, Fatima, Adolfo, Julio, Francisco and Lara), you guys are awesome and thanks you for helping in the course of my journey to this thesis.

A big thanks to the professor who introduced me to research, Prof. P K Iyer (Dept. of Chemistry, IIT Guwahati), I am forever grateful to you sir.

A big thanks to my IITG family, you guys have been a big motivation to push me forward and I have missed hanging with you guys a lot; Ganesh, Utkarsh, Akhil, Gaurav, Ravi, Arnav, Lalli, Gajbhe, Chhao, Avinash, Tapan and Srijan.

Finally, my family without whom this study would simply not have been accomplished-

Mom, Dad, Shubhanshu (brother) and Ayushi (sister), I would be absolutely nowhere without you guys. Thank you for the never-ending love and support.

A big thank you to the most awesome, loving and caring "*Shivani Agrawal*", you have been a constant source of support throughout the ups and downs of my life. I am always inspired by your passion and enthusiasm, thank you for tolerating me and cheering me up when needed.

"*Happiness can be found even in the darkest of times, if one only remembers to turn on the lights"*

-*Albus Dumbledore,* Harry potter and the prisoner of Azkaban.

"*Life is like topography, Hobbes. There are summits of happiness and success, hat stretches of boring routine and valley of frustration and failure*"

-Calvin and Hobbes.

Chapter-1

Introduction

1.1 Background information on Cytochrome P450s

Cytochrome P450 (CYPs or P450s) enzymes were first observed in 1958, independently by Garfinkel and Klingenberg. Each of them identified a CO-bound pigment at 450 nm in rat and pig liver microsomes [1, 2]. Later, keywork by Omura and Sato confirmed the haemoprotein nature of these pigments [3]. These enzymes make up a large superfamily of haem-dependent monooxygenases, which catalyse a diverse range of biological oxidative transformations. Enzymes are often favoured over chemical catalysts due to high energy efficiency and low environmental impact, specifically the absence of waste product. The high efficiency of CYP enzymes under mild conditions and their ability to catalyse numerous reactions has led to a significant body of research into the mechanisms of substrate binding and oxidation [4, 5].

CYP enzymes are found across all kingdoms of life, including bacteria, fungi, plants and mammals. In prokaryotic organisms, P450s are involved in a number of oxidation reactions while in eukaryotes, P450s are involved in a wide range of biosynthetic and biodegradative transformations which include the synthesis of steroids and xenobiotic metabolism [6]. Due to their characteristic reactions, these enzymes have been proposed as catalysts for the synthesis of fine chemicals and intermediates which are very difficult to synthesise using the usual chemical synthesis techniques. Enantioselectivity is an important concern when dealing with pharmaceuticals. For example; the thalidomide disaster in 1950 where pregnant women were given thalidomide to treat nausea, but it was given as a racemic mixture. The R enantiomer was a sedative but the S enantiomer encouraged the release of alpha tumour “necrosis”, which caused more than 12,000 birth defects [7]. Cytochrome P450 enzymes could provide an enantio- and regio-selective route for hydroxylation reactions for the synthesis of fine chemicals.

Poulos and team reported the first high resolution three dimensional structure of a P450 in 1987 [8]. It showed that the P450s contain a central iron (III) atom coordinated to four nitrogen ligand donors of porphyrin ring, a proximal cysteine (Cys) residue and a water molecule as the sixth ligand in the resting state (Figure 1.1) [9].

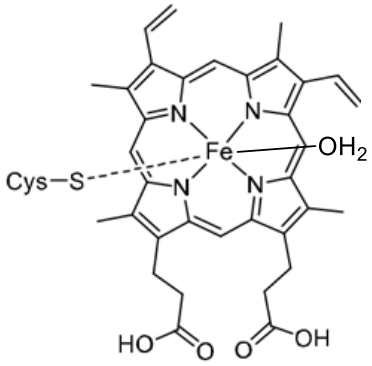

Figure 1.1: Haem centre in P450 enzymes [9].

1.2 P450's structure and characteristics

In their resting ferric state, P450s absorb visible light at 419 nm, which accounts for their distinctive red colour. In "P450", the "P" stands for pigment, whereas, the "450" is derived from the unique Soret absorbance band in the reduced CO-bound form of the enzyme [3, 4]. At the time of writing, more than 41,000 P450 enzymes have been named and categorised, although genome mining has revealed a total of more than 300,000 P450 sequences across all life kingdoms, majority of which remain uncategorised [10]. Systematic naming of members of the P450 superfamily is based on sequence similarity and in some instances function [11, 12]. The family to which P450s belong to is denoted by the number following its CYP prefix, this indicates the cytochrome P450 enzyme, and the subfamily is denoted by the subsequent numeral [13]. For example, the bacterial enzyme CYP101B1 from the bacterium *Novosphingobium aromaticivorans*, is a member of the family 101 and the first member identified for subfamily B [14]. CYP family members are defined as those with a similarity in amino acid sequence of > 40%, while subfamilies have members with similarity > 55% [15]. Although sequence conservation between P450 proteins of different families may be less than 20%, the overall structural fold is highly conserved between most P450 enzymes. However, the active site environment for substrate recognition differs significantly between P450s, which makes cytochrome P450 one of the most versatile superfamily of biological catalysts. Some bacterial P450s, such as $P450_{cam}$ from *Psuedomonas putida*, can be easily produced using *Escherichia coli* (*E. coli*) and hence, they have been researched extensively since their discovery [16-18]. The P450s derived from plant and animal cells are anchored in the cell membrane, and are often more difficult to express and purify. Furthermore, these P450s are prone to denaturing, which can make experiments employing these systems difficult to perform.

Hydroxylation and C-H bond oxidation reactions are still one of the biggest challenges faced by the chemical and pharmaceutical industries, the reason being the unreactive nature of the saturated C-H bond. The approach used by industry currently requires high temperatures and pressures. Furthermore, the inorganic catalysts that are used are very expensive and often do not provide sufficient selectivity. The insertion of an oxygen atom from atmospheric dioxygen into an unactivated carbon-hydrogen bond within an organic substrate, is the primary function of P450s (Equation 1). This process occurs along with the formation of a H_2O molecule. Commonly, the two electrons required for oxidation are derived from NADH or NAD(P)H (Nicotinamide Adenine Dinucleotide Phosphate), and these are transferred one at a time by electron transfer partner proteins (Equation 1).

$$\text{R-H} + \text{NAD(P)H} + \text{O}_2 + \text{H}^+ \longrightarrow \text{R-OH} + \text{NAD(P)}^+ + \text{H}_2\text{O} \qquad (1)$$

Along with mono hydroxylation, P450 enzymes are also able to perform other reactions such as dealkylation of methoxy and methylamino groups, oxidation of sulfur containing compounds, desaturation of alkyl chains and oxidation of alkenes and alkynes [19-22].

1.3 Mechanisms followed during catalysis by Cytochrome P450s

The distinguishing feature in the structure of P450 enzymes is the heme centre (iron porphyrin IX), which is attached to the rest of the enzyme via a proximal cysteine thiolate (Cys) ligand bound to the iron (Figure 1.1) [15]. The P450 catalytic cycle is largely conserved for all the members of the superfamily [5, 9]. The catalytic cycle of P450 enzymes begins with Fe^{III}, with a water ligand coordinated to the 6th distal site (I), see Figure 1.2. Generally, this water ligand dissociates on substrate (R-H) binding (II). Next an electron sourced from NAD(P)H/NADH is supplied via electron transfer protein, which reduces the iron to Fe^{II} (III). This is followed by dioxygen binding to the Fe^{II} centre to form the dioxy complex (IV) followed by reduction by another electron (V). Protonation of the terminal oxygen atom (VI), then occurs which facilitates O-O bond heterolytic cleavage to form an iron(IV)-oxo porphyrin radical cation (VII) with release of a water molecule. The oxygen atom can now be inserted into the substrate via a radical rebound mechanism (Figure 1.3). The oxidised substrate now leaves the active site of P450 enzyme (VIII) while a water can now rebind to the distal site returning the enzyme to its resting state (I) [14].

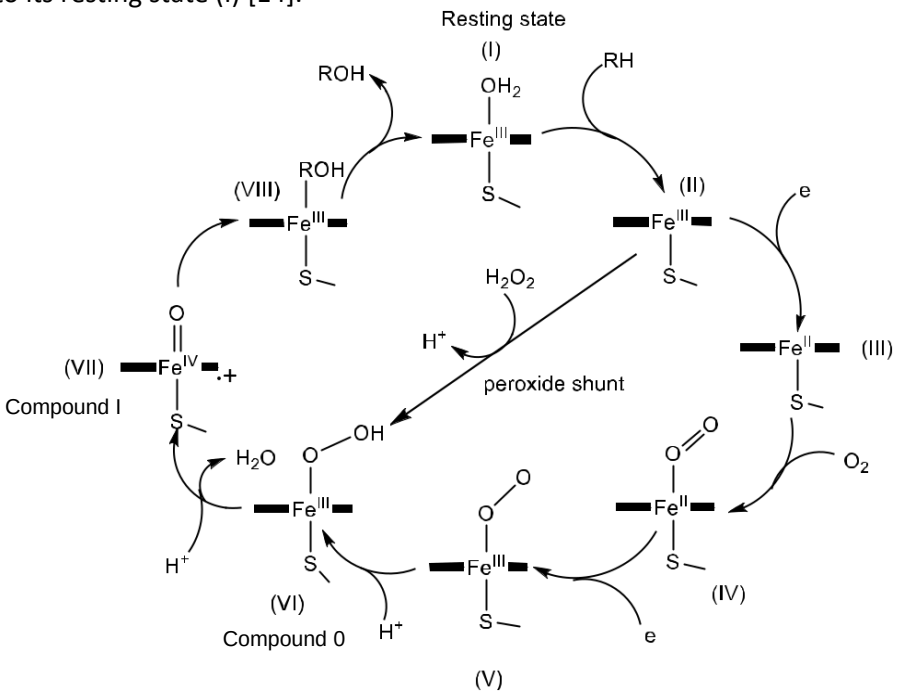

Figure 1.2: The catalytic cycle of P450 enzymes.

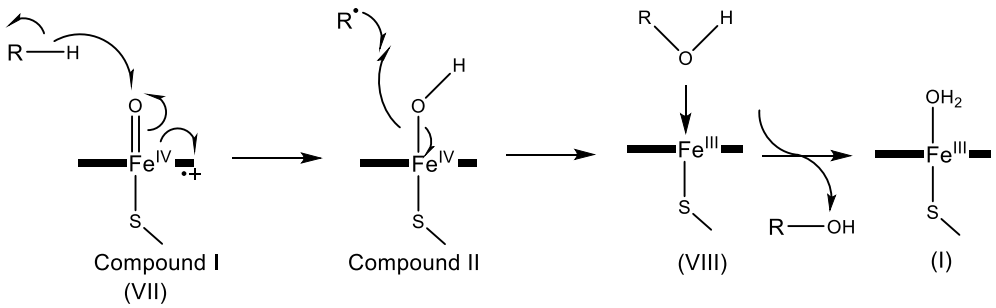

Figure 1.3: Oxidation of substrate (R-H) by Compound I via radical rebound mechanism [23].

The differences in the substrate range of P450s arises from the region around the enzyme active site. This also determines the overall chemical selectivity of the enzyme [9]. From the catalytic cycle (Figure 1.2), it is evident that the electrons are of utmost importance for a catalytic cycle to function successfully. The selective oxidation of a single C-H bond inside a specific substrate, is the most renowned ability of P450 enzymes. This occurs because the enzyme can hold one C-H bond of the substrate in a close vicinity of the iron haem centre of the involved enzyme. This selectivity is the reason for the popularity of P450 enzymes, which cannot be replicated using conventional chemistry methods [9, 24].

Uncoupling reactions take place to either produce water via an oxidase pathway or hydrogen peroxide, this could result in inactivation of the P450 instead of forming the desired product (Figure 1.4) [9, 10]. This uncoupling occurs, if the substrate is not held tightly in the active sight of enzyme. Due to this, even though a significant cycling of the catalytic cycle could be observed it would still not lead to the formation of product.

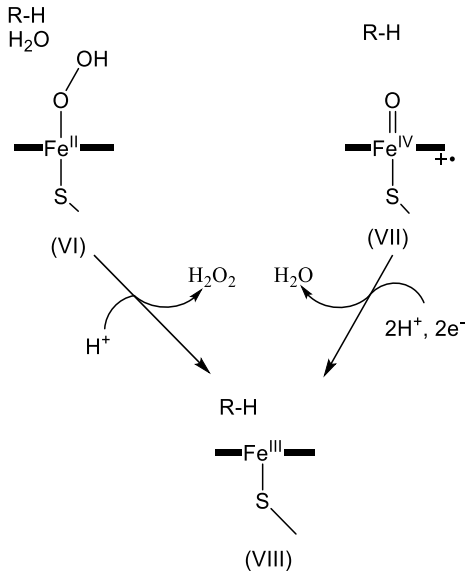

Figure 1.4: Uncoupling pathway followed by P450s.

The pathway that is followed by a reaction while hydrogen peroxide is produced, occurs during the reaction of a proton (H^+) with the oxygen atom connected to the iron haem at the centre in the compound (VI) rather than terminal oxygen. This pathway is more likely to be followed when the active site of enzyme contains an excessive amount of water [9]. The oxidase pathway occurs when two additional protons and electrons are added to the reactive oxygen atom in compound I (VII) [9, 10].

1.4 Electron transfer system of Cytochrome P450s

The electron transfer in Cytochrome P450 is mediated by multiple protein transfer partner systems, in which reducing equivalents from NADH are transferred to haem via one or more electron transfer partner proteins. The nature and number of these electron transfer partners varies between organisms [25]. The electron transfer partner of P450s are divided into two general classes, class I and class II. The class I electron transfer system consists of two electrons transfer proteins, a flavin containing reductase (FAD), which transfers reduction equivalents from a pyridine nucleotide (i.e. NADH or NAD(P)H) to an iron-sulphur ferredoxin (Fe_2S_2 or FMN) (Figure 1.5). This system is observed mostly in bacterial and mammalian mitochondrial P450s [26]. Whereas, in class II electron system both FAD and Flavin mononucleotide (FMN) cofactors are present together in one protein, which transfer electrons to the P450 enzyme. Both the enzymes in class II system are membrane bound (Figure 1.5: Right).These are mostly observed in eukaryotic system [26].

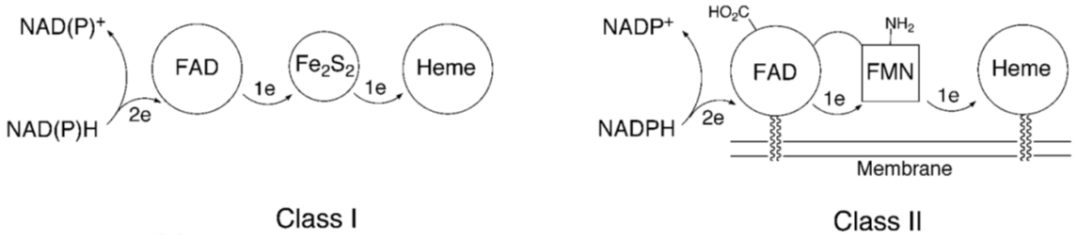

Figure 1.5: Electron transfer systems of cytochrome P450s. Shown are classes I and II. Left: shows the bacterial class I system. Right: class II, a diflavin membrane-bound system [25].

Numerous CYP enzymes with potentially interesting and desirable activities have been discovered. However, many of these enzymes are orphaned due to the absence of electron partners (FAD or FMN) located nearby in the genome sequence [19, 27-29]. Close clustering of CYP genes and electron transfer partner such as those found for CYP101A1, CYP176A1 and CYP105D1, is an exception rather than a rule [30-33]. For example, of the 174 CYP gene discovered from 45 different *Streptomyces* species, only 18 are clustered with a ferredoxin gene [34]. In these organisms, the genes encoding all possible electron transfer proteins could be expressed and then assessed for activity [33]. Alternatively, a known ferredoxin-reductase/ferredoxin system can be recruited to reconstitute the activity of enzyme in *in vitro* and *in vivo* oxidation system but such cross-reactions between different P450 electron transfer chains are often slow [35-37]. Sixteen potential P450 monooxygenase genes have been identified so far, within the genome of *Novosphingobium aromaticivorans* [14, 19]. In addition, a class I electron transfer system, containing of a flavin-dependent ferredoxin reductase, ArR and a ferredoxin, Arx, has been successfully identified that is able to reconstitute the monooxygenase activity of CYP101B1, CYP101C1, CYP101D1 CYP101D2 and CYP111A2 [14, 19, 38]. Other than carrying and transferring electrons, electron transfer proteins can also have additional roles. For example, putidaredoxin (Pdx) has an effector role in CYP101A1 ($P450_{cam}$) activity [39, 40]. Hence, in order to get an optimal catalytic activity, the identification of functional CYP electron transfer chains are often essential.

1.5 Oxidation of substrate by P450s

The catalytic cycle of P450s uses a highly reactive oxidising species, the ferryl intermediate (Figure 1.2, Compound I). This is generally believed to be the oxygen activating species in most P450 catalysis. The role of Compound I in hydroxylation reaction of P450s, has been broadly studied [41-43]. However, experimental studies have shown that the electrophilic ferric-hydroperoxide (Compound 0 or VI, see Figure 1.2) and the nucleophilic ferric-peroxo anion (V) could also be responsible for some monooxygenase activity [42, 44-46]. For example, Compound 0 has been reported to catalyse alkene epoxidation [44, 46], while the peroxo-anion has been implicated in aldehyde oxidation [47].

1.5.1 Hydrocarbon hydroxylation

The hydroxylation reaction catalysed by P450 enzymes is believed to proceed via the radical or oxygen rebound mechanism (Figure 1.3), which was first proposed by Groves and McClusky in 1976 [23, 48]. In the first step, the highly reactive ferryl oxygen abstracts a hydrogen atom from the alkyl substrate generating a Fe(IV)-OH species (Compound II) and the substrate radical (Figure 1.3). This remains bound within the active site of the enzyme, where it immediately recombines with the hydroxyl radical derived from the Fe(IV)-OH intermediate to give the alcohol product (Figure 1.3) [23, 49].

To further understand the involved mechanism, radical clock substrates containing strained ring systems like cyclopropyl have been widely employed to determine the rate of radical rebound in C-H hydroxylation (Figure 1.6 (a)). These substrates undergo rapid ring-opening reactions at known rates via a radical intermediate. If rebound occurs at the initial site of H-abstraction, hydroxylation product results with a rate of k_t (Figure 1.6 (a)). On the other hand, the radical can also go for rearrangement (k_r) followed by trapping of the rearranged radical yielding a different hydroxylated product (Figure 1.6 (a)). The ratio of these products together with the known rate constant of the rearrangement reaction enables the lifetime of the radical to be calculated. Using radical clocks, radical lifetimes (~50 ps) were calculated for norcarane and bicyclo[2,1,0]pentane when oxidised by P450s like, CYP2B1, CYP2E1, $P450_{cam}$ and $P450_{BM3}$ [50].

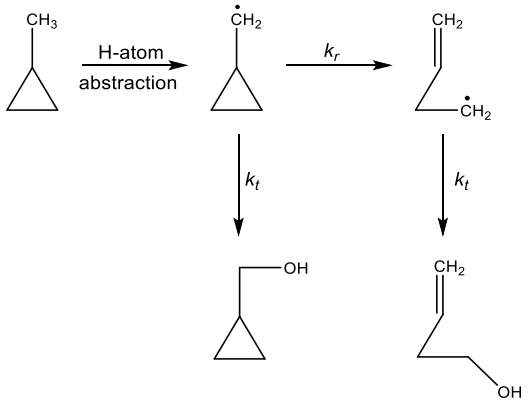

Figure 1.6 (a): Function of a methyl cyclopropane as a radical clock. Radical trapping (k_t) and rearrangement (k_r) resulting in different products.

However, recent studies using ultrafast radical clock suggest that the norcrane radical has a significantly shorter lifetime 0.5-25 ps [51, 52]. Furthermore, several ultrafast clocks displayed shorter than expected radical lifetimes, which suggests that the radical to be a transition state not a reaction intermediate [53-56].

A two-state reactivity model calculated that the hydroxylation can proceed via a radical or a cation intermediate character dependent on the dominant spin-state of the iron in Compound I (Figure 1.6 (b)) [57]. Based on DFT calculations, the short radical lifetime observed in certain experiment is explained by barrier-free radical rebound pathway when Compound I is in the low spin state (doublet) and the longer lifetime due to the high energy barrier in the high spin state (quartet) (Figure 1.6 (b)). The energy barrier in the radical rebound mechanism for the high spin pathway leads to an alternate reaction involving a cationic intermediate, while this barrier for the low spin state is negligible. Consequently, if Compound I is in low spin state, the radical rebound mechanism is favoured (Figure 1.6 (b)) [57].

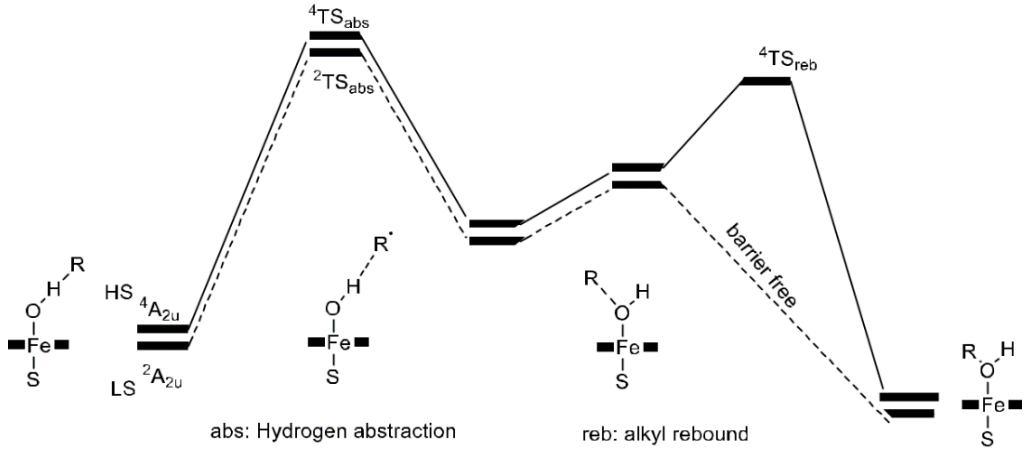

Figure 1.6 (b): DFT-based mechanism for hydroxylation from high spin (HS: $^4A_{2u}$, solid line) and low spin states (LS: $^2A_{2u}$, dashed line) of Compound I. TS refers to the transition state [58-61].

Recently, a concerted catalytic mechanism has been proposed, which suggests that along with two-state reactivity, it is also important to consider the way in which the enzyme controls the reaction trajectory [49]. The C-H abstraction and rebound phase of the hydroxylation can be brought closer together in time to generate a dynamically concerted mechanism. A reaction is considered as dynamically concerted if it consists of two bond forming / bond breaking processes and the time gap between the first and the second bond forming / bond breaking event is less 60 fs (which is the lifetime for a transition state with a zero-energy barrier). The reaction is considered to be dynamically stepwise if the time gap is longer than 60 fs [49].

1.5.2 Epoxidation of alkenes

Alkene epoxidation is also a common reaction catalysed by P450s which usually displays stereoselectivity. This suggests a concerted mechanism by the enzyme in which the ferryl oxygen interacts with both the carbon atoms of the alkene at the same time [62, 63] (Figure 1.7).

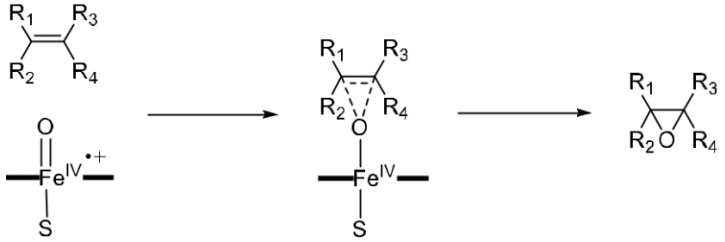

Figure 1.7: The concerted mechanism of alkene epoxidation by Compound I [62, 63].

Both Compound I and Compound 0, have been reported to be capable of epoxidation. The two-state reactivity model (TSR) of the low spin and high spin states of Compound I has been assessed [64]. The low spin state gives rise to the radical intermediate taking place due to the low energy barrier (Figure 1.8). On the other hand, the high spin state has a higher energy barrier which increases the lifetime of the intermediate, which leads to a stereoselective product via a carbocation (Figure 1.8) [65-68]. Compound 0 has been reported to have a much larger barrier for epoxidation reactions compared to Compound I [64].

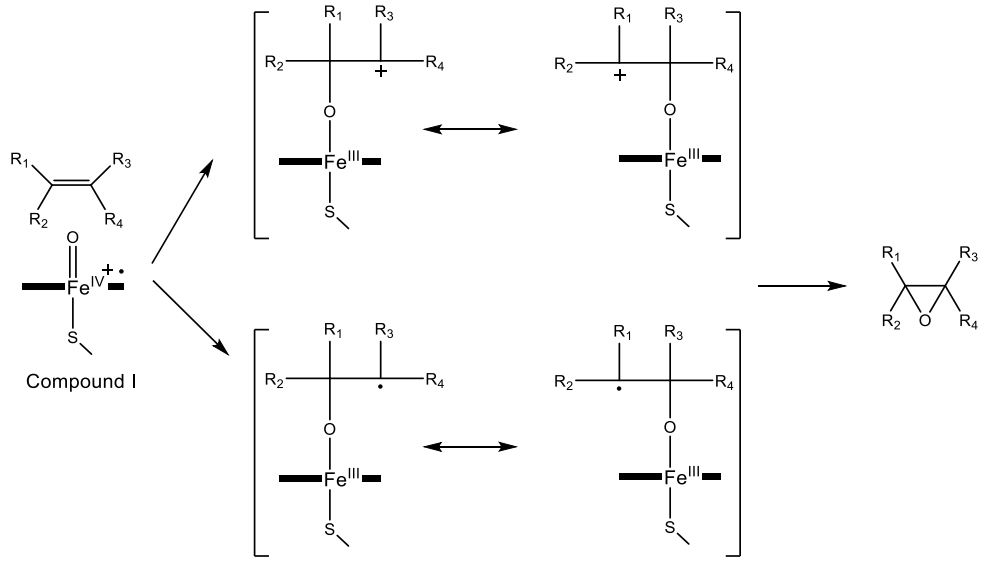

Figure 1.8: Epoxidation of alkene by Compound I through a cationic (top) and radical (bottom) pathways.

However, epoxides are not the only products that can arise from P450-catalysed alkene oxidation and rearranged products like aldehydes or ketones can also be observed. This could be explained by the transfer of an electron between a C-radical and Fe (IV) with the generation of a carbocation intermediate. In this case, the less substituted carbon binds to the Fe(IV)-oxyl and one substituent migrates to generate a ketone or aldehyde product (Figure 1.9) [65].

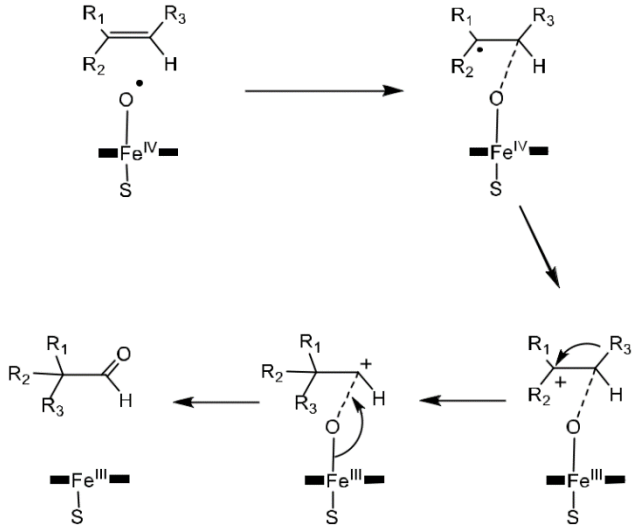

Figure 1.9: Mechanism of rearrangement product by P450 enzyme instead of epoxidation.

1.5 CYP101A1

CYP101A1, also referred as $P450_{cam}$ catalyses the selective oxidation of camphor to 5-*exo*-hydroxycamphor (Figure 1.10) [69, 70]. This enzyme is extracted from the soil bacterium *Pseudomonas putida* [69, 70]. Since its discovery in 1968, it has been used extensively to study the general mechanism of P450s [70, 71]. $P450_{cam}$ was the first bacterial P450 enzyme to be successfully expressed using *E. coli.* and isolated recombinantly for *in vitro* oxidation turnover studies [16, 17]. $P450_{cam}$ uses a class I electron transfer system with two electron transfer partners, a FAD containing putidaredoxin reductase (PdR) and a [2Fe-2S] putidaredoxin ferredoxin (Pdx) [25].

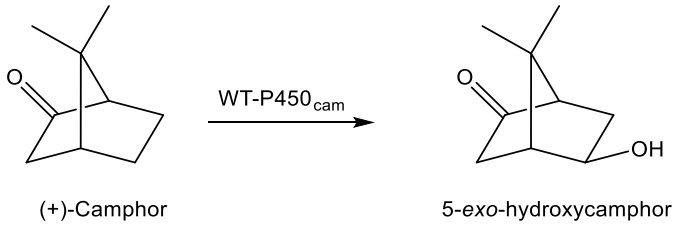

Figure 1.10: Conversion of camphor to 5-*exo*-hydroxycamphor by $P450_{cam}$.

The reported crystallographic structure of $P450_{cam}$ (PDB ID: 3WRH) (Figure 1.11) is of interest for protein engineering studies [8]. Many crystallographic studies of this enzyme have enhanced our understanding regarding which active site residues are responsible for the biocatalytic selectivity of $P450_{cam}$ [72, 73]. This led to the development of mutated $P450_{cam}$ enzymes by substituting alternative residues in the active site. This optimisation improved the biocatalytic activity towards different substrates. For example, $P450_{cam}$ naturally binds to camphor and exclusively oxidises it to 5-*exo*-hydroxycamphor as the sole biproduct (Figure 1.10). However, the bicyclic compound (+)-α-pinene, which has structural similarity with (+)-camphor, the selectivity for the oxidation by $P450_{cam}$ is much lower, it generates minor products along with the expected product, (+)-verbenol [74] (Figure 1.12).

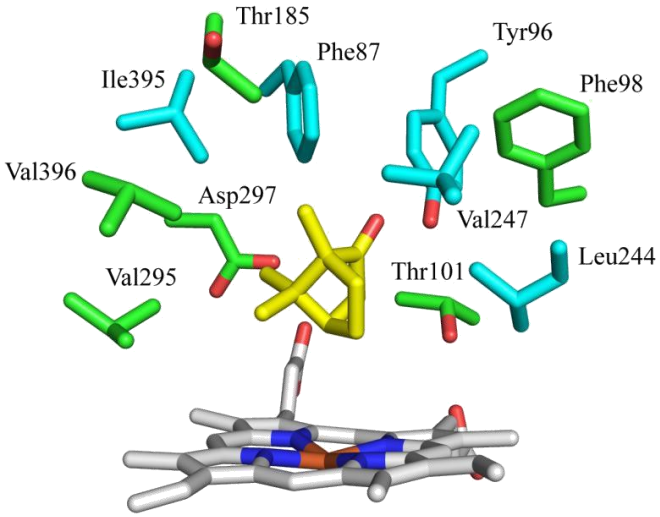

Figure 1.11: Crystal structure of camphor bound CYP101A1 ($P450_{cam}$) (PDB ID: 3WRH) [8].

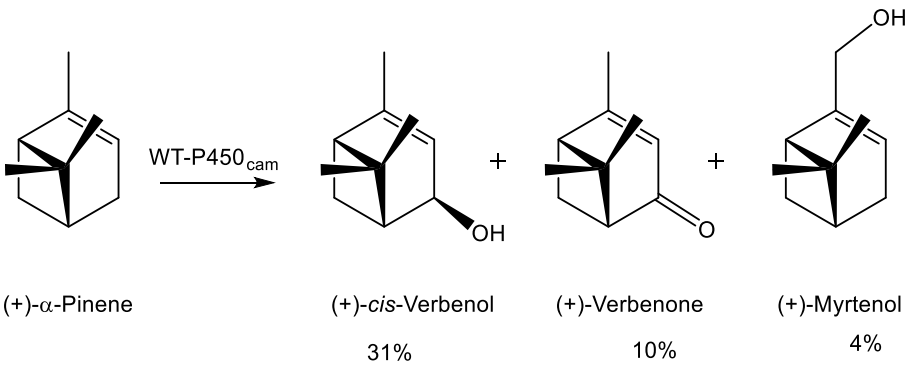

Figure 1.12: Products from (+)-α-pinene oxidation catalysed by $P450_{cam}$ [74].

1.6 P450 enzymes from *Novosphingobium aromaticivorans*.

Novosphingobium aromaticivorans DSM12444, is a gram-negative aerobic bacterium. It possess sixteen genes that encode for P450 enzymes which are capable of oxidising a wide variety of substrates including terpenes, linear alkanes and polyaromatic hydrocarbons [14, 75, 76]. This range of substrates of monooxygenase enzymes of *N. aromaticivorans* is believed to be due to the need of bacteria to metabolise xenobiotic compounds present in its environment in order to grow [77]. The sixteen P450s of this bacterium were classified into ten different families which includes CYP101 and CYP111 [19, 77]. The four CYP101 member and CYP111 use a common class I electron transfer system (Figure 1.5), which consists of a FAD containing ferredoxin reductase (ArR) and a [2Fe-2S] ferredoxin (Arx) [19]. The physiological electron transfer partner of five enzymes (CYP101B1, CYP101C1, CYP101D1, CYP101D2 and CYP111A2) have been successfully produced using *E. coli* [14, 19]. *E. coli* has also been used as a host for whole cell oxidation using these enzymes for the formation of product at a gram per litre scale. Therefore, these enzyme systems are suitable for use in larger scale biocatalysis [19]. It is of noteworthy that the gene for CYP101B1 is located on a plasmid, whereas those of CYP101C1, CYP101D1, CYP101D2, along with ArR and Arx, are on the chromosomal genomic DNA [14, 19].

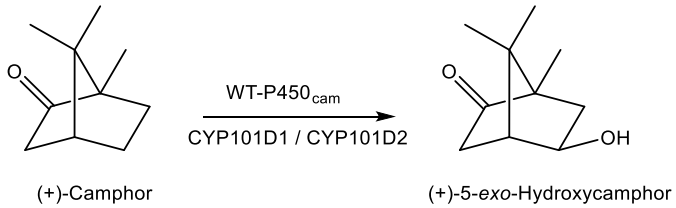

Figure 1.13: Oxidation of camphor by $P450_{cam}$, CYP101D1 and CYP101D2.

CYP101A1 ($P450_{cam}$) belongs to the same family as these CYP101 enzymes. Selective camphor hydroxylation is also observed with both the CYP101D1 and CYP101D2 enzymes (Figure 1.13) [14, 19]. However, in case of CYP101B1, camphor is oxidised to form 5-*exo*-hydroxycamphor as the major product along with the formation of four separate metabolites in minor quantities (Figure 1.14) [14]. Instead of camphor, CYP101B1 has been reported to selectively oxidise β-ionone to 3-hydroxy-β-ionone with higher activity and binding affinity (Figure 1.14) [14]. β-Ionone induces a large type-I spin state shift of > 95% and a tight dissociation constant of K_d = 0.23 μM [76].

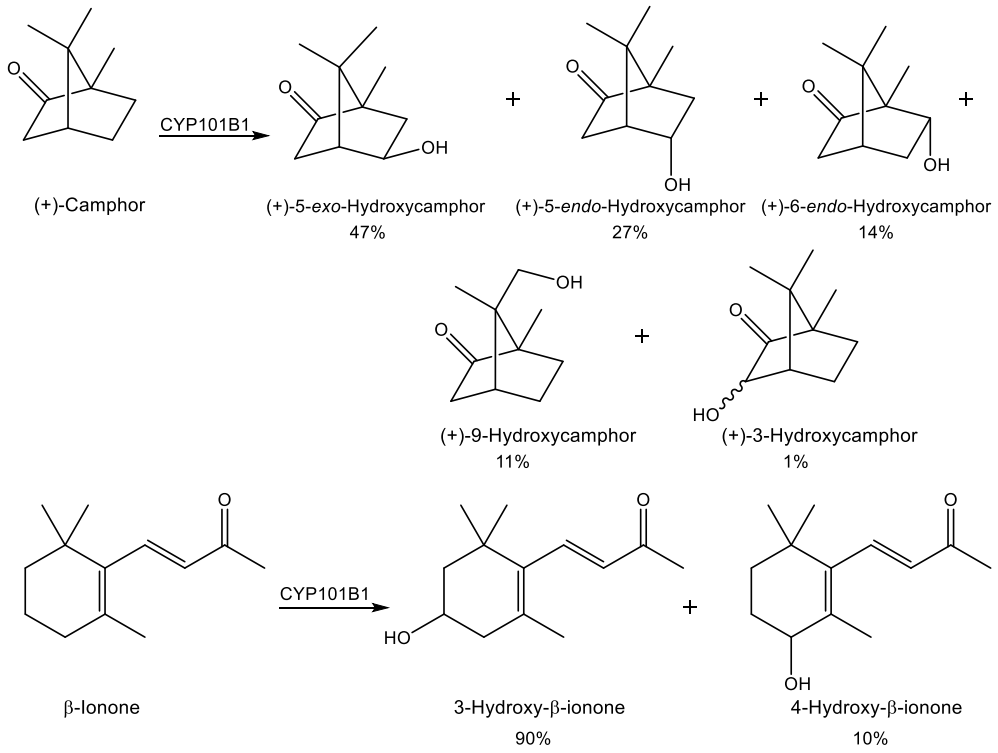

Figure 1.14: Oxidation of camphor (top) and β-ionone (bottom) by CYP101B1. The product distribution is given in percentage.

CYP101C1, which is also from *N. aromaticivorans,* is a homologue of $P450_{cam}$ (CYP101A1) and CYP101B1. It shares the same electron transfer partner (ArR/Arx) with CYP101B1 and use a class I electron transfer system [78]. Even though CYP101C1 shares 43% sequence identity with $P450_{cam}$, it displays minimal activity for camphor oxidation [78]. However, like CYP101B1, CYP101C1 also oxidises norisoprenoid substrates [14]. Even though, CYP101C1 oxidises β-ionone to generate the same metabolites as CYP101B1, its selectivity is altered to generate the 4-hydroxy-β-ionone as the major product (Figure 1.15) [14].

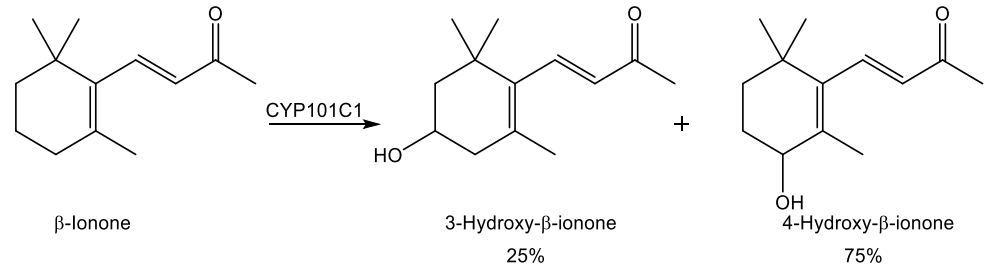

Figure 1.15: Oxidation of β-ionone by CYP101C1. The product distribution is given in percentage.

The crystal structure of CYP101A1, CYP101C1, CYP101D1 and CYP101D2 have been solved but not for CYP101B1. The crystal structure of CYP101C1 bound to β-ionone (Figure 1.16) has been reported, which shows that it has a open conformation with an access channel in similar position to those found in CYP101A1 [78]. However, the structure of CYP101C1 displays various differences at the active site, and the proximal face [78]. The crystal structure of β-ionone bound CYP101C1 shows that the substrate is in van der Waals contact with majority of the active site residues, and that the butenyl side chain is pointing away from the heme [78]. There is an interaction between the carbonyl group

of the substrate with the Met82 residue, this suggest that the Met82 active site might help orient the substrate.

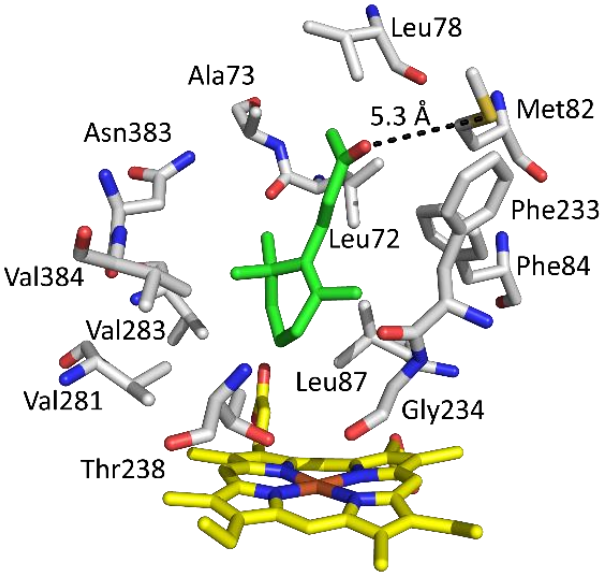

Figure 1.16: Crystal structure of β-ionone bound CYP101C1 (PDB ID: 3OFU) [78].

1.7 Thesis objective

In this thesis we will study the activity and selectivity of CYP101C1 enzyme on addition of norisoprenoid substrates. Using protein engineering, site specific mutation was performed on CYP101C1 enzyme to generate the M82L-CYP101C1 mutant variant with the intention of investigating the effect of this change on the activity of norisoprenoid substrates. This mutated enzyme will be tested alongside both wild type CYP101C1 and CYP101B1 enzyme to identify the change in selectivity. The whole-cell system will also be used to synthesise the metabolites in a larger quantity for characterisation.

Furthermore, the CYP101B1 and CYP101C1 enzyme has been reported to efficiently oxidise various other substrates like cyclic ketones, cyclic esters and monoterpenoids. To further explore the potential of these enzymes to be used as biocatalysts for other valuable chemical or drug metabolite synthesis, they will be tested with a series of compounds which contains ester, ketone, amide and other similar functional groups. This will give us the data to explore the substrate range of both CYP101B1 and CYP101C1. The best suited substrate to the enzyme will then be studied extensively using whole-cell turnover.

Chapter-2

Experimental

2.1 General

Substrates, solvents and the reagents were purchased from Merk (Australia), Tokyo Chemical Industry (Tokyo), Australian Botanical Products (Australia), Alfa Aesar (United Kingdom) and Flurochem (United Kingdom). Biological reagents such as antibiotics, dithiothreitol (DTT) and isopropyl β-D-1-thiogalactopyranoside (IPTG) were purchased from Anachem (Astral Scientific, Australia) or Biovectra (Scimar, Australia).

2.2 Cell culture media and Buffer solutions

Media and buffers used for bacterial growth and whole-cell turnovers were as follows (all reagent quantities listed below are for one litre of media in MQ water):

Super Optimal broth with Catabolite repression (SOC):

- Tryptone (20 g)
- Yeast extract (5 g)
- $MgCl_2$ (1 g)
- NaCl (0.5 g)
- KCl (0.2 g)
- 0.2% w/v glucose

Lysogeny Broth (LB):

- Tryptone (10g)
- Yeast extract (5g)
- NaCl (10g)

20X PBS† (pH = 7.2):

- NaCl (160 g)
- KCl (4 g)
- Na_2HPO_4 (2.88 g)
- KH_2PO_4 (4 g)

Trace Elements:

- Na_2EDTA (20.1g)
- $FeCl_3.6H_2O$ (16.7g)
- $CaCl_2.H_2O$ (0.74g)
- $CoCl_2.6H_2O$ (0.25g)
- $ZnSO_4.7H_2O$ (0.18g)
- $MnSO_4.4H_2O$ (0.132g)
- $CuSO_4.5H_2O$ (0.10g)

E. Coli minimal media (EMM):

- K_2HPO_4 (7g)
- KH_2PO_4 (3g)
- $(NH_4)_2SO_4$ (1g)
- Na_3Citrate (0.5g)
- $MgSO_4$ (0.1g) and 20% w/v glucose (20mL) were added after autoclaving.

Tris buffer[†] (1M stock) (pH = 7.4):

- Tris(hydroxymethyl)aminomethane (121.1 g)

[†]pH adjusted using HCl or NaOH

For LB media, antibiotics were added to working concentrations: of 100 µg/mL and 30 µg/mL for ampicillin (amp) and kanamycin (kan) respectively.

UV/Vis spectroscopy was performed on a Varian Cary 60 spectrophotometer (Agilent), and the assays were recorded at 30 ± 0.5˚C. Details of gas chromatography-mass spectrometry (GC-MS) and gas chromatography (GC) analyses, methods, columns and instrument conditions are provided in Table 1.1. High performance liquid chromatography (HPLC) analyses were performed using a Shimadzu HPLC, in combination with six different units comprising of a DGO-20AR degassing unit, two LC-20AR solvent delivery modules, CBM-20A/20Alite system controller, SIL-20AC$_{HT}$UFLC autosampler, SPD-M20A photodiode array UV-Vis detector (monitored between 250 to 400 nm range) and a FRC-10A fraction collector connected to a straight phase silica column (250 mm x 10 mm, 5 µm). The products were separated using a 5-70% isopropanol-hexane gradient with 3 mL min^{-1} flow rate over 38 minutes.

NMR spectra were acquired on an Agilent DD2 spectrometer operating at 500 MHz for ^{1}H and 126 MHz for ^{13}C or a Varian Inova-600 spectrometer operating at 600 MHz for ^{1}H and 151 MHz for ^{13}C. A combination of ^{1}H, ^{13}C, COSY, HSQC and HMBC experiments were used to determine the structure of the products.

Table 1.1: GC and GC-MS operating conditions

GC-MS	Shimadzu GC-2010 coupled with GC-MS-QP2010S detector
Column	SPB5 MS fused silica column (30 mm x 0.25 mm x 0.25 µm)
Column carrier gas **Injector and interface temperature**	Helium (flow rate 1.3 ml^{-1}) 250 ˚C and 280 ˚C
Oven Method for norisoprenoids	120 ˚C (hold 3 min), 10 ˚C min^{-1} to 240 ˚C (hold 5 min)
Oven Method for sesquiterpenes	160 ˚C (hold 3 min), 5 ˚C min^{-1} to 250 ˚C (hold 4 min)
Column	Rtx-5 MS fused silica column (30 mm x 0.25 mm x 0.25 µm)
Column carrier gas **Injector and interface temperature**	Helium (flow rate 1.3 ml min^{-1}) 250 ˚C and 280 ˚C
Oven Method for Norcarane ester and norcarane alcohol	120 ˚C (hold 3 min), 9 ˚C min^{-1} to 240 ˚C
GC	**Shimadzu Nexis GC-2030 coupled to flame ionisation detector (FID)**
Column	Agilent DB-wax UI column (30 mm x 0.25 mm x 0.25 µm)
Column carrier gas **Injector and FID temprature**	Helium (flowrate 1.3 ml min^{-1}) 250 ˚C
Oven Method for Norisoprenoids	160 ˚C (hold 3 min), 5 ˚C min^{-1} to 220 ˚C

2.3 Whole-cell turnovers

DNA vectors pETDuet containing ferredoxin reductase (ArR) and ferredoxin (Arx) genes and pRSFDuet harbouring the appropriate CYP101B1 or CYP101C1 gene with Arx were transformed into BL21(DE3) (40 µL) *Escherichia coli* (*E. coli*) cells and kept on ice for 1 h [19]. The sample was then heat shocked at 42˚C for 1 min before being returned to the ice for 2 min. SOC media (150 µL) was added to the sample, which was shaken at 37˚C at 200 rpm for 1 h. The solution was then spread onto an $LB_{amp/kan}$ antibiotic plate and heated at 37˚C for 5 min with the lid partially open to get rid of any residual liquid. The plate was inverted and incubated at 37˚C overnight. A single colony was removed and grown in $LB_{amp/kan}$ (500 mL) supplemented with kanamycin (0.1% v/v from 30 µg/mL stock solution) and ampicillin (0.1% v/v from 100 µg/mL stock solution) antibiotics and grown at 37˚C at 120 rpm for 8 h. The temperature was decreased to 18˚C over 30 mins, followed by the addition of ethanol (2% v/v), benzyl alcohol (0.02% v/v) and trace element solution (1.5 mL). Protein production was induced by adding IPTG (100 µL of 0.1 M stock solution). The culture was then incubated for a further 48 to 72 h at 18˚C and 90 rpm. Cells were harvested by centrifugation (5000g, 10 min, 4˚C) and resuspended in EMM media (1 L per 500 mL of culture). The resuspended cells were split and 200 mL aliquots were transferred to a 2 L baffled flask and substrate (1-2 mM) was added. The flask was then shaken at 30˚C and 160 rpm for 2 h. Two aliquots of substrate (2 mM) were added at an interval of 2 h. Additional glucose (2 mL from 20% v/v solution) and phosphate-buffered saline (20x PBS, 2.5% v/v) was added with the last aliquot and continued to incubate for 8 h before the cells were removed from the supernatant by centrifugation (5000 g, 10 min, 4˚C).

The supernatant from the whole-cell turnover was extracted in ethyl acetate (3 x 100 mL), washed with brine (100 mL) and dried using sodium sulphate (Na_2SO_4). The organic extracts were pooled and the solvent was removed under reduced pressure. The UV inactive substrate and their metabolite were loaded onto a silica column for flash chromatography using a hexane/ethyl acetate stepwise gradient ranging from 85:15 to 20:80 hexane to ethyl acetate system using 1.5% increase in ethyl

acetate every 50 mL. The composition of the fractions was assessed by TLC and GC and those containing a single product were combined for characterisation. The solvent was removed under reduced pressure again.

The UV active substrates and their metabolites were purified using HPLC with a straight phase silica column (250 mm, 10 mm; 0.5 µm) using a binary gradient 10:90 to 70:30 isopropanol to hexane system. The solvent was then removed under reduced pressure and then a stream of nitrogen. The purified products (ranging from 4~15 mg) were dissolved in $CDCl_3$ with tetramethyl silane (TMS) and the organics analysed by NMR spectroscopy.

2.4 Enzyme Purification

2.4.1 Purification of CYP101B1 and CYP101C1

BL21(DE3) *E.coli.* competent cells were transformed with a plasmid vector (pET26; Merck Milipore, United States) harbouring the appropriate CYP101B1 and CYP101C1 gene and grown on LB_{kan} plate [14]. A single colony was added to each flask of LB_{kan} (500 mL in 2 L conical flask) and incubated at 37˚C at 120 rpm for 8 h. The temperature was decreased to 18˚C over 30 min. Ethanol (2% v/v) and benzyl alcohol (0.02% v/v) were then added. The culture was allowed to shake for another 20 min and then protein expression was induced with 0.1 mM IPTG. The culture was further incubated for 48 to 72 hours at 18˚C and 90 rpm. Cells were harvested by centrifugation (5000g, 10 min, 4˚C) and stored before purification at -20˚C. Pallets were resuspended in 50 mM Tris buffer (pH 7.4, 250 mL) containing 1 mM DTT (buffer T) and lysed by sonication (Autotune CV334, Sonics and Materials, United States) using 80 x 20 s pulses with 40 s intervals. The resulting suspension was immediately centrifuged (40000 rpm, 25 min, 4˚C) to remove cell debris and the pellet was discarded. The supernatant was then loaded onto a DEAE Sepharose column (XK50, 200 mm x 40 mm; GE Healthcare,US), and purified using a gradient from 100 to 250 mM KCl in buffer T at a flow rate of 6 mL min^{-1}. Red coloured fractions were combined and concentrated by ultrafiltration (10 kDa exclusion membrane). The concentrated protein was desalted using a Sephadex G-25 medium grain column from (200 mm x 40 mm; GE Healthcare), eluted using buffer T.

The desalted protein was concentrated and loaded onto a Source-Q ion exchange column (XK26, 80 mm x 30 mm; GE Healthcare) linked to an AKTA Pure (GE Healthcare), and eluted using a linear gradient from 0 to 500 mM KCl in buffer T. Fractions with $A_{419}/A_{280} > 2$ were collected and concentrated using an ultrafiltration cell with a 10 kDa exclusion membrane until the P450 reached approximately 10 mL volume. The solution was then centrifuged (5000 g, 10 min, 4˚C) to remove any debris. The protein was mixed with an equal amount of 80% glycerol and then filtered using a 0.22 µm syringe filter and stored at -20˚C. The extinction coefficients of CYP101B1 and CYP101C1 were reported as $\varepsilon_{417} = 113$ mM^{-1} cm^{-1} and $\varepsilon_{417} = 121$ mM^{-1} cm^{-1}, respectively and were henceforth used to determine the concentration of the enzymes [19].

2.4.2 Purification of ArR (Ferredoxin Reductase)

BL21(DE3) *E.coli.* competent cells (30 µL) were transformed with pET26 vector containing ArR gene and grown on a LB_{kan} antibiotic plate overnight at 37˚C [19]. Four of the grown colonies were picked and added to four separate LB_{kan} (4 X 500 mL) solutions. The culture was then incubated and harvested as described in section 2.4.1. The cell pellets were then resuspended in 50 mM buffer T (pH 7.4, 200 mL). The cells were then lysed via sonication (Autotune CV334) using 80 x 20 s cycle with 40 s intervals. The resulting suspension was centrifuged (37,000 g, 20 min, 4˚C) to discard any cell debris and the yellow coloured supernatant containing the protein was retained.

The protein was loaded onto a DEAE Sepharose Column (XK50, 200 mm x 40 mm; GE healthcare) using a gradient from 100mM to 400mM KCl in buffer T at a flow rate of 6 mL min^{-1}. The yellow coloured fractions were combined and concentrated by ultrafiltration (10 kDa exclusion membrane). The concentrated protein was then desalted using a Sephadex G-25 medium grain column (250mm x 40 mm; GE Healthcare) using buffer T. Desalted protein was further purified using a Source-Q ion exchange column (XK26, 80 mm x 30mm; GE Healthcare) using a linear gradient from 0 to 400 mM KCl in buffer T. The yellow coloured fractions with $A_{280}/A_{458} < 8$ were combined together and concentrated using ultrafiltration until the ArR reached an approximate volume of 10 mL. The concentrated protein was centrifuged (5000 g, 10 min, 4˚C) to remove any particulate matter and diluted with an equal amount of 80% glycerol before filtering with a sterile 0.22 µm syringe filter and stored at -20˚C. The ArR concentration was estimated using extinction coefficient, ε_{458} = 10 mM^{-1} cm^{-1}, which were henceforth used to determine the concentration of the enzyme [19].

2.4.3 Purification of Arx (Ferredoxin)

DNA vector pRSFDuet-Arx was transformed into BL21(DE3) *E. coli.* Competent cells (40 µL) and grown on an LB_{kan} antibiotic plate at 37˚C overnight [19]. A single colony was then removed and added to a flask of 500 mL of LB_{kan} media and incubated at 37˚C and 120 rpm overnight. The culture was incubated to produce protein and harvest cell pellets as described in section 2.4.1. The cell pellets were resuspended in 10 mM buffer T (pH 7.4, 300 mL) containing 1 mM DTT, 20% v/v glycerol, 1% v/v 2-mercaptoethanol, 300 mg lysozyme, 2 mL Trixton X-100 and 2 mL Tween 20. Resuspended cells were stirred for 30 min at 4˚C. The cells were lysed by sonication using 80 x 20 s pulses with 40 s interval. The resulting suspension was centrifuged (37000 g, 20 min, 4˚C) to remove the cell debris. Brown supernatant was collected and loaded onto a DEAE Sepharose column (XK50, 200 mm x 40 mm; GE Healthcare) and the protein was eluted using a salt gradient of 100 to 400 mM KCl in buffer T at a flow rate of 6 mL min^{-1}. Brown coloured fractions containing ferredoxin were then collected and concentrated by ultrafiltration (10 kDa exclusion membrane). The concentrated protein was desalted using Sephadex G-25 medium grain column (200 mm x 40 mm) pre-equilibrated with buffer T (pH 7.4, 50 mM). The desalted protein was further purified using a Source-Q ion-exchange column (XK26, 80 mm x 30 mm; GE Healthcare) with elution using a gradient from 0 to 200 mM KCl in buffer T (pH 7.4, 50 mM) at a flow rate of 6 mL min^{-1}. Fractions with $A_{415}/A_{280} > 0.6$, were collected and concentrated using ultrafiltration (10 kDa exclusion membrane). The concentrated protein was then centrifuged (5000 g, 10 min, 4˚C) to get rid of any particulate matter which was then diluted with an equal amount of 80% glycerol. The protein was then filtered with a sterile 0.22 µm syringe filter and stored at -20˚C. The concentration for Arx was calculated using ε_{415}= 9.2 mM^{-1} cm^{-1} and were henceforth used to determine the concentration of Arx [19].

2.5 Spin-State Shift

The relevant P450 enzyme was diluted to ~3 µM concentration with 50 mM Tris buffer (pH 7.4). The UV-Vis spectrum was recorded from 600 to 250 nm. Aliquots of the substrate (0.5 µL from 100 mM stock solution in ethanol) was added to 600 µL of the enzyme solution and their spectrum was recorded. Further addition of substrates was made till the shift from low spin (420 nm) to high spin (390 nm) did not change. For example, α-damascone induces a type-I spin-state shift of 80% HS to CYP101B1 (Figure 2.1 (a)). The percentage of high-spin (HS) state shift induced by the substrate was estimated by comparing different properties of the spectra of camphor free and camphor bound $P450_{cam}$ (CYP101A1; Figure 2.1(b)).

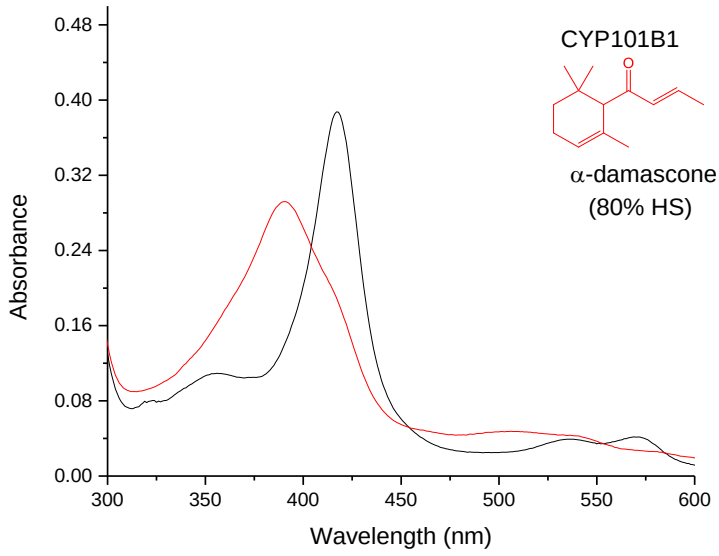

Figure 2.1 (a): Spin-state shift of CYP101B1 in α-damascone free (black) and bound (80% HS) form (red) of CYP101B1.

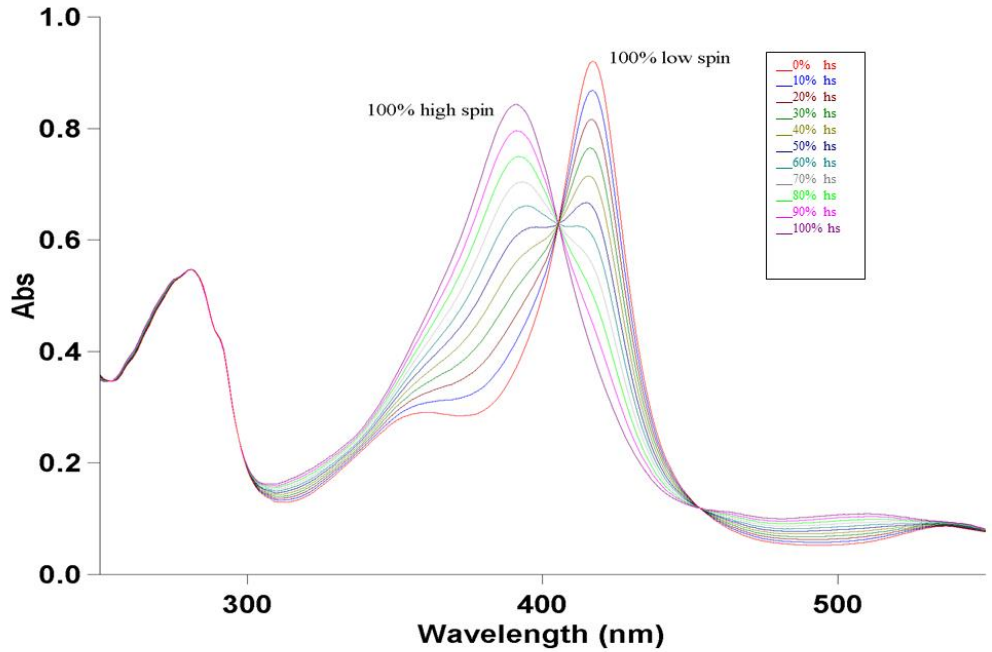

Figure 2.1 (b): Spin state shift diagram for $P450_{cam}$ in camphor free/bound state from 0% to 100%.

2.6 Dissociation constant

Dissociation constants (K_d) were determined to measure how tightly different substrates bind with the enzyme. The respective P450 enzyme was diluted to ~1 µM with 50 mM buffer T (pH 7.4, 2.5 mL). The UV-Vis spectrum between 600 nm to 300 nm was recorded and used to baseline the spectrometer. Increasing aliquots (1-5 µL) of 1 mM stock solution (in ethanol) of the substrate was added to the enzyme and the spectra was recorded. A maximum of 10 µL of 1 mM of substrate was added, to make sure the enzyme concentration was not diluted. Further aliquots (1-5 µL, cumulative of 10 µL in total) of substrate from 10 mM stock solution (in ethanol) were added and the spectra recorded. Finally, aliquots of 100 mM stock solution were added until the peak to trough absorbance difference was constant. The peak to trough absorbance difference was plotted against the concentration of substrate to determine the dissociation constant of the substrate with the enzyme and fitted to hyperbolic function (Eq. 2.1) [79, 80].

$$\Delta A = \frac{(\Delta A_{max}\,[S])}{K_d + [S]} \qquad \text{(Eq. 2.1)}$$

Where, ΔA represents the absorbance difference between the peak and the trough, ΔA_{max} is the maximum absorbance difference, [S] is the substrate concentration and K_d is the dissociation constant

If the dissociation constant is less than five times the enzyme concentration ($K_d < 5[E]$), the assumption used to derive the equation (Eq 2.1) becomes invalid. Rather, the tight binding quadratic equation (Morrison equation 2.2) must be used to determine the dissociation constant (Eq 2.2) [81].

$$\frac{\Delta A}{\Delta A_{max}} = \frac{[E] + [S] + K_d - \sqrt{([E] + [S] + K_d)^2 - 4[E][S]}}{2[E]} \qquad \text{(Eq 2.2)}$$

Where ΔA represents the peak to trough difference, ΔA_{max} represents the maximum peak to trough difference, [E] is the enzyme concentration, [S] is the substrate concentration and K_d is the dissociation constant.

Three sets of data were collected to determine the K_d value for each substrate. The error in K_d is based on the range of values produced from this curve of best fit (Figure 2.2).

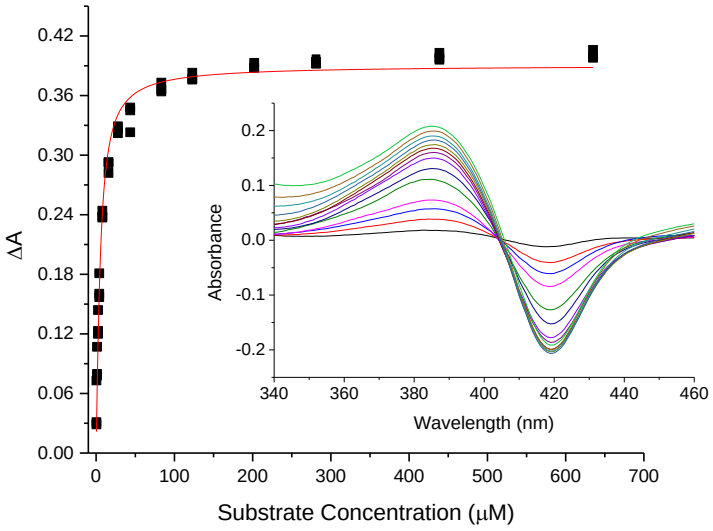

Figure 2.2 Dissociation constant example CYP101B1 + α-damascone (K_d = 3.7 ± 0.3 μM)

2.7 *In vitro* Turnovers and NADH consumption rates

The respective P450 enzyme (0.5 μM), Arx (5 μM), ArR (1 μM), bovine liver catalase (12 μL of 10 mg mL^{-1} stock in glycerol) and oxygenated 50 mM Tris (pH 7.4) were combined to a volume of 1.2 mL in a cuvette. The mixture was equilibrated at 30˚C for 1 min and NADH ($A_{340} \approx 2$, 320 μM) was added from a 20 mg mL^{-1} stock and the absorbance at 340 nm was recorded for the remainder of the experiment (Figure 2.3 (a)). After 1 minute, substrate (1 mM, 100 mM stock in EtOH) was added. The gradient of the plot and A_{340} against time was used to calculate the rate of NADH consumption using the extinction coefficient, ε = 6.22 mM^{-1} cm^{-1}.

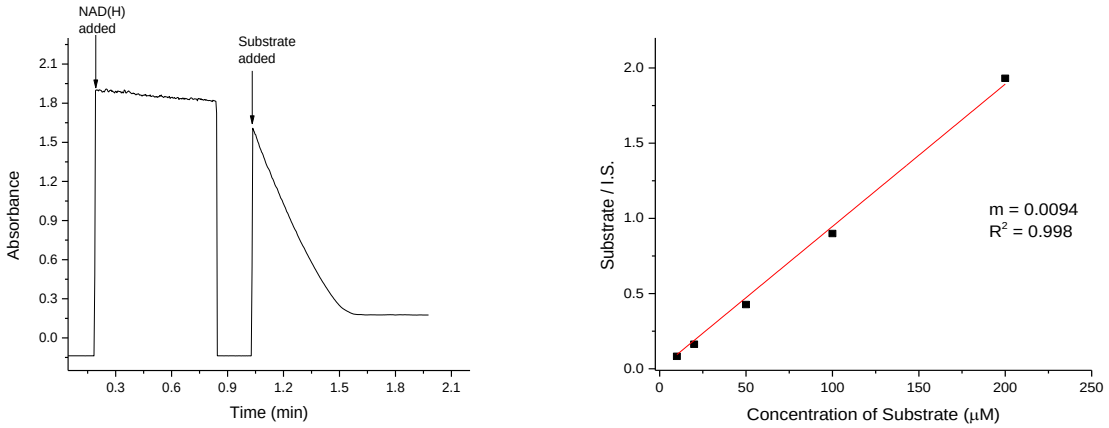

(a) β-damascone *in vitro* turnover with CYP101C1

(b) Calibration curve for β-damascone R^2 = 0.998; m = 0.0094

Figure 2.3 Example of NADH turnover assay and calibration curve.

In vivo and *in vitro* turnovers were analysed via HPLC/GC/GC-MS. A 990 µL sample of the turnover was mixed with the internal standard (*p*-cresol, 10 µL, 20 mM). The organic metabolites were then extracted with ethyl acetate (400 µL) and separated by centrifugation (13000 rpm, 3 min), the organic layer was then removed and analysed via GC and GC-MS.

The product formation rates were determined by analysing the samples with an internal standard (500 µM) via GC and GC-MS. The ratio of total product area and internal standard was plotted against the concentrations to create the calibration curve which was used to determine the amount of metabolite generated in turnovers (Figure 2.3 (b)). To calculate the coupling efficiency (productive use of reducing equivalents), the concentration of the product formed in the turnover was divided by the concentration of NADH that was added. The coupling efficiency when multiplied by the NADH oxidation rate, gave the product formation rate (Eq 2.3).

$$\text{Product formation rate} = \text{Coupling efficiency} \times \text{NADH oxidation rate} \quad (\text{Eq } 2.3)$$

2.8 Total Turnover Number (TTN)

The total turnover number was determined with the best substrates to monitor the efficiency and activity of the enzyme over an extended period (2 h). ArR:Arx:CYP-enzyme was used in the concentration of 1:10:1. The CYP enzyme (0.1 µM) was combined with ArR (0.1 mM), Arx (1 µM), 2 mM substrate and 4 mM NADH and oxygenated 50 mM buffer T pH 7.4 was used to bring the final volume up to 1.2 mL. The turnover mixture was then kept at room temperature for 2 hours before the extraction with 400 µL of ethyl acetate and analysed by GC and GC-MS.

Chapter-3

Norisoprenoid oxidation by M82L-CYP10C1 compared to WT-CYP101C1 and WT-CYP101B1

3.1 Introduction

Ionone, damascone and their derivatives are known to be among the most highly valued fragrance constituents for their distinctive fine violet and rose scent [82, 83]. Besides their use in the perfume industry, these natural products are also useful as synthetic building blocks [84]. For example, α-ionone has been identified as a flavour ingredient of raspberries, carrots and black tea as well as a fragrant extract of plants including violet flower [85-87]. Structurally, ionones and damascones are C13 norisoprenoids which are differentiated by their butenone side chain and the position of the ketone functional group (Figure 3.1). In comparison ionols exhibit a similar structure with ionones and damascones, but differ in the functional group on the butenyl side chain which contains an alcohol functional group (Figure 3.1). The α, β and δ isomers of ionones, damascones and ionols differ by the position of the double bond in the cyclohexenyl ring (Figure 3.1).

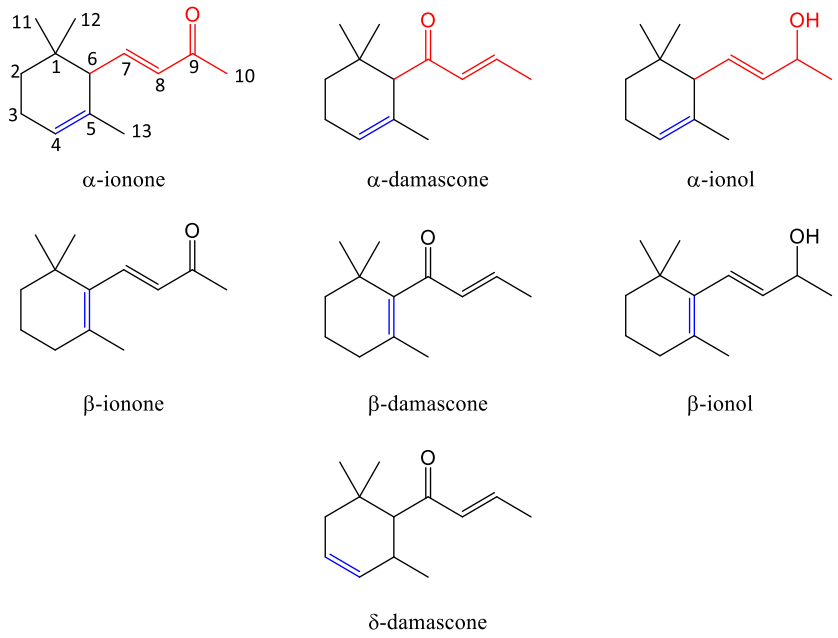

Figure 3.1 Structures of norisoprenoid substrates used in this thesis. The butenone side chain of α-ionone and α-damascone and the butenyl side chain of α-ionol is highlighted in red, the alkene moiety inside each cyclohexane ring is highlighted in blue.

3.1.1 Site specific Mutation of CYP101C1

Several of the CYP monooxygenases from *Novosphingobium aromaticivorans* including CYP101B1, CYP101C1, CYP101D1 and CYP101D2 are closely related to CYP101A1 ($P450_{cam}$) from *Pseudomonas putida*. For example, CYP101C1 shares 36% sequence identity with CYP101D1, 38% with CYP101D2 and 43% with CYP101A1 [78]. Whereas CYP101B1 is known to share 46% sequence identity with CYP101D2 and 44% with CYP101A1 and CYP101D1 [76]. The crystal structures of CYP101C1, CYP101D1 and CYP101A1, along with a predicted homology modelled structure of the CYP101B1, shows that the Met82 residue of CYP101C1 spatially and structurally aligns with the His85 residue of CYP101B1 (Figure 3.2) [9]. Moreover, this Met82 residue of CYP101C1 also aligns with the Tyr96 residue of CYP101A1 enzyme and Tyr98 residue of CYP101D1 enzyme (Figure 3.2) [78]. This tyrosine residue is also conserved in CYP101D2 enzyme. In these CYP101 enzymes the tyrosine forms a hydrogen bond to the carbonyl group of the camphor substrate [78] (Figure 3.2).

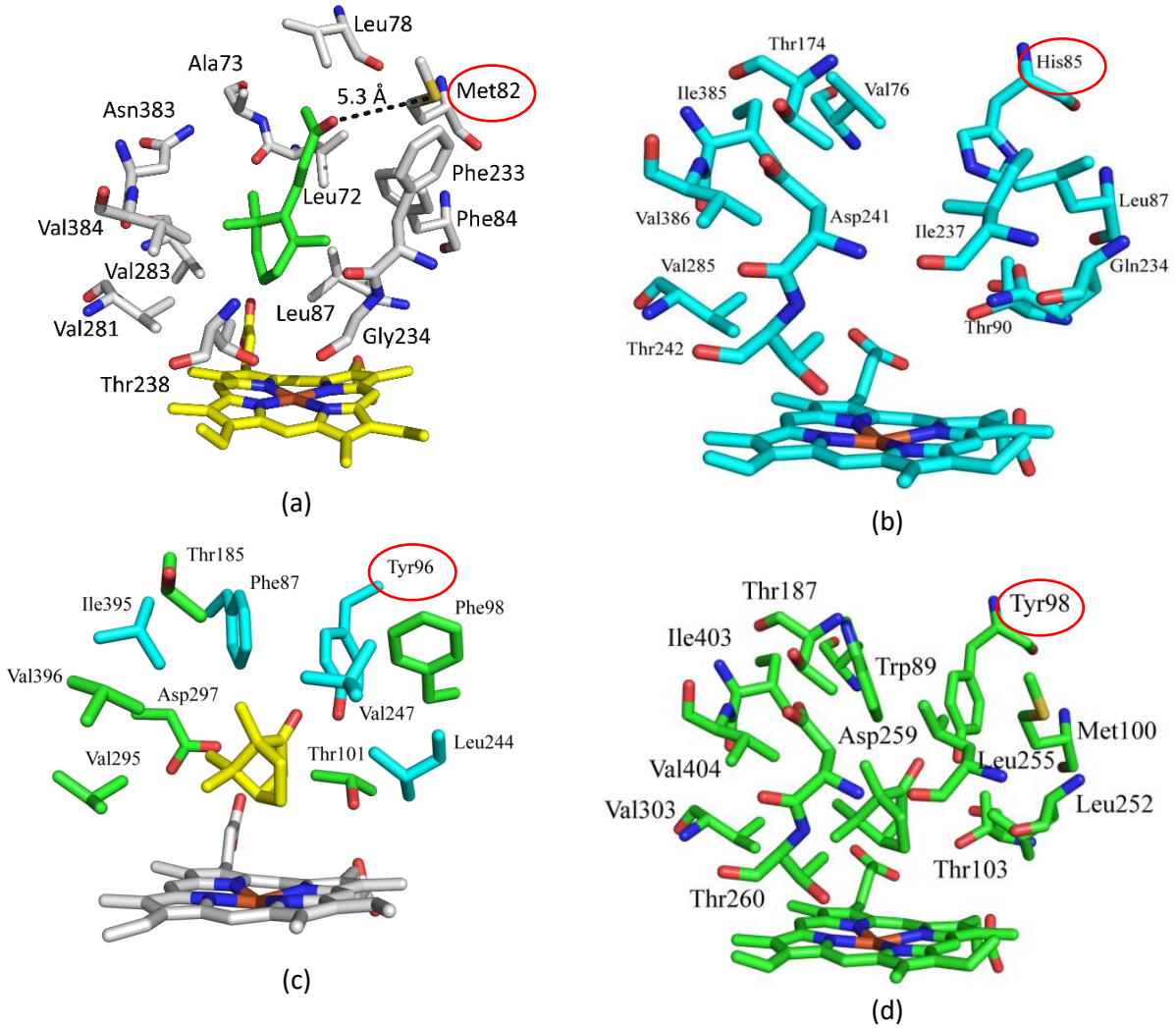

Figure 3.2 a) Crystal structure of β-ionone bound CYP101C1 (PDB ID: 3OFU) [78]. b) Modelled structure of CYP101B1 created using Swiss Model [88]. c) Crystal structure of camphor-bound CYP101A1 ($P450_{cam}$) (PDB ID: 3WRH). d) Crystal structure of CYP101D1 with bound camphor (PDB ID: 3LXI) [38]. The mutation site has been highlighted with a red circle.

Mutation of the tyrosine residue to remove the hydroxy group has been shown to enhance the affinity of both CYP101A1 and CYP101D2 against hydrophobic substrates [89, 90]. In addition, mutation of the histidine residue (His85) in CYP101B1 to a more hydrophobic phenylalanine is also reported to make the CYP101B1 more suitable for hydrophobic substrates including alkylbenzenes and naphthalene [88].

The reported crystal structure of β-ionone bound CYP101C1, indicates that the active site is predominantly hydrophobic and the substrate forms Van der Waal contacts with the majority of residues in active site [78]. The substrate is oriented with the butenone chain pointing away from the heme where it interacts with the active side residues (Met82, Leu72, Ala73 and Leu78) (Figure 3.2) [88]. In addition, there is an interaction of the keto oxygen of β-ionone with the sulfur atom of Met82 residue. Therefore, it is hypothesised that replacing the Met82 with a more hydrophobic residue such as leucine, which is similar in size compared to methionine, may alter the affinity of CYP101C1 for norisoprenoid substrates like ionones and damascones. In this project, the M82L variant of CYP101C1 enzyme was tested alongside the WT-CYP101C1 and WT-CYP101B1 enzyme with substrates like ionone, damascone and ionol (Figure 3.1).

3.2 Results

To assess the binding affinity of the WT-CYP101B1, WT-CYP101C1 and M82L-CYP101C1 enzymes, the substrates were first assessed by determining both the dissociation constant (K_d) and spin-state shifts (% HS). The dissociation constant measures how tightly the substrate binds to the enzyme and the spin-state shift induced by substrate binding provides a general indication of the ability of substrate to replace the water ligand bound to the heme iron, thereby determining accessibility to the active site pocket of the enzyme. Following this, *in vitro* turnovers were performed to analyse the NADH oxidation rate and product formation rate (PFR) (Section 2.7). These data were subsequently used to calculate the coupling efficiency, which is the percentage efficiency of NADH utilisation for the formation of products. Finally, experiments were performed to calculate the total turnover number (TTN) which is the number of turnovers catalysed per enzyme, for each substrate (Section 2.8). The spin-state shifts, NADH oxidation rate, PFR, coupling efficiencies, K_d and TTN for each enzyme substrate combinations are mentioned in Table 3.1. The enzyme-substrate combinations that exhibited the highest binding affinity and activity were then selected to scale up the product formation using a whole-cell oxidation system (Section 2.3).

3.2.1 Spin state shift and dissociation constant studies

Based on available structural data, the affinity of the M82L-CYP101C1 enzyme with norisoprenoids was determined and compared with both WT-CYP101C1 and WT-CYP101B1. β-Ionone induces a large type-I spin state shift (≥95% HS) and has a high affinity (K_d = 0.23 ± 0.1 µM) for WT-CYP101B1 [76]. This indicates that β-ionone maybe, or is at least a close relative to the physiological substrate of CYP101B1 [76]. α-Ionone, a structural analog of β-ionone, was observed to have a similar spin state shift and dissociation constant of ≥95% HS and K_d = 0.26 ± 0.04 µM respectively with WT-CYP101B1 [14, 19]. In the case of WT-CYP101C1, a small type-I spin-state shift of 20% HS (Figure 3.3 (a)) and a weaker dissociation constant of K_d = 63 ± 14 µM (Appendix, Figure A.3 (b)) was observed with β-ionone. The spin-state shift of α-ionone was comparatively larger (40% HS, Figure 3.3 (b)), however, the dissociation constant was weaker (K_d = 117 ± 13 µM) (Appendix, A.3 (a)) [78]. With M82L-CYP101C1 both, β-ionone and α-ionone displayed significantly smaller type-I spin state shift (20% HS with β-ionone and 30% HS with α-ionone, Figure 3.4). The dissociation constant was only calculated for M82L-CYP1201C1 with α-ionone (K_d = 80 ± 7 µM) (Appendix, Figure A.5 (a)). Due to the small spin state shift, the dissociation constant was only calculated for substrates with spin state shift higher than 20% HS (refer to α-ionol K_d in Appendix, Figure A.5 (c)).

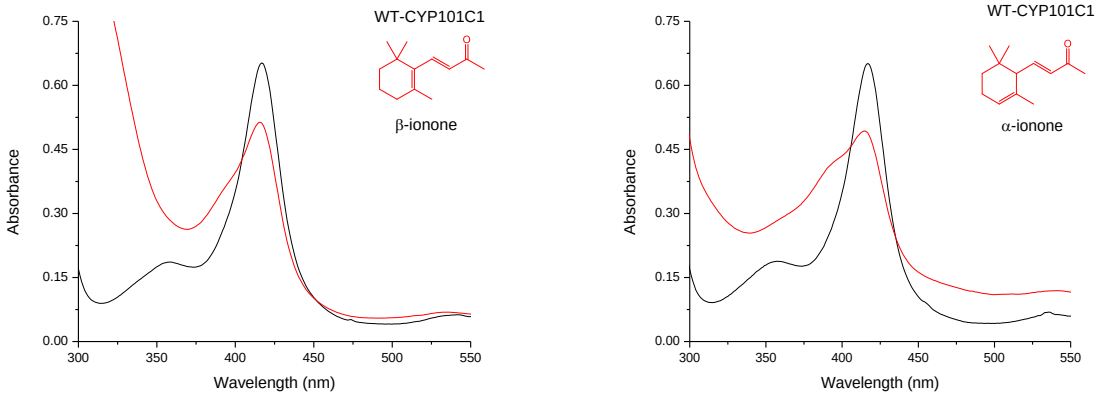

a) b)

Figure 3.3 Spin state shifts of WT CYP101C1 with a) β-ionone and b) α-ionone.

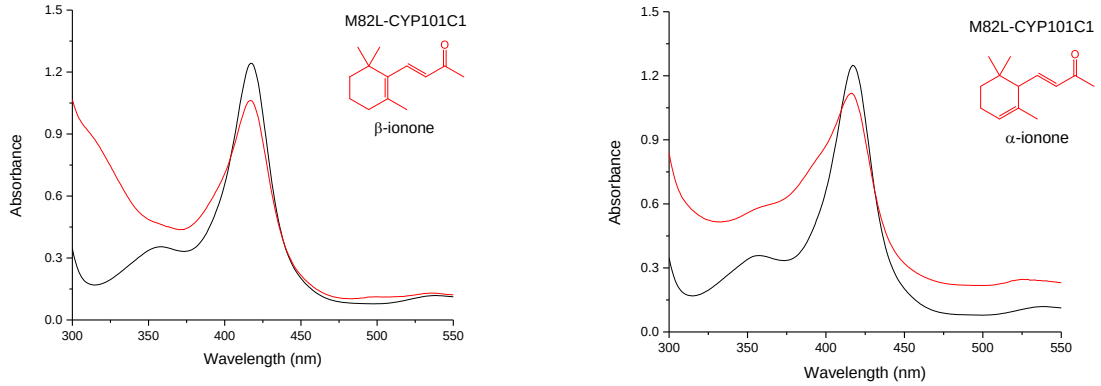

a) b)

Figure 3.4 Spin state shifts of M82L-CYP101C1 with a) β-ionone and b) α-ionone.

To explore the effect of the position and function of the keto group on the butenone side chain, β-damascone and β-ionol substrates were examined. WT-CYP101B1 shows a large type-I spin state shift of 80% HS on addition of β-damascone and 90% HS with β-ionol [76, 91]. Both substrates showed similar binding affinity (K_d = 8.3 ± 0.9 µM and 7.4 ± 0.2 µM respectively) with WT-CYP101B1, which was weaker compared to β-ionone [91]. With WT-CYP101C1, β-damascone exhibited a very small spin state shift (5% HS, Figure 3.5 (a)). β-Ionol induced a larger spin-state shift of 35% HS (Figure 3.6 (a)).

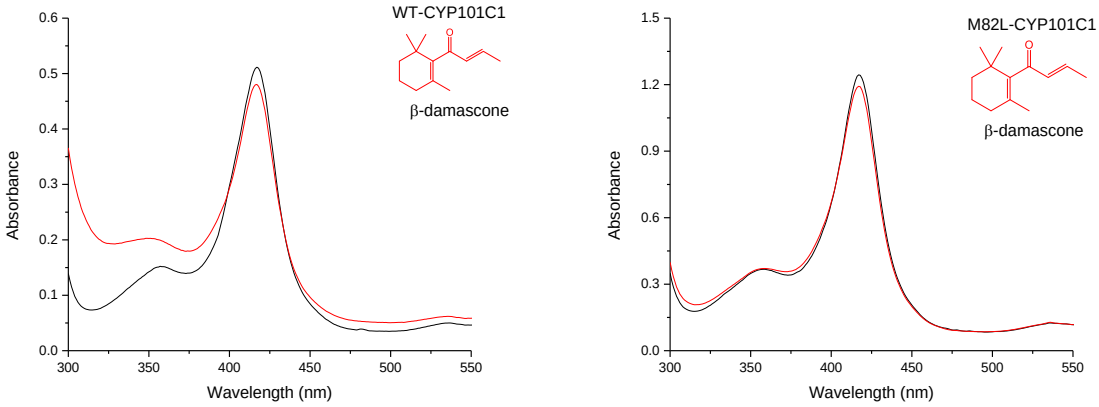

a) b)

Figure 3.5: Spin state shift for β-damascone with a) WT-CYP101C1 and b) M82L-CYP101C1.

The dissociation constant of β-ionol with WT-CYP101C1 (K_d = 46 ± 3 µM, Figure 3.6 (b)), suggests that the substrate is binding somewhat tighter compared to β-ionone (K_d = 63 ± 14 µM). The M82L-CYP101C1 variant displayed a smaller spin-state shift with β-damascone (< 5% HS; Figure 3.5 (b)) compared to β-ionol (20% HS, Figure 3.7 (a)). The dissociation constant for β-ionol (K_d = 34 ± 4 µM, Figure 3.7 (b)) also shows that the substrate is binding with higher affinity to the M82L mutant compared to WT-CYP101C1 enzyme (Table 3.1). In summary, the magnitude of the spin state shift of β-substituted substrates trends were as follows: β-ionol > β-ionone > β-damascone, with both M82L-CYP101C1 and WT-CYP101C1.

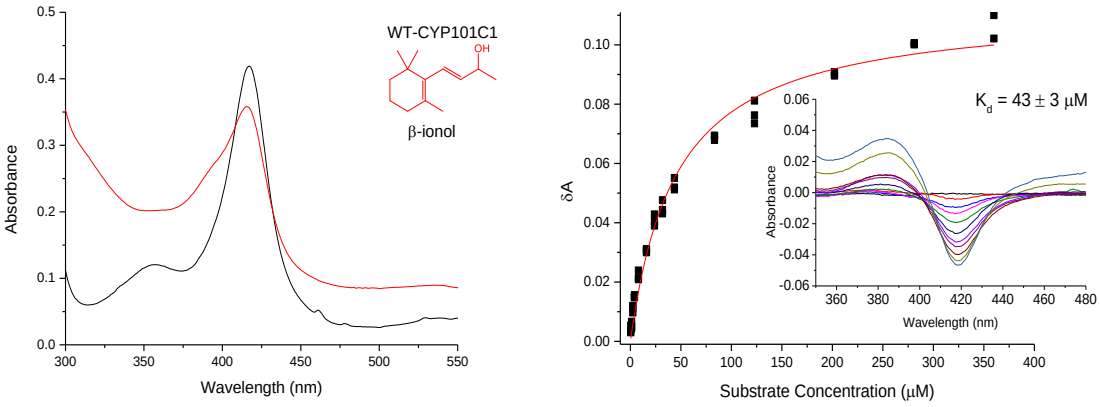

(a) (b)

Figure 3.6 (a) spin state shift of β-ionol with WT-CYP101C1, (b) dissociation constant analyses of β-ionol with WT-CYP101C1.

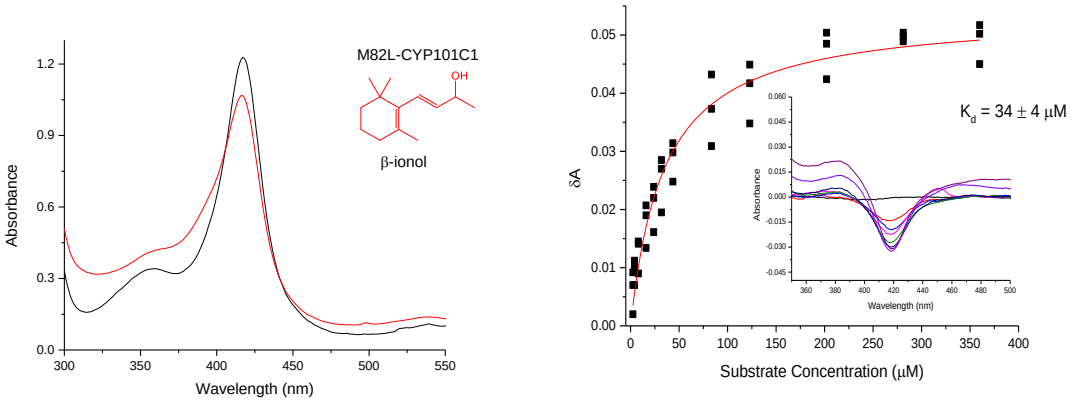

(a) (b)

Figure 3.7 (a) Spin state shift of β-ionol with M82L-CYP101C1. (b) Dissociation constant analyses of β-ionol with M82L-CYP101C1.

The substrate α-ionol differs from α-ionones by replacing the carbonyl group with an alcohol functional group (Figure 3.1). α-Ionol has been reported to induce a large type-I spin-state shift of 70% HS when added to the WT-CYP101B1 enzyme [91]. This is lower than the spin-state shift of α-ionone and α-damascone with WT-CYP101B1 (Table 3.1). α-Ionol binds weakly to WT-CYP101B1 compared to α-ionone (40-fold) and α-damascone (3-fold) (Table 3.1). In the case of WT-CYP101C1, α-ionol induces a spin-state shift of 25% HS, which is smaller than that induced by α-ionone (40% HS) and greater than α-damascone (< 5% HS) (Table 3.1). α-Ionol is also observed to bind lightly with WT-CYP101C1 than with WT-CYP101B1 (Table 3.1). Whereas, α-ionol binds with higher affinity to WT-CYP101C1 compared to α-ionone (Table 3.1). α-Ionol induced a spin state shift of 20% HS with M82L-CYP101C1 enzyme (Table 3.1) which is smaller in comparison to α-ionone but higher than α-damascone.

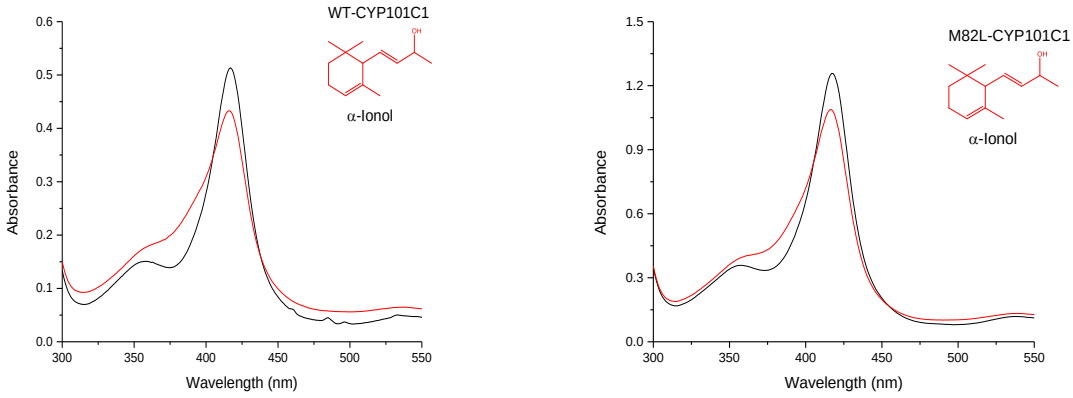

(a) (b)

Figure 3.8: Spin state shift for α-ionol with a) WT-CYP101C1 and b) M82L-CYP101C1.

Both α-damascone and δ-damascone, are reported to induce a lower spin state shift of 80% HS and 65% HS respectively with CYP101B1 in comparison to β-ionone [91, 92]. The α-damascone substrate binds to CYP101B1 (K_d = 3.7 ± 0.3 µM) less tightly than δ-damascone (K_d = 0.9 ± 0.1 µM) and β-ionone (Table 3.1). Both these substrates display a minimal spin state shift when screened with WT-CYP101C1 (< 5% HS with α-damascone and 10% HS with δ-damascone; Figure 3.9). This was lower than the spin-state shift induced by β-ionone (30% HS) and α-ionone (40% HS) on WT-CYP101C1 (Table 3.1). The M82L-CYP101C1 enzyme also had a similar display of spin state shifts on addition of these substrates (5% HS with α-damascone and 10% HS with δ-damascone; Figure 3.10).

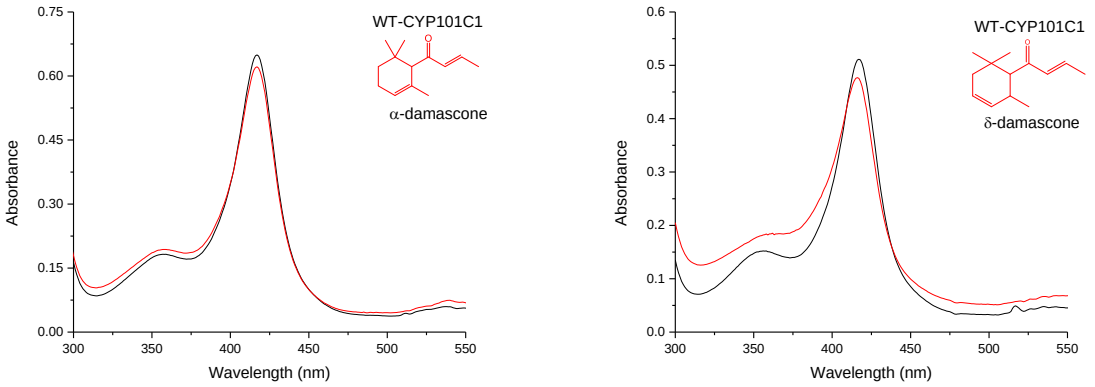

(a) (b)

Figure 3.9: (a) Spin state shift of α-damascone with WT-CYP101C1. (b) Spin state of δ-damascone with WT-CYP101C1.

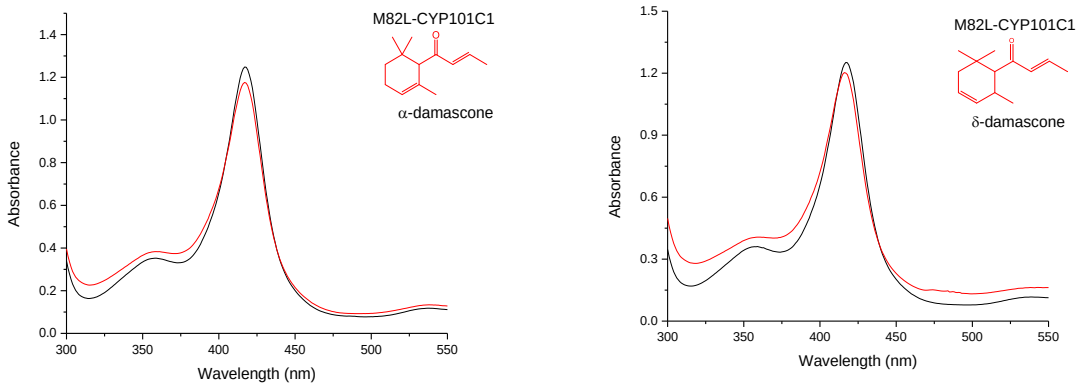

(a) (b)

Figure 3.10: (a) Spin state shift of α-damascone with M82L-CYP101C1. (b) Spin state of δ-damascone with M82L-CYP101C1.

Table 3.1: Substrate binding and *in vitro* turnover data for WT-CYP101B1, WT-CYP101C1 and M82L-CYP101C1 variant with various norisoprenoid substrates.

Enzyme/ Substrate	NADH	PFR	C %	HS %	K_d (μM)	TTN
CYP101B1 α-Ionone	1380 ± 140	660 ± 60	48	95	0.26 ± 0.04	8660
CYP101C1 α-Ionone	710 ± 5	510 ± 40	74	40	117 ± 13	4000
M82L-CYP101C1 α-Ionone	810 ± 40	790 ± 20	97	30	80 ± 7	3140
CYP101B1 β-Ionone[91]	1600 ± 100	1010 ± 60	63	95	0.23 ± 0.1	5240
CYP101C1 β-Ionone	1600 ± 10	840 ± 80	51	30	63 ± 14	3000
M82L-CYP101C1 β-Ionone	900 ± 20	500 ± 50	56	20	-	1600
CYP101B1 α-damascone[92]	890 ± 10	460 ± 33	52	80	3.7 ± 0.3	2150
CYP101C1 α-damascone	990 ± 10	520 ± 70	52	< 5	-	2070
M82L-CYP101C1 α-damascone	900 ± 60	560 ± 60	62	5	-	940
CYP101B1 β-damascone[91]	930 ± 13	560 ± 12	60	80	8.3 ± 0.9	7700
CYP101C1 β-damascone	1220 ± 40	860 ± 100	70	10	-	850
M82L-CYP101C1 β-damascone	1080 ± 85	665 ± 25	63	< 5	-	690
CYP101B1 δ-damascone[92]	705 ± 32	420 ± 35	59	60	0.9 ± 0.1	1570
CYP101C1 δ-damascone	1600 ± 20	1040 ± 40	63	10	-	2080
M82L-CYP101C1 δ-damascone	1010 ± 30	680 ± 10	67	5 - 10	-	1540
CYP101B1 α-ionol[91]	1030 ± 50	770 ± 76	75	70	11.4 ± 0.5	1400
CYP101C1 α-ionol	870 ± 40	590 ± 30	68	25	40 ± 4	2800
M82L-CYP101C1 α-ionol	475 ± 60	250 ± 50	53	20	-	700
CYP101B1 β-Ionol[91]	1030 ± 55	670 ± 84	65	90	7.4 ± 0.2	1200
CYP101C1 β-Ionol	2020 ± 100	1130 ± 30	56	35	46 ± 3	2600
M82L-CYP101C1 β-Ionol	1080 ± 80	530 ± 80	48	20	34 ± 4	1000

NADH is the NADH oxidation rate, PFR is the product formation rate, C is the coupling efficiency, HS% is the spin state shift, K_d is the dissociation constant and TTN is the total turnover number. Data reported from previous studies is in black and included for comparison with reference, data collected during this thesis is in red. Rates are reported as mean ± S.D. (n ≥ 3) and given in nmol per nmol CYP per min.

3.2.2 *In vitro* turnover studies of norisoprenoids.

The initial substrate binding screening (spin-state shift) with M82L-CYP101C1 enzyme showed little to no significant improvement for any of the tested substrates compared to the WT-CYP101C1 enzyme (Table 3.1). This suggests that the M82L mutation of the CYP101C1 enzyme did not enhance the substrate binding. To further test this hypothesis, *in vitro* experiments were performed with the M82L mutant of CYP101C1 along with WT-CYP101C1 and WT-CYP101B1 enzymes (Section 2.7). The product formation rate and selectivity were determined using GC and GC-MS analysis. The NADH oxidation rate and product formation rate were used to calculate the coupling efficiency. The reaction was scaled up to increase the quantity of metabolite produced using whole-cell turnover to characterise the obtained products (Section 2.3).

WT-CYP101B1 is reported to oxidise β-ionone with a high NADH oxidation rate of 1600 nmol.(nmol.P450)$^{-1}$.min^{-1} (henceforth abbreviated as min^{-1}) [76]. The reported product formation rate is 1010 ± 60 min^{-1} and coupling efficiency is 63% (Table 3.1) [19, 76, 89]. This shows that the enzyme catalyses the oxidation of β-ionone with good efficiency. It supports 5240 turnovers (TTN), which is the number of moles of product per mole of P450 [91]. With WT-CYP101C1, despite a significantly smaller spin state shift, β-ionone was oxidised with a similar NADH oxidation rate (1600 ± 10 min^{-1}). The product formation rate (840 ± 80 min^{-1}) and coupling efficiency (51%) were slightly reduced than that with the CYP101B1. Also, the TTN with WT-CYP101C1 was reduced (3000) almost to half than that with WT-CYP101B1 enzyme (5240) [19, 38]. M82L-CYP101C1 on the other hand, oxidised β-ionone with a slower NADH oxidation rate (900 ± 20 min^{-1}) and product formation rate (500 ± 50 min^{-1}). The coupling efficiency (56%) was similar, whereas, the TTN (1600) was reduced again by half, compared to WT-CYP101C1 (Table 3.1). Overall, in comparison to WT-CYP101B1 both the WT-CYP101C1 and M82L-CYP101C1 enzymes generated less yield of products and overall could not oxidise β-ionone as efficiently.

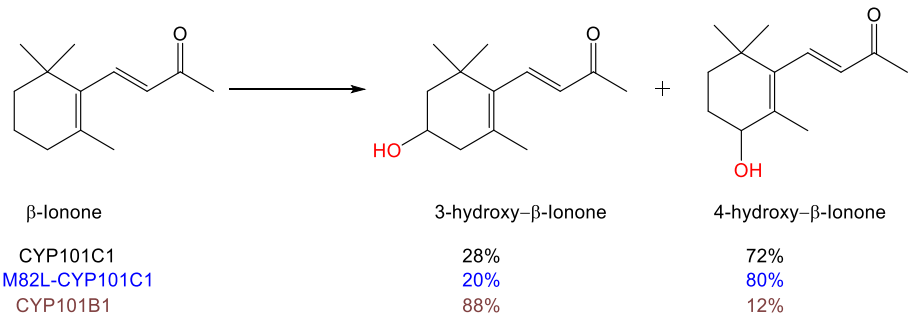

Figure 3.11: *In vitro* oxidation of β-ionone with WT-CYP101B1, WT-CYP101C1 and M82L-CYP101C1.

The product distribution of *in vitro* oxidation of β-ionone with the M82L mutant variant, as observed by the GC analysis shows similar product selectivity to WT-CYP101C1 enzyme. The WT-CYP101C1 enzyme is observed to favour the 4-hydroxy metabolite (t_R = 13.87 min) as the major product (Figure 3.11, Figure 3.12). This distribution is opposite to the selectivity of WT-CYP101B1, that favours the 3-hydroxy product (t_R = 15.03 min) (Figure 3.11, Figure 3.12). Both the products were identified by matching the NMR spectra and MS data with those previously reported [76]. A small peak was observed by the GCMS analysis of *in vitro* turnover with M82L-CYP101C1. This peak was not visible in GC (Figure 3.11, Figure 3.12). This product was yielded by whole-cell oxidation system and identified as *anti*-3,4-dihydroxy-β-ionone by NMR analysis (Figure 3.13). Further discussion on the assignment of the stereochemistry of this product has been explained in Appendix-A, Figure A.11.

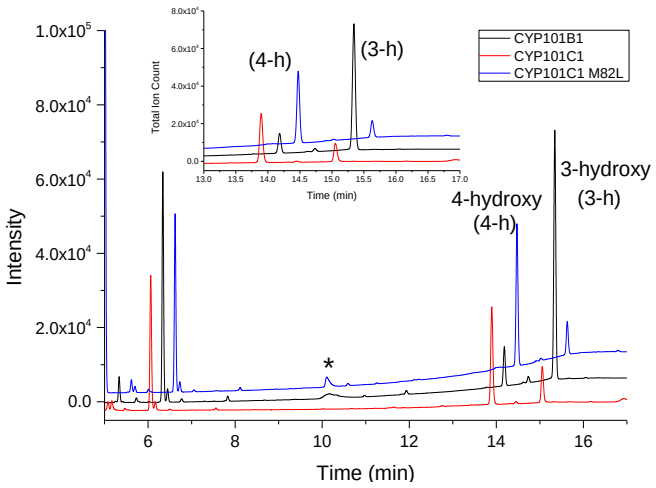

Figure 3.12: GC analysis of the *in vitro* turnover of WT-CYP101B1 (black) with β-ionone in comparison to WT-CYP101C1 (red) and M82L-CYP101C1 (blue). The chromatograms have been offset along the x and y axes for clarity. Internal standard (†), impurity from GC (*). The peak at t_R = 5.22 min and 7.51 min were also present in the substrate.

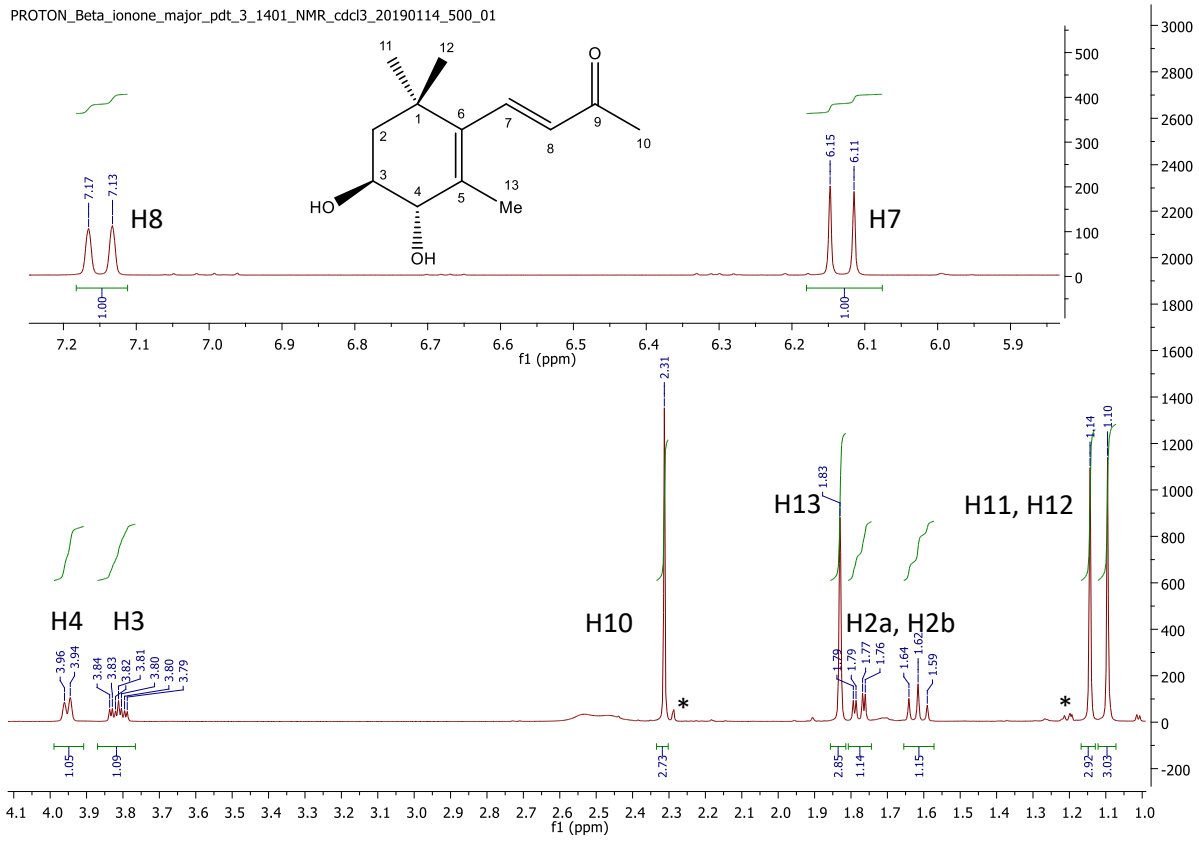

Figure 3.13: ^{1}H NMR of *anti*-3,4-dihydroxy-β-ionone in $CDCl_3$. Impurity / OH (*). Further data is presented in Appendix A (Figure A.11).

WT-CYP101C1 oxidises β-damascone with high activity, as evident by a NADH oxidation rate of 1220 ± 40 min^{-1} and a product formation rate of 860 ± 100 min^{-1} (Table 3.1). Both the NADH oxidation rate and the product formation rate were also slightly lower, 1080 ± 85 min^{-1} and 665 ± 25 min^{-1} respectively, when screened with M82L-CYP101C1. The coupling efficiency of β-damascone with WT-CYP101C1 (70%) was higher compared to M82L-CYP101C1 (63%) and both were greater compared to that of the WT-CYP101B1. Interestingly, the TTN of β-damascone with WT-CYP101B1 (7700) was ten-fold higher than with WT-CYP101C1 (850) and M82L-CYP101C1 (690). This could occur if WT-CYP101B1 stayed catalytically active for longer period of time than the other enzymes or if any of the products formed with β-damascone from the other enzymes are inhibitory in nature.

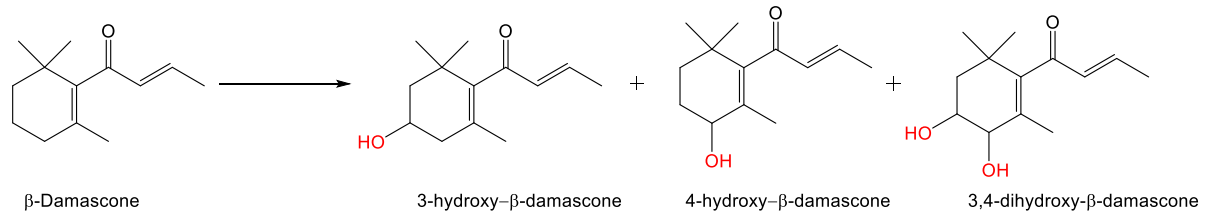

(a)

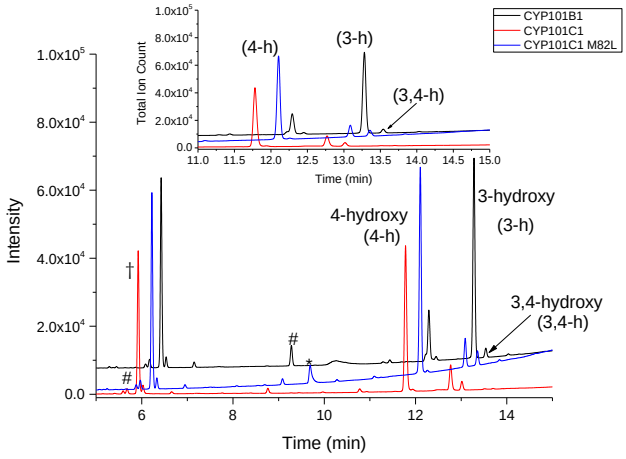

(b)

Figure 3.14: (a) *In vitro* oxidation of β-damascone with WT-CYP101B1, WT-CYP101C1 and M82L-CYP101C1. (b) GC-FID analysis of the *in vitro* turnover of WT-CYP101B1 (black) with β-damascone in comparison to WT-CYP101C1 (red) and M82L-CYP101C1 (blue). The chromatograms have been offset along the x and y axes for clarity. Internal standard (†), impurity from GC (*). The impurity from substrate is marked (#). The minor peak at t_R = 6.75 min is an impurity from β-ionol and at 12.05 min is from α-damascone, which are present in substrate.

The product distribution of β-damascone oxidation by WT-CYP101C1 and M82L-CYP101C1 were altered in comparison to WT-CYP101B1. The metabolites were generated in a higher quantity through whole-cell turnovers and separated by HPLC. The products were analysed by NMR (Figure 3.14) and compared to published literature [76]. Both WT-CYP101C1 and M82L-CYP101C1 yielded the 4-hydroxy metabolite (t_R = 11.9 min) as the major product (81%, 84%) and 3-hydroxy (t_R = 12.88 min) as the

secondary metabolite (19%, 16%) as previously reported (Figure 3.14) [76]. The other minor product (t_R = 13.05 min; Figure 3.14(b)) is characterised as *anti*-3,4-dihydroxy-β-damascone by GCMS.

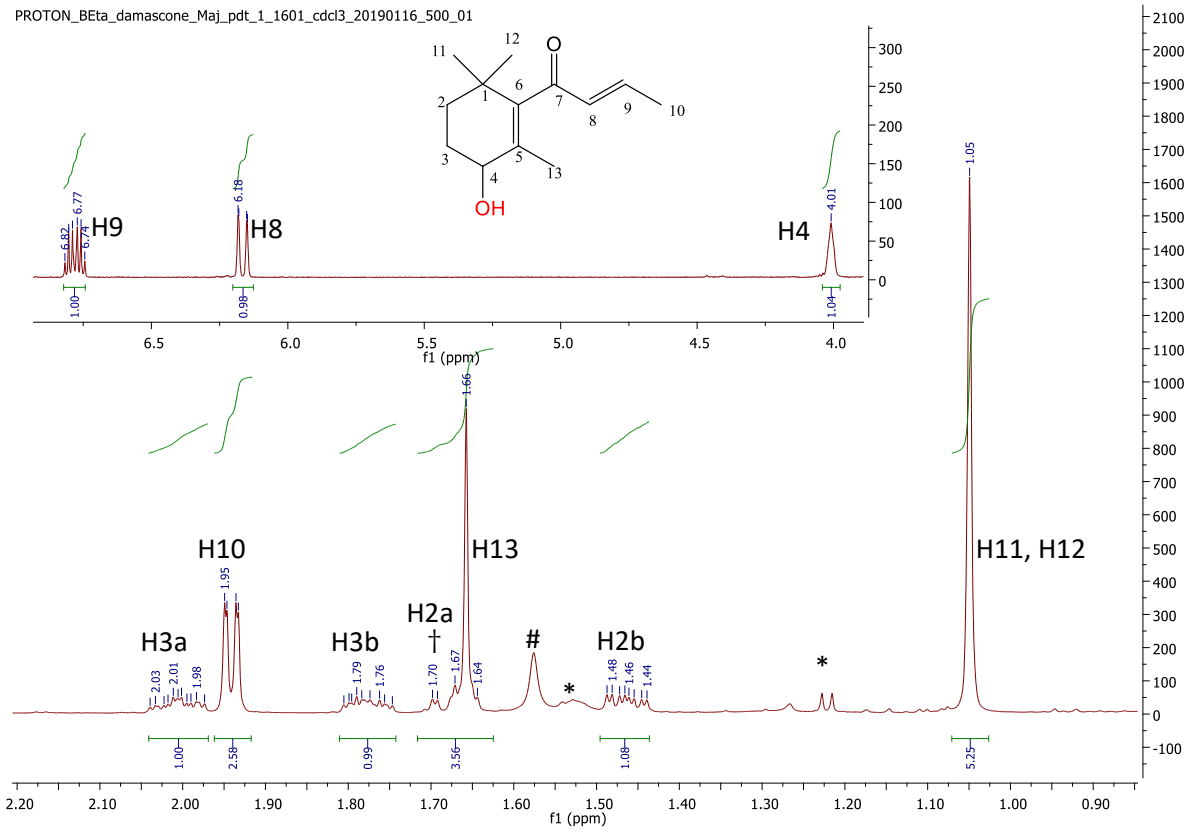

Figure 3.15: ^{1}H NMR of 4-hydroxy-β-damascone in $CDCl_3$. Impurity (*), H_2O (#). (†) The signal for H2a is present as a multiplet signal which is partly visible at 1.7 ppm and partly hidden behind the signal for H10 at 1.66 ppm. Further data provided in Appendix-A, Figure A.14.

The norisoprenoid β-ionol, in which the carboxyl group on the butenone side chain of β-ionone is replaced by an alcohol functional group, was oxidised with a product formation rate of 670 ± 84 min^{-1} by WT-CYP101B1. The NADH oxidation rate was 1030 ± 55 min^{-1} and the coupling efficiency was 65%. The TTN was reduced 4-fold (1200) in comparison to β-ionone [91]. WT-CYP101C1 oxidised β-ionol with the fastest NADH oxidation rate (2020 ± 100 min^{-1}) and product formation rate (1130 ± 30 min^{-1}) compared to any other substrate. This rate of the enzyme turnover was reduced by half (1080 ± 80 min^{-1} and 530 ± 80 min^{-1} respectively) when β-ionol was oxidised with M82L-CYP101C1. The coupling efficiency (56%) was lower with WT-CYP101C1 enzyme in comparison with WT-CYP101B1 (65%). The TTN (2600) of β-ionol oxidation was highest with WT-CYP101C1, amongst the three enzymes. With M82L-CYP101C1, the coupling efficiency (48%) and the TTN (1000) was lower than both WT enzymes.

β-Ionol yielded a mixture of 4-hydroxy-β-ionol (49%, t_R = 13.74 min) and 3-hydroxy-β-ionol (39%, t_R = 14.60 min) as the major products (Figure 3.16) which was identified by comparison with previously reported data with CYP101B1 [76, 91]. This selectivity of β-Ionol WT-CYP101B1 contrasted with that of β-ionone with WT-CYP101B1 (Figure 3.12). The 4-hydroxy metabolite was generated as the major product with both the WT-CYP101C1 (79%) and M82L-CYP101C1 (66%). The 3-hydroxy metabolite was generated in a smaller quantity with both the WT-CYP101C1 (12%) and M82L-CYP101C1 (23%) enzymes (Figure 3.16). A minor product (t_R = 14.97 min) is observed with all three enzymes and has not been identified yet.

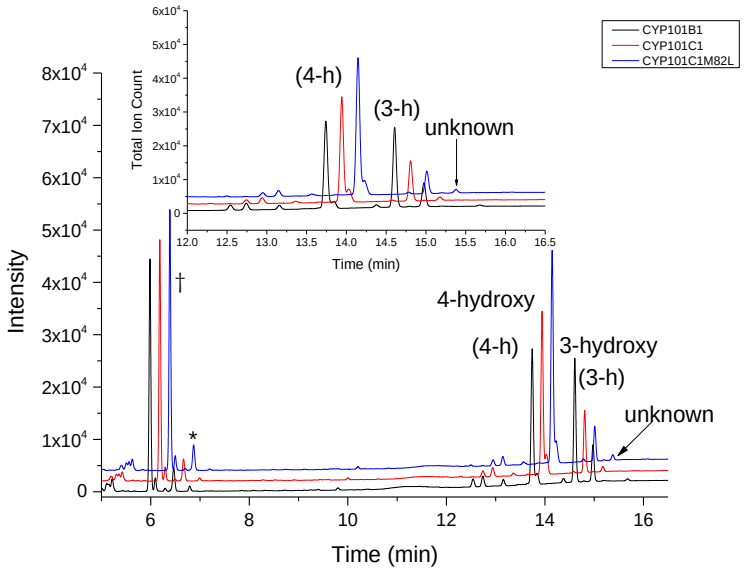

Figure 3.16: GC-FID analysis of the *in vitro* turnover of WT-CYP101B1 (black) with β-ionol in comparison to WT-CYP101C1 (red) and M82L-CYP101C1 (blue). The chromatograms have been offset along the x and y axes for clarity. Internal standard (†), impurity from substrate is marked as (*). The peak at t_R = 12.55 min and 13.17 min are oxidation of α-ionone impurity present in substrate. The peak at t_R = 12.75 min is the oxidation of β-damascone impurity present in substrate. The peak at t_R = 5.22 min, 13.74 min and 14.37 min are from β-ionone and its oxidation. The product at 14.97 is not yet characterised and labelled as (unknown).

To understand the importance of the carbonyl and alcohol groups, the data for α-ionone was compared to that seen for α-ionol (Figure 3.1). α-Ionol differs from α-ionone only by the functional group on the butenyl side chain (Figure 3.1). With WT-CYP101B1, both α-ionone and α-ionol yielded fast NADH oxidation rates of 1380 ± 140 min^{-1} and 1030 ± 50 min^{-1}, respectively. The product formation rates of both substrates were also similar (660 ± 60 min^{-1} and 770 ± 76 min^{-1}, respectively). However, the coupling efficiency with α-ionol (75%) was higher than for α-ionone (48%). Among all the substrates tested, α-ionone resulted in the highest TTN (8660) with WT-CYP101B1 (Table 3.1). In the case of oxidation by WT-CYP101C1, α-ionol exhibits higher NADH oxidation rate (870 ± 40 min^{-1}) and product formation rate (590 ± 30 min^{-1}), in comparison to α-ionone that shows a NADH oxidation rate of 710 ± 5 min^{-1} and product formation rate of 510 ± 40 min^{-1} (Table 3.1). Whereas, with M82L-CYP101C1, the NADH oxidation rate and product formation rate of α-ionol was reduced to almost half (475 ± 60 min^{-1} and 250 ± 50 min^{-1}) in comparison to its oxidation by WT-CYP101C1. Interestingly, in the case of α-ionone both the NADH oxidation rate (810 ± 40 min^{-1}) and the product formation rate (790 ± 20 min^{-1}) were increased in comparison to WT-CYP101C1 and these rates were much higher than α-ionol. The coupling efficiency (74%) and TTN (4000) were higher for α-ionone with WT-CYP101C1, in comparison to α-ionol (Coupling efficiency = 68%, TTN = 2800) (Table 3.1). Whereas, α-ionone oxidation by M82L-CYP101C1 was supported by a TTN of 3140 and coupling efficiency of 97%, which was much higher than the TTN (700) and coupling efficiency (53%) of α-ionol oxidation by M82L-CYP101C1.

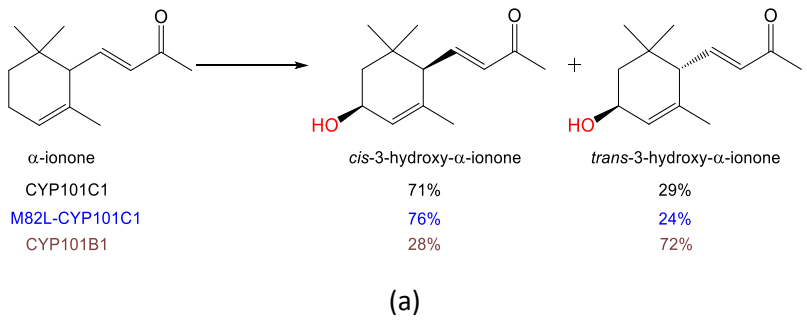

(a)

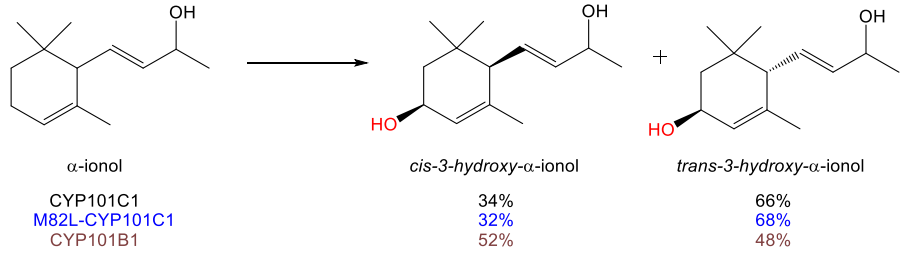

(b)

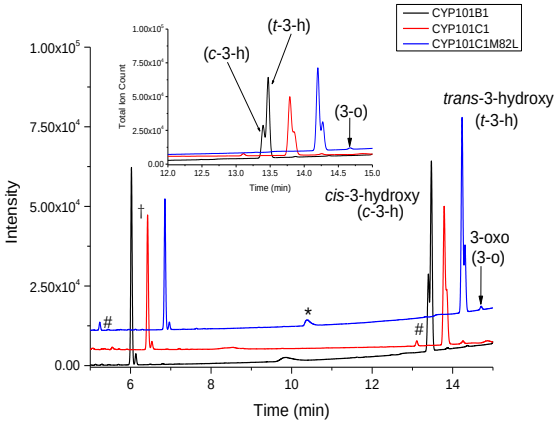

(c)

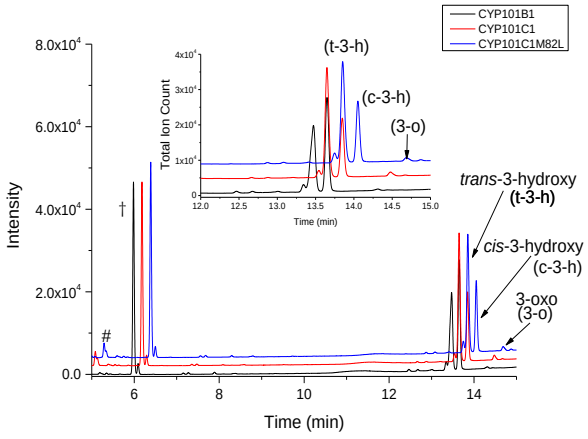

(d)

Figure 3.17: (a) *In vitro* oxidation of α-ionone with WT-CYP101B1, WT-CYP101C1 and M82L-CYP101C1. (b) *In vitro* oxidation of α-ionol with WT-CYP101B1, WT-CYP101C1 and M82L-CYP101C1. (c) GC-FID analysis of the *in vitro* turnover of WT-CYP101B1 (black) with α-ionone in comparison to WT-CYP101C1 (red) and M82L-CYP101C1 (blue). (d) GC-FID analysis of the *in vitro* turnover of WT-CYP101B1 (black) with α-ionol in comparison to WT-CYP101C1 (red) and M82L-CYP101C1 (blue). Both the substrates have trace amount of β-Ionone and its oxidation product, labelled as (#). The chromatograms have been offset along the x and y axes for clarity. Internal standard (†), impurity from GC (*). In (d), the peak at t_R = 7.89 min is an impurity from δ-damascone. The peak at t_R = 12.55 min and 13.17 min are oxidation of α-ionone impurity present in substrate. The peak at t_R = 12.75 min is the oxidation of β-damascone impurity present in substrate.

GC analysis of *in vitro* oxidation of α-ionone revealed the formation of two products (Figure 3.17 (a)) which were characterised by NMR analysis, this data was in agreement with previously published data [76]. Intriguingly, both the products were found to be oxidised at C3 position but with different configurational isomers (Figure 3.17 (a)). These *cis* / *trans* metabolites eluted closely on a DB-wax column using GC (Figure 3.18 (c)). However, these isomers were separated for characterisation using a normal phase HPLC column (Figure 3.18 (a)). The oxidation of α-ionone by WT-CYP101B1 generated

trans-3-hydroxy-α-ionone (t_R = 13.4 min) as the major product (72%) (Figure 3.18 (b)), whereas both WT-CYP101C1 and M82L-CYP101C1 enzymes favoured the *cis*-3-hydroxy-α-ionone (t_R = 13.47 min, 68% with WT-CYP101C1 and 77% with M82L-CYP101C1; Figure 3.17 (a)). A minor product was observed at t_R = 13.90 min with α-ionone oxidation by WT-CYP101B1 and M82L-CYP101C1. The mass spectra of this metabolite matches with the reported mass spectra of 3-oxo-α-ionone (Figure A.20). In the case of α-Ionol, WT-CYP101B1 favoured the *cis* isomer (t_R = 13.65 min, 52%) whereas the M82L-CYP101C1 and WT-CYP101C1 both favoured the *trans* isomer (t_R = 13.45 min, 68%, 66%; Figure 3.17 (b)). A minor product at t_R = 13.85 min was characterised as 3-oxo-α-ionol by GCMS analysis (Figure A.25).

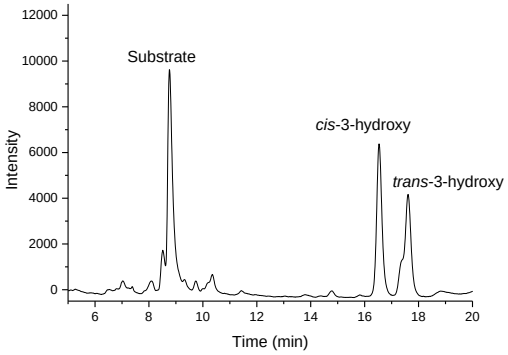

(a)

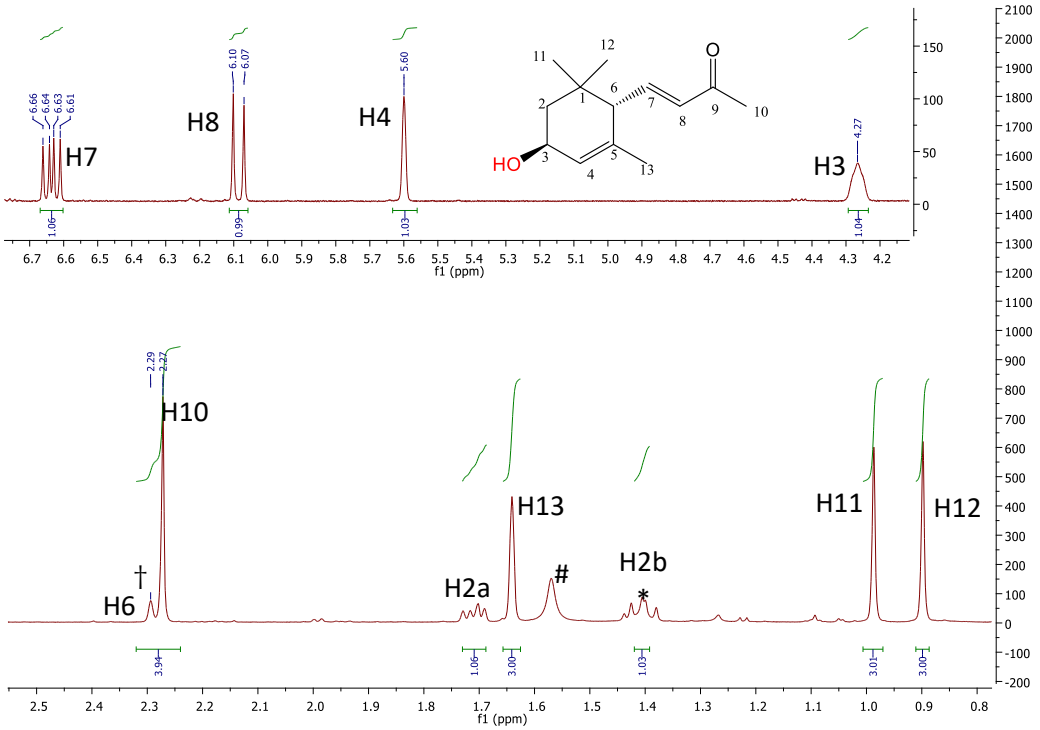

(a)

Figure 3.18: (a) HPLC analysis showing the separation of *cis*-3-hydroxy-α-ionone and *trans*-3-hydroxy-α-ionone metabolite (b) ^{1}H NMR of *trans*-3-hydroxy-α-ionone in $CDCl_3$. Impurity / OH (*). H_2O (#), The proton signal for H6 is shown as a multiplet, which is partly seen at 2.29 ppm and partly hidden behind the signal for H10 at 2.27ppm (†). The signal for H2b at 1.4 ppm overlays with an impurity.

To assess the role of alkene moiety inside the cyclohexyl ring, α-damascone and δ-damascone (Figure 3.1) were screened with all three enzymes. Both α-damascone and δ-damascone were oxidised by WT-CYP101B1 with NADH oxidation rates of 890 ± 10 min^{-1} and 705 ± 32 min^{-1} respectively [92]. The product formation rates (460 ± 33 min^{-1}, 420 ± 35 min^{-1}) and coupling efficiencies (52%, 59%) were similar for both substrates with WT-CYP101B1 [92]. This shows that changing the alkene position did not alter the rate of product formation or coupling efficiency significantly with WT-CYP101B1. WT-CYP101C1 oxidised both the substrates with an NADH oxidation rates of 990 ± 11 min^{-1} and product formation rate of 520 ± 70 min^{-1} for α-damascone and 1600 ± 20 min^{-1} and 1040 ± 40 min^{-1} for δ-damascone. The NADH oxidation rate of δ-damascone with WT-CYP101C1 is similar to the oxidation of β-ionone by the same enzyme. Whereas, the product formation rate is higher for δ-damascone, this suggests that δ-damascone is more efficiently oxidised than β-ionone by WT-CYP101C1. With M82L-CYP101C1, the NADH oxidation rates of both α-damascone and δ-damascone were decreased to 900 ± 60 min^{-1} and 1010 ± 30 min^{-1} respectively. The product formation rate was increased to 560 ± 60 min^{-1} for the oxidation of α-damascone by M82L-CYP101C1. Whereas, the same enzyme decreased the product formation rate to 680 ± 10 min^{-1} for δ-damascone. The coupling efficiency was higher for δ-damascone in comparison to α-damascone with all three enzymes (Table 3.1). TTN of α-damascone (2070) was similar in comparison to δ-damascone (2080) with WT-CYP101C1. With M82L-CYP101C1 the TTN was much higher for δ-damascone (1540) than α-damascone (940).

Similar to the α-ionone and α-ionol reported previously, α-damascone is also oxidised at C3 position by all three enzymes. The GC analysis of *in vitro* turnovers of α-damascone shows that both WT-CYP101C1 and M82L-CYP101C1, generated the *cis*-3-hydroxy-α-damascone as a major product (t_R = 11.31 min, 84% with WT-CYP101C1 and 80% with M82L-CYP101C1) (Figure 3.19 (a)). Interestingly, the turnovers with WT-CYP101B1 also generated the *cis*-3-hydroxy metabolite in excess (61%, Figure 3.19 (a)). This is in contrast to its behaviour with α-ionone, where the *trans* isomer is the major metabolite (Figure 3.17 (a)). Both the metabolites were generated in larger quantity by whole-cell oxidation system and characterised by comparing the NMR spectra with the reported literature data [92]. A third product was also generated by all three of the enzymes (t_R = 11.67 min, ≤ 4%; Figure 3.19 (a)), which was not generated in high enough amount to be characterised by NMR analysis. By GC-MS analysis we observed that it has a mass indicating it arises from further oxidation of an alcohol product to a ketone (t_R = 13.38 min, 206 AMU; Appendix-A, Figure A.22). In the case of δ-damascone, both WT-CYP101C1 enzyme and M82L-CYP101C1 formed the same major product (Figure 3.19 (b)), which was characterised by NMR analysis as 3,4-epoxy-δ-damascone (t_R = 8.01 min, Figure 3. 20). A minor product which was characterised by NMR analysis as 2-hydroxy-δ-damascone (t_R = 11.44 min, Figure 3.21) was only generated with M82L-CYP101C1 and WT-CYP101C1 (Figure 3.19 (b, d)). WT-CYP101B1 generated a single product with δ-damascone. δ-Damascone is the only substrate that yielded a 2-hydroxy metabolite which led us to believe that the position of alkene moiety inside the cyclohexyl ring does play a significant role in defining the selectivity of oxidation.

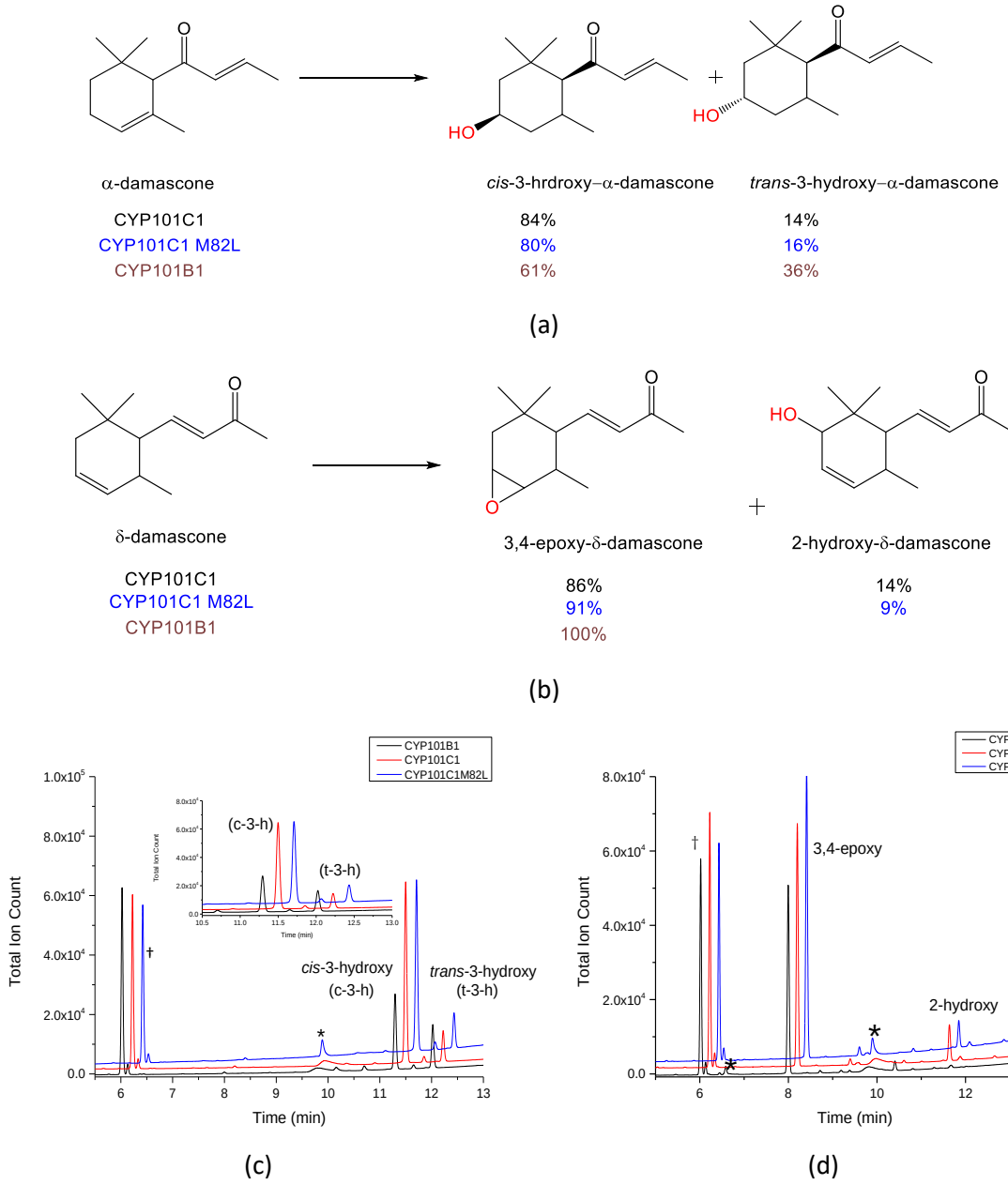

Figure 3.19:(a) *In vitro* oxidation of α-damascone with WT-CYP101B1, WT-CYP101C1 and M82L-CYP101C1. (b) *In vitro* oxidation of δ-damascone with WT-CYP101B1, WT-CYP101C1 and M82L-CYP101C1. (c) GC-FID analysis of the *in vitro* turnover of WT-CYP101B1 (black) with α-damascone in comparison to WT-CYP101C1 (red) and M82L-CYP101C1 (blue). (d) GC-FID analysis of the *in vitro* turnover of WT-CYP101B1 (black) with δ-damascone in comparison to WT-CYP101C1 (red) and M82L-CYP101C1 (blue). The chromatograms have been offset along the x and y axes for clarity. Internal standard (†), impurity from GC (*). In (c), the peak at t_R = 7.89 min is an impurity of δ-damascone. The peak at t_R = 10.65 min is an impurity from β-ionone. The peak at t_R = 11.65 min is present in the turnover of δ-damascone, β-ionone and the substrate as well. In (d), the peak at t_R = 11.69 min is an

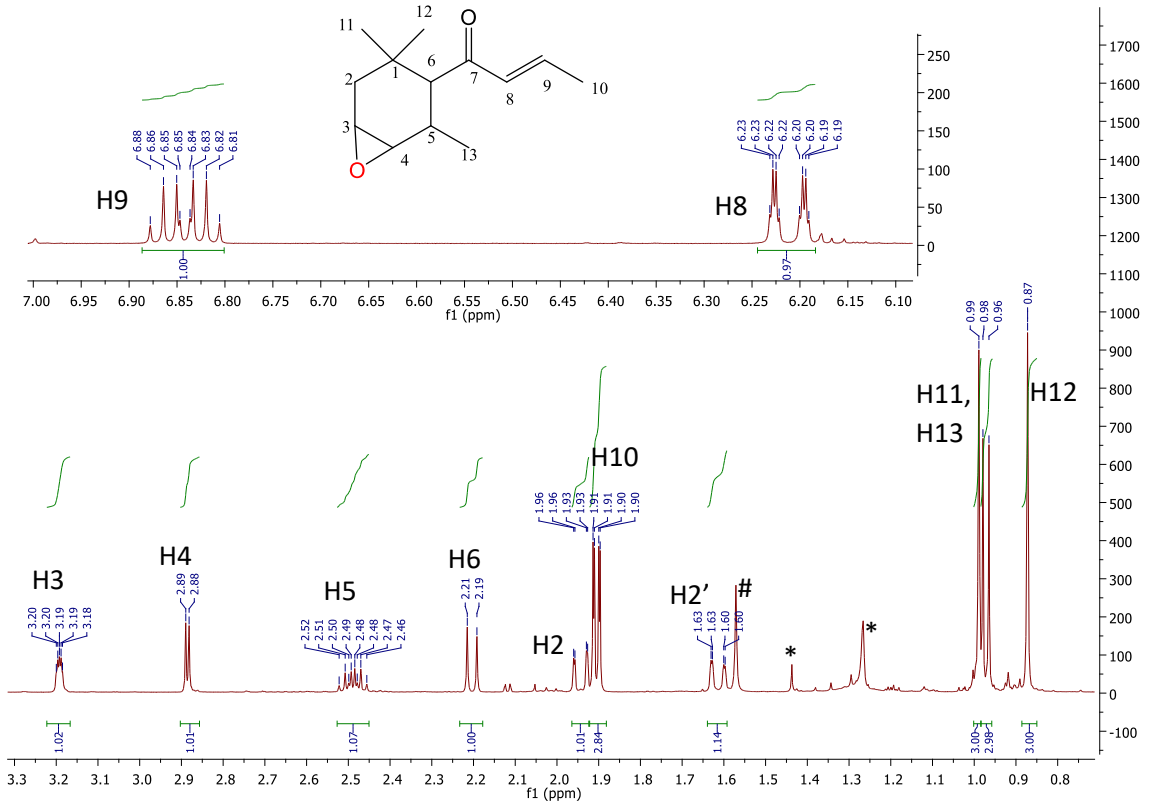

(a)

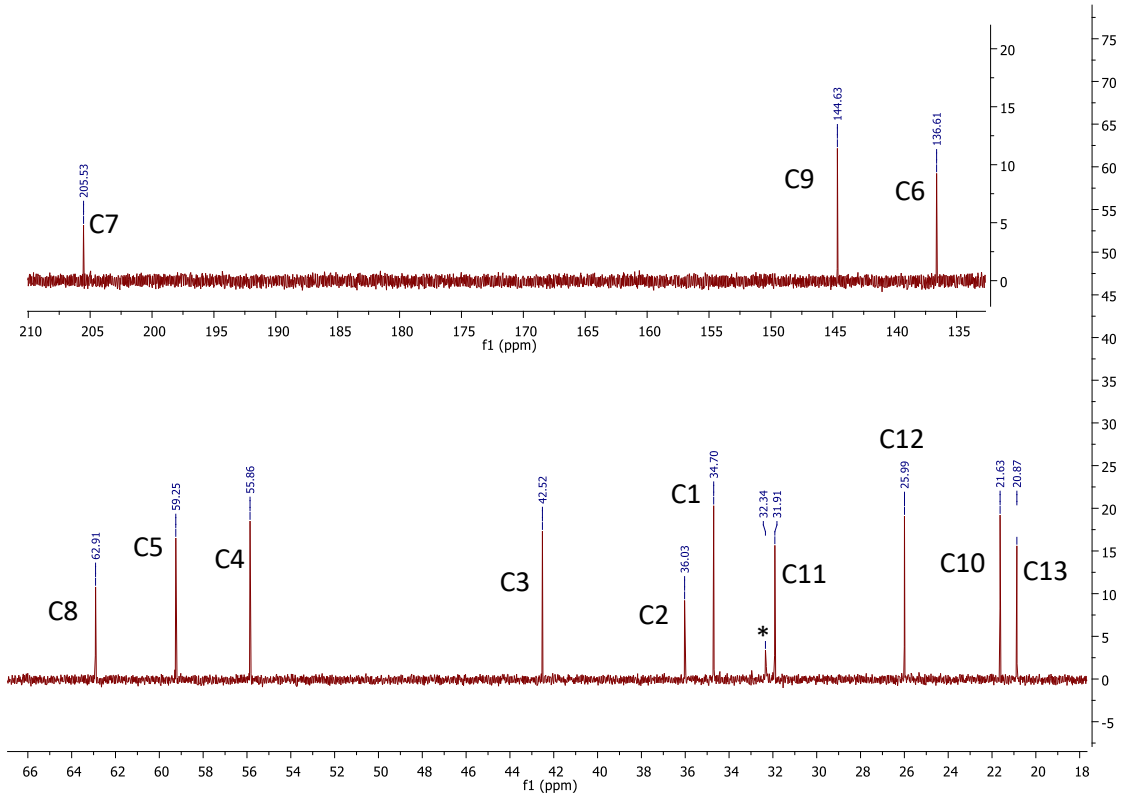

(b)

Figure 3.20: (a) (a) ^{1}H NMR of 3,4-epoxy-δ-damascone in $CDCl_3$. (b): ^{13}C NMR of 3,4-epoxy-δ-damascone in $CDCl_3$. Impurity (*), H_2O (#).

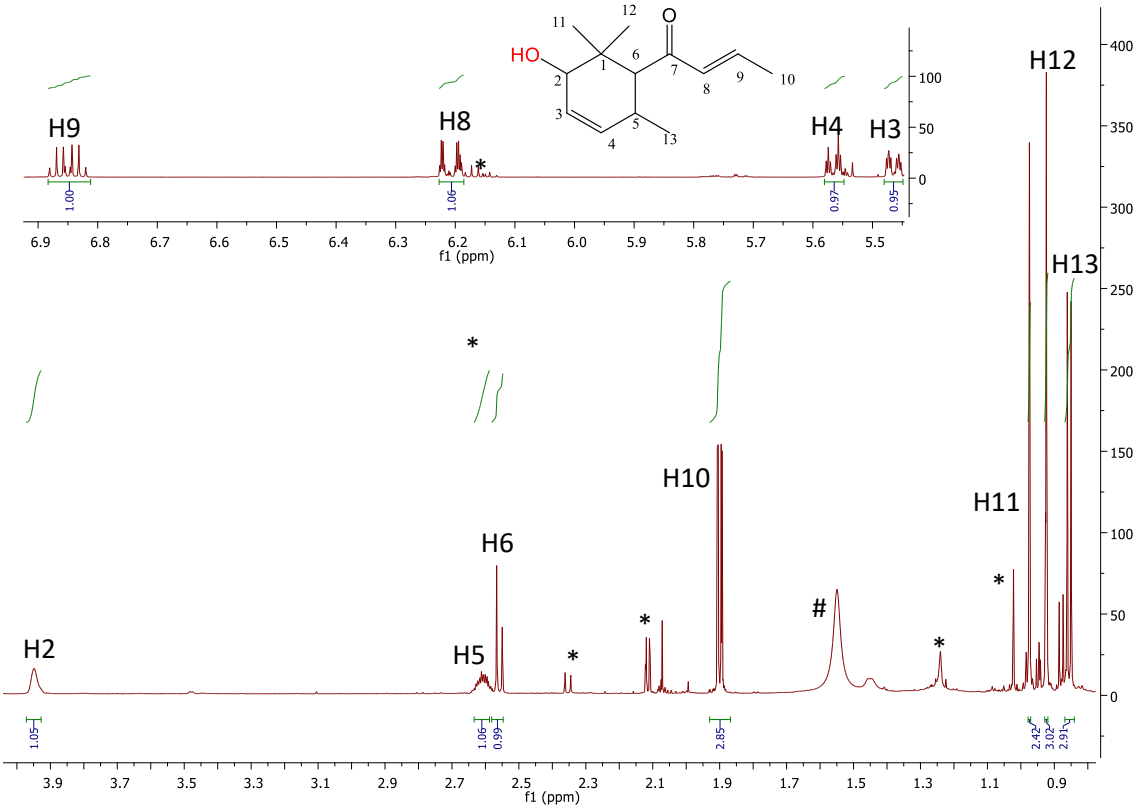

(a)

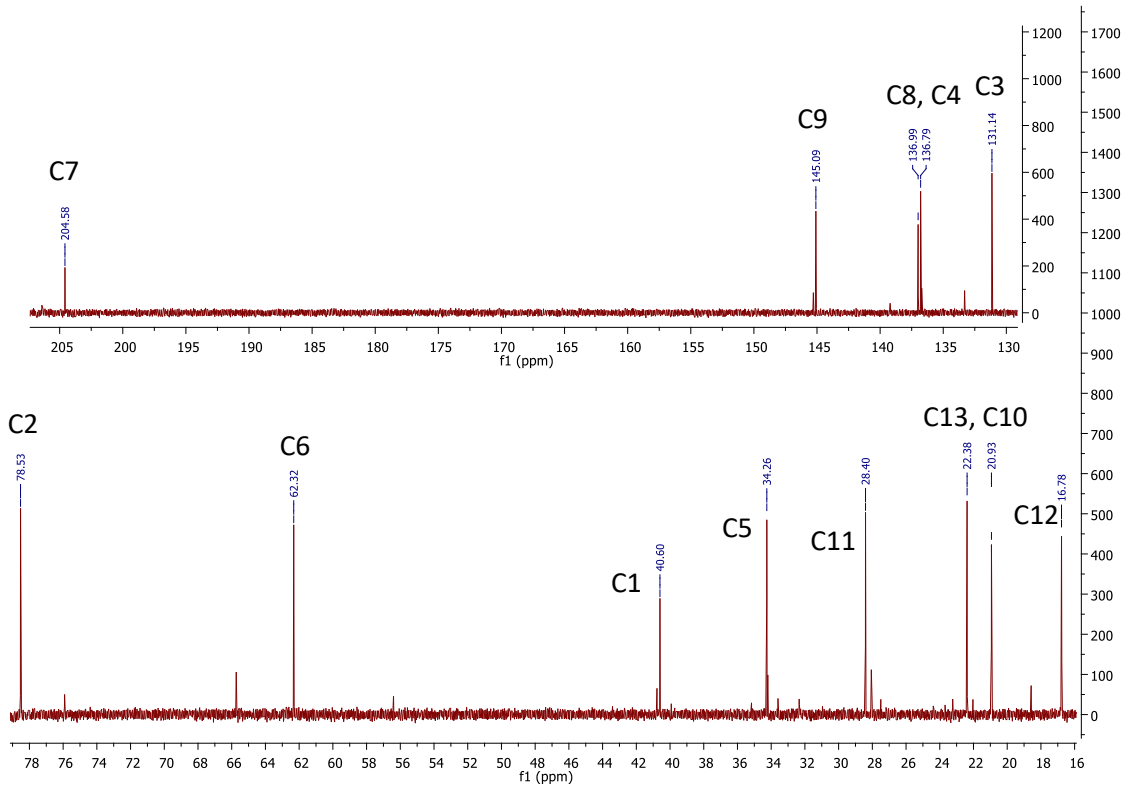

(b)

Figure 3.21: (a) ^{1}H NMR of 2-hydroxy-δ-damascone in $CDCl_3$. (b): ^{13}C NMR of 2-hydroxy-δ-damascone in $CDCl_3$. Impurity (*), H_2O (#).

3.3 Discussion

Norisoprenoids can be derived from the breakdown of carotenoids and carotenoid dioxygenase (13,14-dioxygenase), which are known to be present in *N. aromaticivorans* [93, 94]. These norisoprenoids have a common cyclohexyl ring with an alkene and a butene side chain with ketone as a functional group for ionones and damascones whereas, ionols have an alcohol functional group.

The crystal structure of CYP101C1 bound to β-ionone has revealed that the active site residues of CYP101C1 are significantly different from those of camphor oxidising CYP101A1, CYP101D1 and CYP101D2 (Figure 3.2). For example, Met82 aligns with Tyr96 (CYP101A1 numbering given), Leu87 with Thr101 and Asn383 with Ile395. Such differences are bound to alter the substrate profile for CYP101C1. The physiological substrate of both CYP101C1 and CYP101B1 enzymes are yet to be confirmed, however CYP101B1 has been studied to oxidise norisoprenoids (ionones, damascones) with high efficiency and high binding affinity, these substrates induce large type-I spin state shifts with CYP101B1. Whereas, the same norisoprenoid substrates show a weak binding (30-117 μM) and induce a small spin state shift of ≤ 40% with CYP101C1.

The functional data (section 3.3) aligns with the crystallographic data that shows that the C3 and C4 atoms are held closest to the heme iron and thus more favoured for oxidation. In the case of β-ionone and β-damascone, the majority of product was obtained by C4 hydroxylation with both the M82L mutant and WT-CYP101C1 indicating that the enzymes prefer allylic C4 position for hydroxylation which is altered in the case of CYP101B1, that prefers the allylic C3 position (Figure 3.11, Figure 3.14(a)). This shows that altering the position of the keto group on butene side chain does not significantly affect the oxidation or the product distribution for WT-CYP101B1. But when the keto group itself is substituted by an alcohol group (β-ionol), both CYP101C1 and its M82L variant mutant enzyme yielded C3 hydroxylation in majority with all three enzymes (Figure 3.22). This suggests that on changing the keto group to alcohol, CYP101B1 still prefers oxidation at the C3 position but an interesting change is observed by both M82L-CYP101C1 mutant and WT-CYP101C1 enzyme that prefer the C3 position instead of C4 like the corresponding ionone and damascone.

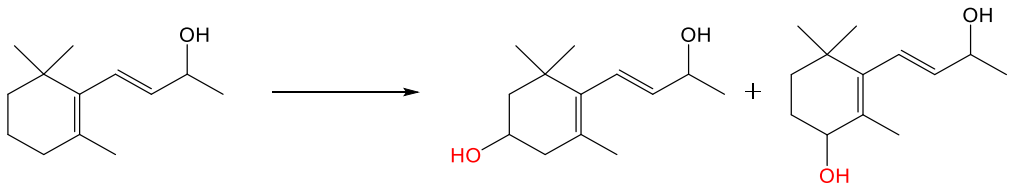

Figure 3.22: *in vitro* oxidation of β-ionol with WT-CYP101B1, WT-CYP101C1 and M82L-CYP101C1.

In terms of activity, the trend for tested norisoprenoid substrates with WT-CYP101B1 were as follow: β-ionone > α-ionone > α-ionol > β-ionol > β-damascone > α-damascone > δ-damascone. With WT-CYP101C1 the trend follows: β-ionol > δ-damascone > β-ionone > β-damascone > α-damascone > α-ionol > α-ionone. Whereas, the M82L-CYP101C1 shows a different trend: β-damascone > β-ionol > δ-damascone > α-ionone > α-damascone > β-ionone > α-ionol.

On comparing the α substituted norisoprenoids of respective ionone, damascone and ionol with the results of β substituted norisoprenoids. We observed that the alkene moiety present inside the cyclohexyl ring of α substituted norisoprenoids helps the substrate to orient in a way that ensures the C3 carbon is present closest to the heme and hence oxidises the carbon exclusively at C3 as opposed to the β substituted equivalents. The major product generated during the oxidation of α-ionone with CYP101B1 favours the *trans* configuration whereas the M82L-CYP101C1 and its wild type enzyme favours *cis* configuration. This product distribution is altered in the case of α-damascone, where all three of the enzymes generate the *cis*-3-hydroxy-α-damascone. This suggests that by changing the position of keto group on the butenone side chain enables the enzyme to orient the substrate within active site of CYP101B1, in the same way that α-damascone and α-ionone is arranged in the active site of M82L-CYP101C1 and WT-CYP101C1 enzyme. In terms of oxidation behaviour α-ionol replicates the α-ionone by generating the *cis*-3-hydroxy-α-ionol in majority with CYP101B1 and the corresponding *trans* equivalent in majority with both M82L-CYP101C1 and WT-CYP101C1.

To check our hypothesis, we tested the oxidation behaviour of δ-damascone, that differ simply by the position of the alkene moiety (between C3 and C4) inside the cyclohexyl ring with WT-CYP101C1, M82L-CYP101C1 and WT-CYP101B1. As expected, the M82L-CYP101C1 mutant and WT-CYP101C1 enzyme both yielded the 3,4-epoxy- δ-damascone as the major product (Figure 3.19 (b, d). The 2-hydroxy-δ-damascone could arise because of the affinity of the enzyme for allylic hydrogen. On the other hand, the *in vitro* oxidation of δ-damascone with WT-CYP101B1 generated one single product of the 3,4-epoxy metabolite, that shows C2 is further away from the heme of WT-CYP101B1 than with WT-CYP101C1 enzyme. This suggests that the position of the carbonyl group on the butenone side chain and the alkene in the cyclohexyl ring plays a crucial role in orienting the substrate in the active site of WT-CYP101B1, WT-CYP101C1 and M82L-CYP101C1 for oxidation.

In future, the enantio and stereoselectivity of hydroxylated metabolite can be observed by running the metabolites on a chiral column and getting a ROESY NMR. Also, the crystal structure of the substrates mentioned in this chapter with WT-CYP101B1 could provide more insight into the orientation of these substrates in active site. The whole cell turnovers could also be optimised to generate the minor products in a larger quantity for characterisation by NMR analysis.

Chapter-4

Oxidation of cyclic ketone, amide or ester containing molecules by CYP101B1 and CYP101C1 enzymes.

4.1 Introduction

Terpenoids are a class of naturally occurring organic compounds that are derived from isoprene units. Terpenoid oxidation by natural and modified P450 enzymes is of high interest due to their biological properties and use as flavour and fragrance agents [74, 95]. For example, terpenoids contribute to the scent and fragrance profiles of eucalyptus, cinnamon, cloves and ginger [96]. Along with norisoprenoids, monoterpenoid acetates (which also possess a carbonyl group on a side chain) have been reported to be oxidised by CYP101B1 with high catalytic efficiency [91]. For example, fenchyl acetate was selectively oxidised by CYP101B1 to 5-*exo*-hydroxyfenchyl acetate with a product formation rate greater than 1000 min^{-1}, exceeding that for norisoprenoids (Figure 4.1 (a)) [91]. Cycloalkanones and cycloalkyl esters are another class of compounds which are used in the manufacturing of perfumes, flavours, essential oils and pharmaceutical drugs [97, 98].

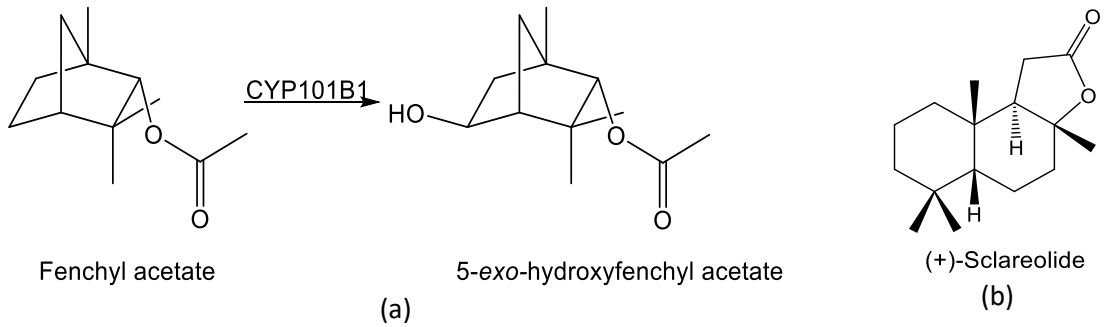

Figure 4.1: (a) Fenchyl acetate oxidation by CYP101B1 [91]. (b) Structure of (+)-Sclareolide.

Sesquiterpene lactones, which have structural similarity to norisoprenoids, have been shown to bind to CYP101B1 with moderate affinity and induce a large type-I spin state shift. For example, (+)-Sclareolide (Figure 4.1(b)), a plant natural product containing a carbonyl functional group in a similar position relative to the methyl-substituted cyclohexane ring of norisoprenoids. This binds to CYP101B1 with a K_d = 20 ± 4 µM and induces a spin-state shift of 50% [91].

Activation of the C-H bond of these compounds is a challenging task in the field of fine chemical synthesis [99-101]. For example, cyclohexanone and cyclohexanol, which are essential chemical intermediates for the synthesis of polyamides and plastics are synthesised using H_2O_2 hydroxylation and Au-Pd bimetallic catalysts [25, 102, 103]. An alternate and efficient approach to use biocatalysis instead of toxic chemical catalyst could be of high interest. Various bacterial and fungal species have been reported to oxidise the C-H bond of these cyclic compounds [86, 104].

The monooxygenase enzyme CYP101B1 and CYP101C1, from *Novosphingobium aromaticivorans* DSM12444, has been reported to oxidise norisoprenoids (Chapter-3) and other structurally diverse classes of substrate [14, 19, 76, 91]. β-ionone has been reported to be oxidised by CYP101B1 preferentially at the C3 (80%) position whereas, CYP101C1 prefers to oxidise at the C4 (75%) position [38, 78]. Previously (Chapter-3), we have discussed the importance of the butenone side chain of β-ionone in binding the substrate in the active site of these enzymes.

It has been shown that the addition of a carbonyl group to larger ring structures improves the binding affinity of the substrate towards CYP101B1 and CYP101C1 [105, 106]. For example, cyclododecane binds to CYP101B1 with lower affinity (30% HS; K_d = 0.16 ± 0.03 µM) and generates a diol instead of a monohydroxy product (Figure 4.2). The monohydroxy is generated but not observed because it acts as a better substrate than cyclododecane (Figure 4.2).

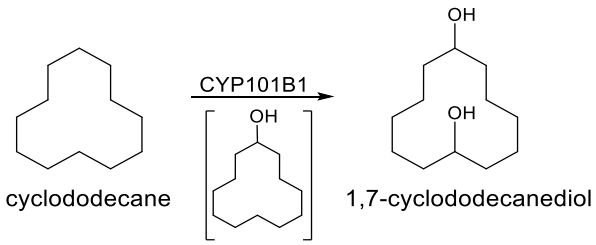

Figure 4.2: Cyclododecane oxidation by CYP101B1.

However, cyclododecanone binds to CYP101B1 higher affinity (90% HS; 0.16 ± 0.03 µM) and high selectivity generating a single monohydroxy major product in high yield with both CYP101B1 and CYP101C1 enzyme (Figure 4.3) [105]. This suggests that the ketone moiety enables more favourable binding in the active site of these enzymes. CYP101B1 has been reported to oxidise cyclic ketones selectively at the position opposite to the keto group, whereas, CYP101C1 prefers the position next to the keto group (Figure 4.3) [106].

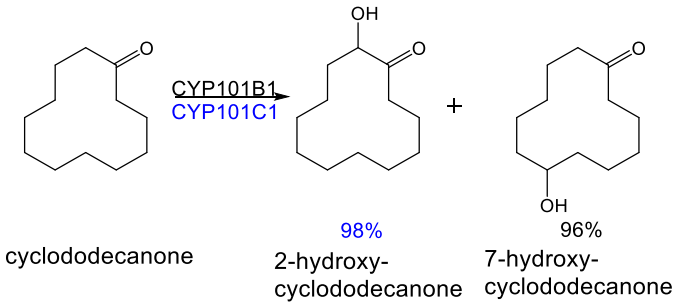

Figure 4.3: Cyclodedecanone oxidation by CYP101B1 and CYP101C1.

CYP101B1 and CYP101C1 have also been demonstrated to oxidise cycloalkanes with an ester directing group more efficiently than their parent cycloalkanes [91]. The ester directing group is thought to resemble the butenone side chain of a norisoprenoid and helps to hold the substrate in a suitable orientation for efficient and selective oxidation [91]. For example, cyclododecyl acetate bound to CYP101B1 induces a spin state shift of almost completely high spin (95% HS) and binds to the enzyme with high affinity (K_d = 0.05 ± 0.01 µM) [105]. It was oxidised to generate 7-*trans*-cyclododecyl acetate with 74% selectivity (Figure 4.4) [105].

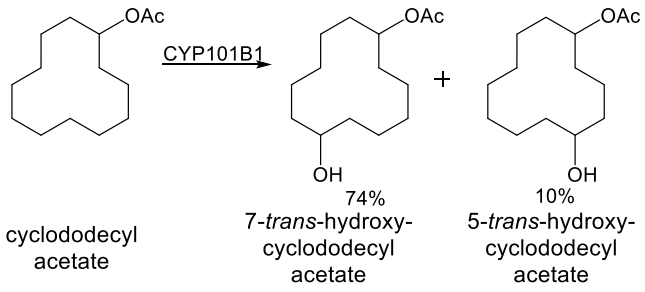

Figure 4.4: The oxidation of cyclododecyl acetate by CYP101B1. The remaining 16% of product yield was another hydroxy species, not generated in sufficient quantity for characterisation.

Keeping all this in mind, we selected a range of diverse substrates containing a carbonyl group or ester directing group (Figure 4.5), to further explore the substrate range of both CYP101B1 and CYP101C1.

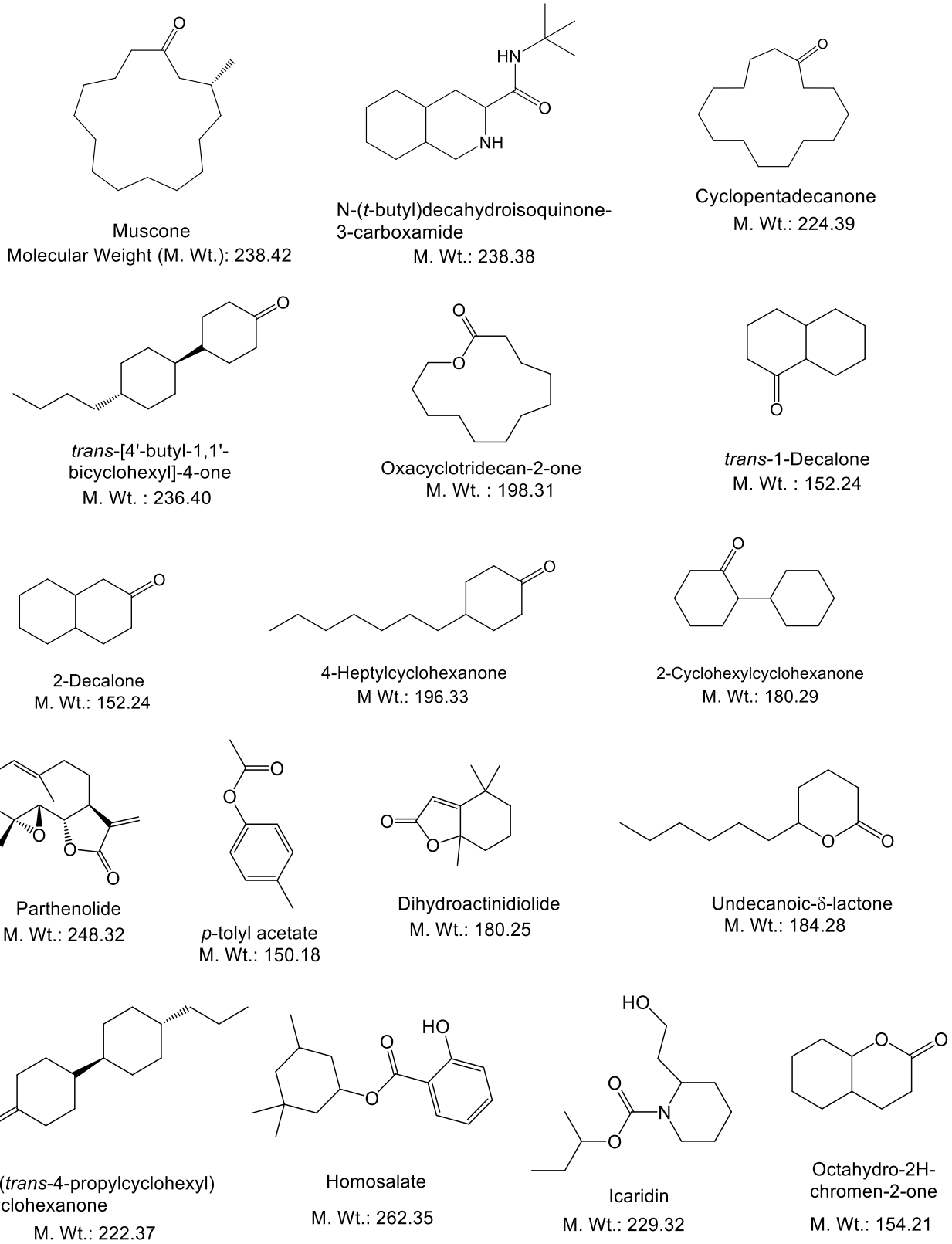

Figure 4.5: Substrates screened with CYP101B1 and CYP101C1 (except p-tolyl acetate, which was only screened with CYP101B1). Molecular weights are mentioned to indicate the range of molecular weights that could be accommodated by the enzyme.

Most of these substrates (Figure 4.5) are industrially useful. The two decalones (*trans*-1-decalone and 2-decalone) are used as fragrance agents. Muscone is considered a valuable compound and a primary contributor to the odour of musk. Homosalate is widely used as a chemical in sunscreens and skin care products with SPF. Icaridin is used as an insect repellent.

4.2 Results

These substrates (Figure 4.5) were initially screened to access if they induce a spin-state shift when added to both CYP101B1 and CYP101C1. The spin-state shift induced by substrate binding gives an indication of the ability of substrate to replace the water ligand bound to the heme centre and hence if it fits in the active site pocket of the enzyme. Later, *in vitro* oxidation studies (section 2.7) were carried out for the substrates with both CYP101B1 and CYP101C1, the products were then analysed for product formation by GCMS. Amongst the substrates tested, those with a reasonable NADH oxidation rate were again screened for *in vitro* oxidation studies in triplicate and analysed again for product formation by GCMS. Finally, dissociation constant studies were performed for the best substrates (Figure 4.19). The best enzyme / substrate combination was then used to scale up the products formed using a whole-cell turnover system (Section 2.3). The obtained products were then separated or purified by flash chromatography on a silica column using a hexane / ethyl acetate stepwise gradient before characterisation (Section 2.3).

4.2.1 Spin-state shift studies

With CYP101B1 enzyme, the cyclic ketone substrates showed a significant type-I spin-state shift. For example, *trans*-1-decalone and 2-decalone both showed moderately high spin state shifts of 60% HS and 50% HS (Figure 4.6, Table 4.1). Muscone displayed a spin state shift of 45% HS (Figure 4.6, Table 4.1) with CYP101B1. The spin state shift of 2-cyclohexylcyclohexanone was observed to be 55% (Table 4.1). Other cycloketone derivatives such as *trans*-[4'-butyl-1,1'-bicyclohexyl]-4-one, 4-(*trans*-4-propylcyclohexyl) cyclohexanone and 4-heptylcyclohexanone exhibits spin-state ranging from 15% HS to 30% HS (Table 4.1). Cyclic esters and lactones such as 8-oxaspiro[4.5]decane-7,9-dione, dihydroactinidiolide, octahydro-2H-chromen-2-one and undecanoic-δ-lactone exhibited a low spin state shift ranging from (5-35%, Figure 4.6, Table 4.1). On the other hand, oxacyclotridecan-2-one, which is also a lactone, displayed a spin state shift of 70% HS with CYP101B1 (Figure 4.6, Table 4.1). Homosalate, that contains an ester group exhibits a spin-state shift of 15% HS (Table 4.1). Parthenolide, a sesquiterpene lactone that shifts the spin state by 40% HS (Table 4.1). Icaridin induces a small spin-state shift of 20% HS (Table 4.1). N-(Ter-butyl) decahydroisoquinone-3-carboxamide, where the decahydroisoquinoline ring is attached to a *t*-butyl group via an amide linkage showed a spin-state shift of 5% HS (Figure 4.6, Table 4.1). *p*-Tolyl acetate induced the highest spin-state shift of 75% HS (Table 4.1).

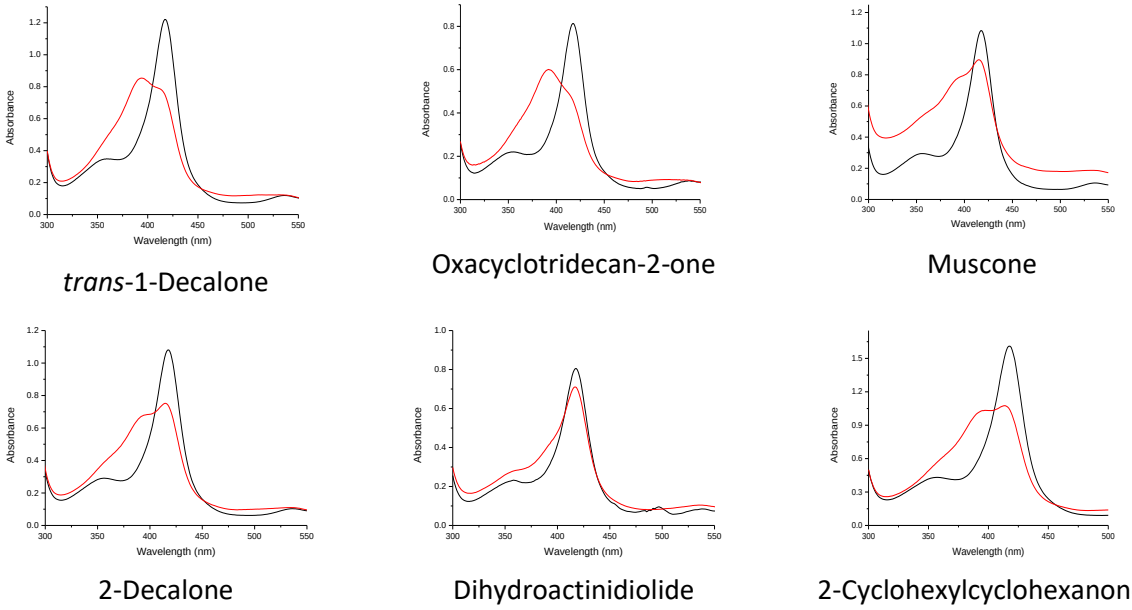

Figure 4.6: Spin state shift graphs of selected substrate with CYP101B1. Further spin state spectra of the substrates with CYP101B1 are shown in Appendix-B (Figure B.1)

Table 4.1: Spin state data of selected substrate with CYP101B1.

Substrate	**%HS**[a]	**Substrate**	**%HS**[a]
p-tolyl acetate	75	Undecanoic-δ-lactone	30
Cyclopentadecanone	75	Dihydroactinidiolide	25
Oxacyclotridecan-2-one	70	Octahydro-2H-chromen-2-one	25
trans-1-Decalone	60	Icaridin	20
2-Cyclohexylcyclohexanone	55	4-Heptylcyclohexanone	20
2-Decalone	50	*trans*-[4'-Butyl-1,1'-bicyclohexyl]-4-one	15
Muscone	45	Homosalate	15
Parthenolide	40	N-(*t*-butyl) decahydroisoquinone-3-carboxamide	5
4-(*trans*-4-Propylcyclohexyl) cyclohexanone	30		

[a] the spin-state shift induced by substrate binding is given by the percentage of high spin heme (%HS).

With CYP101C1, all the substrates (Figure 4.5) exhibits a spin state shift in range of 0% HS to 10% HS (Table 4.2).

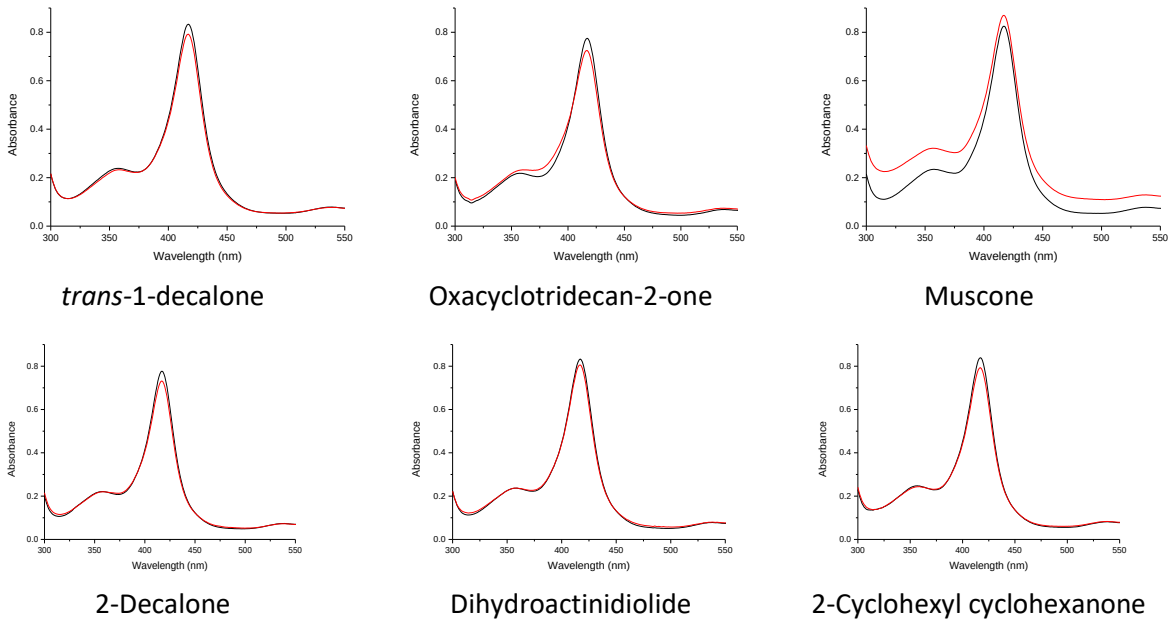

Figure 4.7: Spin-state shift graphs of selected substrates with CYP101C1. Further spin state spectra of the substrates with CYP101C1 are shown in Appendix-B (Figure B.3)

Table 4.2: Spin-state shift data of selected substrate with CYP101C1

Substrate	**%HS**[a]	**Substrate**	**%HS**[a]
p-Tolyl acetate	0	Undecanoic-δ-lactone	10
Cyclopentadecanone	10	Dihydroactinidiolide	0
Oxacyclotridecan-2-one	≤ 5	Octahydro-2H-chromen-2-one	0
trans-1-Decalone	0	Icaridin	0
2-Cyclohexylcyclohexanone	0	4-Heptylcyclohexanone	10
2-Decalone	0	*trans*-[4'-Butyl-1,1'-bicyclohexyl]-4-one	10
Muscone	10	Homosalate	10
Parthenolide	0	N-(*t*-butyl) decahydroisoquinone-3-carboxamide	0
4-(*trans*-4-Propylcyclohexyl) cyclohexanone	< 5		

[a]the spin-state shift induced by substrate binding is given by the percentage of high spin heme (%HS).

4.2.2 *In vitro* oxidation turnover studies

In vitro oxidation studies were carried out for all the selected substrates (Figure 4.5) with both CYP101B1 and CYP101C1. These substrates were evaluated for the rate at which they consume NADH, which could either lead to generation of product or uncoupling side reactions (Chapter-1). The oxidation products were analysed by GCMS based on the change in mass (Δm/z) compared to the substrate.

The substrate *trans*-1-decalone when oxidised by CYP101B1 exhibits an NADH oxidation rate of ~265 min^{-1} (Figure 4.8 (a)). The GCMS analysis of this turnover reaction solution reveals three separate products at t_R = 9.06, 9.27, 9.4 min (Figure 4.8 (c)). Mass spectra of all the three products indicates that they are mono-hydroxylated products with a mass of m/z = 168 AMU (Δm/z = +16 AMU) (Figure B.6). The substrate 2-decalone was supplied as a mixture of its *cis* and *trans* isomers. The addition of substrate caused an NADH oxidation rate of ~470 min^{-1} (Figure 4.8 (b)). This substrate generated four different metabolites at t_R = 8.40, 9.53, 9.86 and 10.02 min (Figure 4.8 (d)) which on analysis showed a mass of m/z = 168.05 AMU (Δm/z = +16 AMU) (Figure B.7). This indicates that they were all monohydroxylated products.

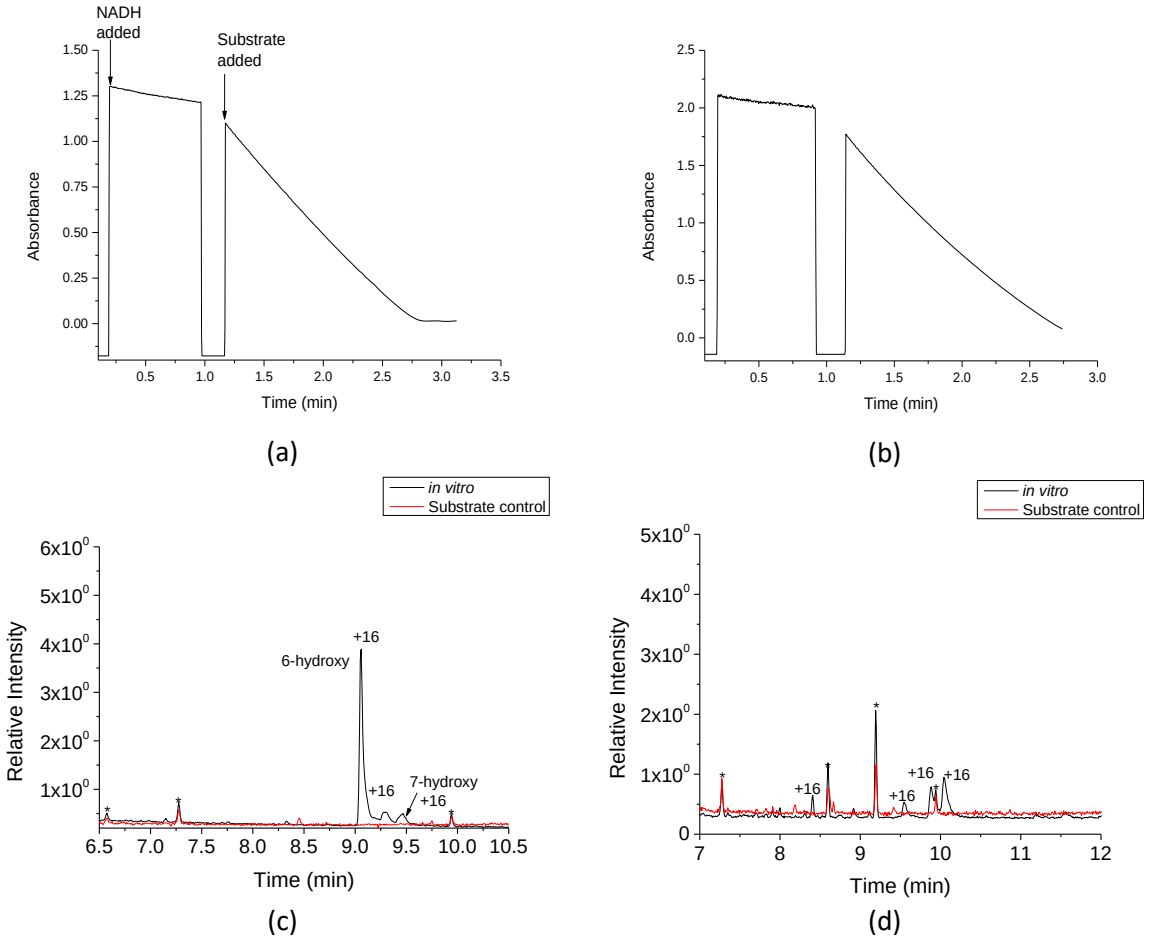

Figure 4.8: UV-Vis plots of *in vitro* turnover of (a) *trans*-1-decalone and (b) 2-decalone at 340 nm. GCMS analysis of the *in vitro* turnover (zoomed in) of (c) *trans*-1-decalone and (d) 2-decalone with CYP101B1 (black) with substrate control (red). The impurities are marked as (*), also present in substrate control.

Cyclopentadecanone was oxidised by CYP101B1 with a NADH oxidation rate of ~100 min^{-1} (Figure B.2). The GCMS analysis exhibits the generation of two metabolites (Figure 4.9). The metabolite at t_R = 14.65 min exhibits a mass of, m/z = 238 AMU (Δm/z = +14 AMU), the change in mass by two units compared to the oxidation product that would indicate an oxygen has been added to the compound with an additional abstraction of hydrogen to generate a ketone further oxidation product. The second metabolite at t_R = 15.08 min (Figure 4.9) has a mass of m/z = 240.25 AMU (Δm/z = +16 AMU) (Figure B.8). This suggests that it is a monooxygenase product.

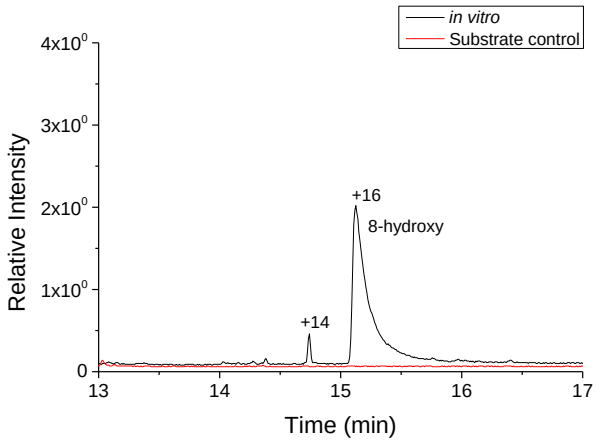

Figure 4.9: GCMS analysis of the *in vitro* turnover (zoomed in) of cyclopentadecanone (m/z = 224 AMU) by CYP101B1 (black) with substrate control (red). The products are identified at t_R = 14.65 min and t_R = 15.08 min. Further data given in Appendix-B, Figure B.8.

CYP101B1 mediated *in vitro* oxidation of oxacyclotridecan-2-one caused an NADH oxidation rate of ~360 min^{-1} (Figure B.2). The GCMS analysis of this turnover shows that three different metabolites were generated at t_R = 11.99 min, 12.1 min and 13.18 min (Figure 4.10). All three metabolites showed mass of m/z = 214.1 AMU (Δm/z = +16 AMU) suggesting all three of them may be a monooxygenase product (Figure B.10).

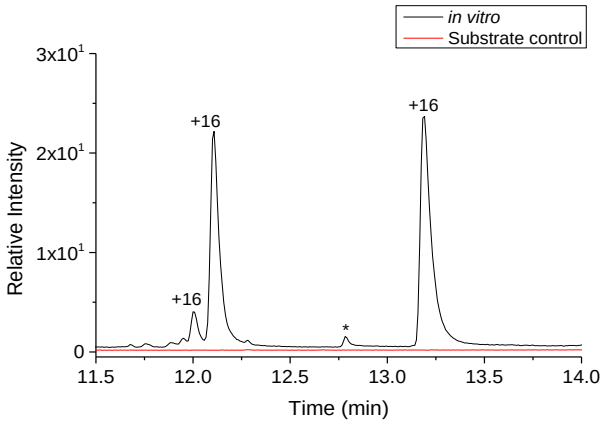

Figure 4.10: GCMS analysis of the *in vitro* turnover (zoomed in) of oxacyclotridecan-2-one by CYP101B1 (black) with substrate control (red). Products at t_R = 11.99 and 13.18 min. The metabolite marked as (*) is the oxidation of the impurity present in substrate. Further data given in Appendix-B, Figure B.10.

GCMS analysis of *in vitro* oxidation of *p*-tolyl acetate by CYP101B1 showed production of two metabolites. The substrate was observed at t_R = 4.25 min with a mass of (m/z = 150.05 AMU) (Figure 4.11 (a)). The metabolite at t_R = 8.0 min has a mass of (m/z = 166.05 AMU, Δm/z = +16) (Figure 4.12, which was later characterised as 7-hydroxy-*p*-tolyl acetate by NMR analysis (Figure 4.25). The peak at t_R = 6.58 min corresponds to the mass of (m/z = 124 AMU, Δm/z = -26 AMU) suggests that it could be 4-hydroxybenzyl alcohol generated from the hydroxylation of *p*-cresol (m/z = 108.05 AMU) (Figure 4.11). This could also be generated from the hydrolysis of the ester group in the 7-hydroxy-*p*-tolyl acetate product. This was confirmed by comparing the mass spec data to the reported data in NIST chemistry WebBook, SRD 69.

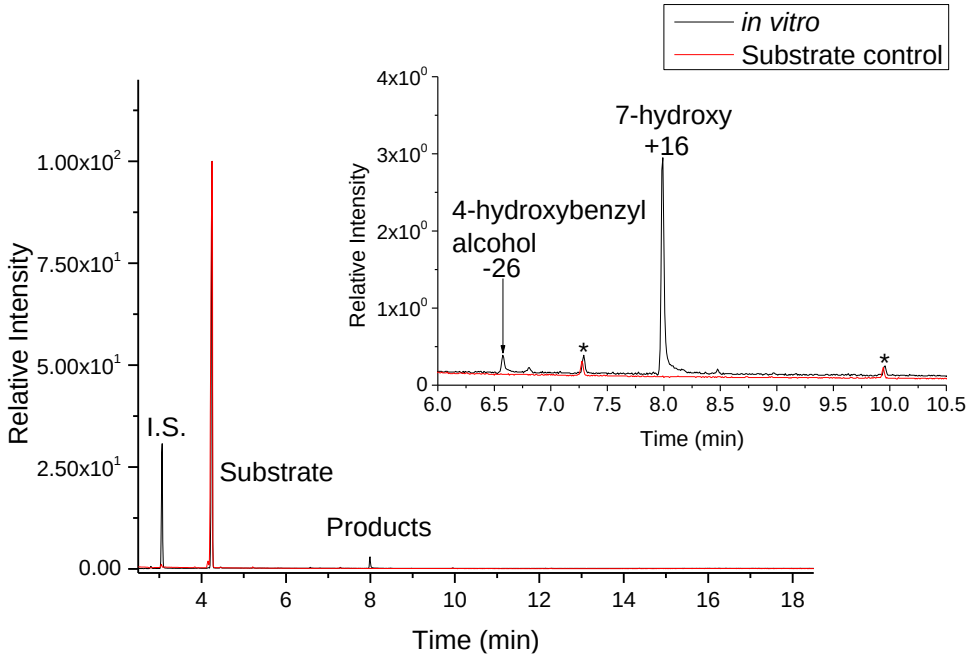

Figure 4.11: (a) GCMS analysis of the *in vitro* turnover of *p*-tolyl acetate by CYP101B1 (black) with substrate control (red). Products observed at t_R = 6.58, 8.0 min. The impurity from substrate and its oxidation product is marked as (*), Internal standard is marked as (I.S.).

MS analysis of *p*-tolyl acetate oxidation product (4-hydroxybenzyl alcohol) at t_R = 6.58 min (m/z = 124.05 AMU, Δm/z = + 16 AMU) (NIST MS number: 231451).

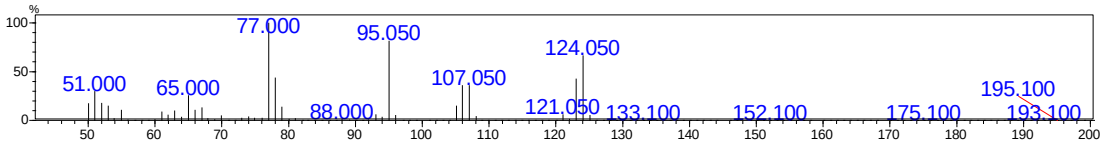

MS analysis of *p*-tolyl acetate oxidation product (7-hydroxy-*p*-tolyl acetate) at t_R = 8.00 min (m/z = 166.050 AMU, Δm/z = + 16 AMU)

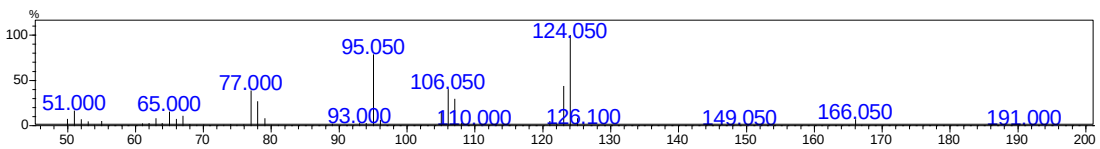

Figure 4.11 (b): Mass spectra analysis of *in vitro* oxidation of *p*-tolyl acetate by CYP101B1.

Dihydroactinidiolide oxidation by CYP101B1 occurred with a NADH oxidation rate of ~700 min^{-1} (Figure B.2). In the GCMS analysis of *in vitro* turnover, the substrate peak is seen at t_R = 9.41 min (m/z = 180.05 AMU) (Figure B.11). Three oxidation products were observed at t_R = 12.04 min, 12.21 min and 12.28 min (Figure 4.12). All the three products correspond to a mass of m/z = 196 AMU (Δm/z = +16 AMU) suggesting they arise from monooxygenation (Figure B.11).

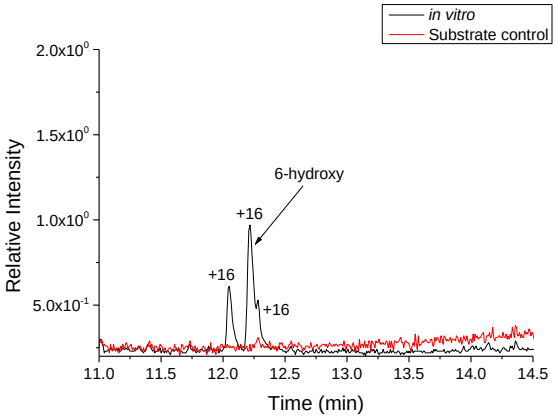

Figure 4.12: GCMS analysis of the *in vitro* turnover (zoomed in) of dihydroactinidiolide by CYP101B1 (black) with substrate control (red). Products are observed at t_R = 12.04, 12.21 and 12.28 min. Further data given in Figure B.11.

Other substrates did not display a significant slope to suggest, rapid NADH consumption and therefore turnover of the catalytic cycle. However, GCMS analysis was performed on all the *in vitro* turnovers regardless of their ability to display a good NADH consumption. Little or no product was observed for all these substrates. For example, the 4-(*trans*-4-propylcyclohexyl) cyclohexanone, which on addition to the *in vitro* turnover by CYP101B1 induced a poor NADH decay similar to the leak rate (Figure B.2). The GCMS analysis of this turnover did not show any signs of product formation (Figure 4.13 (a)). The undecanoic-δ-lactone turnover by CYP101B1 was run on GCMS shows that product is generated (Figure 4.13 (b)). However, the product could not be rationalised as simple oxy-functionalised metabolite based on its mass spectrum. This analysis was complicated by the fragmentation of the molecule.

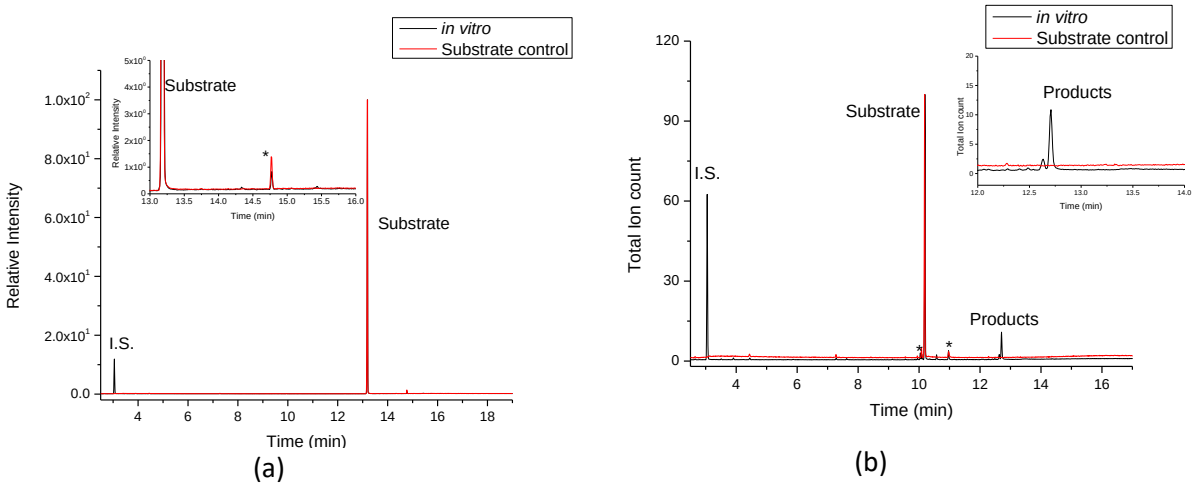

Figure 4.13: GCMS analysis of the *in vitro* turnover of (a) 4-(*trans*-4-propylcyclohexyl) cyclohexanone and (b) Undecanoic-δ-lactone by CYP101B1 (black) with substrate control (red). The impurities are marked as (*) and the internal standard is denoted by (I.S.).

CYP101C1 was less selective than CYP101B1 for *in vitro* turnovers with decalones. For example, the *in vitro* turnover of *trans*-1-decalone by CYP101C1 (Figure 4.14) generated seven metabolites, which were different from the three metabolites generated by the *in vitro* turnover of *trans*-1-decalone by CYP101B1 (Figure 4.14 (a)). The GCMS analysis of the peaks at t_R = 7.15, 7.48, 7.75, 8.34, 10.04 min suggests that they are monooxygenase product (Δm/z = +16 AMU) (Figure 4.14). The peaks at t_R = 7.86 min had a mass of m/z = 150 AMU (Δm/z = -2 AMU) and could arise from a desaturation metabolite (Appendix, Figure B.15).

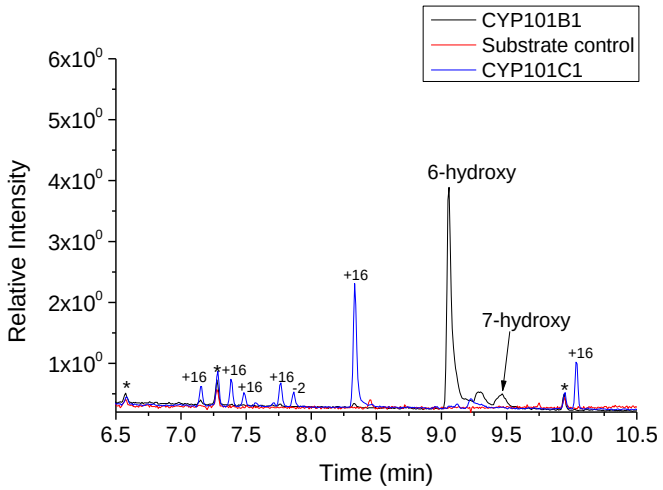

Figure 4.14 (a): GCMS analysis of *in vitro* turnover (zoomed in) of *trans*-1-decalone with CYP101C1 (blue) in comparison to CYP101B1 (black) and substrate control (red). The impurities are marked as (*) and the internal standard is denoted as (I.S.). Further data given in Figure B.6, B.12.

MS analysis of major product of *in vitro* oxidation of *trans*-1-decalone by CYP101C1 at t_R = 8.34 min (m/z = 168.100 AMU, Δm/z = + 16 AMU)

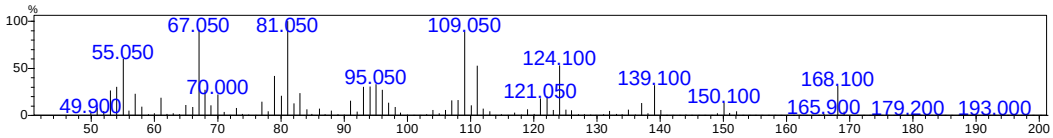

MS analysis of major product of *in vitro* oxidation of *trans*-1-decalone by CYP101B1 at t_R = 9.06 min (m/z = 168.050 AMU, Δm/z = + 16 AMU)

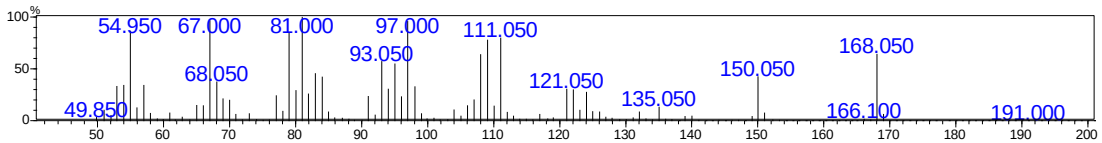

Figure 4.14 (b): Mass spectra comparison of the major product of *trans*-1-decalone on *in vitro* oxidation by CYP101C1 (top) and CYP101B1 (bottom). Further information is provided in Appendix-B, Figure B.12.

Similarly, the GCMS analysis of the *in vitro* turnover of 2-decalone by CYP101C1 shows that it generated five metabolites (Figure 4.15). The metabolite at t_R = 8.40 min has a mass suggesting it to be a monooxygenase metabolite (m/z = 168.05 AMU, Δm/z = +16 AMU), it also co-eluted with the metabolite generated from the *in vitro* turnover of 2-decalone by CYP101B1. All the other metabolites were different from those generated using CYP101B1 (Figure 4.15). These metabolites exhibited a mass suggesting they were all monooxygenase products (Δm/z = + 16 AMU, Figure B.13).

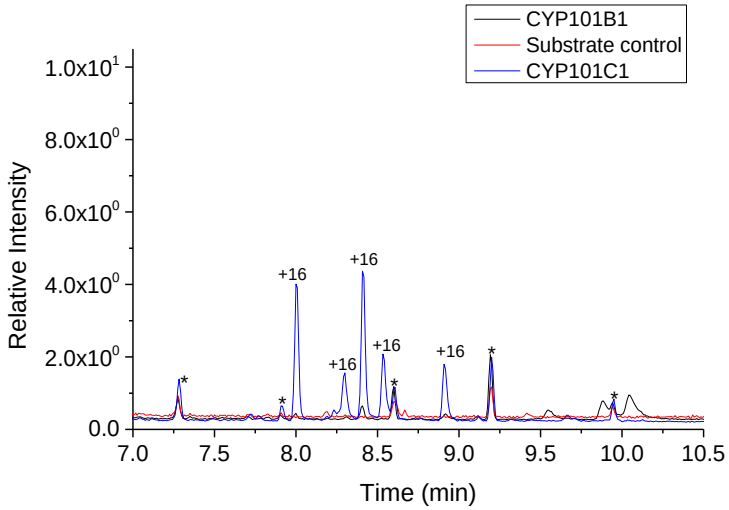

Figure 4.15: GCMS analysis of the *in vitro* turnover (zoomed in) of 2-decalone by CYP101C1 (blue) in comparison with CYP101B1 (black) and substrate control (red). The impurities are marked as (*). Further data given in Figure B.7, B.13.

In the case of dihydroactinidiolide, CYP101C1 was more selective, the *in vitro* oxidation generated a single product at t_R = 10.03 min (Figure 4.16). This peak was not observed in the *in vitro* oxidation by CYP101B1 (Figure 4.16). The MS analysis for this peak suggests that it is a monooxygenase product with a mass corresponding to m/z = 196.2 AMU (Δm/z = +16 AMU) (Figure B.14).

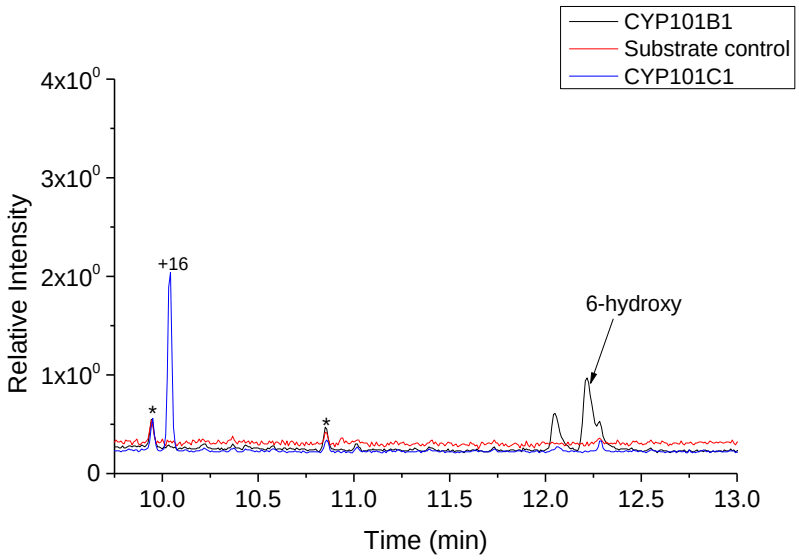

Figure 4.16: GCMS analysis of *in vitro* turnover (zoomed in) of dihydroactinidiolide with CYP101C1 (blue) in comparison to CYP101B1 (black) and substrate control (red). The impurities are marked as (*). Further data given in Figure B.11, B.14.

An additional metabolite was observed at t_R = 11.06 min upon GCMS analysis of the *in vitro* oxidation of oxacyclotridecan-2-one by CYP101C1 which was absent in its oxidation by CYP101B1. The other metabolites generated by the oxidation of oxacyclotridecan-2-one by CYP101B1 at t_R = 12.12 min and 13.17 min, were also generated by CYP101C1 (Figure 4.17). The mass spectra for all three of these metabolites suggests that they are monooxygenase products (Δm/z = +16 AMU; Figure B. 15).

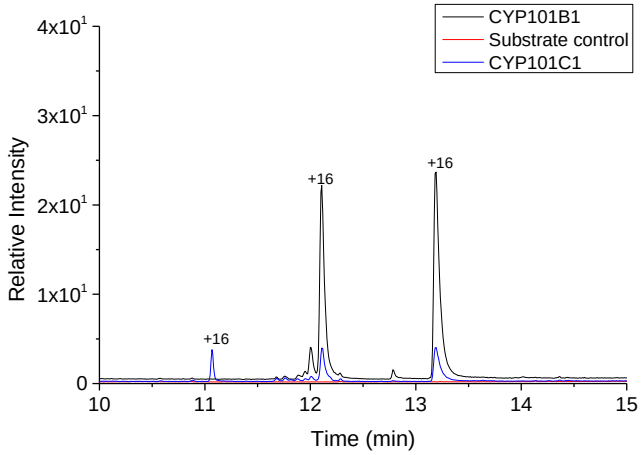

Figure 4.17: GCMS analysis of *in vitro* turnover (zoomed in) of oxacyclotridecan-2-one with CYP101C1 (blue) in comparison to CYP101B1 (black) and substrate control (red). The impurities are marked as (*). Further data given in Figure B.10, B.15.

The CYP101C1 enzyme was unable to oxidise any other of the selected substrates. For example, muscone was observed as one of the tightest binding substrate with CYP101B1 with a dissociation constant of k_d = 0.27 ± 0.05 µM (Figure 4.18 (a)), generating a single major product but its *in vitro* oxidation by CYP101C1 did not generate any significant oxidation metabolite (Figure 4.18 (b)).

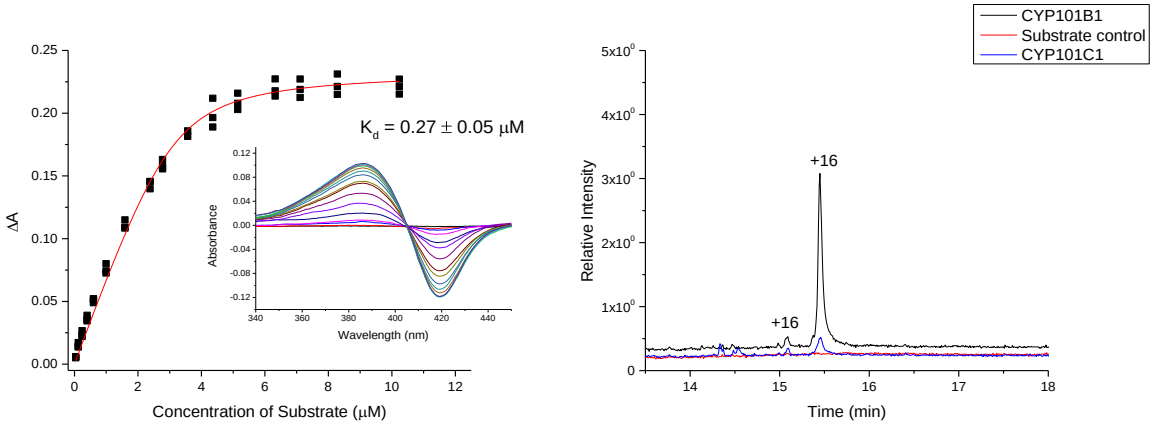

(a) (b)

Figure 4.18: (a) Dissociation constant analysis of muscone with CYP101B1. (b)GCMS analysis of *in vitro* turnover (zoomed in) of muscone with CYP101C1 (blue) in comparison to CYP101B1 (black) and substrate control (red). The impurities are marked as (*). Further data given in Figure B.9.

After analysing the spin-state studies and the *in vitro* studies, for the selected substrates (Figure 4.5) with both CYP101B1 and CYP101C1, five substrates (Figure 4.19) were chosen for scale up with the whole-cell turnover system. The CYP101B1 enzyme is observed to oxidise the substrates more efficiently generating larger quantities of metabolite compared to the CYP101C1 enzyme. Hence, this enzyme was used for the whole-cell turnovers. The products were then extracted and separated by flash chromatography using a hexane-ethyl acetate system ranging from 5% to 60% ethyl acetate. Due to absence of a chromophore group in most of the substrates, the separation could not be performed on HPLC.

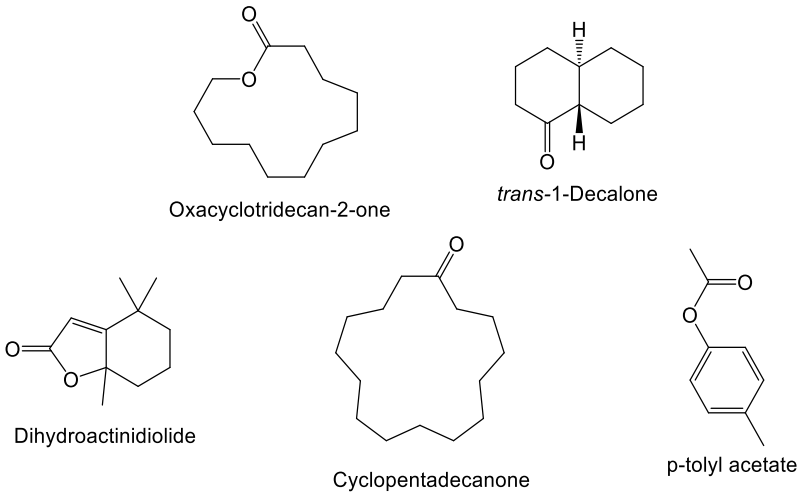

Figure 4.19: Structure of substrates chosen for whole-cell oxidation.

The oxidation of dihydroactinidiolide by CYP101B1, induced a NADH oxidation rate of 564 ± 45 min^{-1}. However, the product formation rate (33 ± 4 min^{-1}) and the coupling efficiency (6%) were low. The whole-cell oxidation system generated a major product (t_R = 12.21 min, Figure 4.20) which was separated by flash chromatography and characterised as the 6-hydroxy-dihydroactinidiolide by NMR analysis (Figure 4.21). The other two metabolites (t_R = 12.04 min and 12.28 min) were not generated in sufficient quantity to be characterised.

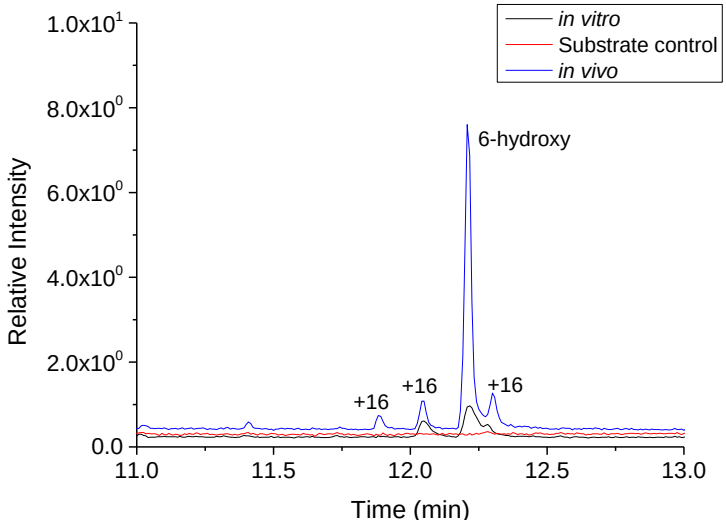

Figure 4.20: GCMS analysis of the *in vitro* turnover (zoomed in) of dihydroactinidiolide by CYP101B1 (black) in comparison with *in vivo* (blue) and substrate control (red).

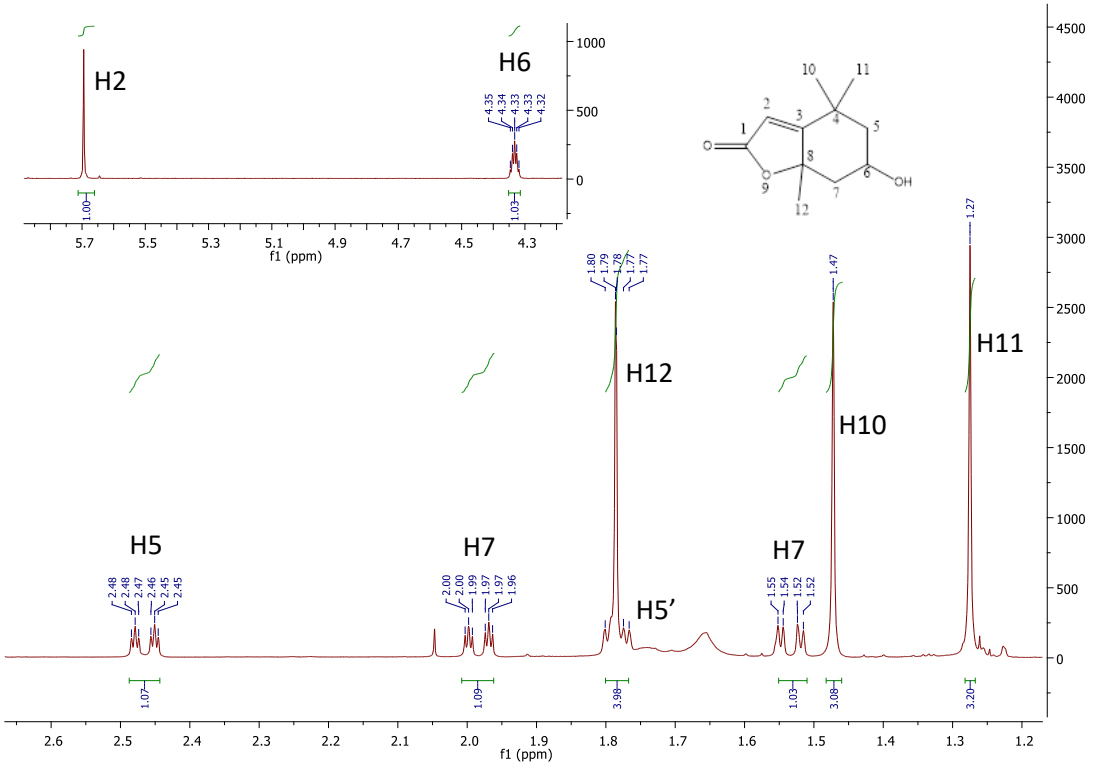

(a)

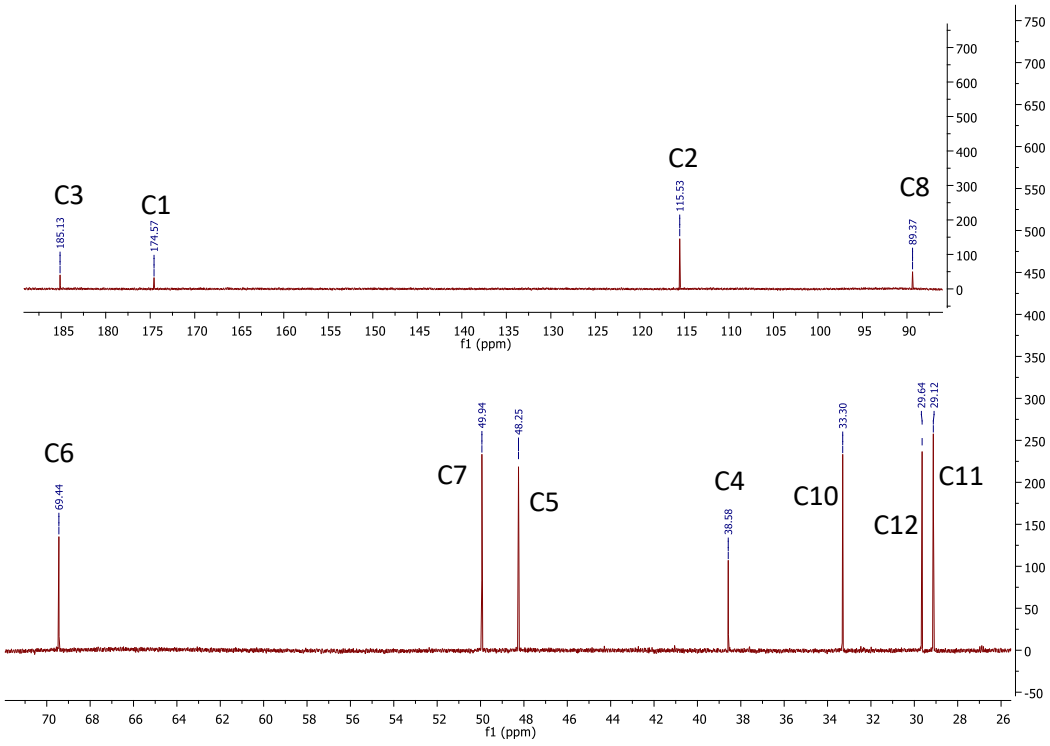

(b)

Figure 4.21 (a): ^{1}H NMR of 6-hydroxy-dihydroactinidiolide in $CDCl_3$. The signal for H5' is partly visible in the range 1.80-1.76 ppm and partly hidden behind the signal for H12 at 1.78 ppm (b): ^{13}C NMR of 6-hydroxy-dihydroactinidiolide in $CDCl_3$. Impurity is marked as (*) Further data provided in Appendix-B (Figure B.23).

Oxacyclotridecan-2-one binds to CYP101B1 with a high dissociation constant (K_d = 3.5 ± 0.2 µM) (Figure 4.22 (a), Table 4.3). It was oxidised with a NADH oxidation rate of 423 ± 5 min^{-1}. The product formation rate and the coupling efficiency were observed as 307 ± 81 min^{-1} and 72% (Table 4.3). The whole-cell oxidation system, generated a single product at t_R = 12.10 min (Figure 4.22). It was separated from the substrate using flash chromatography. The products were present as a mixture along with impurities that could not be separated. However, the products were distinguished via ^{13}C NMR carbon signals (Figure 4.23 (a)) based on their relative intensities (Table 4.4). The two products could not be completely characterised. However, the ^{13}C NMR depicts a total of 24 signals (12 for each compound), the signals for the carbonyl group (C=O) around 176 ppm region, the carbon next to ester (CH_2O) around 72 ppm region and the hydroxylated carbon (CHOH) around 66-67 ppm region (Table 4.4). Later these signals were matched to the ^1H NMR using HSQC NMR (Figure 4.23 (b)) and the carbon next to them could be identified by HMBC NMR. In HMBC NMR we can see that the signal for C1 at 176 ppm correlates with three CH_2 signals, which do not correlate to the signal for hydroxylated carbon (CHOH). Also, the signal at 72 ppm (CHOH) is next to three CH_2 signals and the signal for C12 (CH_2O) is next to three different CH_2 signals which do not relate to the CHOH signal. This suggests that the oxacyclotrideca-2-one could be hydroxylated opposite to the ester group at C6, C7 or C8. The remaining carbon signals could not be assigned due to their close vicinity with other signals and the specific site of hydroxylation could not be determined. This data agrees to the reported data that in case of cyclic ketones and cyclic esters, CYP101B1 preferred to hydroxylate the substrate at the carbon opposite to the respective ketone and ester functional group [105].

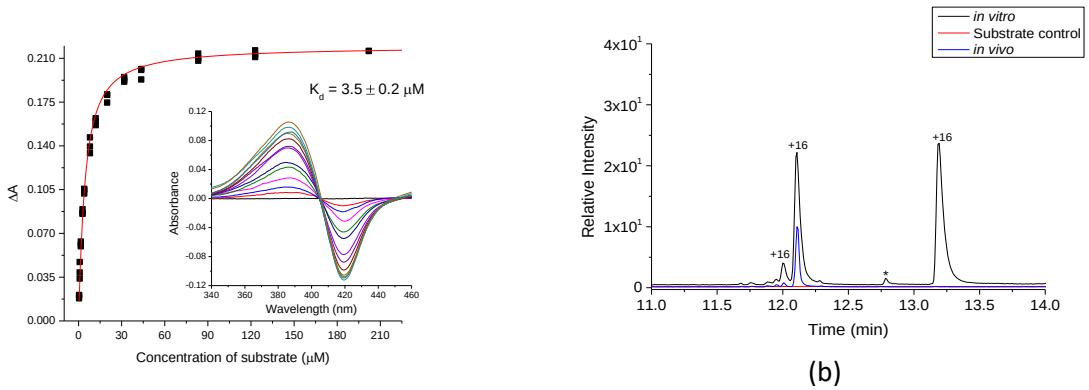

(a) (b)

Figure 4.22: (a) Dissociation constant analysis of oxacyclotridecan-2-one with CYP101B1. (b) GCMS analysis of the *in vitro* turnover (zoomed in) of oxacyclotridecan-2-one by CYP101B1 (black) in comparison with *in vivo* (blue) and substrate control (red). The impurities are marked as (*) and the internal standard is denoted as (I.S.). Further data given in Figure B.10.

Table 4.3: Substrate binding and *in vitro* turnover data for CYP101B1 with selected substrate.

Substrate	HS (%)	K_d (µM)	NADH (min^{-1})	PFR (min^{-1})	C %
Oxacyclotridecan-2-one	70	3.5 ± 0.2	423 ± 5	307 ± 81	72
Dihydroactinidiolide	20	*	564 ± 45	33 ± 4	6
trans 1-Decalone	60	180 ± 8	224 ± 2	37 ± 3	16
Cyclopentadecanone	75	0.2 ± 0.09	126 ± 4	47 ± 3	38
Muscone	60	0.27 ± 0.05	61 ± 3	10 ± 2	17

*K_d not calculated due to the low spin state shift. NADH is the NADH oxidation rate, PFR is the product formation rate, C % is the coupling efficiency, HS% is the spin state shift, K_d is the dissociation constant. Rates are reported as mean ± S.D. (n ≥ 3) and given in nmol per nmol CYP per min.

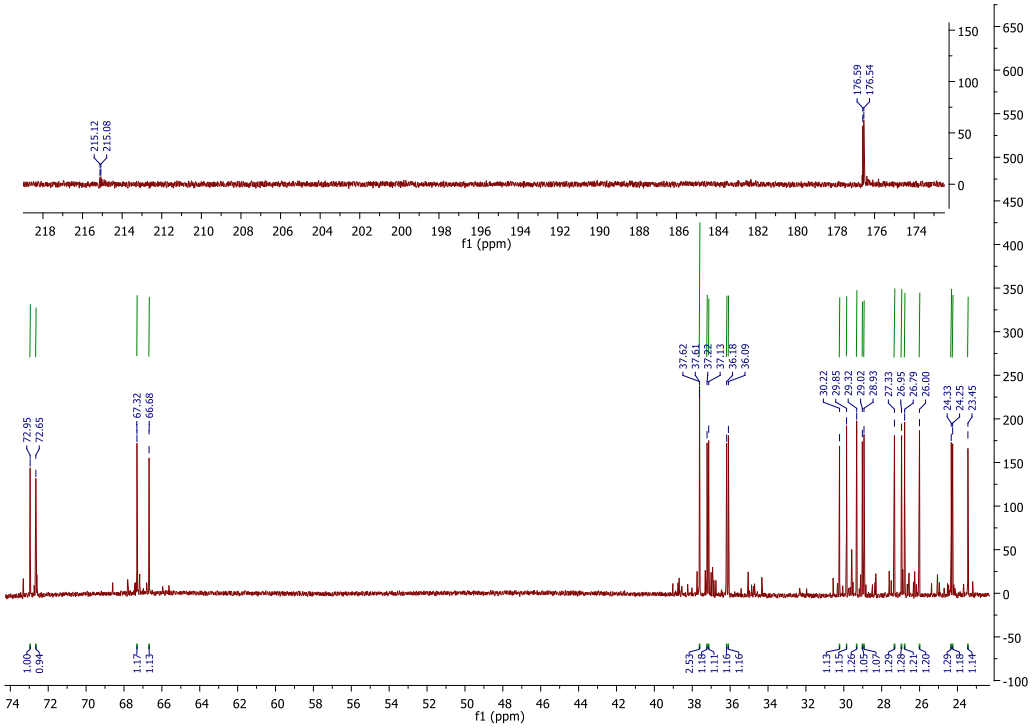

(a)

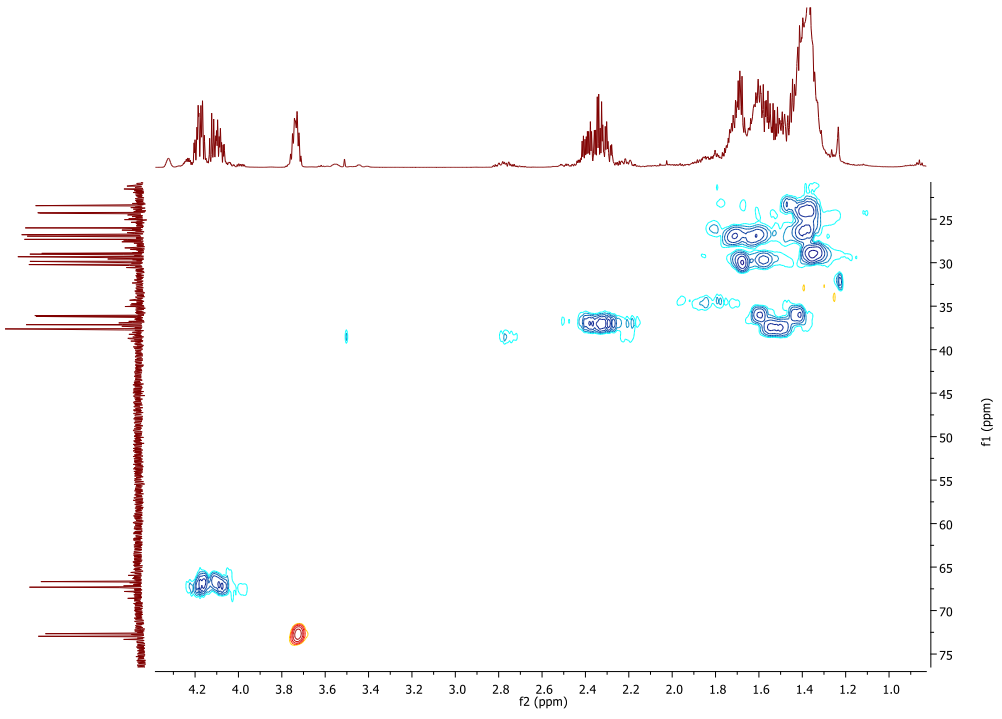

(b)

Figure 4.23: (a) ^{13}C NMR of oxacyclotridecan-2-one oxidation products and impurity. The details of assignment of the carbon peak are mentioned in Table 4.4. (b)HSQC NMR of a mixture of oxacyclotridecan-2-one products and impurity and impurity. Further data is given in Appendix-B (Figure B.22).

Table 4.4: Assignment of oxacyxlotridecan-2-one metabolites using ^{13}C NMR. The figures depict the possible site of hydroxylation (C6/C7/C8). The chiral centre is marked as (*) in the figure. The peak at 72.95 ppm is taken as reference to calculate the integral for other peaks.

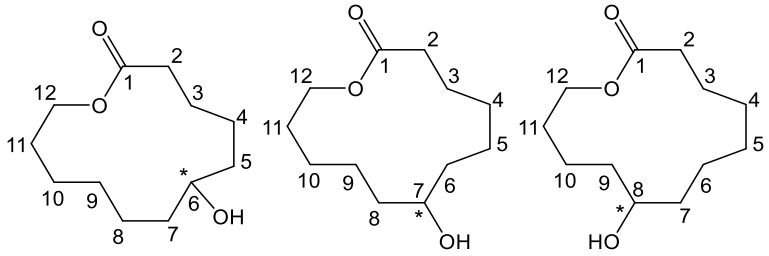

ppm	Integral	Intensity	Compound-1	Compound-2
176.59	0.37	59.7		C1
176.54	0.45	62.2	C1	
72.95	1 (ref)	144.2	COH	
72.65	0.94	132.3		COH
67.32	1.17	172.2	C12	
66.68	1.13	159.4		C12
37.62	1.0	224.2		CH_2
37.61	1.50	228.6	CH_2	
37.22	1.18	176.5	C2	
37.13	1.11	182.9		C2
36.18	1.16	172.5		CH_2
36.09	1.16	182.6	CH_2	
30.22	1.13	173.1		C11
29.85	1.15	192.4	C11	
29.32	1.26	197.8	CH_2	
29.02	1.05	178.0		CH_2
28.93	1.07	182.3		CH_2
27.33	1.29	189.7	CH_2	
26.95	1.28	185.2		CH_2
26.79	1.21	196.8	CH_2	
26.00	1.20	190.3	CH_2	
24.33	1.29	173.5		CH_2
24.25	1.18	180.9	CH_2	
23.45	1.14	176.3		CH_2

p-Tolyl acetate binds to CYP101B1 with a dissociation constant of K_d = 154 ± 4 µM. Its whole-cell oxidation by CYP101B1, generated two metabolites at t_R = 8.0, 14.01 min (Figure 4.24), both monohydroxy metabolites. The peak at t_R = 3.01 coeluted with the internal standard (*p*-cresol) which was also generated in the whole-cell oxidation from ester hydrolysis. The metabolite at t_R = 6.58 min was not generated in sufficient quantity to be characterised by NMR analysis but has been identified as 4-hydroxybenzyl alcohol by GCMS analysis. The metabolite at t_R = 8.0 min was separated successfully and characterised as 7-hydroxy-*p*-tolyl acetate by NMR analysis (Figure 4.25).

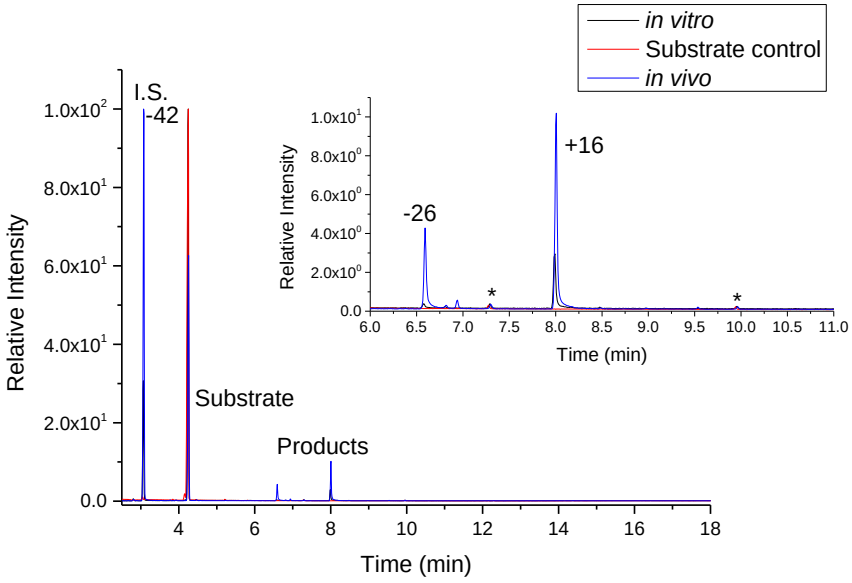

(a)

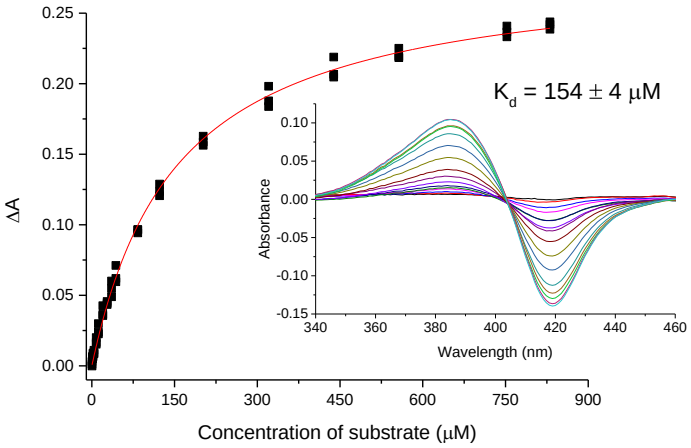

(b)

Figure 4.24: (a) GCMS analysis of the *in vitro* turnover of *p*-tolyl acetate by CYP101B1 (black) in comparison with *in vivo* (blue) and substrate control (red). The impurities are marked as (*) and the internal standard is denoted as (I.S.). (b) Dissociation constant analysis of *p*-tolyl acetate with CYP101B1.

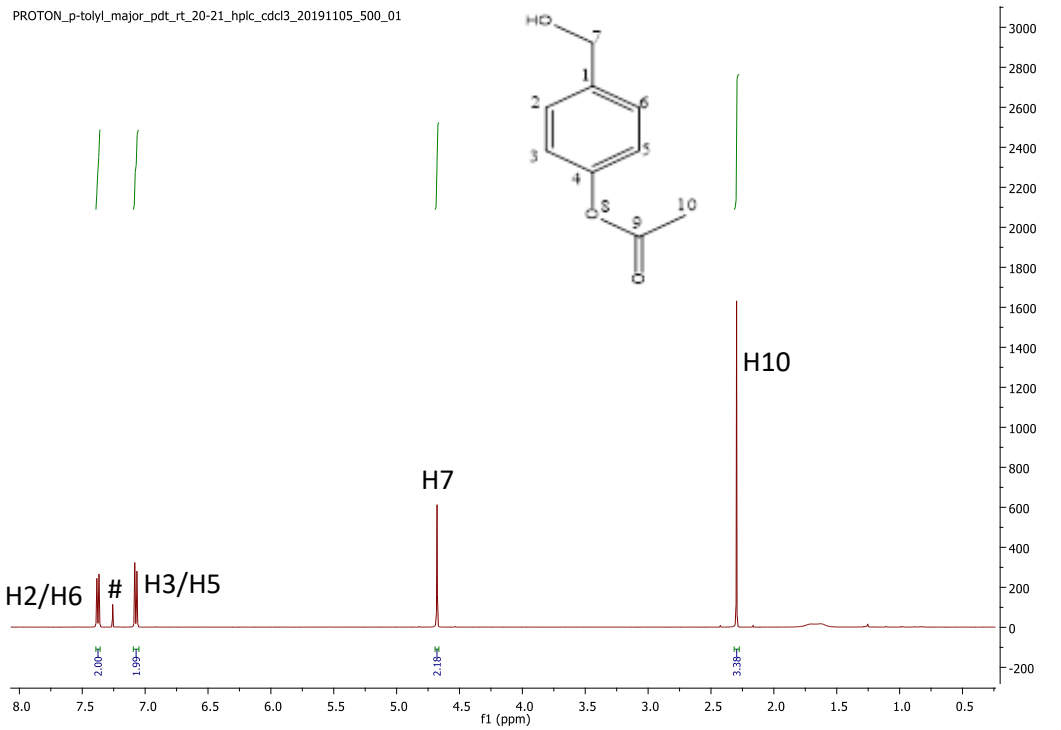

(a)

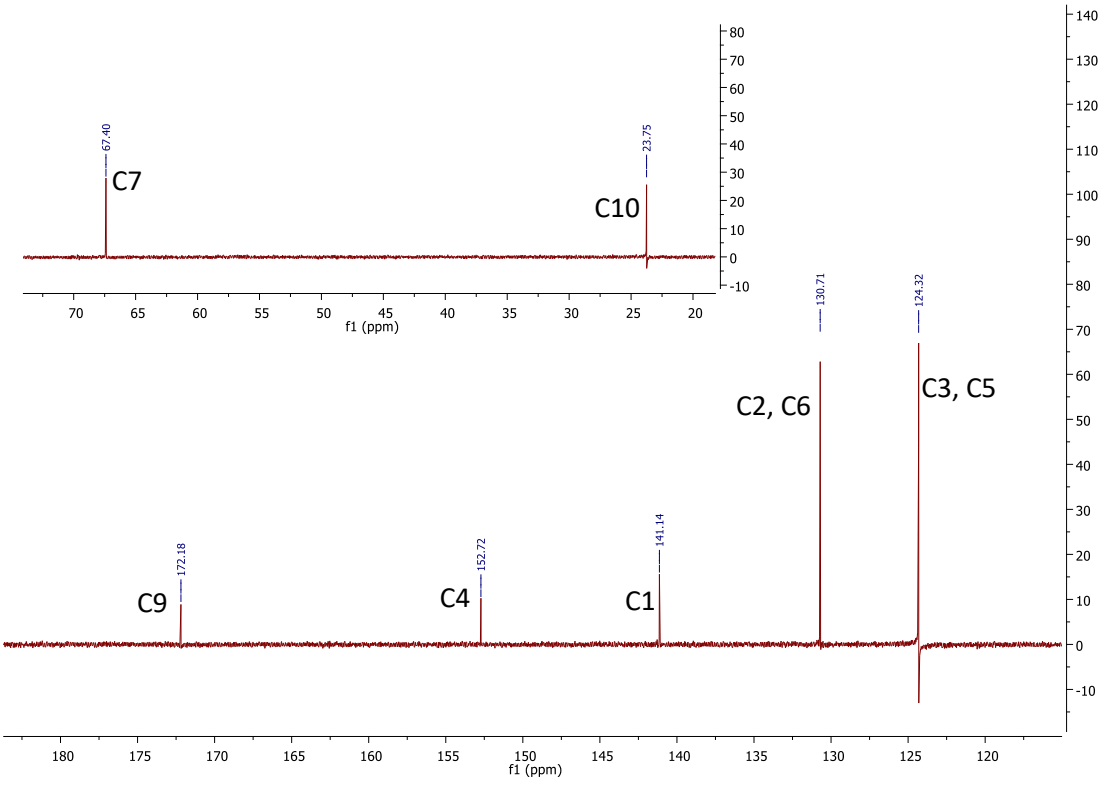

(b)

Figure 4.25 (a): ^{1}H NMR for 7-hydroxy-*p*-tolyl acetate. (b): ^{13}C NMR for 7-hydroxy-*p*-tolyl acetate. Further data given in Figure B.24. $CDCl_3$ signal is marked as (#).

trans-1-Decalone binds to CYP101B1, with lower affinity than the other substrate with K_d = 180 ± 8 µM (Table 4.3). The substrate was oxidised with NADH oxidation rate of 224 ± 2 min^{-1} and product formation rate of 36.8 ± 3 min^{-1} (Table 4.3), the coupling efficiency was 16%. *trans*-1-Decalone was oxidised by CYP101B1 in a whole-cell oxidation system to generate three metabolites which were also generated during the *in vitro* oxidation (Figure 4.26). The peak at t_R = 9.46 min (Figure 4.26 (b)) was observed as split peak of two different metabolites in the whole-cell turnover whereas it was observed as a single peak in the *in vitro* turnover (Figure 4.26 (b)). Both of these metabolites had a mass of (m/z = 168 AMU, Δm/z = +16 AMU), which suggests that they are monohydroxylated products. The products were extracted with ethyl acetate from the whole-cell turnover system and separated using flash chromatography. The metabolites were separated in two different fractions (Figure 4.26 (c)). The first fraction consisted of the metabolite at t_R = 9.06 min as the major component whereas, the second fraction consisted of the metabolite at t_R = 9.46 min as the major component. The major product of the first fraction was identified as 6-hydroxy-trans-1-decalone by comparing its ^{13}C NMR spectrum (Figure 4.27) and mass spectral data to the literature (Table 4.5) [107]. Whereas, the minor product at t_R = 9.46 min was characterised as 7-hydroxy-*trans*-1-decalone using NMR analysis (Table 4.5). The ^1H signal for H6 was assigned by observing its coupling to H5 in gCOSY NMR. The signal for H7 is observed to couple to H6 and H8 by gCOSY NMR. By analysing HMBC NMR, a clear correlation between C7 and H8, H9 is seen. This confirms the generated product as 7-hydroxy-*trans*-1-decalone.

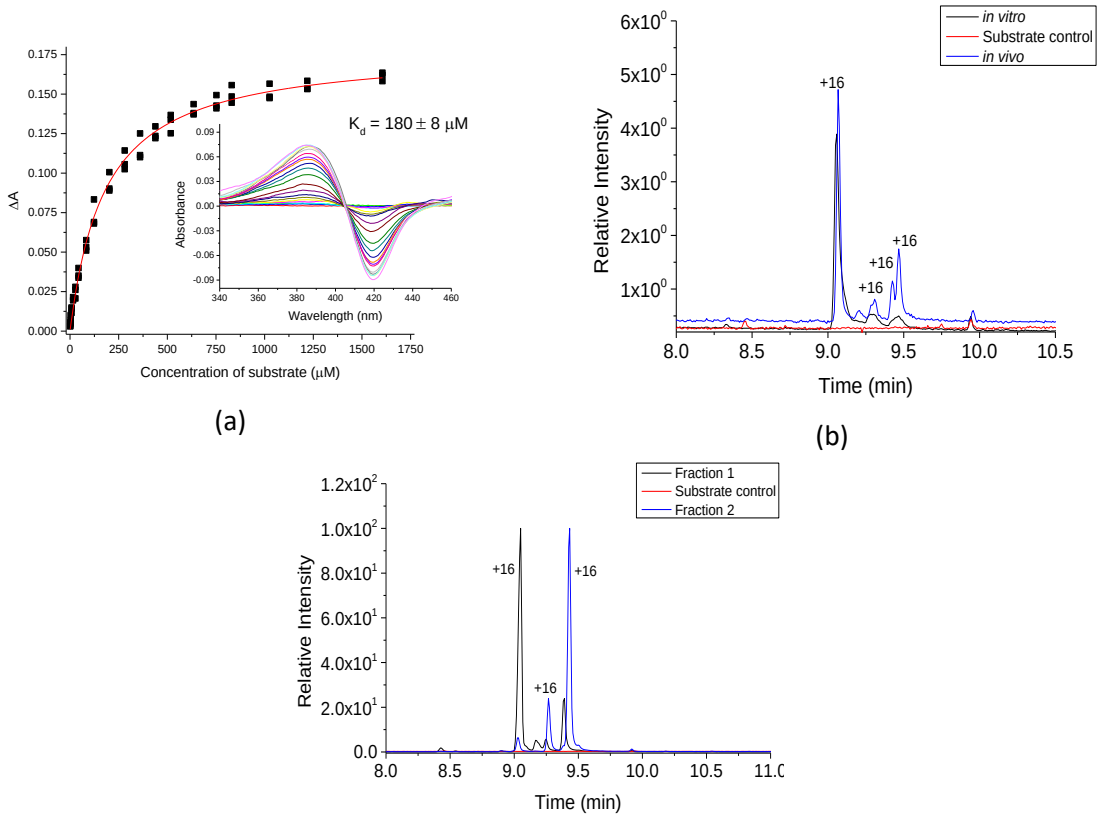

Figure 4.26 (a): Dissociation constant analyses of *trans*-1-decalone with CYP101B1. (b) GCMS analysis of the *in vitro* turnover (zoomed in) of *trans*-1-decalone by CYP101B1 (black) in comparison with whole-cell turnover (blue) and substrate control (red). (c) GCMS analysis of fraction 1 (black) and fraction 2 (blue) along with substrate control (red). The impurities are marked as (*). Further data given in Appendix-B, Figure B.6.

Table 4.5: ^{13}C NMR data of 6-hydroxy-*trans*-1-decalone by comparison to the literature data and experimental data for 7-hydroxy-*trans*-1-decalone metabolite [107]. The assignment of both the metabolites has been further confirmed by a DEPT NMR analysis (Figure B.25 (f), Figure B.26 (g)).

Major product fraction-1 6-hydroxy-*trans*-1-decalone (t_R = 9.06 min)			Major product fraction -2 7-hydroxy-*trans*-1-decalone (t_R = 9.46 min)	
assignment	experimental data (in ppm)	literature data (in ppm)	assignment	experimental data (in ppm)
C1	211.80	211.61	C1	211.06
C6	75.06	74.91	C7	70.49
C10	53.25	53.11	C10	52.87
C5	51.61	51.49	C5	43.81
C2	41.54	41.39	C2	41.35
C7	35.16	35.03	C4	34.86
C9	28.21	28.07	C6	34.58
C4	26.02	25.88	C9/C8[a]	32.26
C8	24.58	24.43	C9/C8[a]	32.17
C3	22.70	22.56	C3	26.31

[a] Due to the presence of both the C8 and C9 signal in a very close vicinity, they could not be identified individually.

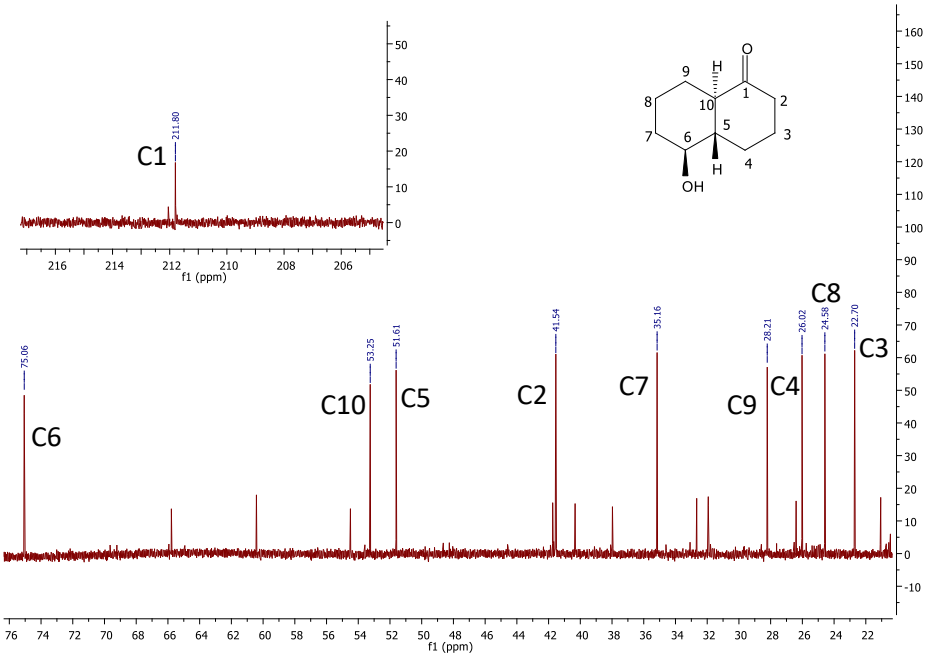

Figure 4.27 (a): ^{13}C NMR for 6-hydroxy-*trans*-1-decalone in $CDCl_3$ along with impurities. Further data given in Appendix-B, Figure B.25.

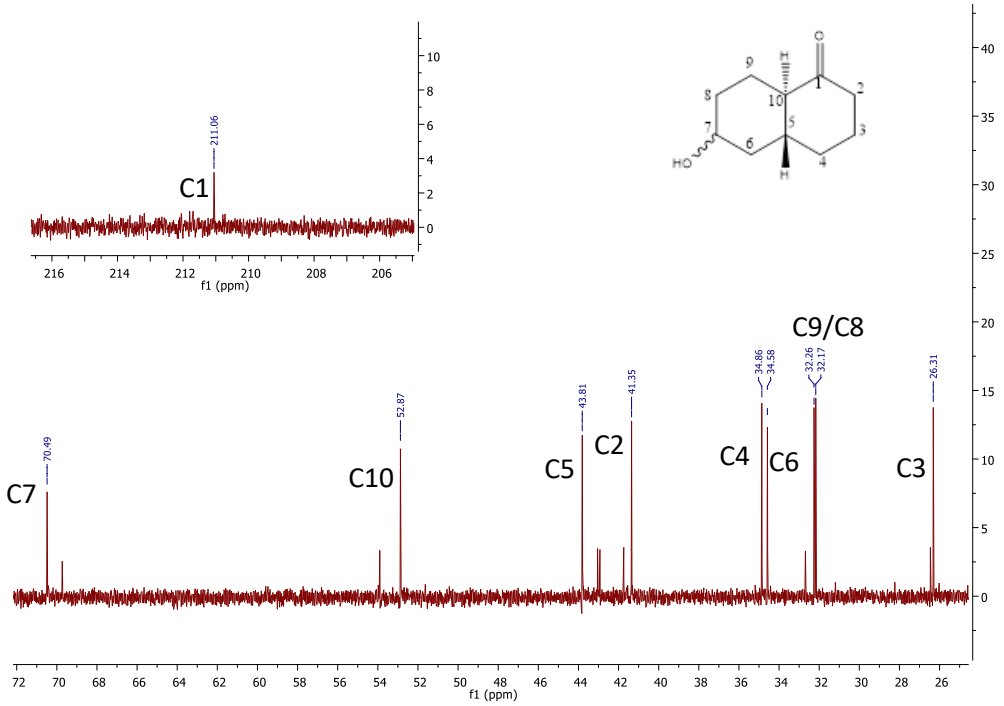

Figure 4.27 (b): ^{13}C NMR for 7-hydroxy-*trans*-1-decalone in $CDCl_3$ along with impurities. Further data given in Appendix-B, Figure B.26.

Cyclopentadecanone binds tightly to CYP101B1 with k_d = 0.27 ± 0.05 µM (Figure 4.28 (a)) compared to oxacyclotridecan-2-one and *trans*-1-Decalone (Table 4.3). It exhibits a NADH oxidation rate of 126 ± 4 min^{-1} and product formation rate of 47 ± 3 min^{-1} (Table 4.3). The coupling efficiency was 38%, which was lower than oxacyclotridecan-2-one but higher compared to *trans*-1-decalone, muscone and dihydroactinidiolide (Table 4.3). The whole-cell oxidation of cyclopentadecanone with CYP101B1 generated a single major product as observed at t_R = 15.08 min (m/z = 240 AMU, Δm/z = +16 AMU) (Figure 4.28 (b)), which was separated using flash chromatography and identified as 8-hydroxy-cyclopentadecanone by comparing the NMR data and mass spectra data to literature [106, 108]. A second metabolite was observed only in ^{13}C NMR (Table 4.6, Figure 4.29). This metabolite has similar signals as 8-hydroxy metabolite in HSQC and HMBC NMRs [106, 108]. This impurity could be the reason for the broad signal of the product in GCMS.

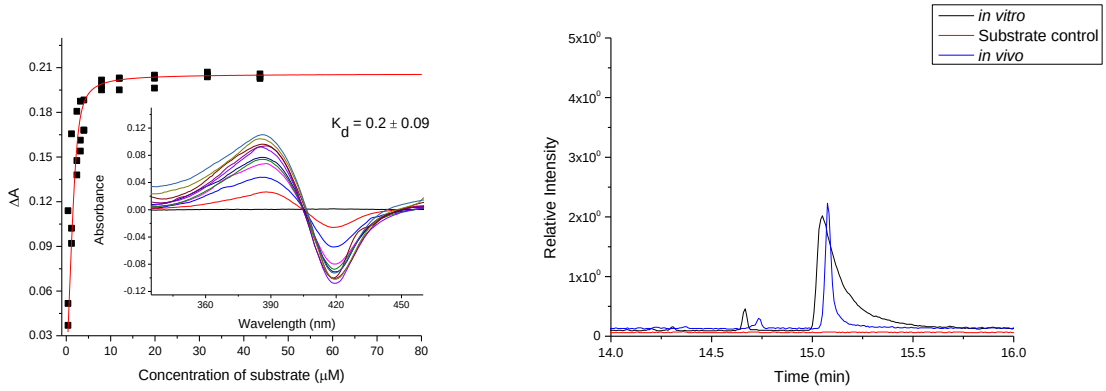

(a) (b)

Figure 4.28: (a) Dissociation constant analysis of cyclopentadecanone with CYP101B1. (b) (b) GCMS analysis of the *in vitro* turnover (zoomed in) of cyclopentadecanone by CYP101B1 (black) in comparison with whole-cell turnover (blue) and substrate control (red).

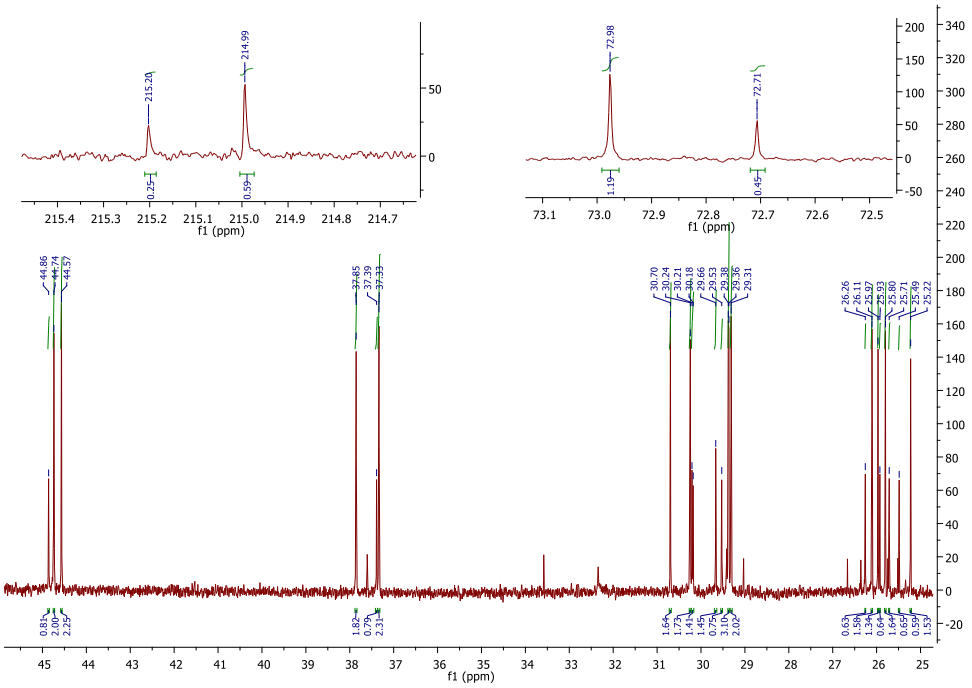

Figure 4.29: ^{13}C NMR of a mixture of 8-hydroxy-cyclopentadecanone diastereomers and impurity. The details of assignment of the carbon peak are mentioned in Table 4.6.

Table 4.6: Comparison of cyclopentadecanone metabolite using ^{13}C NMR signals with reference data [106, 108]. NMR given in Figure B.21. Intensity is mentioned to approximate the relative amount of the compounds present.

Experimental data (in ppm)	Intensity	Reference data (in ppm)	Conformational isomer
214.99	53.6		C1
215.20	22.6	215.30 (C1)	
72.98	129.1		C8
72.71	56.8	72.70 (C8)	
44.86	67.8	44.86 (C2)	
44.74	154.7		C2
44.57	172.4	44.56 (C15)	C15
37.85	150.0		C7
37.39	67.9	37.35 (C7)	
37.33	166.4	37.30 (C9)	C9
30.70	163.2		C5
30.24	152.0		C13
30.21	72.2	30.18 (C5)	
30.18	66.0	30.16 (C13)	
29.66*	85.5	29.64 (C4), 29.63(C11)	
29.53	69.2	29.51 (C12)	
29.38	163.2		C11
29.36	159.9		C4
29.31	165.7		C12
26.26	71.6	26.26 (C3)	
26.11	157.3		C3
25.97	147.0		C6
25.93	69.7	25.90 (C6)	
25.80	157.3		C14
25.71	69.2	25.70 (C14)	
25.49	66.9	25.45 (C10)	
25.22	145.9		C10

* Signal present as a doublet.

4.3 Discussion

CYP101B1 and CYP101C1 can oxidise a variety of substrates, though optimal catalytic activity seems to be achieved for norisoprenoids [14, 76]. CYP101B1 has also been reported to efficiently oxidise certain monoterpenoid acetates. Many of these share common characteristics with norisoprenoids, having a carbonyl group on a side chain attached to a cyclohexyl or bicyclic ring system [91]. Along with this, substrates like cyclic ketones and substrates with an ester directing group have been shown previously to enhance the oxidation activity of CYP101B1 [91].

Amongst the tested substrates, CYP101B1 showed a significant type-I spin-shift with five substrates. CYP101B1 also generated significant amount of oxidation metabolites for these substrates. Whereas, in case of CYP101C1, none of the substrates showed a spin state shift higher than 10% HS. This indicates that the substrates were better suited to fit in the active site pocket of the CYP101B1 but not CYP101C1. The GCMS analysis of the oxidation metabolites from CYP101C1 turnover suggests that in some cases even with a low spin state shift, the substrate was oxidised. The CYP101C1 enzyme was more selective than CYP101B1, in case of dihydroactinidiolide, whereas less selective for *trans*-1-decalone and 2-decalone and oxacyclotridecan-2-one.

The whole-cell oxidation of dihydroactinidiolide generated a single major product with CYP101B1 (> 90%, t_R = 12.21 min) alongside two other metabolites, which was confirmed as the 6-hydroxy-dihydroactinidiolide. This suggests that the active site of CYP101B1 interacts with the keto group of the substrate, orienting the C6 closest to the heme centre. This aligns with the previously reported data that CYP101B1 oxidises the substrate at the position opposite to the keto group.

The GC analysis of oxacyclotridecan-2-one with CYP101B1 seemingly only generated a single major product at t_R = 12.10 min in the whole-cell turnover. However, the NMR analysis shows the presence of two different species. This was characterised to be hydroxylated opposite to the keto group, but the exact location of the hydroxylated position could not be determined from the NMR analysis. Whereas, in the *in vitro* turnover two metabolites were generated in majority. This suggests that the metabolite at t_R = 13.1 min might be hydrolysed to generate the 6-hydroxy metabolite over time.

p-Tolyl acetate was oxidised by CYP101B1 in whole-cell turnover to generate the same products as in the *in vitro* turnover. Interestingly the substrate was also degraded during the whole-cell turnover to generate *p*-cresol, which was confirmed by coelution experiment. This could arise from the hydrolysis of the ester group in *p*-tolyl acetate or the hydrolysis of 7-hydroxy-*p*-tolyl acetate (Figure 4.29).

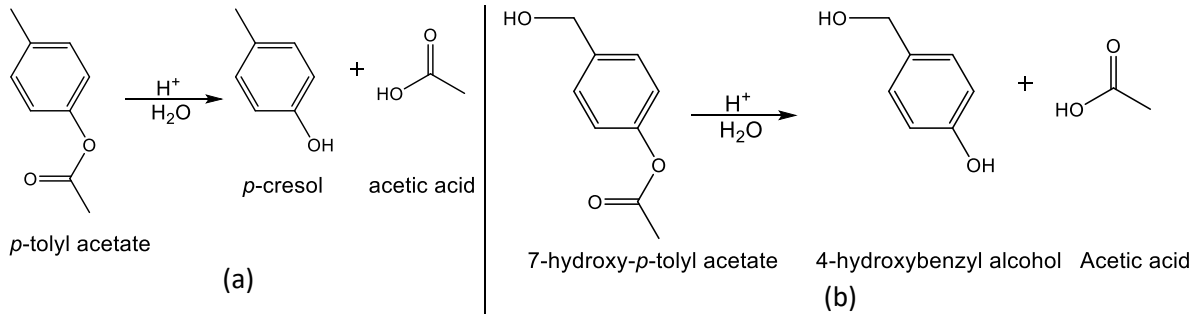

Figure 4.29: Hydrolysis of *p*-tolyl acetate and 7-hydroxy-*p*-tolyl acetate.

The whole-cell oxidation of *trans*-1-decalone generated three oxidation metabolites which could not be separated from each other using silica chromatography. The absence of a chromophore made separation by HPLC difficult. The metabolite at t_R = 9.06 min was assigned as 6-hydroxy-*trans*-1-decalone by comparing the higher intensity peaks of ^{13}C NMR signals to the literature data [107]. The other oxidation product at t_R = 9.46 min was characterised as 7-hydroxy-*trans*-1-decalone by NMR analysis. We have reported previously (Chapter 3) that in case of damascones, the carbonyl group interacts with the active site orienting the C3 and C4 position closest to the heme for oxidation. Hence, the 6-hydroxy metabolite can be compared to the 4-hydroxy oxidation metabolites of damascones and the 7-hydroxy metabolite by *trans*-1-decalone oxidation resembles the 3-hydroxy metabolite of damascones.

Cyclopentadecanone has been reported previously to generate the 8-hydroxy metabolite as the single major product in whole-cell oxidation by CYP101B1 [106, 108]. This was confirmed by comparing the ^{13}C NMR signal to the literature data [108]. However, this 8-hydroxy metabolite was present as a mixture of conformational isomers along with a small amount of cyclopentadecane-1,8-dione. The carbon signal of the two conformers were separated from each other by their relative intensities. The tight binding observed with this substrate suggests that the active site pocket of CYP101B1 is a good fit for large cyclic ketones.

In summary, the screening of various different substrates (Figure 4.5) with CYP101B1 and CYP101C1, demonstrated that, in most instances the CYP101B1 enzyme is better suited for their selective oxidation and capable of generating metabolites in a good yield and often with high selectivity. None of the substrates tested closely resemble the physiological substrate of CYP101C1. However, the tight binding and a high spin state shift in case of cyclopentadecanone and muscone suggest that these substrates might resemble or are closely related to the physiological substrate of CYP101B1.

Chapter-5

Conclusions and Future directions

CYP101B1 and CYP101C1 are valuable additions to the field of monooxygenase biocatalysis. These enzymes are stable, produced in good yield and their electron transfer partners are known. They have been shown to efficiently oxidise norisoprenoids. This work was started to analyse the oxidation of norisoprenoid substrates and to study the role played by the functional group (ketone versus alcohol) on the butenyl side chain and the role of alkene moiety inside the cyclohexyl ring. We have also analysed, whether the M82L mutation in the active site of CYP101C1 enzyme alters the activity and selectivity for norisoprenoid substrates.

In chapter-3, we observed that the spin-state shift induced by norisoprenoids is always higher for CYP101B1 in comparison to CYP101C1 but the activity (NADH oxidation rate and product formation rate) of damascone substrates (α–, β–, δ–) were higher with WT-CYP101C1 but that of ionones were higher with CYP101B1. This suggests that altering the ketone group on the butenyl side chain increases the activity for CYP101C1. In terms of selectivity for hydroxylation, the M82L-CYP101C1 mutant was similar to the WT-CYP101C1 enzyme and did not cause any significant alteration to the expected site of hydroxylation. In agreement to the crystallographic data, this work shows that the C3 and C4 carbons are held closest to the heme centre and hence they are the preferred site of hydroxylation for norisoprenoid substrates. Observing the oxidation of β-ionol we found that both all three enzymes prefer the C3 position instead of C4 for hydroxylation. This shows that changing the keto group of the substrate can alter the selectivity of the enzyme. We also observed that the alkene moiety present inside the cyclohexyl ring plays a crucial role in deciding the site for hydroxylation. With α–substituted ionone and damascone we observed that the position of the keto group on the butenone side chain affects the hydroxylation. The hydroxylation of δ-damascone shows that a 2-hydroxy metabolite can be generated from allylic hydroxylation.

The spin-state shifts used to access the substrate binding with the M82L-CYP101C1 mutant were consistently lower than 20% HS (except for α-ionone). The total turnover number was also lower compared to the WT-CYP101C1 and WT-CYP101B1 enzymes. This shows that simply changing the methionine residue does not significantly increase the affinity of CYP101C1 towards norisoprenoid substrates. Mutagenesis experiments could be undertaken with CYP101C1 by altering other active site residues or by changing the methionine to an amino acid other than leucine, such as histidine to increase its activity towards norisoprenoid substrates. Further optimisation of the whole-cell oxidation system to generate the minor metabolites in a higher yield could provide more insight into the regio and stereo selectivity of the enzymes. The NMR characterisation of the β-ionol products could give a better insight of the selectivity by CYP101B1 and CYP101C1.

In Chapter-4, a range of diverse substrates containing a carbonyl or an ester or amide directing group were tested with CYP101B1 and CYP101C1 to explore their substrate range. However, most of the substrates induced a spin-state shift lower than 40% HS with CYP101B1 and none of the substrate showed a spin-state of more than 10% HS with CYP101C1. Analysing this data along with the *in vitro* turnover data, the best enzyme / substrate combinations were chosen for whole-cell turnover system to generate their oxidation metabolites in a higher quantity for characterisation. Substrates such as oxacyclotridecan-2-one, *p*-tolyl acetate, decalones, dihydroactinidiolide and the cyclic ketones, muscone and cyclopentadecanone, induce a better spin state-shift and have a higher product formation activity than the others. The high spin state shift and tight binding of muscone and cyclopentadecanone with CYP101B1 suggest that they could be a good fit to the active site pocket of CYP101B1 enzyme. The substrates used with the whole-cell oxidation system aligns with those previously reported for CYP101B1 enzyme. This enzyme preferred to hydroxylate these substrates at the carbon opposite to the keto or ester functional group. In future works, these substrates should be used for whole-cell or *in vitro* oxidation by CYP101C1 to provide an insight on the difference in selectivity.

Absence of a chromophore in substrates like oxacyclotridecan-2-one, cyclopentadecanone and muscone, makes the separation of oxidation metabolites by HPLC for these substrates more challenging. In future, these substrates can be functionalized with a chromophore for a more reliable separation of the metabolites to help in their characterisation.

In case of *trans*-1-decalone and 2-decalone, desaturation and hydroxylated metabolites (Figure 5.1) standards could be bought for use as standards for coelution experiments and to compare their mass spectra. This could give a better insight in the catalytic activity of CYP101B1 and CYP101C1 towards the decalone substrates.

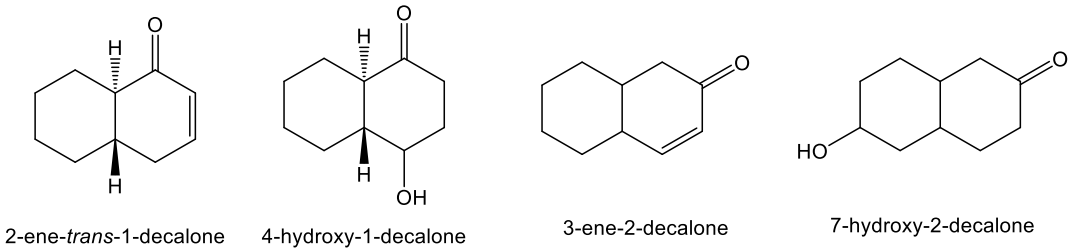

Figure 5.1: Structure of *trans*-1-decalone and 2-decalone metabolites available for purchase online.

With *p*-tolyl acetate, the oxidation metabolites were unstable with ester hydrolysis being observed. However, the major product was identified as 7-hydroxy-*p*-tolyl acetate by NMR analysis. 4-Hydroxybenzyl alcohol was also detected by comparing the mass spectra to the available NIST data (MS number: 231451). This product was presumably generated from the hydrolysis of the major product. *p*-Cresol was also generated during the whole-cell oxidation, which was confirmed by coelution experiment. This could be generated from hydrolysis of the *p*-tolyl acetate substrate.

Overall, the substrates with a keto group or an ester group are well suited for oxidation by CYP101B1 but the substrate range for CYP101C1 is less clear. In future, keeping in mind the substrates which are good fit with CYP101C1, a different range of molecules which mimic norisoprenoids should be screened with both CYP101B1 and CYP101C1. Also, in case of Undecanoic-d-lactone, further investigation is required to analyse, if other changes in the molecules have occurred during the turnover. For example, hydrolysis of the ester group. Further work is also required to understand the conformation of these large ring substrates in the active site of these P450 enzymes.

References

1. Garfinkel, D., *Studies on pig liver microsomes. I. Enzymic and pigment composition of different microsomal fractions.* Archives of biochemistry and biophysics, 1958. **77**(2): p. 493-509.
2. Klingenberg, M., *Pigments of rat liver microsomes.* Archives of biochemistry and biophysics, 1958. **75**(2): p. 376-386.
3. Omura, T. and R. Sato, *The carbon monoxide-binding pigment of liver microsomes I. Evidence for its hemoprotein nature.* Journal of Biological Chemistry, 1964. **239**(7): p. 2370-2378.
4. Poulos, T.L., *Heme enzyme structure and function.* Chemical reviews, 2014. **114**(7): p. 3919-3962.
5. Guengerich, F.P., *Common and uncommon cytochrome P450 reactions related to metabolism and chemical toxicity.* Chemical research in toxicology, 2001. **14**(6): p. 611-650.
6. Omura, T., *Forty years of cytochrome P450.* Biochemical and biophysical research communications, 1999. **266**(3): p. 690-698.
7. Kim, J.H. and A.R. Scialli, *Thalidomide: the tragedy of birth defects and the effective treatment of disease.* Toxicological Sciences, 2011. **122**(1): p. 1-6.
8. Poulos, T.L., B.C. Finzel, and A.J. Howard, *High-resolution crystal structure of cytochrome P450cam.* Journal of molecular biology, 1987. **195**(3): p. 687-700.
9. Meunier, B., S.P. de Visser, and S. Shaik, *Mechanism of oxidation reactions catalyzed by cytochrome P450 enzymes.* Chemical reviews, 2004. **104**(9): p. 3947-3980.
10. Guengerich, F.P. and A.W. Munro, *Unusual cytochrome P450 enzymes and reactions.* Journal of Biological Chemistry, 2013: p. jbc. R113. 462275.
11. Nelson, D.R., *Cytochrome P450 nomenclature*, in *Cytochrome P450 Protocols*. 1998, Springer. p. 15-24.
12. Nelson, D.R., *Progress in tracing the evolutionary paths of cytochrome P450.* Biochimica et Biophysica Acta (BBA)-Proteins and Proteomics, 2011. **1814**(1): p. 14-18.
13. Nelson, D.R., L. Koymans, T. Kamataki, J.J. Stegeman, R. Feyereisen, D.J. Waxman, M.R. Waterman, O. Gotoh, M.J. Coon, and R.W. Estabrook, *P450 superfamily: update on new sequences, gene mapping, accession numbers and nomenclature.* Pharmacogenetics, 1996. **6**(1): p. 1-42.
14. Bell, S.G. and L.-L. Wong, *P450 enzymes from the bacterium Novosphingobium aromaticivorans.* Biochemical and biophysical research communications, 2007. **360**(3): p. 666-672.
15. Groves, J., *Models and mechanisms of cytochrome P450 action. In cytochrome P450: structure, mechanism and biochemistry. 3rd edn, Ortiz de Montellano, PR, Ed*. 2005, Kluwer Academic/Plenum Publishers, New York.
16. Dus, K., M. Katagiri, C. Yu, D. Erbes, and I. Gunsalus, *Chemical characterization of cytochrome P-450cam.* Biochemical and biophysical research communications, 1970. **40**(6): p. 1423-1430.
17. Unger, B., I. Gunsalus, and S. Sligar, *Nucleotide sequence of the Pseudomonas putida cytochrome P-450cam gene and its expression in Escherichia coli.* Journal of Biological Chemistry, 1986. **261**(3): p. 1158-1163.
18. Poulos, T.L. and R. Raag, *Cytochrome P450cam: crystallography, oxygen activation, and electron transfer.* the FASEB journal, 1992. **6**(2): p. 674-679.
19. Bell, S.G., A. Dale, N.H. Rees, and L.-L. Wong, *A cytochrome P450 class I electron transfer system from Novosphingobium aromaticivorans.* Applied microbiology and biotechnology, 2010. **86**(1): p. 163-175.
20. Cryle, M.J., P.Y. Hayes, and J.J. De Voss, *Enzyme–Substrate Complementarity Governs Access to a Cationic Reaction Manifold in the P450BM3-Catalysed Oxidation of Cyclopropyl Fatty Acids.* Chemistry–A European Journal, 2012. **18**(50): p. 15994-15999.

21. Bell, S.G., R. Zhou, W. Yang, A.B. Tan, A.S. Gentleman, L.L. Wong, and W. Zhou, *Investigation of the substrate range of CYP199A4: Modification of the partition between hydroxylation and desaturation activities by substrate and protein engineering.* Chemistry–A European Journal, 2012. **18**(52): p. 16677-16688.
22. Chao, R.R., J.J. De Voss, and S.G. Bell, *The efficient and selective catalytic oxidation of para-substituted cinnamic acid derivatives by the cytochrome P450 monooxygenase, CYP199A4.* RSC advances, 2016. **6**(60): p. 55286-55297.
23. Groves, J.T. and G.A. McClusky, *Aliphatic hydroxylation via oxygen rebound. Oxygen transfer catalyzed by iron.* Journal of the American Chemical Society, 1976. **98**(3): p. 859-861.
24. Yosca, T.H., J. Rittle, C.M. Krest, E.L. Onderko, A. Silakov, J.C. Calixto, R.K. Behan, and M.T. Green, *Iron (IV) hydroxide pKa and the role of thiolate ligation in C–H bond activation by cytochrome P450.* Science, 2013. **342**(6160): p. 825-829.
25. Hannemann, F., A. Bichet, K.M. Ewen, and R. Bernhardt, *Cytochrome P450 systems—biological variations of electron transport chains.* Biochimica et Biophysica Acta (BBA)-General Subjects, 2007. **1770**(3): p. 330-344.
26. Paine, M.J., N.S. Scrutton, A.W. Munro, A. Gutierrez, G.C. Roberts, and C.R. Wolf, *Electron transfer partners of cytochrome P450*, in *Cytochrome P450*. 2005, Springer. p. 115-148.
27. Guengerich, F., *Structure, mechanism and biochemistry.* Cytochrome P450, 1995: p. 473-535.
28. Ullah, A., R. Murray, P. Bhattacharyya, G. Wagner, and I.C. Gunsalus, *Protein components of a cytochrome P-450 linalool 8-methyl hydroxylase.* Journal of Biological Chemistry, 1990. **265**(3): p. 1345-1351.
29. Schiffler, B. and R. Bernhardt, *Bacterial (CYP101) and mitochondrial P450 systems—how comparable are they?* Biochemical and biophysical research communications, 2003. **312**(1): p. 223-228.
30. König, W.A., P. Evers, R. Krebber, S. Schulz, C. Fehr, and G. Ohloff, *Determination of the absolute configuration of α-damascone and α-ionone from black tea by enantioselective capillary gas chromatography.* Tetrahedron, 1989. **45**(22): p. 7003-7006.
31. Zotchev, S.B. and C.R. Hutchinson, *Cloning and heterologous expression of the genes encoding nonspecific electron transport components for a cytochrome P450 system of Saccharopolyspora erythraea involved in erythromycin production.* Gene, 1995. **156**(1): p. 101-106.
32. Hawkes, D.B., G.W. Adams, A.L. Burlingame, P.R.O. de Montellano, and J.J. De Voss, *Cytochrome P450cin (CYP176A), isolation, expression, and characterization.* Journal of Biological Chemistry, 2002. **277**(31): p. 27725-27732.
33. Chun, Y.-J., T. Shimada, R. Sanchez-Ponce, M.V. Martin, L. Lei, B. Zhao, S.L. Kelly, M.R. Waterman, D.C. Lamb, and F.P. Guengerich, *Electron Transport Pathway for a Streptomyces Cytochrome P450 CYTOCHROME P450 105D5-CATALYZED FATTY ACID HYDROXYLATION IN STREPTOMYCES COELICOLOR A3 (2).* Journal of Biological Chemistry, 2007. **282**(24): p. 17486-17500.
34. Parajuli, N., D.B. Basnet, H.C. Lee, J.K. Sohng, and K. Liou, *Genome analyses of Streptomyces peucetius ATCC 27952 for the identification and comparison of cytochrome P450 complement with other Streptomyces.* Archives of biochemistry and biophysics, 2004. **425**(2): p. 233-241.
35. van Beilen, J.B., E.G. Funhoff, A. van Loon, A. Just, L. Kaysser, M. Bouza, R. Holtackers, M. Röthlisberger, Z. Li, and B. Witholt, *Cytochrome P450 alkane hydroxylases of the CYP153 family are common in alkane-degrading eubacteria lacking integral membrane alkane hydroxylases.* Appl. Environ. Microbiol., 2006. **72**(1): p. 59-65.
36. Agematu, H., N. Matsumoto, Y. Fujii, H. Kabumoto, S. Doi, K. Machida, J. Ishikawa, and A. Arisawa, *Hydroxylation of testosterone by bacterial cytochromes P450 using the Escherichia coli expression system.* Bioscience, biotechnology, and biochemistry, 2006. **70**(1): p. 307-311.

37. Momoi, K., U. Hofmann, R.D. Schmid, and V.B. Urlacher, *Reconstitution of β-carotene hydroxylase activity of thermostable CYP175A1 monooxygenase.* Biochemical and biophysical research communications, 2006. **339**(1): p. 331-336.
38. Yang, W., G. Stephen, H. Wang, W. Zhou, N. Hoskins, A. Dale, M. Bartlam, L.L. Wong, and Z. Rao, *Molecular characterization of a class I P450 electron transfer system from Novosphingobium aromaticivorans DSM12444.* Journal of Biological Chemistry, 2010: p. jbc. M110. 118349.
39. Tyson, C.A., J.D. Lipscomb, and I. Gunsalus, *The roles of putidaredoxin and P450cam in methylene hydroxylation.* Journal of Biological Chemistry, 1972. **247**(18): p. 5777-5784.
40. Kuznetsov, V.Y., T.L. Poulos, and I.F. Sevrioukova, *Putidaredoxin-to-cytochrome P450cam electron transfer: differences between the two reductive steps required for catalysis.* Biochemistry, 2006. **45**(39): p. 11934-11944.
41. Raag, R., S.A. Martinis, S.G. Sligar, and T.L. Poulos, *Crystal structure of the cytochrome P-450CAM active site mutant Thr252Ala.* Biochemistry, 1991. **30**(48): p. 11420-11429.
42. Davydov, R., R. Perera, S. Jin, T.-C. Yang, T.A. Bryson, M. Sono, J.H. Dawson, and B.M. Hoffman, *Substrate modulation of the properties and reactivity of the oxy-ferrous and hydroperoxo-ferric intermediates of cytochrome P450cam as shown by cryoreduction-EPR/ENDOR spectroscopy.* Journal of the American Chemical Society, 2005. **127**(5): p. 1403-1413.
43. Ortiz de Montellano, P.R., *Hydrocarbon hydroxylation by cytochrome P450 enzymes.* Chemical reviews, 2010. **110**(2): p. 932-948.
44. Jin, S., T.M. Makris, T.A. Bryson, S.G. Sligar, and J.H. Dawson, *Epoxidation of olefins by hydroperoxo− ferric cytochrome P450.* Journal of the American Chemical Society, 2003. **125**(12): p. 3406-3407.
45. Cryle, M.J. and J.J. De Voss, *Is the ferric hydroperoxy species responsible for sulfur oxidation in cytochrome P450s?* Angewandte Chemie International Edition, 2006. **45**(48): p. 8221-8223.
46. Kerber, W.D., B. Ramdhanie, and D.P. Goldberg, *H2O2 Oxidations Catalyzed by an Iron (III) Corrolazine: Avoiding High-Valent Iron–Oxido Species?* Angewandte Chemie International Edition, 2007. **46**(20): p. 3718-3721.
47. Duester, G., *Involvement of alcohol dehydrogenase, short-chain dehydrogenase/reductase, aldehyde dehydrogenase, and cytochrome P450 in the control of retinoid signaling by activation of retinoic acid synthesis.* Biochemistry, 1996. **35**(38): p. 12221-12227.
48. Groves, J.T., G.A. McClusky, R.E. White, and M.J. Coon, *Aliphatic hydroxylation by highly purified liver microsomal cytochrome P-450. Evidence for a carbon radical intermediate.* 1978.
49. Sarkar, M.R., S.D. Houston, G.P. Savage, C.M. Williams, E.H. Krenske, S.G. Bell, and J.J. De Voss, *Rearrangement-Free Hydroxylation of Methylcubanes by a Cytochrome P450: The Case for Dynamical Coupling of C–H Abstraction and Rebound.* Journal of the American Chemical Society, 2019. **141**(50): p. 19688-19699.
50. Atkinson, J.K. and K. Ingold, *Cytochrome P450 hydroxylation of hydrocarbons: variation in the rate of oxygen rebound using cyclopropyl radical clocks including two new ultrafast probes.* Biochemistry, 1993. **32**(35): p. 9209-9214.
51. Atkinson, J.K., P.F. Hollenberg, K. Ingold, C.C. Johnson, M.-H. Le Tadic, M. Newcomb, and D.A. Putt, *Cytochrome P450-catalyzed hydroxylation of hydrocarbons: kinetic deuterium isotope effects for the hydroxylation of an ultrafast radical clock.* Biochemistry, 1994. **33**(35): p. 10630-10637.
52. Newcomb, M., R.E.P. Chandrasena, D.S. Lansakara-P, H.-Y. Kim, S.J. Lippard, L.G. Beauvais, L.J. Murray, V. Izzo, P.F. Hollenberg, and M.J. Coon, *Desaturase reactions complicate the use of norcarane as a mechanistic probe. Unraveling the mixture of twenty-plus products formed in enzyme-catalyzed oxidations of norcarane.* The Journal of organic chemistry, 2007. **72**(4): p. 1121-1127.

53. Newcomb, M., M.-H. Le Tadic, D.A. Putt, and P.F. Hollenberg, *An incredibly fast apparent oxygen rebound rate constant for hydrocarbon hydroxylation by cytochrome P-450 enzymes.* Journal of the American Chemical Society, 1995. **117**(11): p. 3312-3313.
54. Newcomb, M., R. Shen, S.-Y. Choi, P.H. Toy, P.F. Hollenberg, A.D. Vaz, and M.J. Coon, *Cytochrome P450-catalyzed hydroxylation of mechanistic probes that distinguish between radicals and cations. Evidence for cationic but not for radical intermediates.* Journal of the American Chemical Society, 2000. **122**(12): p. 2677-2686.
55. Newcomb, M., R. Shen, Y. Lu, M.J. Coon, P.F. Hollenberg, D.A. Kopp, and S.J. Lippard, *Evaluation of norcarane as a probe for radicals in cytochome P450-and soluble methane monooxygenase-catalyzed hydroxylation reactions.* Journal of the American Chemical Society, 2002. **124**(24): p. 6879-6886.
56. Hiroya, K., Y. Murakami, T. Shimizu, M. Hatano, and P.O. Demontellano, *Differential roles of Glu318 and Thr319 in cytochrome P450 1A2 catalysis supported by NADPH-cytochrome P450 reductase and tert-butyl hydroperoxide.* Archives of biochemistry and biophysics, 1994. **310**(2): p. 397-401.
57. Shaik, S., S.P. de Visser, and D. Kumar, *External electric field will control the selectivity of enzymatic-like bond activations.* Journal of the American Chemical Society, 2004. **126**(37): p. 11746-11749.
58. Shaik, S., S. Cohen, Y. Wang, H. Chen, D. Kumar, and W. Thiel, *P450 Enzymes: Their Structure, Reactivity, and Selectivity・ Modeled by QM/MM Calculations.* Chemical reviews, 2010. **110**(2): p. 949-1017.
59. Kumar, D., S.P. de Visser, and S. Shaik, *Oxygen Economy of Cytochrome P450: What Is the Origin of the Mixed Functionality as a Dehydrogenase− Oxidase Enzyme Compared with Its Normal Function?* Journal of the American Chemical Society, 2004. **126**(16): p. 5072-5073.
60. Kumar, D., S.P. de Visser, and S. Shaik, *How Does Product Isotope Effect Prove the Operation of a Two-State "Rebound" Mechanism in C− H Hydroxylation by Cytochrome P450?* Journal of the American Chemical Society, 2003. **125**(43): p. 13024-13025.
61. Kumar, D., S.P. de Visser, P.K. Sharma, S. Cohen, and S. Shaik, *Radical Clock Substrates, Their C− H Hydroxylation Mechanism by Cytochrome P450, and Other Reactivity Patterns: What Does Theory Reveal about the Clocks' Behavior?* Journal of the American Chemical Society, 2004. **126**(6): p. 1907-1920.
62. Newcomb, M. and P.H. Toy, *Hypersensitive radical probes and the mechanisms of cytochrome P450-catalyzed hydroxylation reactions.* Accounts of Chemical Research, 2000. **33**(7): p. 449-455.
63. Vaz, A.D., D.F. McGinnity, and M.J. Coon, *Epoxidation of olefins by cytochrome P450: evidence from site-specific mutagenesis for hydroperoxo-iron as an electrophilic oxidant.* Proceedings of the National Academy of Sciences, 1998. **95**(7): p. 3555-3560.
64. Ogliaro, F., S.P. de Visser, S. Cohen, P.K. Sharma, and S. Shaik, *Searching for the second oxidant in the catalytic cycle of cytochrome P450: a theoretical investigation of the iron (III)-hydroperoxo species and its epoxidation pathways.* Journal of the American Chemical Society, 2002. **124**(11): p. 2806-2817.
65. de Visser, S.P., F. Ogliaro, P.K. Sharma, and S. Shaik, *What factors affect the regioselectivity of oxidation by cytochrome P450? A DFT study of allylic hydroxylation and double bond epoxidation in a model reaction.* Journal of the American Chemical Society, 2002. **124**(39): p. 11809-11826.
66. de Visser, S.P., F. Ogliaro, P.K. Sharma, and S. Shaik, *Hydrogen bonding modulates the selectivity of enzymatic oxidation by P450: Chameleon oxidant behavior by compound I.* Angewandte Chemie International Edition, 2002. **41**(11): p. 1947-1951.
67. Kamachi, T., Y. Shiota, T. Ohta, and K. Yoshizawa, *Does the hydroperoxo species of cytochrome P450 participate in olefin epoxidation with the main oxidant, compound I? Criticism from*

density functional theory calculations. Bulletin of the Chemical Society of Japan, 2003. **76**(4): p. 721-732.
68. de Visser, S.P., F. Ogliaro, and S. Shaik, *How does ethene inactivate cytochrome P450 en route to its epoxidation? A density functional study.* Angewandte Chemie International Edition, 2001. **40**(15): p. 2871-2874.
69. Nebert, D.W., D.R. Nelson, M.J. Coon, R.W. Estabrook, R. Feyereisen, Y. Fujii-Kuriyama, F.J. Gonzalez, F.P. Guengerich, I.C. Gunsalus, and E.F. Johnson, *The P450 superfamily: update on new sequences, gene mapping, and recommended nomenclature.* DNA and cell biology, 1991. **10**(1): p. 1-14.
70. Mueller, E.J., P.J. Loida, and S.G. Sligar, *Twenty-five years of P450 cam research*, in *Cytochrome P450*. 1995, Springer. p. 83-124.
71. Katagiri, M., B. Ganguli, and I. Gunsalus, *A soluble cytochrome P-450 functional in methylene hydroxylation.* Journal of Biological Chemistry, 1968. **243**(12): p. 3543-3546.
72. Poulos, T.L., B. Finzel, I. Gunsalus, G.C. Wagner, and J. Kraut, *The 2.6-A crystal structure of Pseudomonas putida cytochrome P-450.* Journal of Biological Chemistry, 1985. **260**(30): p. 16122-16130.
73. Li, H., S. Narasimhulu, L.M. Havran, J.D. Winkler, and T.L. Poulos, *Crystal structure of cytochrome P450cam complexed with its catalytic product, 5-exo-hydroxycamphor.* Journal of the American Chemical Society, 1995. **117**(23): p. 6297-6299.
74. Bell, S.G., X. Chen, R.J. Sowden, F. Xu, J.N. Williams, L.-L. Wong, and Z. Rao, *Molecular recognition in (+)-α-pinene oxidation by cytochrome P450cam.* Journal of the American Chemical Society, 2003. **125**(3): p. 705-714.
75. Fredrickson, J., F. Brockman, D. Workman, S. Li, and T. Stevens, *Isolation and characterization of a subsurface bacterium capable of growth on toluene, naphthalene, and other aromatic compounds.* Applied and environmental microbiology, 1991. **57**(3): p. 796-803.
76. Hall, E.A. and S.G. Bell, *The efficient and selective biocatalytic oxidation of norisoprenoid and aromatic substrates by CYP101B1 from Novosphingobium aromaticivorans DSM12444.* RSC Advances, 2015. **5**(8): p. 5762-5773.
77. Fredrickson, J., D. Balkwill, G. Drake, M. Romine, D. Ringelberg, and D. White, *Aromatic-degrading Sphingomonas isolates from the deep subsurface.* Applied and environmental microbiology, 1995. **61**(5): p. 1917-1922.
78. Ma, M., S.G. Bell, W. Yang, Y. Hao, N.H. Rees, M. Bartlam, W. Zhou, L.L. Wong, and Z. Rao, *Structural analysis of CYP101C1 from Novosphingobium aromaticivorans DSM12444.* Chembiochem, 2011. **12**(1): p. 88-99.
79. Michaelis, L., *Kinetics of invertase action.* Biochem. Z., 1913. **49**: p. 333.
80. Briggs, G.E. and J.B.S. Haldane, *A note on the kinetics of enzyme action.* Biochemical journal, 1925. **19**(2): p. 338.
81. Williams, J.W. and J.F. Morrison, *[17] The kinetics of reversible tight-binding inhibition*, in *Methods in enzymology*. 1979, Elsevier. p. 437-467.
82. Ohloff, G., *The fashion of odors and their chemical perspectives: scent and fragrances*. 1994, Berlin, Germany: Springer-Verlag.
83. Pybus, D.H., C.S. Sell, D. Pybus, and L. Small, *The brief submission.* The Chemistry of Fragrances, 1999. **17**: p. 255.
84. Fráter, G., J.A. Bajgrowicz, and P. Kraft, *Fragrance chemistry.* Tetrahedron, 1998. **54**(27): p. 7633-7703.
85. Winter, M. and E. Sundt, *Recherches sur les arŏmes. 5e communication. Analyse de l'arŏme des framboises. I. Les constituants carbonylés volatils.* Helvetica Chimica Acta, 1962. **45**(6): p. 2195-2211.
86. Guroff, G., J.W. Daly, D.M. Jerina, J. Renson, B. Witkop, and S. Udenfriend, *Hydroxylation-induced migration: the NIH shift.* Science, 1967. **157**(3796): p. 1524-1530.

87. Uhde, G. and G. Ohloff, *Parmon, eine phantomverbindung im veilchenblütenöl.* Helvetica Chimica Acta, 1972. **55**(7): p. 2621-2625.
88. Sarkar, M.R., J.H. Lee, and S.G. Bell, *The oxidation of hydrophobic aromatic substrates by using a variant of the P450 monooxygenase CYP101B1.* ChemBioChem, 2017. **18**(21): p. 2119-2128.
89. Bell, S.G., N. Hoskins, C.J. Whitehouse, and L.L. Wong, *Design and engineering of cytochrome P450 systems.* Metal Ions Life Sci, 2007. **3**: p. 437-476.
90. Bell, S.G., W. Yang, A. Dale, W. Zhou, and L.-L. Wong, *Improving the affinity and activity of CYP101D2 for hydrophobic substrates.* Applied microbiology and biotechnology, 2013. **97**(9): p. 3979-3990.
91. Hall, E.A., M.R. Sarkar, J.H. Lee, S.D. Munday, and S.G. Bell, *Improving the monooxygenase activity and the regio-and stereoselectivity of terpenoid hydroxylation using ester directing groups.* Acs Catalysis, 2016. **6**(9): p. 6306-6317.
92. Lee, J.H.Z., *Harnessing P450 Enzymes as Biocatalysts for Selective C-H Bond Hydroxylation*, in *Chemistry*. 2018, University of Adelaide.
93. Guth, H., *Quantitation and sensory studies of character impact odorants of different white wine varieties.* Journal of Agricultural and Food Chemistry, 1997. **45**(8): p. 3027-3032.
94. Kotseridis, Y., A.A. Beloqui, A. Bertrand, and J. Doazan, *An analytical method for studying the volatile compounds of Merlot noir clone wines.* American journal of enology and viticulture, 1998. **49**(1): p. 44-48.
95. Zhang, K., S. El Damaty, and R. Fasan, *P450 fingerprinting method for rapid discovery of terpene hydroxylating P450 catalysts with diversified regioselectivity.* Journal of the American Chemical Society, 2011. **133**(10): p. 3242-3245.
96. Specter, M., *A life of its own.* The New Yorker, 2009. **28**.
97. Thomas, A.F. and G. Ohloff, *Alicyclic compounds, their use and process for preparing same*. 1976, Google Patents.
98. Cheng, Q., S. Thomas, and P. Rouviere, *Biological conversion of cyclic alkanes and cyclic alcohols into dicarboxylic acids: biochemical and molecular basis.* Applied microbiology and biotechnology, 2002. **58**(6): p. 704-711.
99. Morgan, P. and R. Watkinson, *Biodegradation of components of petroleum. In. Biochemistry of Microbial Degradation, eds. Ratledge, C*. 1994, Kluwer Academic Publishers, Dordrecht.
100. Kostichka, K., S.M. Thomas, K.J. Gibson, V. Nagarajan, and Q. Cheng, *Cloning and characterization of a gene cluster for cyclododecanone oxidation in Rhodococcus ruber SC1.* Journal of Bacteriology, 2001. **183**(21): p. 6478-6486.
101. Shanka, T., V. Quintal, and R. Taylor, *Factors influencing international students' choice of an education destination–A correspondence analysis.* Journal of Marketing for Higher Education, 2006. **15**(2): p. 31-46.
102. Kamata, K., K. Yonehara, Y. Nakagawa, K. Uehara, and N. Mizuno, *Efficient stereo-and regioselective hydroxylation of alkanes catalysed by a bulky polyoxometalate.* Nature chemistry, 2010. **2**(6): p. 478.
103. Schuchardt, U., W.A. Carvalho, and E.V. Spinacé, *Why is it interesting to study cyclohexane oxidation?* Synlett, 1993. **1993**(10): p. 713-718.
104. Ashton, M.J., A.S. Bailey, and E.R. Jones, *Microbiological hydroxylation. Part XII. Comparative behaviour of D-homogonane (perhydrochrysene) ketones and steroids.* Journal of the Chemical Society, Perkin Transactions 1, 1974: p. 1658-1665.
105. Sarkar, M.R., S. Dasgupta, S.M. Pyke, and S.G. Bell, *Selective biocatalytic hydroxylation of unactivated methylene C–H bonds in cyclic alkyl substrates.* Chemical Communications, 2019. **55**(34): p. 5029-5032.
106. Sarkar, M.R., *Application of the Monooxygenase Enzymes CYP101B1 and CYP101C1 from Novosphingobium aromaticivorans for Selective and Efficient Functionalisation of Inert C-H bonds*, in *Department of Chemistry*. 2019, The University of Adelaide.

107. Wasnaire, P., M. Wiaux, R. Touillaux, and I.E. Markó, *Reductive cyclisation of Morita–Baylis–Hillman adducts. A simple approach towards substituted hydrindanones and decalones.* Tetrahedron letters, 2006. **47**(6): p. 985-989.
108. Ashton, M.J., A.S. Bailey, and E.R. Jones, *Microbiological hydroxylation. Part XIII. Cyclododecanone and cyclopentadecanone as substrates for steroid-hydroxylating fungi.* Journal of the Chemical Society, Perkin Transactions 1, 1974: p. 1665-1669.
109. Hall, E.A., *The efficient and selective catalytic oxidation of terpenoids and aromatic hydrocarbons by the P450 monooxygenase CYP101B1*, in *Department of Chemistry*. 2015, The University of Adelaide.

Appendix-A (Data for Chapter-3)

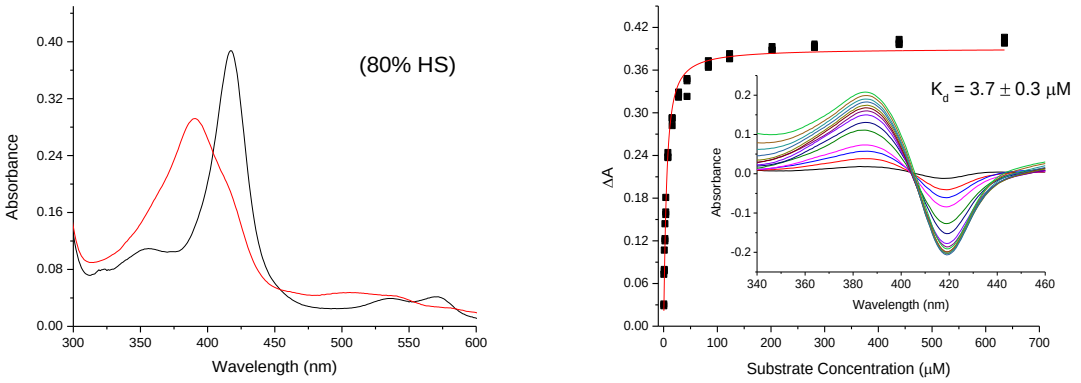

(a)

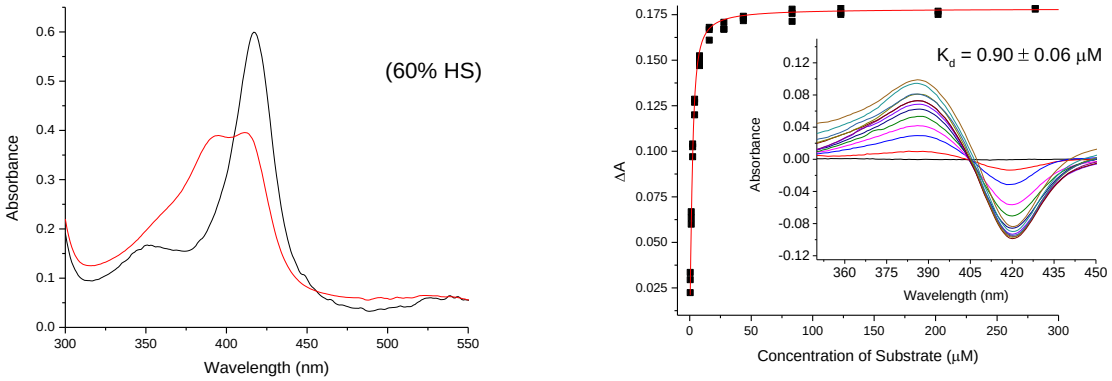

(b)

Figure A.1: Spin state shifts and dissociation constant for a) α-damascone and b) δ-damascone with WT-CYP101B1.

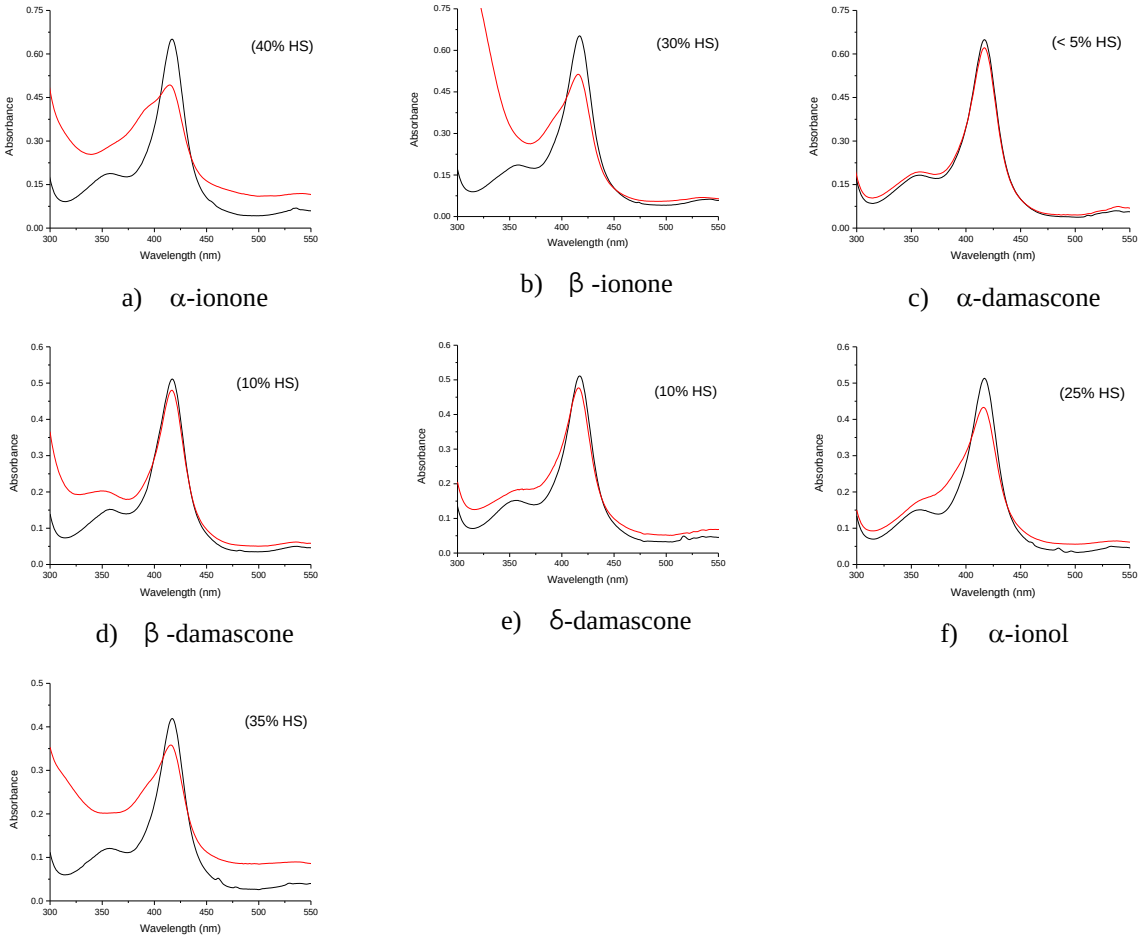

Figure A.2: Spin state shifts of aforementioned substrates with WT-CYP101C1.

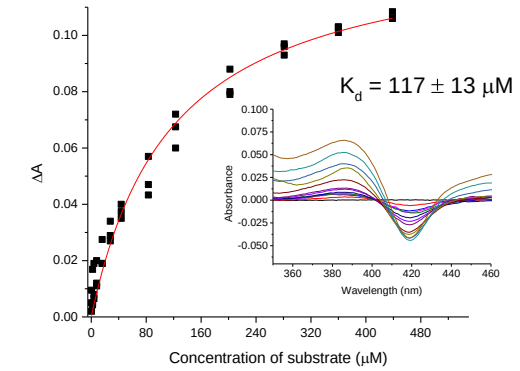

a) α-ionone

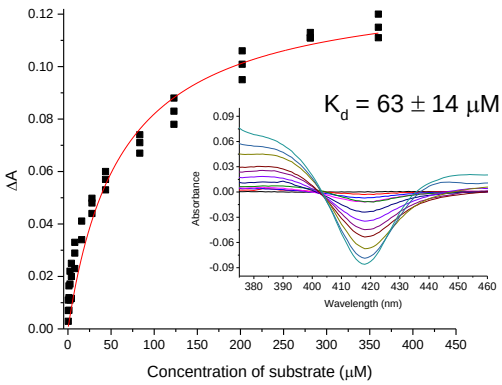

b) β-ionone

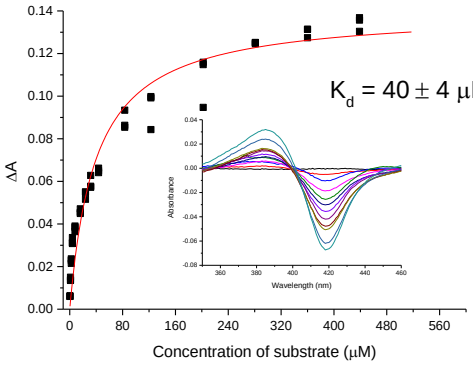

c) α-ionol

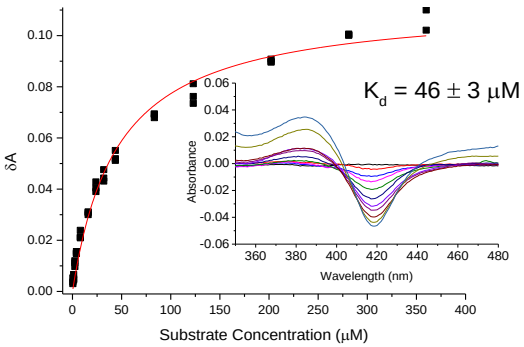

d) β-ionol

Figure A.3: Dissociation constant of aforementioned substrates with WT-CYP101C1.

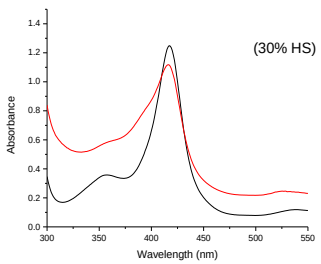

a) α-ionone

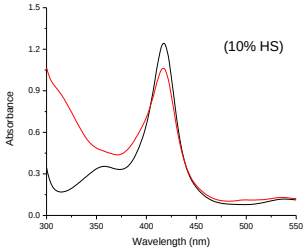

b) β -ionone

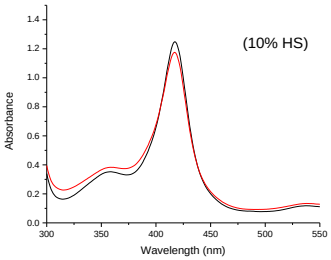

c) α-damascone

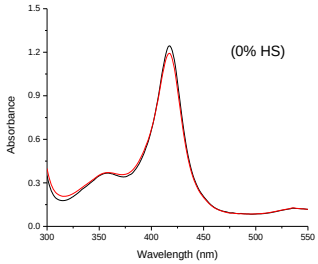

d) β -damascone

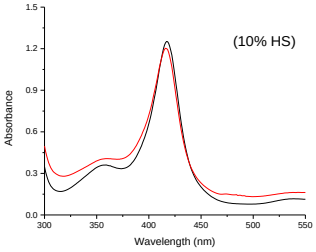

e) δ-damascone

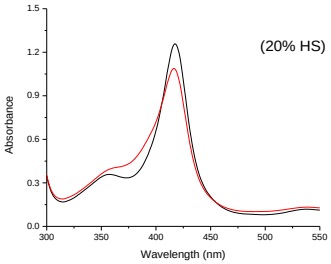

f) α-ionol

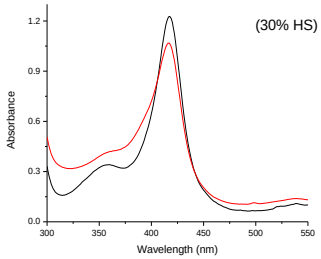

g) β -ionol

Figure A.4: Spin state shifts of aforementioned substrates with M82L-CYP101C1.

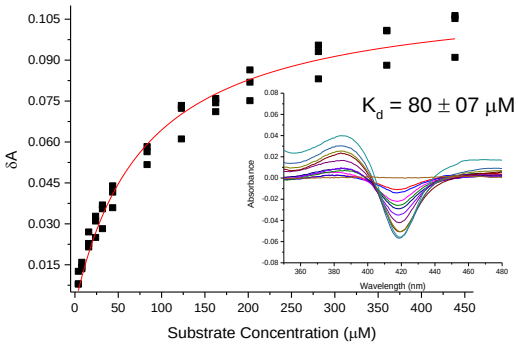

a) α-ionone

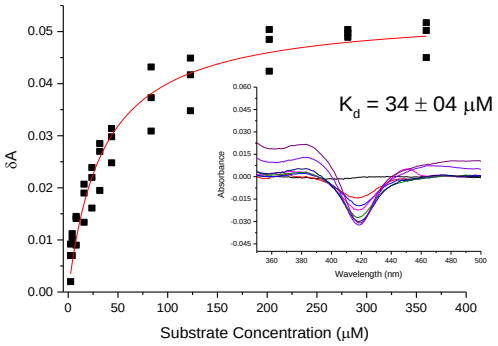

b) β-ionol

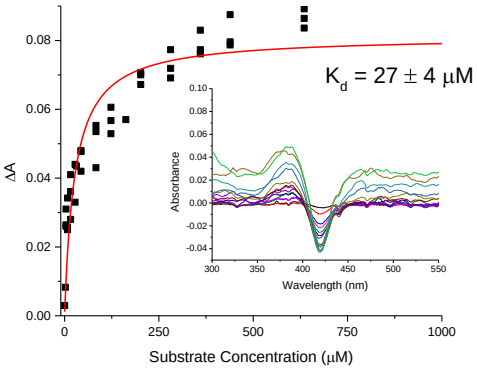

c) α-ionol

Figure A.5: Dissociation constant of aforementioned substrates with M82L-CYP101C1.

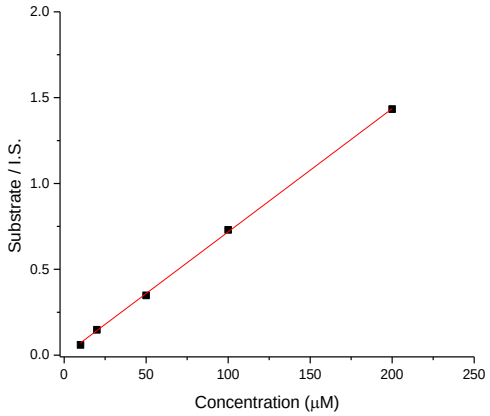

a) α-ionone
R^2 = 0.9998; m = 0.0071

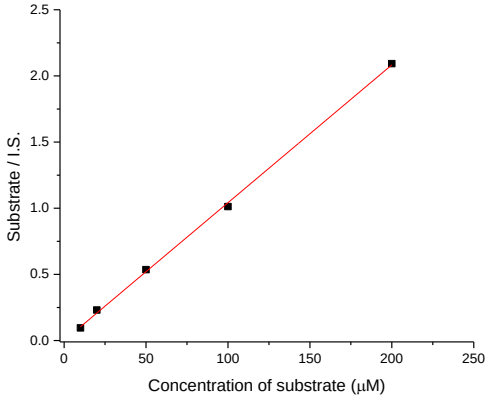

b) β-ionone
R^2 = 0.9996; m = 0.0104

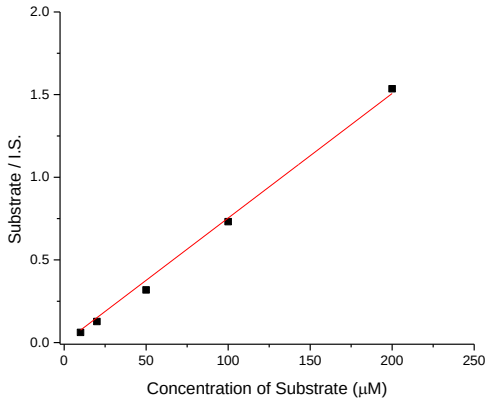

c) α-damascone
R^2 = 0.997; m = 0.00753

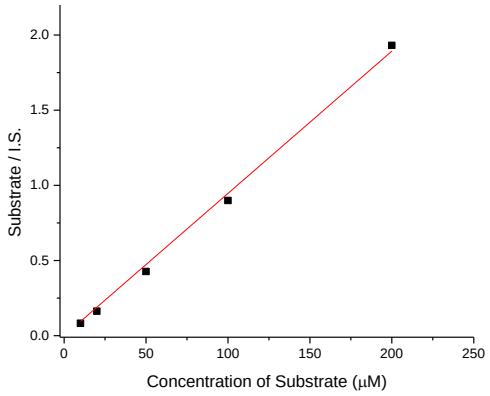

d) β-damascone
R^2 = 0.998; m = 0.0094

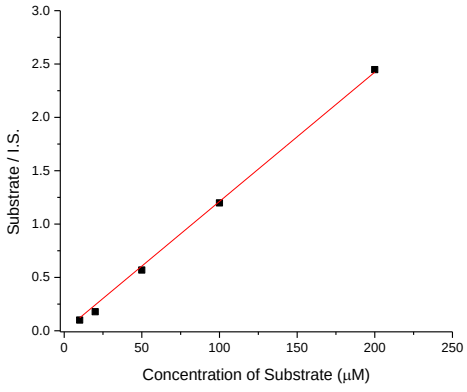

e) δ-damascone
R^2 = 0.998; m = 0.0121

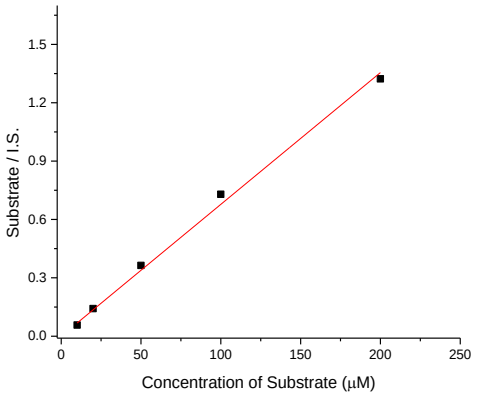

f) α-ionol
R^2 = 0.997; m = 0.0067

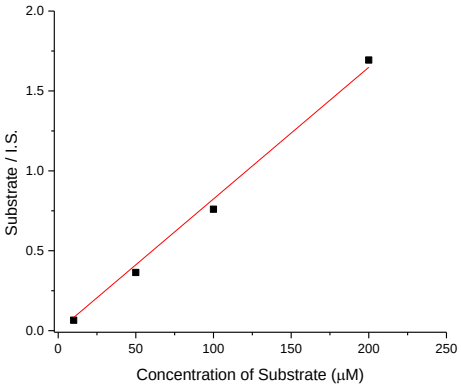

g) β -ionol

R^2 = 0.996; m = 0.0082

Figure A.6: Calibration data of aforementioned substrates. The slope (m) of the calibration curve is used to determine the amount of metabolites generated in turnovers.

Table 3.2: Slopes of calibration curves for norisoprenoid substrates

Substrate	Slope (m)
α-ionone	0.0071
β-ionone	0.0104
α-damascone	0.0075
β-damascone	0.0094
δ-damascone	0.0121
α-ionol	0.0067
β-ionol	0.0082

NMR Analysis

Data for *cis*-3-hydroxy-α-ionone [76]:

^{1}H NMR (500 MHz, $CDCl_3$) δ 6.54 (dd, *J* = 15.8, 10.1 Hz, 1H'; H7), 6.11 (d, *J* = 15.8 Hz, 1H'; H8), 5.64 (s, 1H'; H4), 4.28 (s, 1H'; H3), 2.51 (d, *J* = 10.1 Hz, 1H'; H6), 2.27 (s, 3H'; H10), 1.85 (dd, *J* = 13.5, 5.9 Hz, 1H'; H2a), 1.63 (s, 3H'; H13), 1.42 (dd, J = 13.5, 5.9 Hz, 1H'; H2b), 1.04 (s, 3H'; H11), 0.90 (s, 3H'; H12); Carbon NMR: ^{13}C NMR (126 MHz, $CDCl_3$) δ 200.67 (C9), 149.75 (C7), 138.08 (C5), 136.26 (C8), 128.48 (C4), 68.11 (C3), 56.93 (C6), 46.48 (C2), 36.50 (C1), 31.96 (C11), 29.86 (C10), 27.34 (C12), 25.31 (C13).

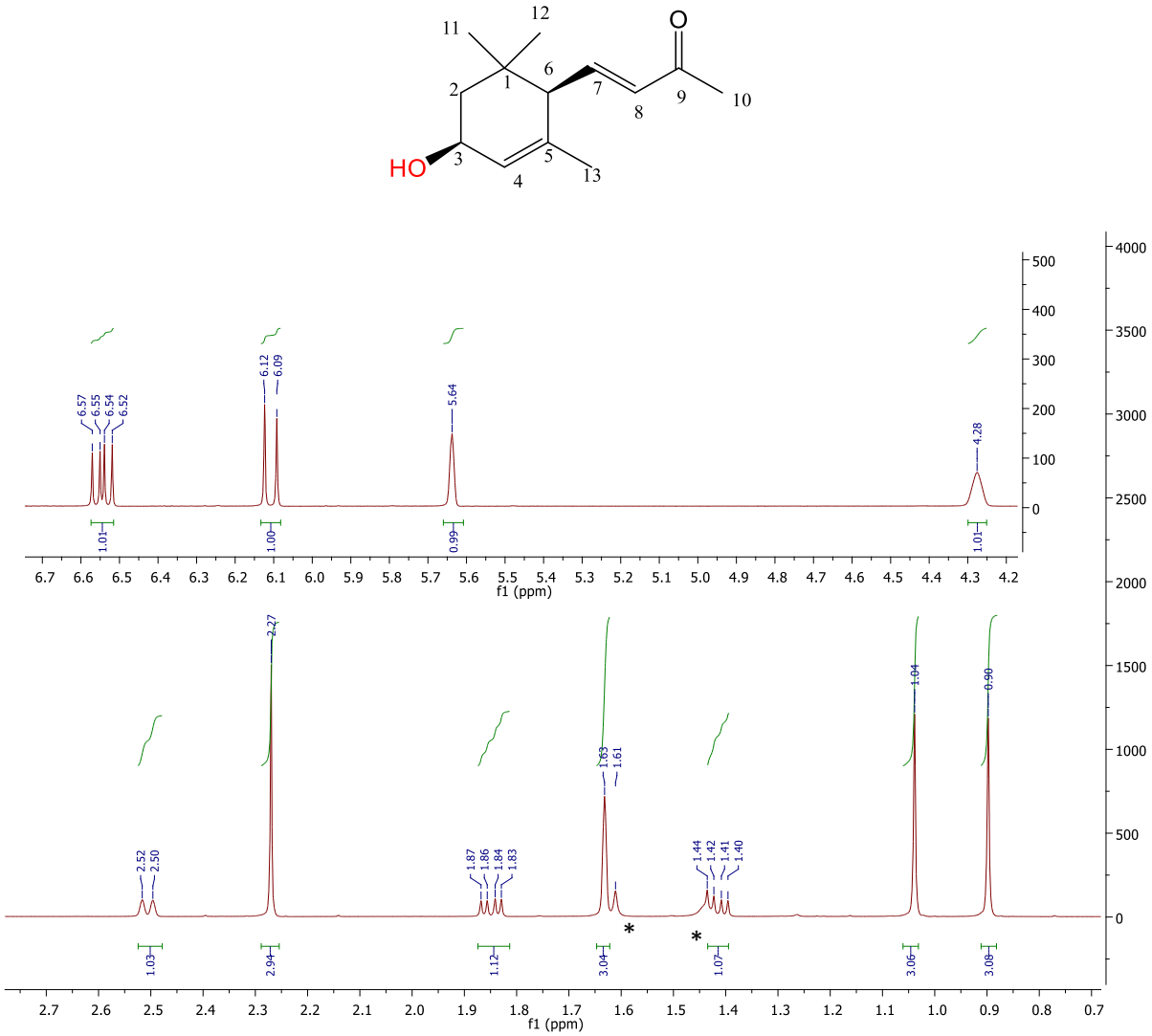

Figure A.7 (a) ^{1}H NMR of *cis*-3-hydroxy-α-ionone in $CDCl_3$. Impurity / OH (*).

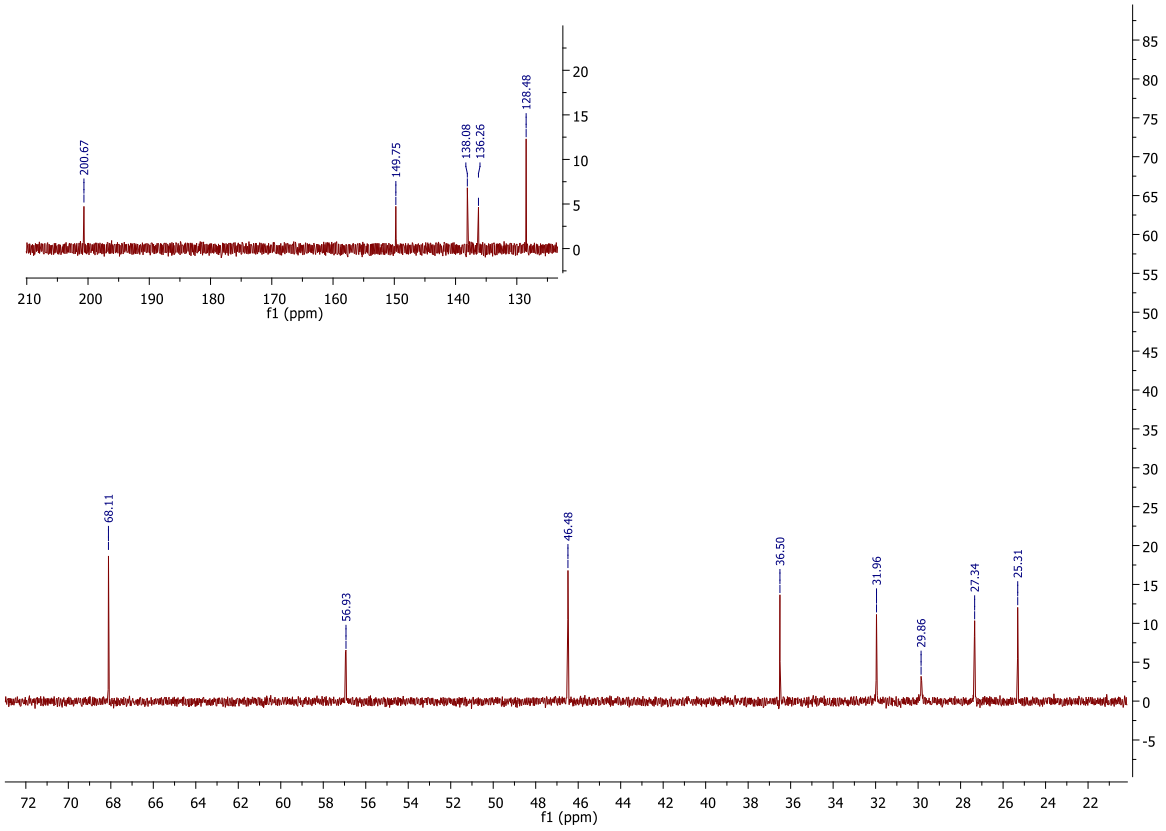

Figure A.7 (b): ^{13}C NMR of *cis*-3-hydroxy-α-ionone in $CDCl_3$.

Data for *trans*-3-hydroxy-α-ionone [76]:

^{1}H NMR: ^{1}H NMR (500 MHz, $CDCl_3$) δ 6.64 (dd, *J* = 15.8, 9.6 Hz, 1H'; H7), 6.09 (d, *J* = 15.8, 9.6 Hz, 1H'; H8), 5.60 (s, 1H'; H4), 4.21 – 4.31 (m, 1H'; H3), 2.27 (m, 4H'; H6, H10), 1.69 – 1.73 (m, 1H'; H2a), 1.64 (s, 3H'; H13), 1.38 - 1.44 (m, H'; H2b), 0.99 (s, 3H'; H11), 0.90 (s, 3H'; H12); ^{13}C NMR (126 MHz, $CDCl_3$) δ 200.94 (C9), 150.29 (C7), 138.12 (C5), 135.39 (C8), 129.02 (C4), 69.11 (C3), 56.98 (C6), 43.40 (C2), 37.60 (C1), 31.73 (C11), 29.73 (C10), 29.63 (C12), 25.06 (H13).

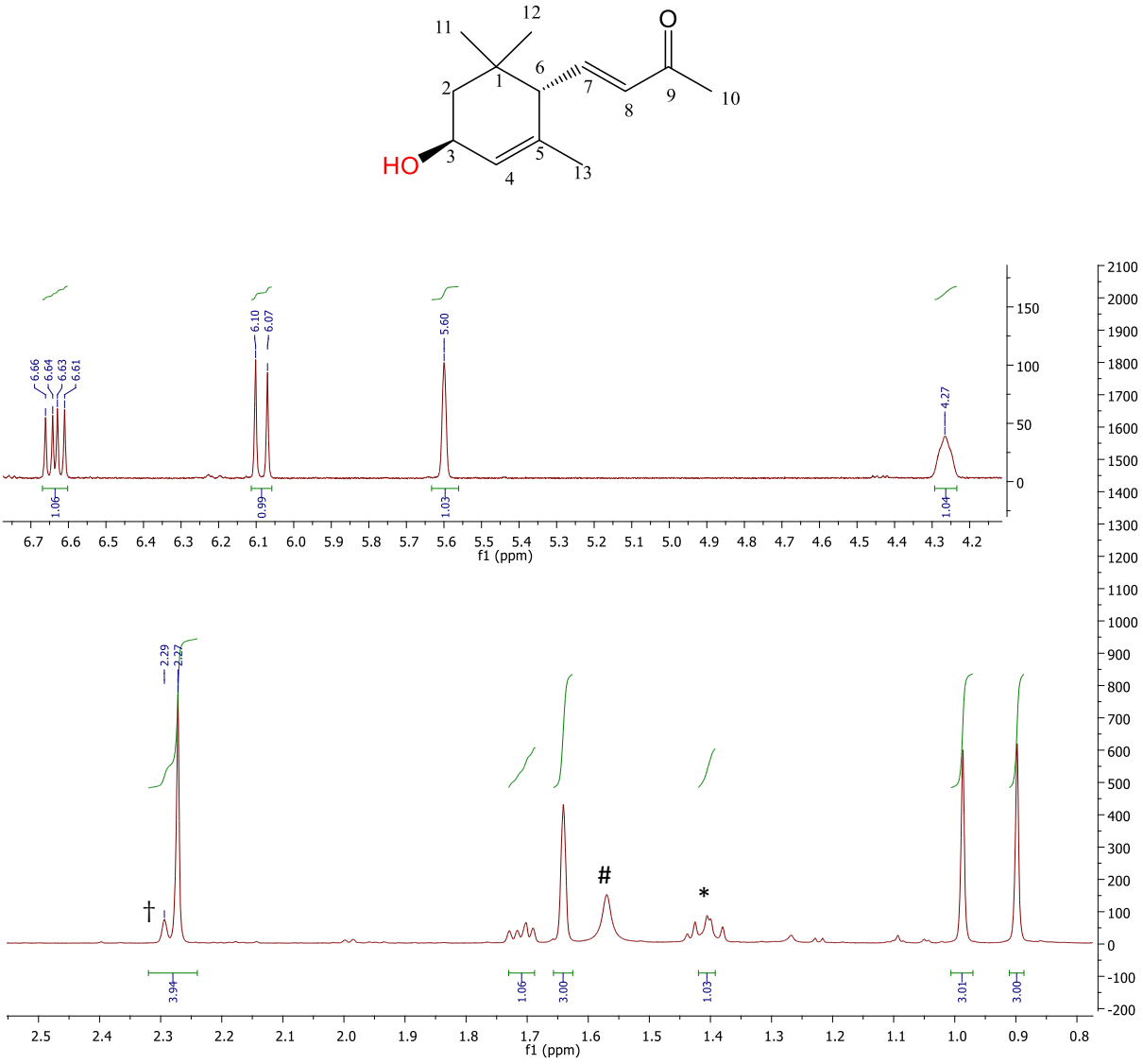

Figure A.8 (a): ^{1}H NMR of *trans*-3-hydroxy-α-ionone in $CDCl_3$. Impurity / OH (*). H_2O (#), The proton signal for H6 is shown as a multiplet, which is partly seen at 2.29 ppm and partly hidden behind the signal for H10 at 2.27ppm (†).

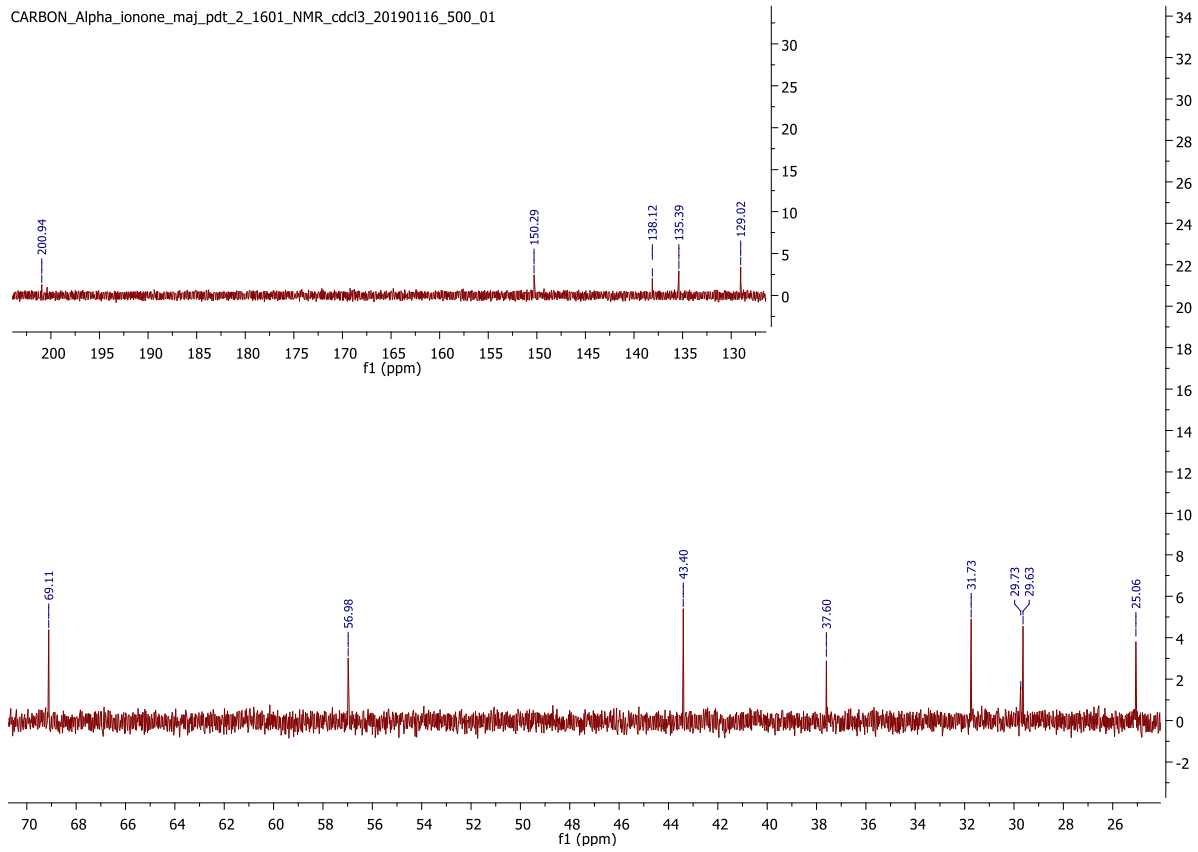

Figure A.8 (b): ^{13}C NMR of *trans*-3-hydroxy-α-ionone in $CDCl_3$.

Data for 4-hydroxy-β-ionone [109]:

^{1}H NMR (500 MHz, $CDCl_3$) δ 7.20 (d, *J* = 16.4 Hz, 1H'; H8), 6.13 (d, *J* = 16.4 Hz, 1H'; H7), 4.02 (s, 1H'; H4), 2.32 (s, 3H'; H10), 1.96 – 1.90 (m, 1H'; H3a), 1.86 (s, 3H'; H13), 1.78 – 1.71 (m, 1H'; H3b), 1.70 – 1.64 (m, 1H'; H2a), 1.45 – 1.49 (m, 1H'; H2b), 1.09 (s, 3H'; H11), 1.06 (s, 3H'; H12); ^{13}C NMR (126 MHz, $CDCl_3$) δ 200.96 (C9), 145.23 (C8), 142.08 (C6), 136.53 (C5), 135.75 (C7), 72.58 (C4), 37.31 (C2), 31.49 (11), 30.97 (C3), 30.14 (C12), 30.02 (C10), 28.00 (C1), 21.12 (C13).

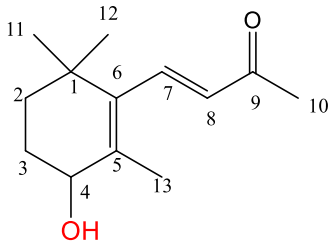

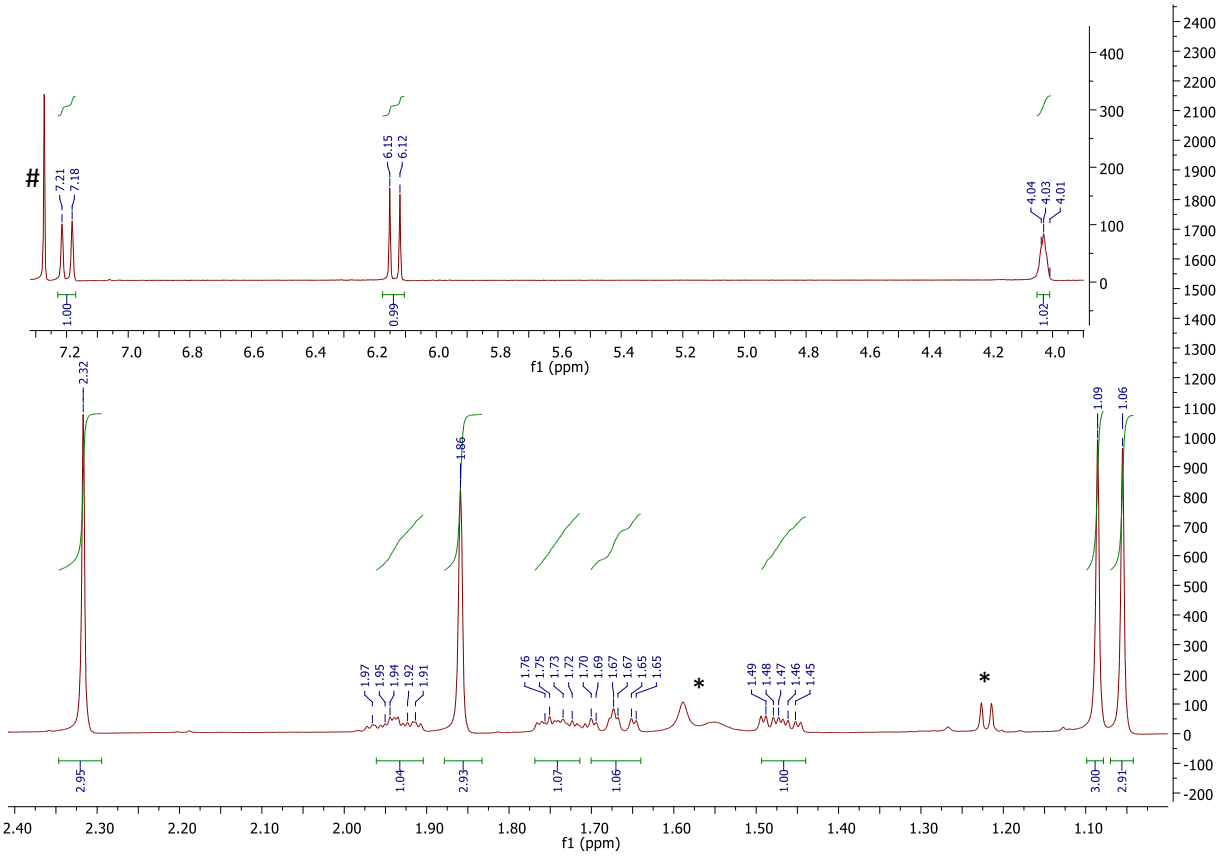

Figure A.9 (a): ^{1}H NMR of 4-hydroxy-β-ionone in $CDCl_3$. Impurity (*), $CDCl_3$ (#)

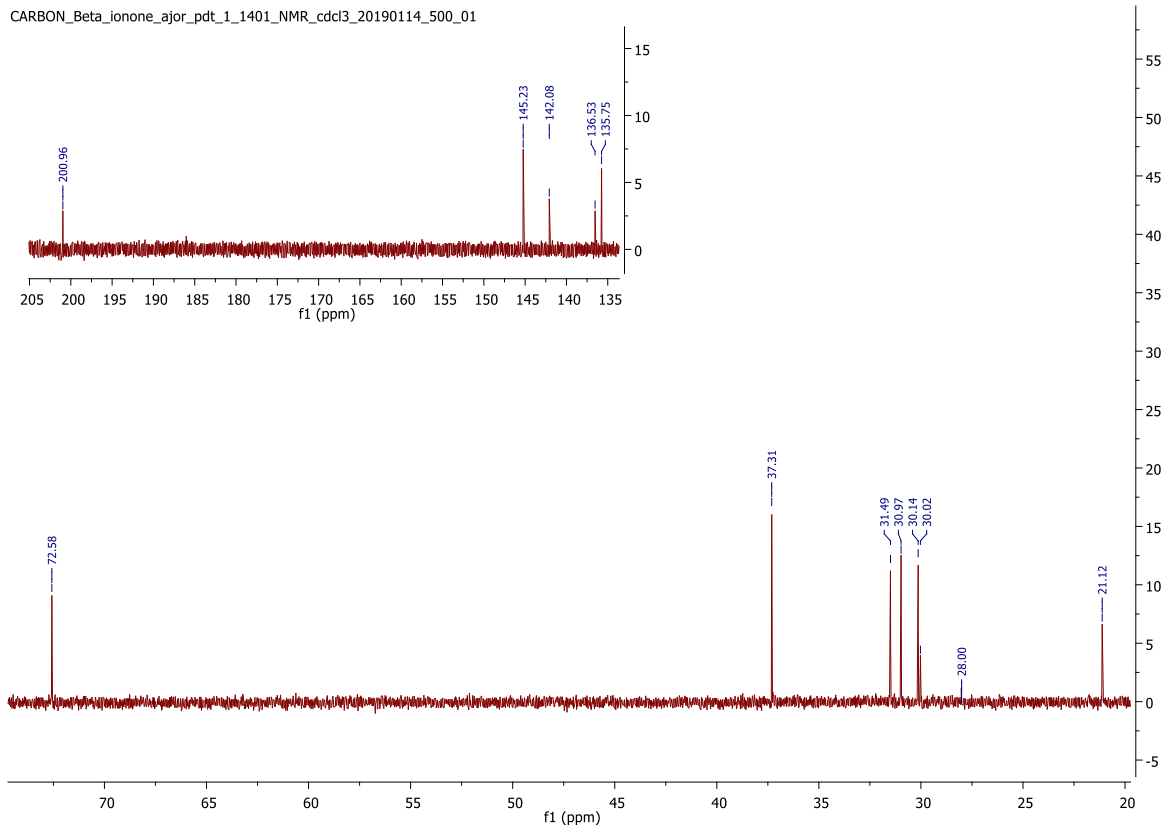

Figure A.9 (b): ^{13}C NMR of 4-hydroxy-β-ionone in $CDCl_3$.

Data for 3-hydroxy-β-ionone [76]:

^{1}H NMR (500 MHz, $CDCl_3$) δ 7.22 (d, *J* = 16.4 Hz, 1H'; H8), 6.12 (d, *J* = 16.4 Hz, 1H'; H7), 4.04 – 3.99 (m, 1H'; H3), 2.45 (dd, *J* = 17.5, 1H'; H4a), 2.31 (s, 3H'; H10), 2.10 (dd, *J* = 17.5 Hz, 1H'; H4b), 1.82 - 1.79 (m, 4H'; H2a, H13), 1.53 – 1.48 (m, 1H'; H2b), 1.13 (s, 3H'; H11), 1.12 (s, 3H'; H12); ^{13}C NMR (126 MHz, $CDCl_3$) δ 201.09 (C9), 144.91 (C8), 138.30 (C6), 135.04 (C5), 134.83 (C7), 67.20 (C3), 51.09 (C2), 45.42 (C4), 39.56 (C1), 32.73 (C11), 31.23 (C12), 29.97 (C10), 24.22 (C13).

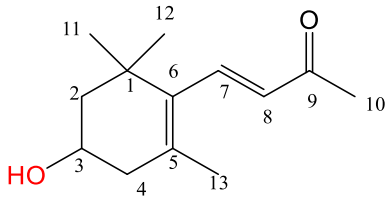

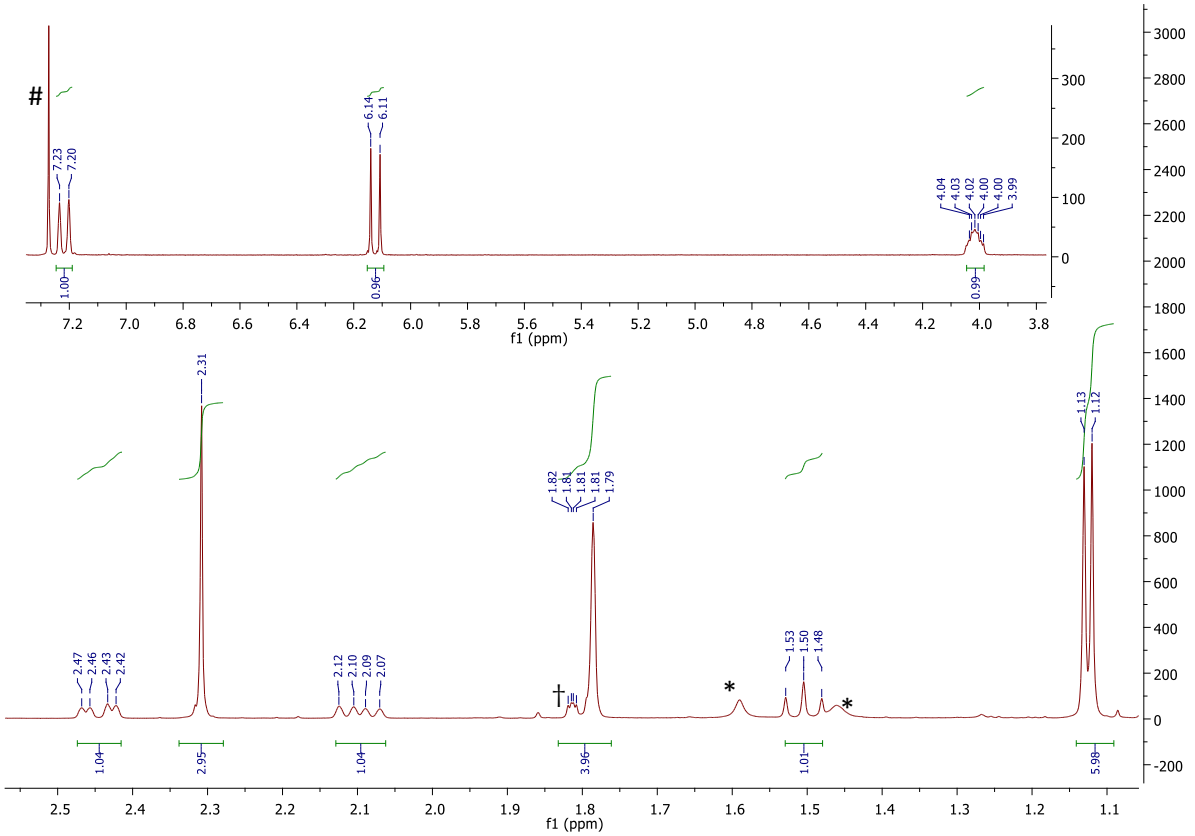

Figure A.10 (a): ^{1}H NMR of 3-hydroxy-β-ionone in $CDCl_3$. impurity (*), $CDCl_3$ (#). The signal for H2a is present as a multiplet, which is partly visible at 1.81 ppm and partly hidden behind the signal for H13 at 1.79 ppm.

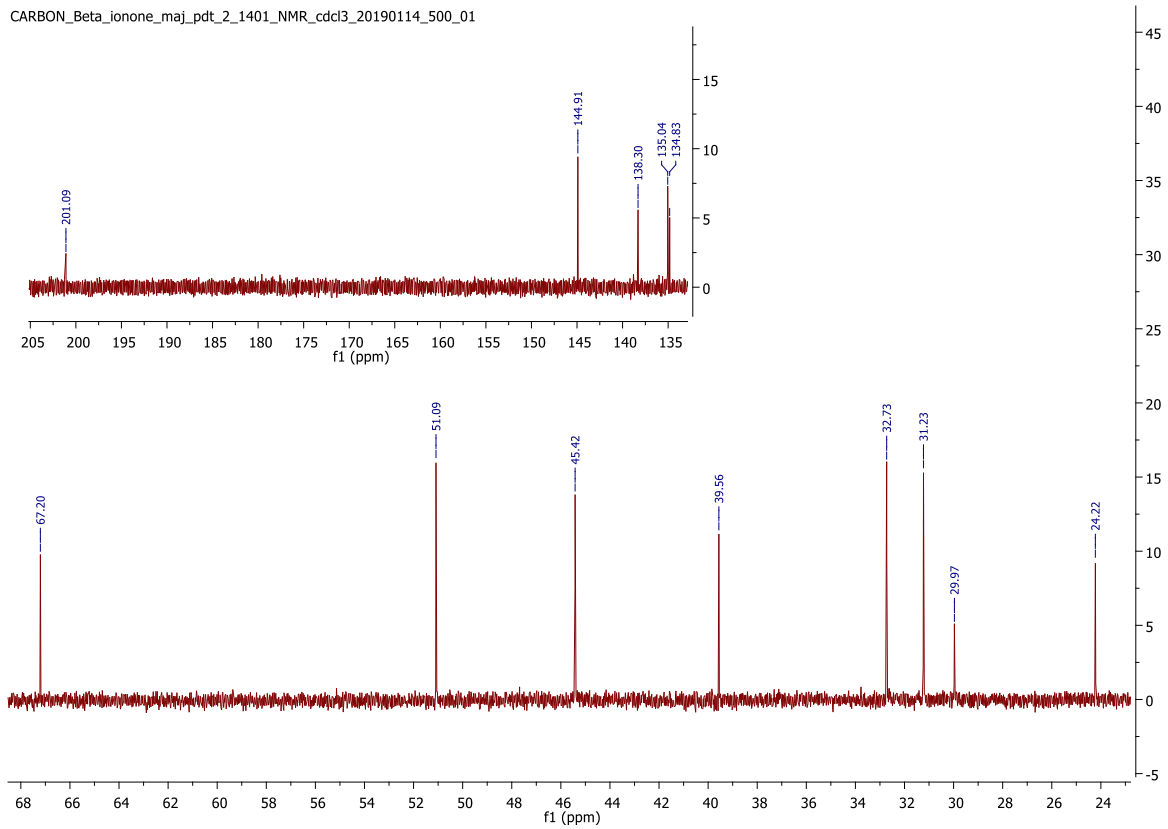

Figure A.10 (b): ^{13}C NMR of 3-hydroxy-β-ionone in $CDCl_3$.

Data for *anti*-3-4-dihydroxy-β-ionone **:

^{1}H NMR (500 MHz, $CDCl_3$) δ 7.15 (d, *J* = 16.4 Hz, 1H'; H8), 6.13 (d, *J* = 16.4 Hz, 1H'; H7), 3.95 (d, *J* = 7.8 Hz, 1H'; H4), 3.81 (ddd, *J* = 12.4 Hz, 7.8 Hz, 3.5 Hz, 1H'; H3), 2.31 (s, 3H'; H10), 1.83 (s, 3H'; H13), 1.78 (dd, *J* = 12.4, 3.5 Hz, 1H'; H2a), 1.62 (t, *J* = 12.4 Hz, 1H'; H2b), 1.14 (s, 3H'; H11), 1.10 (s, 3H'; H12); ^{13}C NMR (126 MHz, $CDCl_3$) δ 200.94 (C9), 144.66 (C8), 140.66 (C6), 136.10 (C7), 135.24 (C5), 80.26 (C4), 73.24 (C3), 47.24 (C2), 39.53 (C1), 32.85 (C12), 30.81 (C11), 30.14 (C10), 19.01 (C13).

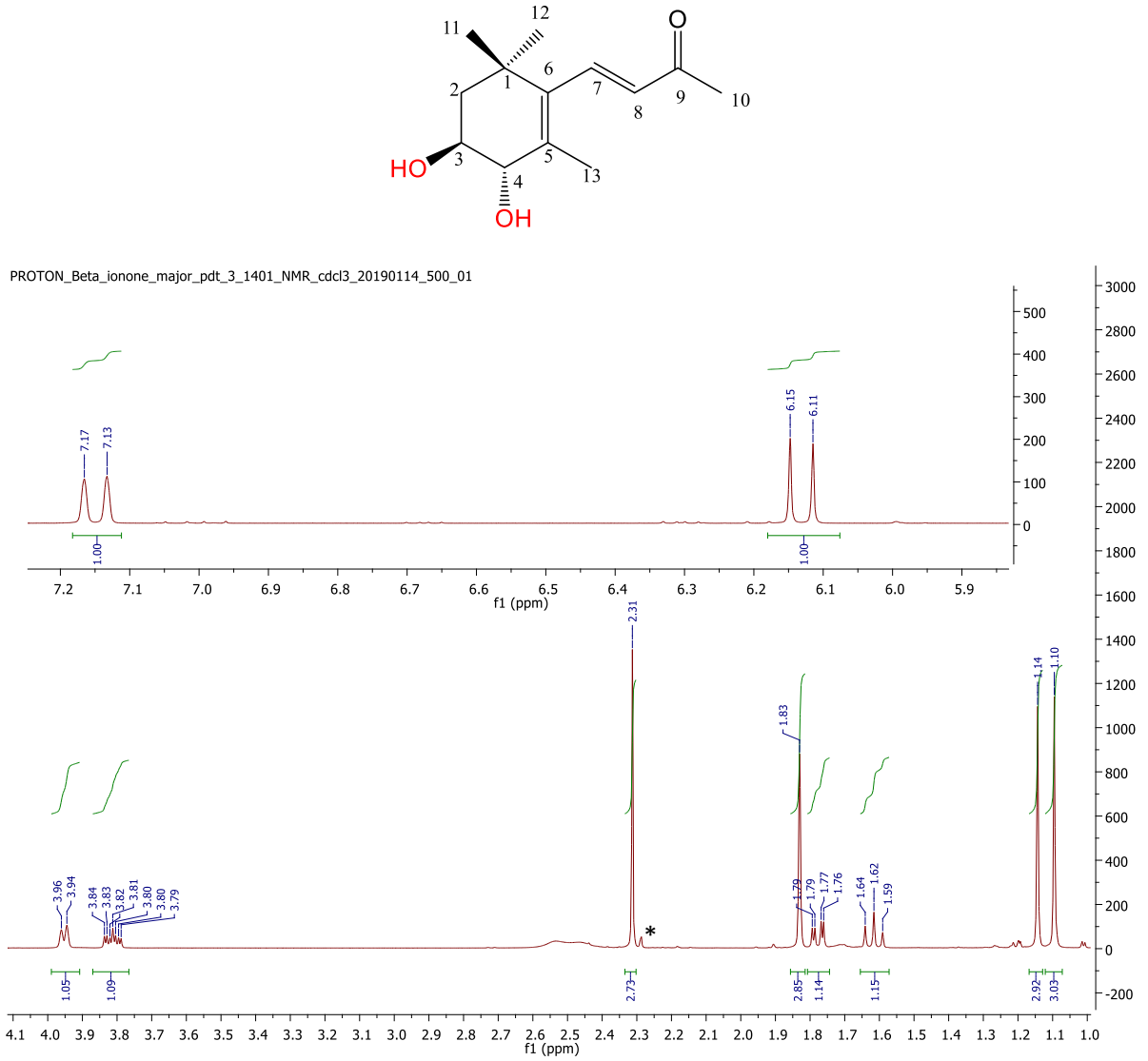

Figure A.11 (a): ^{1}H NMR of *anti*-3,4-dihydroxy-β-ionone in $CDCl_3$. Impurity / OH (*).

** The NMR was compared to the reported NMRs of 3-cyclohexene-1,2-diol, 1,2-dihydroxy-3,5-dimethyl-3-cyclohexene and 7-oxabicyclo-[4.1.0]hepy-3-ene. The proton and carbon signals for 3-cyclohexene-1,2-diol were, H_a = 4.14 ppm; C_a = 68.8 ppm, H_b = 3.83 ppm; C_b = 66.5 ppm. For 1,2-dihydroxy-3,5-dimethyl-3-cyclohexene it was, H_c = 3.79 ppm; C_c = 69.8 ppm, H_d = 3.59 ppm; C_d = 69.7 ppm. For 7-oxabicyclo-[4.1.0]hepy-3-ene, H_e = 3.50 ppm; C_e = 55.2 ppm, H_f = 3.23 ppm; C_f = 47.1 ppm. This suggests that the metabolite is 3,4-dihydroxy-β-ionone.

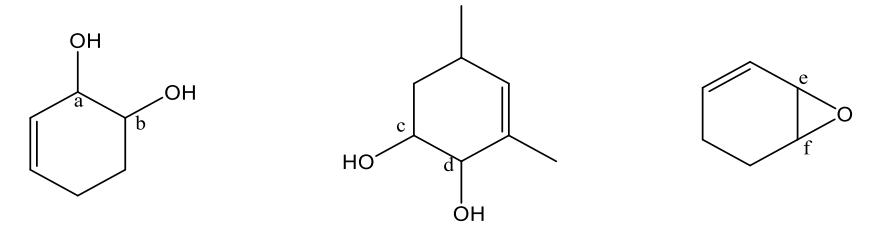

3-Cyclohexene-1,2-diol

1,2-Dihydroxy-3,5-dimethyl-3-cyclohexene

7-Oxabicyclo-[4.1.0] hept-2-ene

Figure A.9 (b): Structure of 3-cyclohexene-1,2-diol, 1,2-dihydroxy-3,5-dimethyl-3-cyclohexene and 7-oxabicyclo-[4.1.0]hepy-3-ene [17-19].

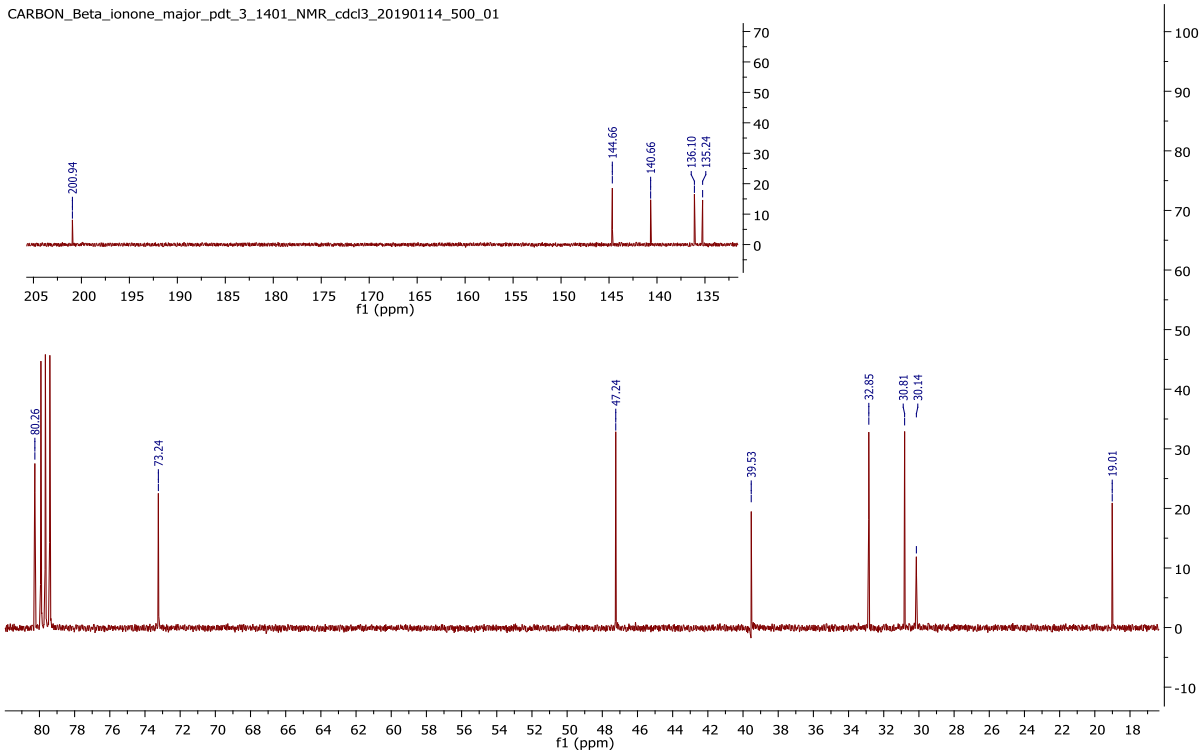

Figure A.11 (b): ^{13}C NMR of *anti*-3,4-dihydroxy-β-ionone in $CDCl_3$.

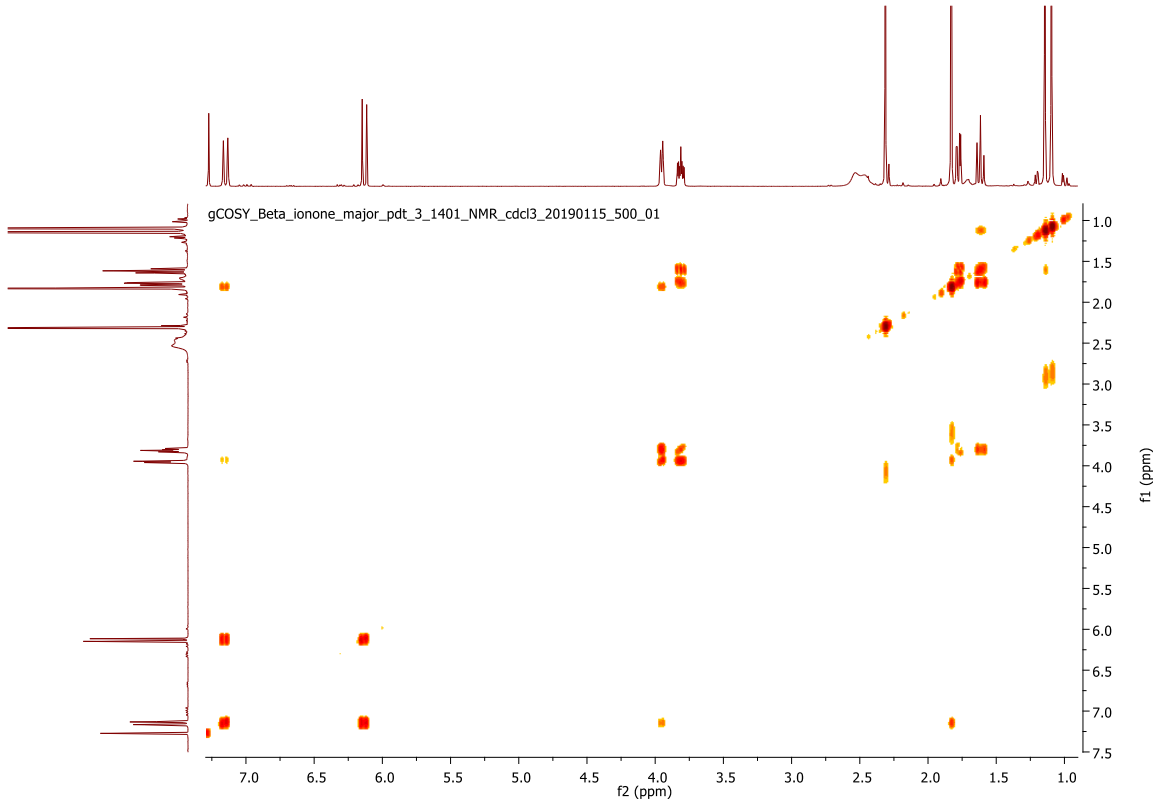

Figure A.11 (c1): g-COSY NMR of *anti*-3,4-dihydroxy-β-ionone in $CDCl_3$.

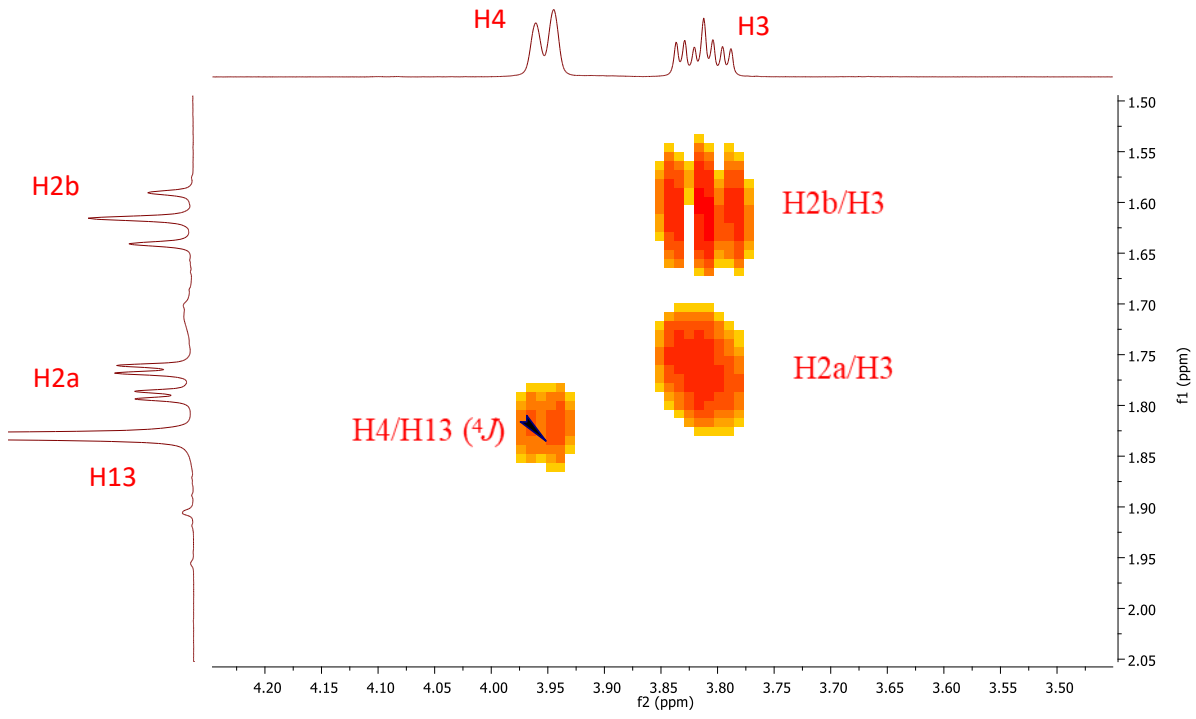

Figure A.11 (c2): g-COSY NMR of *anti*-3,4-dihydroxy-β-ionone in $CDCl_3$ (Range (f2): 4.2-3.5 ppm).

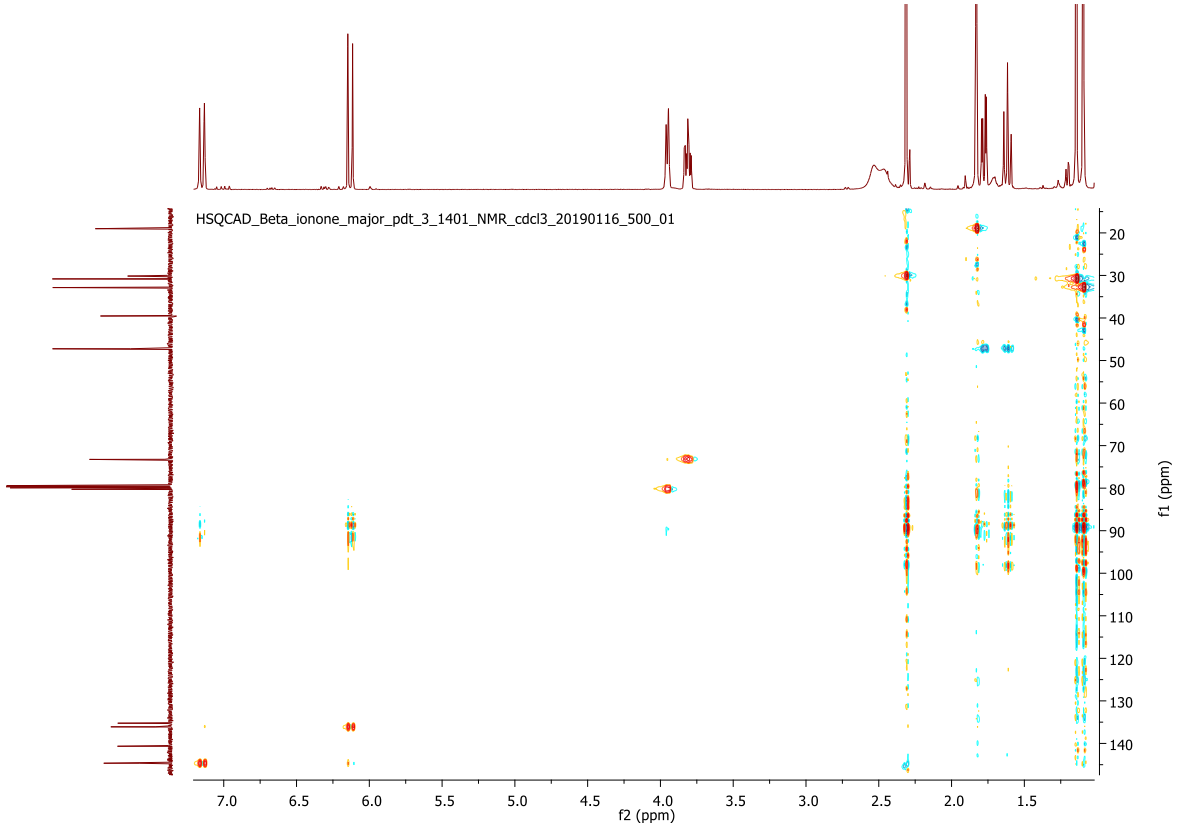

Figure A.11 (d): HSQC NMR of *anti*-3,4-dihydroxy-β-ionone in $CDCl_3$.

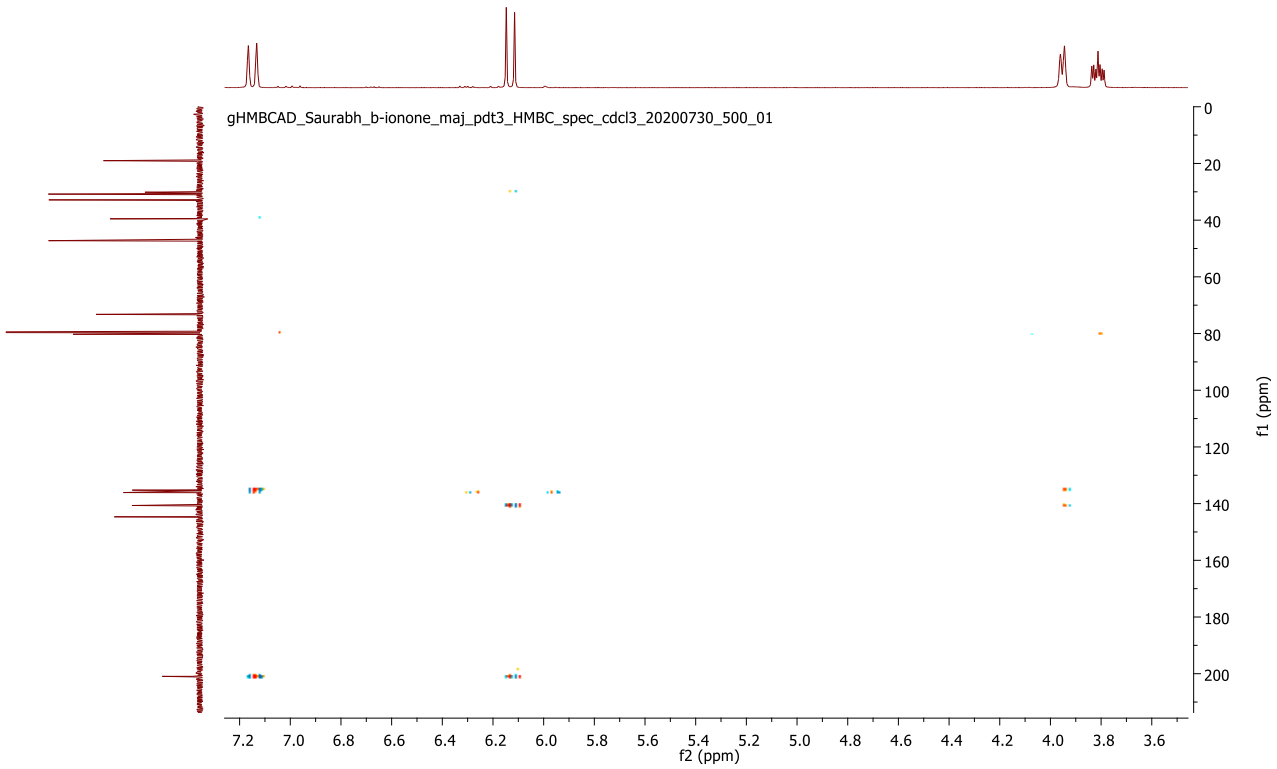

Figure A.11 (e1): HMBC NMR of *anti*-3,4-dihydroxy-β-ionone in $CDCl_3$ (Range (f2): 7.2-3.6 ppm).

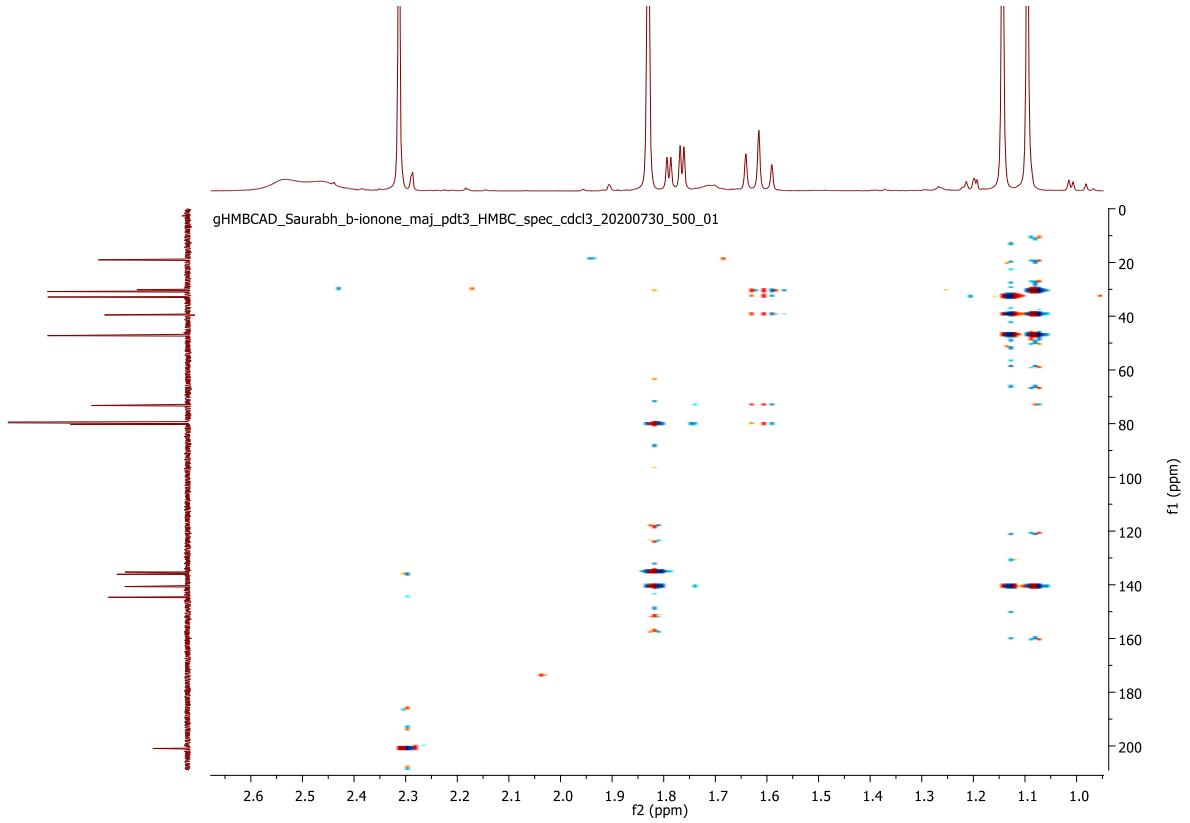

Figure A.11 (e2): HMBC NMR of *anti*-3,4-dihydroxy-β-ionone in $CDCl_3$ (Range (f2): 1-2.6 ppm).

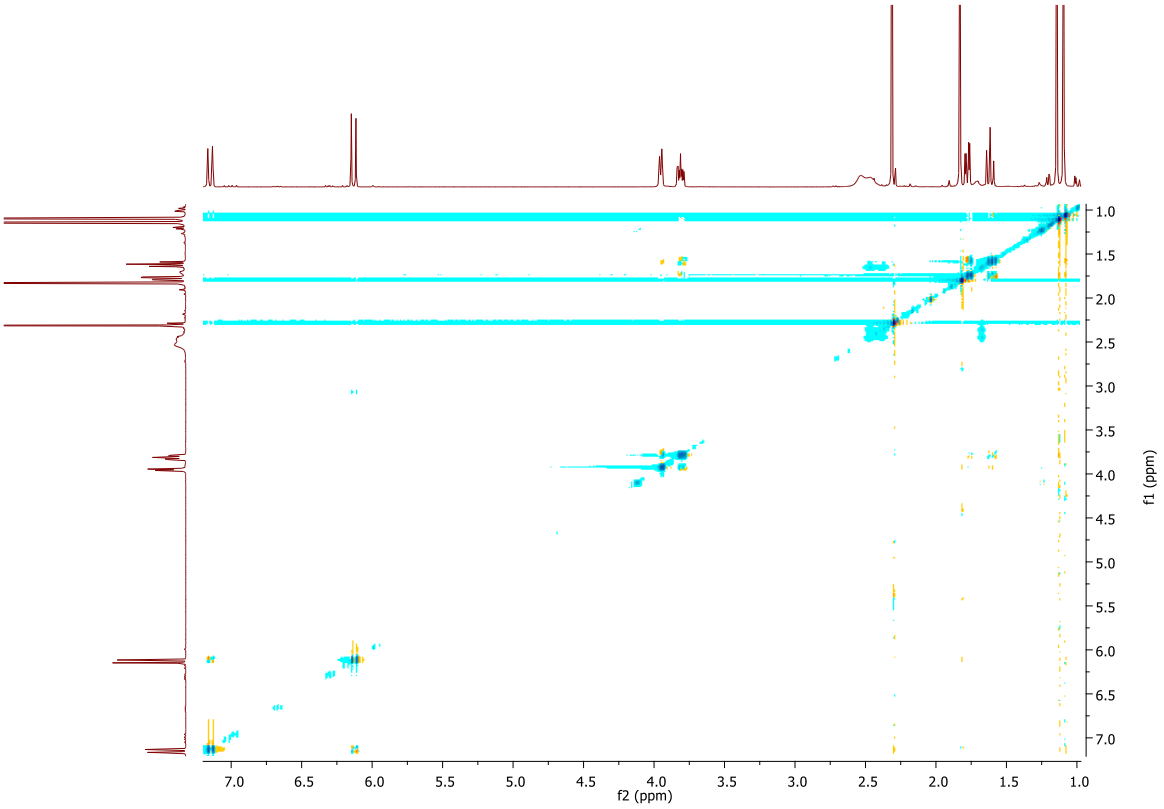

Figure A.11 (f1): ROSEY NMR of *anti*-3,4-dihydroxy-β-ionone in $CDCl_3$ (Range (f2): 4.6-3.3 ppm).

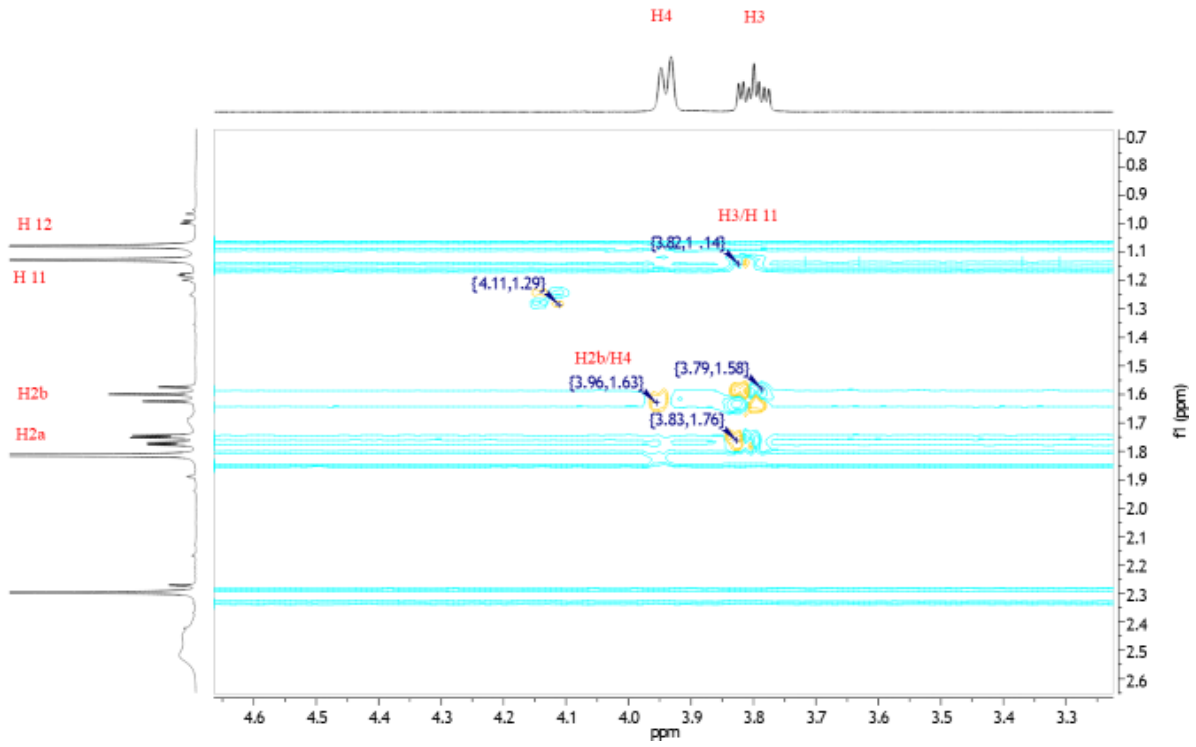

Figure A.11 (f2): ROSEY NMR of *anti*-3,4-dihydroxy-β-ionone in $CDCl_3$ (Range (f2): 4.6-3.3 ppm).

The coupling constant suggests that the interaction between H2b and H3 is axial/axial ($J_{2b,3}$ = 12.4 Hz) and that the interaction between H3 and H4 is also axial/axial ($J_{3,4}$ = 7.8 Hz). The coupling constant for $^{2}J_{2a,2b} = J_{2b,3}$ = 12.4 Hz. The COSY NMR shows interaction of H3 with H2a and H2b (Figure A.11 (c2)). The unresolved coupling constant (^{4}J) between H4 and Me13 (Figure A.11 (C2)) is the reason for the broadening of H4 signal in ^{1}H NMR. Also, The ROSEY NMR shows the interaction between H4 and H2b, H3 and Me11 (Figure A.11 (f2)). Both these NMRs confirm the structure shown in Figure A.11 (g).

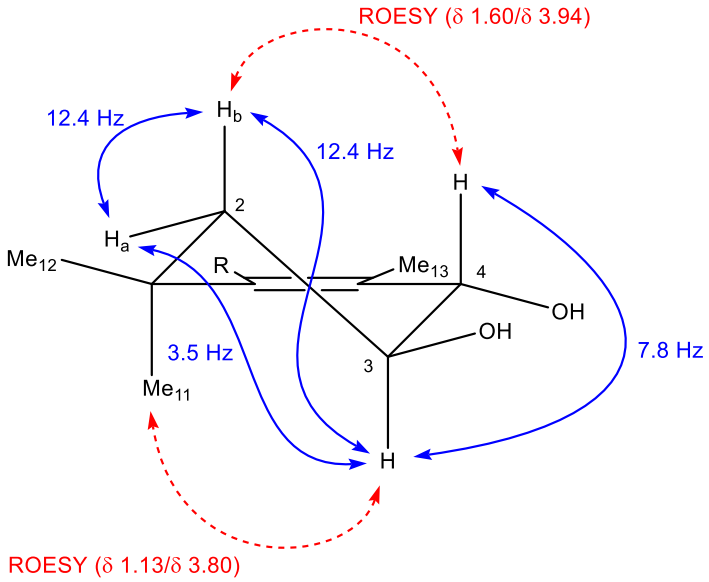

Figure A.11 (g): Half chair structure for *anti*-3,4-dihydroxy-β-ionone. R here is the side chain of β-ionone. The blue arrows represent the COSY interactions and the red arrows indicates the ROSEY interactions.

Data for *cis*-3-hydroxy-α-damascone [92]:

^{1}H NMR (500 MHz, $CDCl_3$) δ 6.92 (dq, *J* = 13.8, 6.9 Hz, 1H'; H9), 6.33 (dd, *J* = 13.8, 1.6 Hz, 1H'; H8), 5.70 (s, 1H'; H4), 4.21 (s, 1H'; H3), 2.94 (s, 1H'; H6), 1.93 (dd, *J* = 6.9, 1.6 Hz, 3H'; H10), 1.66 (d, *J* = 8.2 Hz, 2H, H2a, H2b), 1.61 (s, 3H'; H13), 0.99 (s, 3H'; H12), 0.90 (s, 3H'; H11); ^{13}C NMR (126 MHz, $CDCl_3$) δ 203.89 (C7), 145.90 (C9), 136.15 (C5), 135.08 (C8), 130.28 (C4), 68.84 (C3), 63.45 (C6), 43.61 (C2), 37.63 (C1), 31.29 (C11), 30.97 (C12), 25.69 (C13), 20.97 (C10).

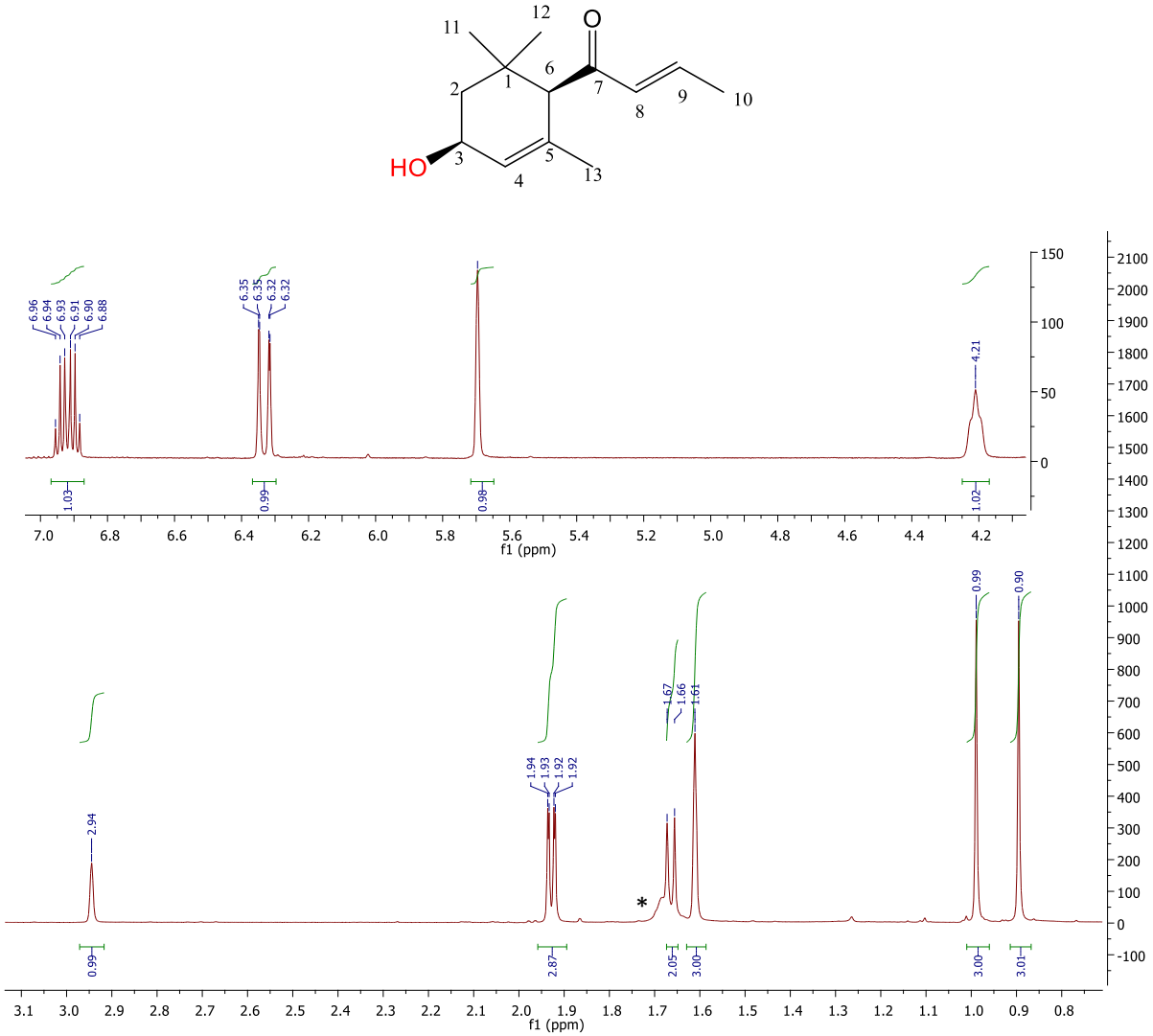

Figure A.12 (a): ^{1}H NMR for *cis*-3-hydroxy-α-damascone in $CDCl_3$. Impurity / OH (*).

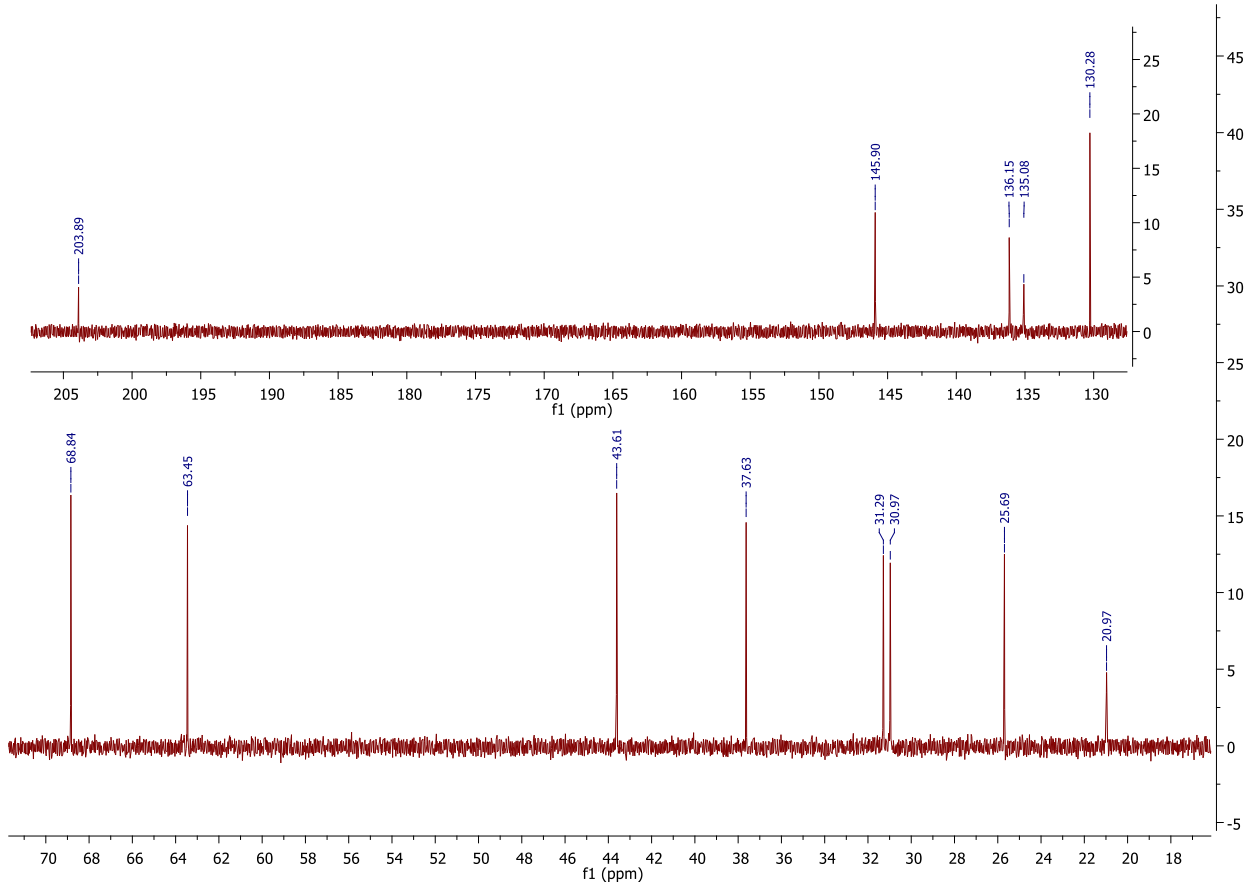

Figure A.12 (b): ^{13}C NMR for *cis*-3-hydroxy-α-damascone in $CDCl_3$.

Data for *trans*-3-hydroxy-α-damascone [92]:

^{1}H NMR (500 MHz, $CDCl_3$) δ 6.91 (td, *J* = 13.8, 6.8 Hz, 1H'; H9), 6.24 (dd, *J* = 13.8, 1.4 Hz, 1H'; H8), 5.72 (s, 1H'; H4), 4.36 (s, 1H'; H3), 3.14 (s, 1H'; H6), 1.94 – 1.98 (m, 1H'; H2a), 1.92 (dd, *J* = 6.8, 1.4 Hz, 3H'; H10), 1.64 (s, 3H'; H13), 1.39 – 1.43 (m, 1H'; H2b), 1.14 (s, 3H'; H11), 0.90 (s, 3H'; H12); ^{13}C NMR (126 MHz, $CDCl_3$) δ 203.68 (C7), 145.69 (C9), 135.96 (C5), 134.89 (C8), 130.07 (C4), 68.65 (C3), 63.24 (C6), 43.42 (C2), 37.43 (C1), 31.08 (C11), 30.77 (C12), 25.49 (C13), 20.77 (C10).

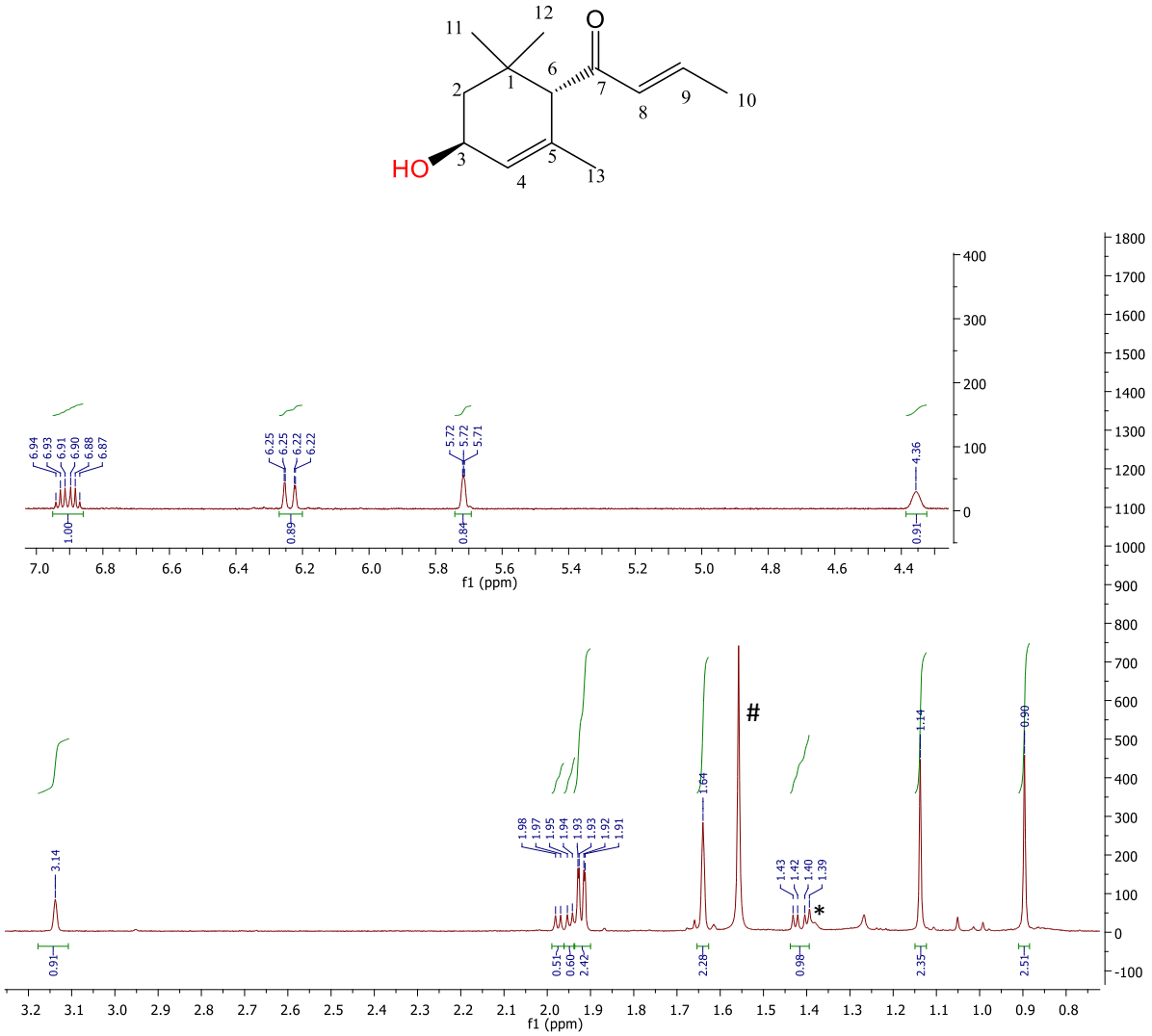

Figure A.13 (a): ^{1}H NMR for *trans*-3-hydroxy-α-damascone in $CDCl_3$. H_2O (#), Impurity (*)

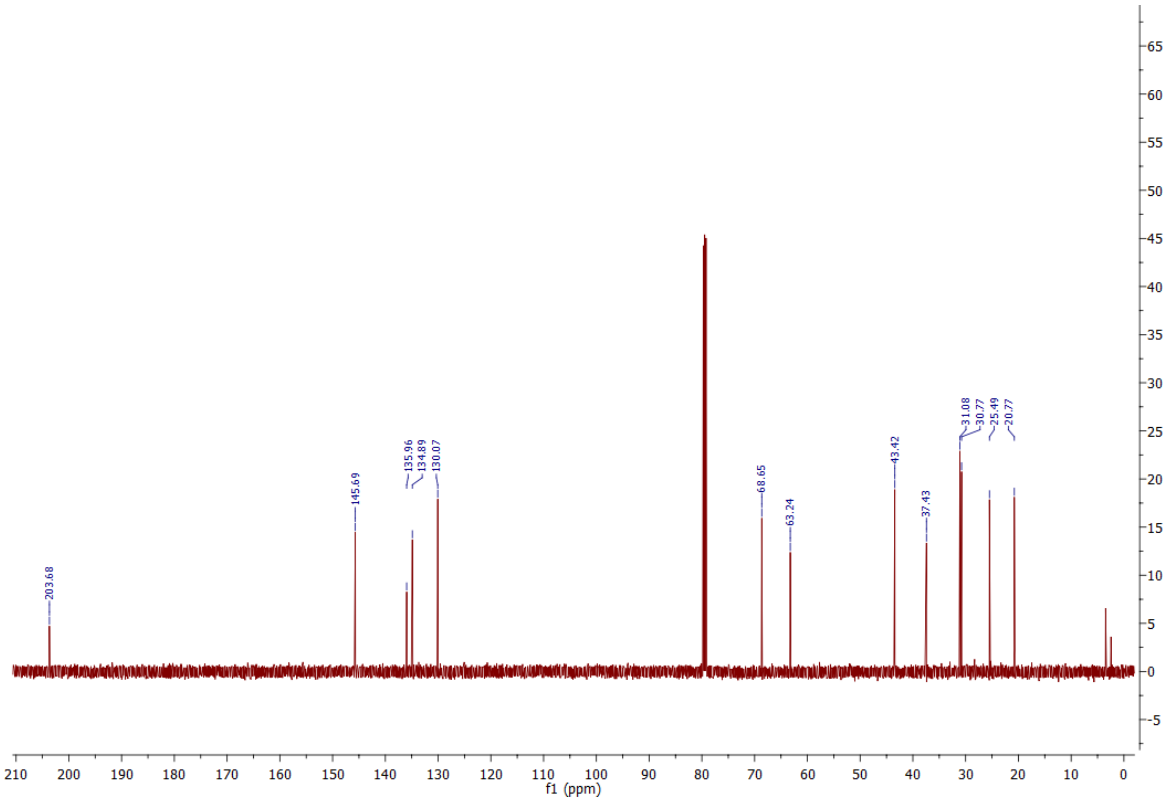

Figure A.13 (b): ^{13}C NMR for *trans*-3-hydroxy-α-damascone in $CDCl_3$.

Data for 4-hydroxy-β-damascone [76]:

^{1}H NMR (500 MHz, $CDCl_3$) δ 6.78 (dq, *J* = 13.7, 6.9 Hz, 1H'; H9), 6.17 (dd, *J* = 13.7, 1.4 Hz, 1H'; H8), 4.01 (s, 1H'; H4), 2.05 – 1.97 (m, 1H'; H3a), 1.94 (dd, *J* = 6.9, 1.4 Hz, 3H'; H10), 1.78 (m, 1H'; H3b), 1.70 - 1.64 (m, 4H'; H10 & H2a), 1.49 – 1.44 (m, 1H'; H2b), 1.05 (s, 6H'; H11 & H12); ^{13}C NMR (126 MHz, $CDCl_3$) δ=203.49 (C7), 149.06 (C9), 146.25 (C6), 136.57 (C8), 133.60 (C5), 71.68 (C4), 37.29 (C2), 36.64 (C1), 31.47 (C11), 31.29 (C3), 30.28 (C12), 21.10 (C10), 20.60 (C13).

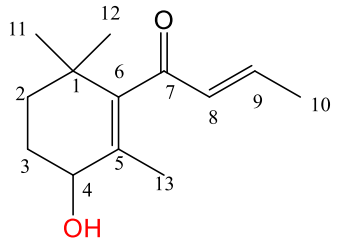

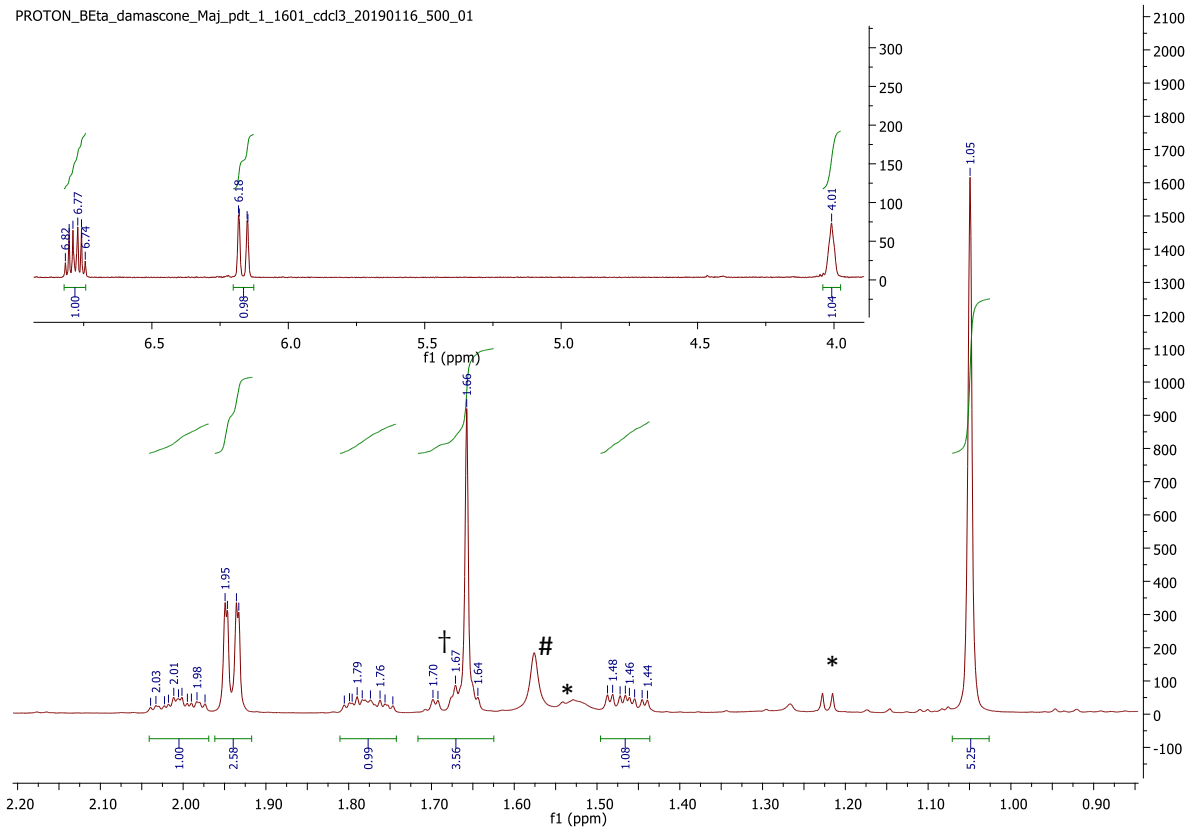

Figure A.14 (a): ^{1}H NMR of 4-hydroxy-β-damascone in $CDCl_3$. Impurity (*), H_2O (#). (†) The signal for H2a is present as a multiplet signal which is partly visible at 1.7 ppm and partly hidden behind the signal for H10 at 1.66 ppm.

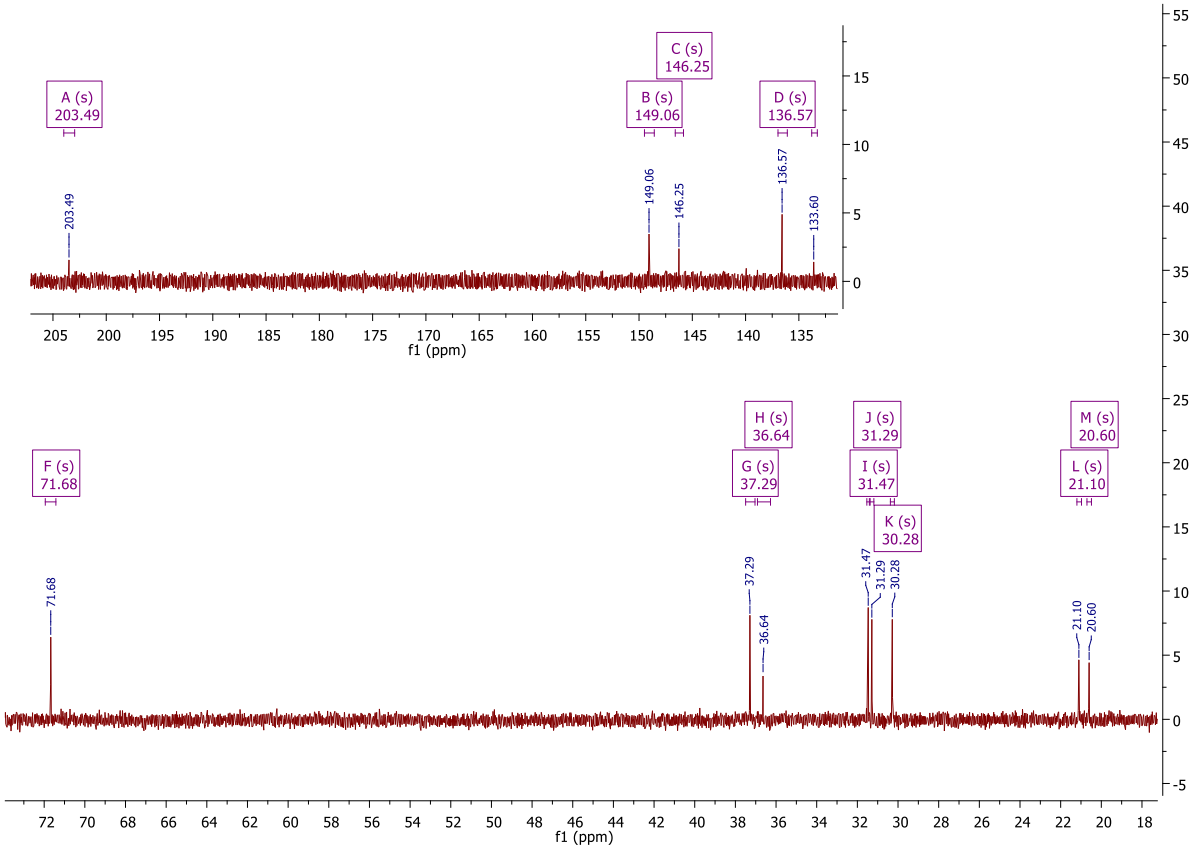

Figure A.14 (b): ^{13}C NMR of 4-hydroxy-β-damascone in $CDCl_3$.

Data for 3-hydroxy-β-damascone [76]:

^{1}H NMR (500 MHz, $CDCl_3$) δ=6.78 (dq, J = 15.6, 6.9 Hz, 1H; H9), 6.16 (dd, J = 15.7, 1.6 Hz, 1H; H8), 4.01 (t, J = 4.9 Hz, 1H; H3), 2.16 (dd, J = 8.6, 5.8 Hz, 1H; H4a), 2.04-1.97 (m, 1H; H4b), 1.94 (dd, J = 6.9, 1.6 Hz, 3H; H10), 1.79 – 1.74 (m, 1H; H2a), 1.65 (s, 3H; H13), 1.48 – 1.44 (m, 1H; H2b), 1.05 (s, 6H; H11 & H12). ^{13}C NMR (126 MHz, $CDCl_3$) δ=203.48 (C7), 149.02 (C9), 145.48 (C6), 136.57 (C8), 132.85 (C5), 71.66 (C3), 55.84 (C2), 37.29 (C4), 31.46 (C1), 31.29 (C11), 30.28 (C12), 21.08 (C13), 20.58 (C10).

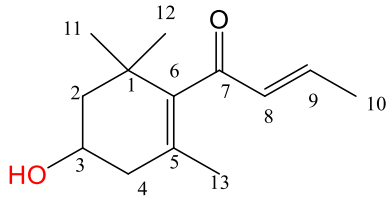

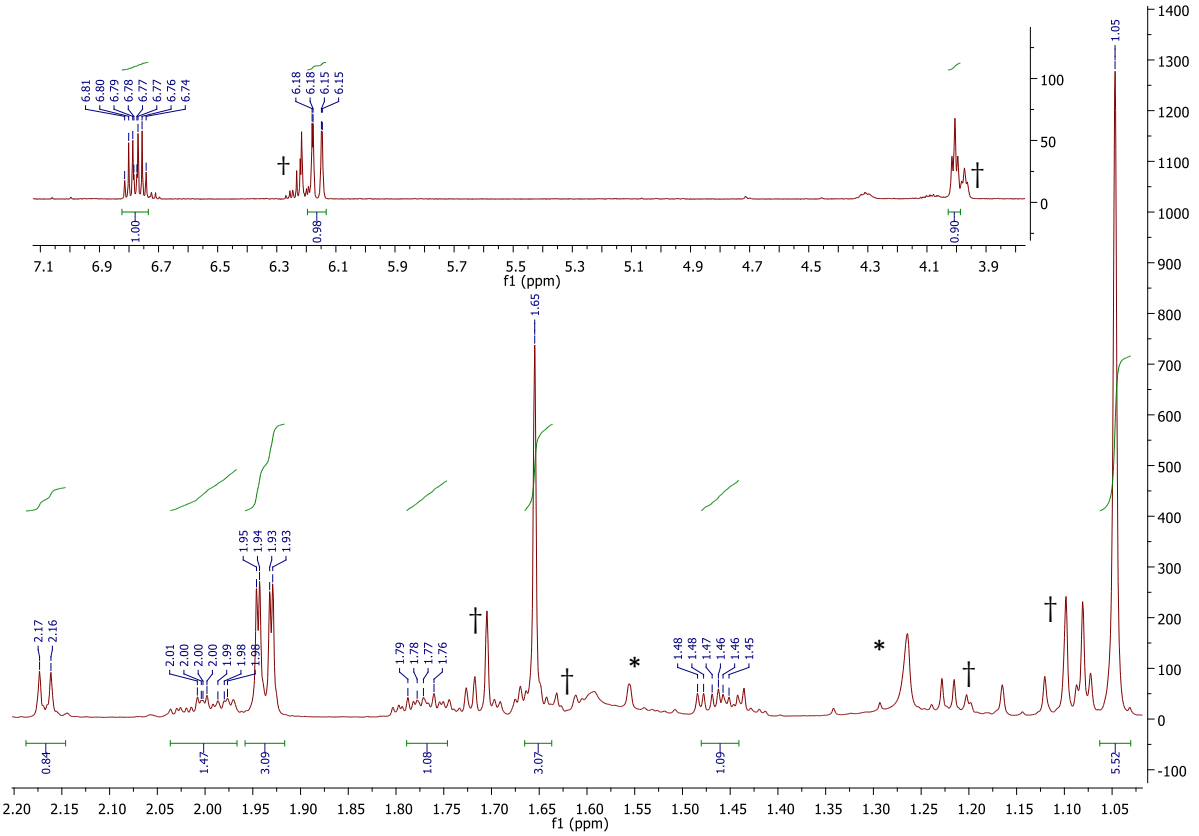

Figure A.15 (a) ^{1}H NNMR for 3-hydroxy-β-damascone in $CDCl_3$. This product was separated with impurity of another monohydroxy product, the signal of second product are labelled as (†). The signal of H13 at 1.65 ppm covers a signal from impurity as well. The signal of solvent residue / H_2O / OH is labelled as (*).

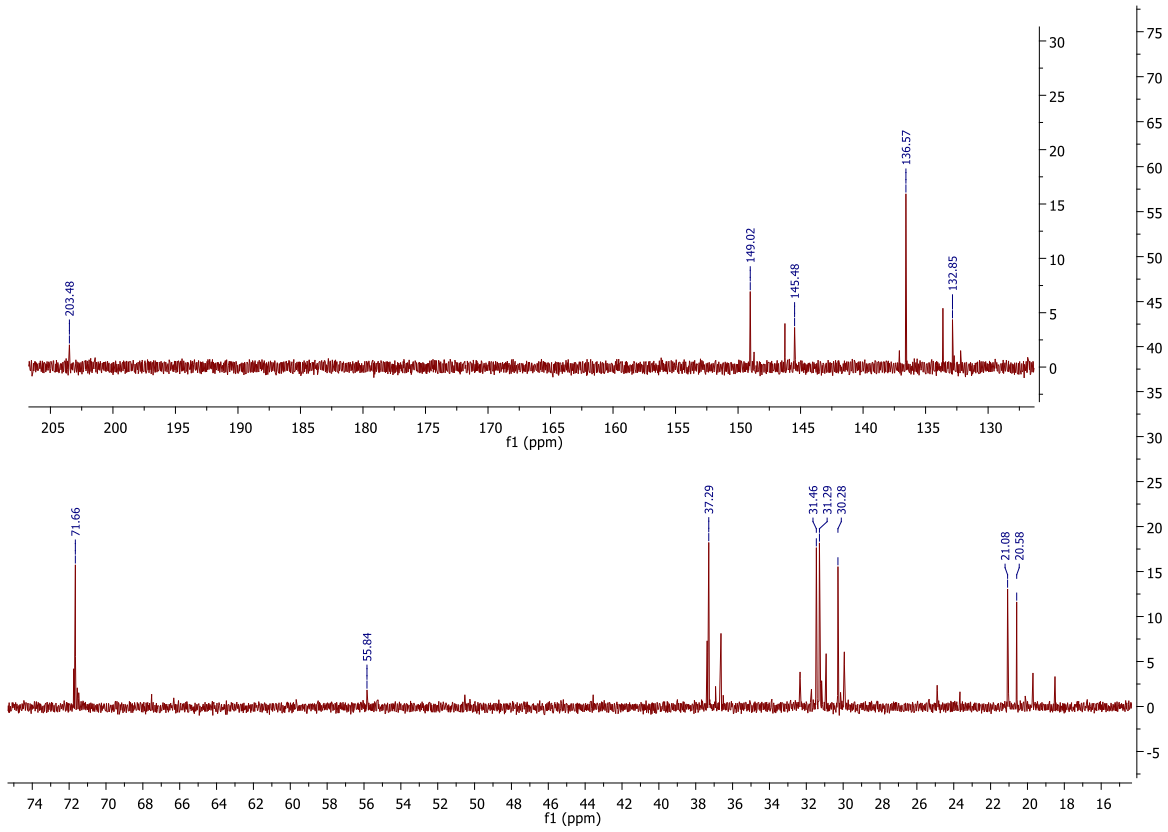

Figure A.15 (b): ^{13}C NMR of 3-hydroxy-β-damascone in $CDCl_3$.

Data for 3,4-epoxy-δ-damascone [92]:

^{1}H NMR (500 MHz, $CDCl_3$) δ=6.84 (dq, *J* = 15.5, 6.9 Hz, 1H, H9), 6.21 (dq, *J* = 15.5, 1.7 Hz, 1H, H8), 3.20 – 3.18 (m, 1H, H3), 2.89 (d, *J* = 4.0 Hz, 1H, H4), 2.49 (dq, *J* = 11.6, 7.2 Hz, 1H, H5), 2.20 (d, *J* = 11.6 Hz, 1H, H6), 1.94 (dd, *J* = 1.6 Hz, 1H, H2), 1.90 (dd, *J* = 6.9, 1.7 Hz, 3H, H10), 1.61 (dd, *J* = 1.6 Hz, 1H, H2'), 0.99 (s, 3H, H11), 0.97 (d, *J* = 7.2 Hz, 3H, H13), 0.87 (s, 3H, H12); ^{13}C NMR (126 MHz, $CDCl_3$) δ 205.53 (C7), 144.63 (C9), 136.61 (C6), 62.91 (C8), 59.25 (C5), 55.86 (C4), 42.52 (C3), 36.03 (C2), 34.70 (C1), 31.91 (C11), 25.99 (C12), 21.63 (C10), 20.87 (C13).

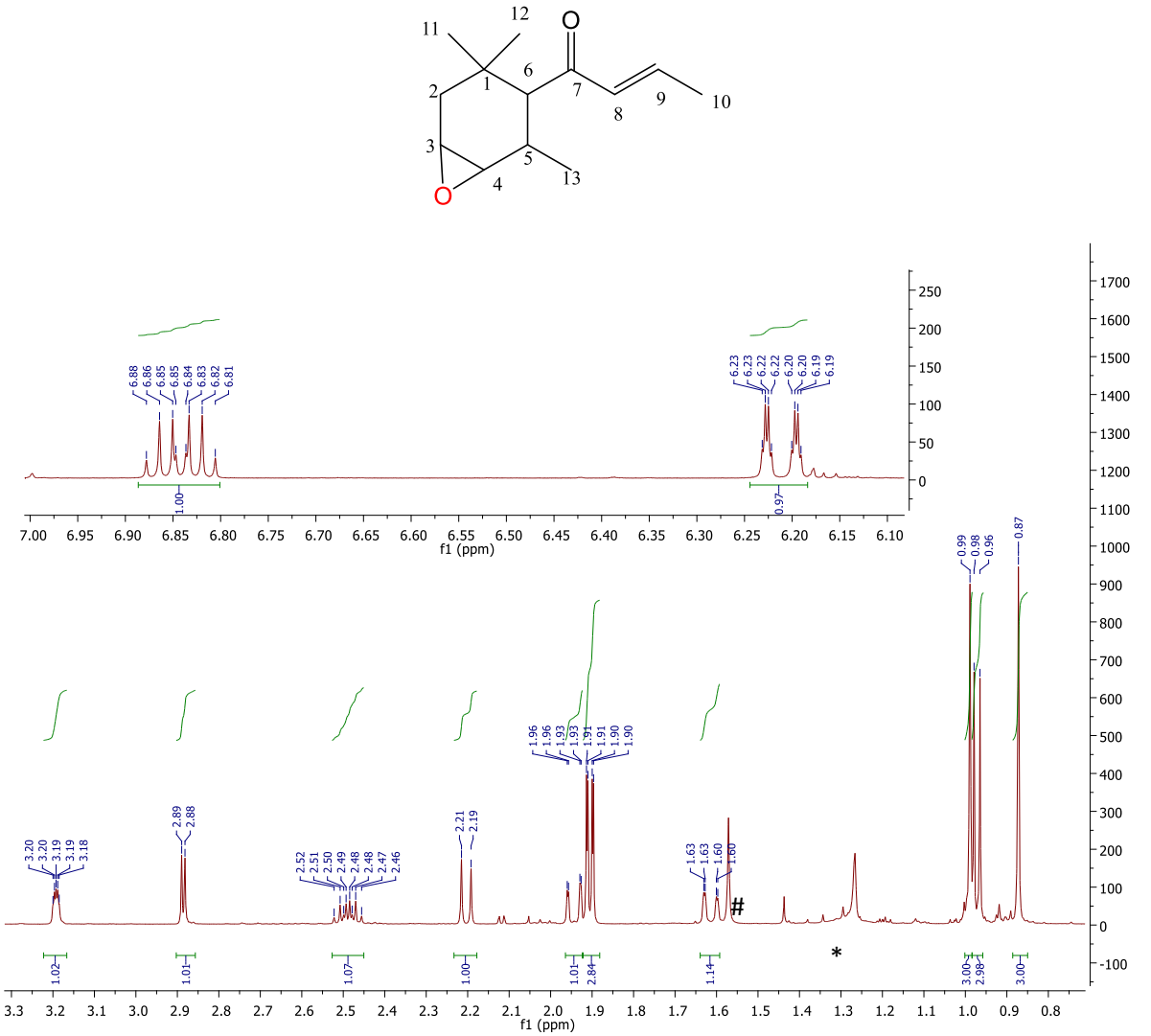

Figure A.16 (a): ^{1}H NMR of 3,4-epoxy-δ-damascone in $CDCl_3$. Impurity (*), H_2O (#).

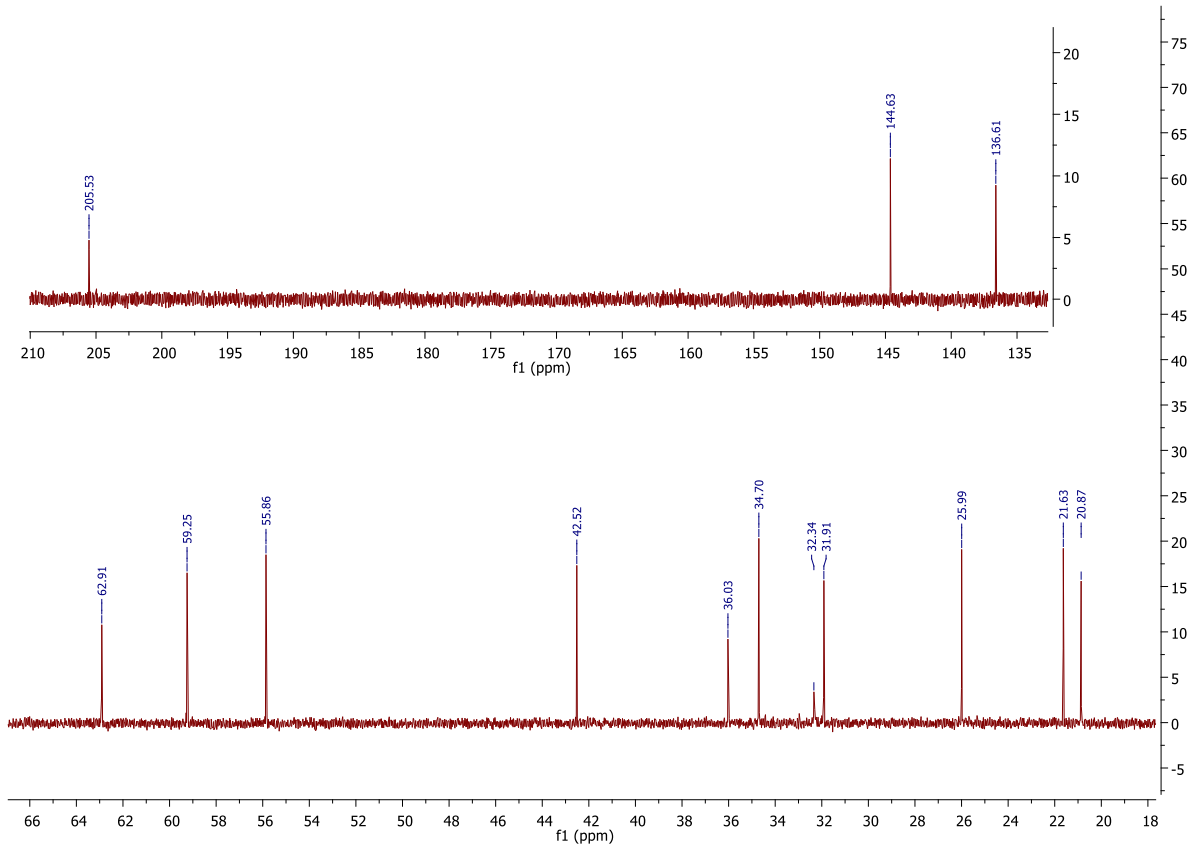

Figure A.16 (b): ^{13}C NMR of 3,4-epoxy-δ-damascone in $CDCl_3$.

Data for 2-hydroxy-δ-damascone:

^{1}H NMR (599 MHz, cdcl$_3$) δ 6.85 (dq, *J* = 15.5, 6.8 Hz, 1H; H9), 6.23 – 6.19 (m, 1H; H8), 5.59 – 5.55 (m, 1H; H4), 5.48 – 5.45 (m, 1H, H3), 3.95 (s, 1H, H2), 2.64 – 2.58 (m, 1H, H5), 2.56 (d, *J* = 10.0 Hz, 1H; H6), 1.91 – 1.89 (m, 3H; H10), 0.97 (s, 3H; H11), 0.92 (s, *J* = 1.5 Hz, 3H; H12), 0.86 (d, *J* = 6.8 Hz, 3H; H13); ^{13}C NMR (151 MHz, cdcl$_3$) δ 204.58 (C7), 145.09 (C9), 136.99 (C8), 136.79 (C4), 131.14 (C3), 78.53 (C2), 62.32 (C6), 40.60 (C1), 34.26 (C5), 28.40 (C11), 22.38 (C13), 20.93 (C10), 16.78 (C12).

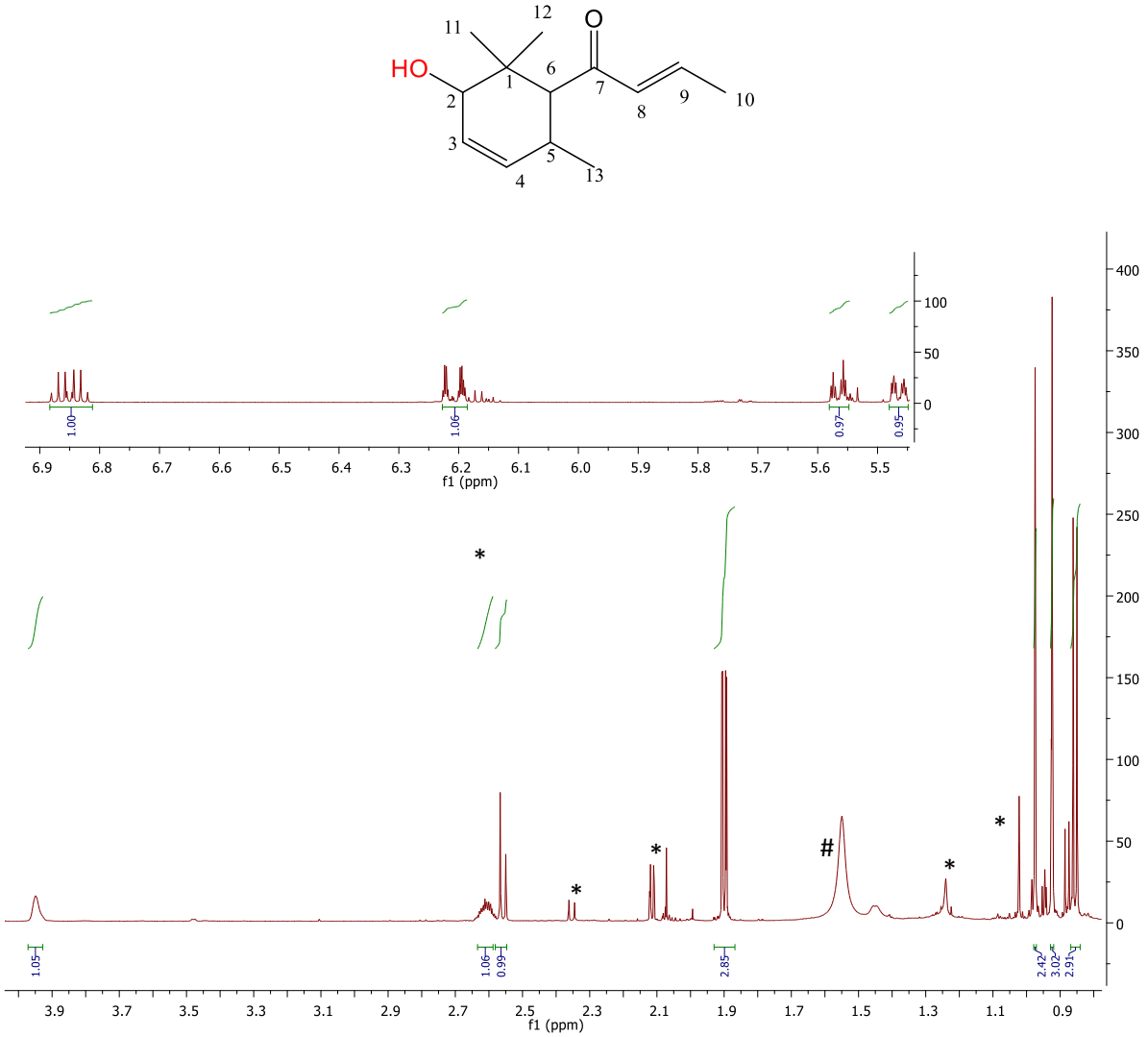

Figure A.17 (a): ^{1}H NMR of 2-hydroxy-δ-damascone in CDCl$_3$. Impurity (*), H$_2$O (#)

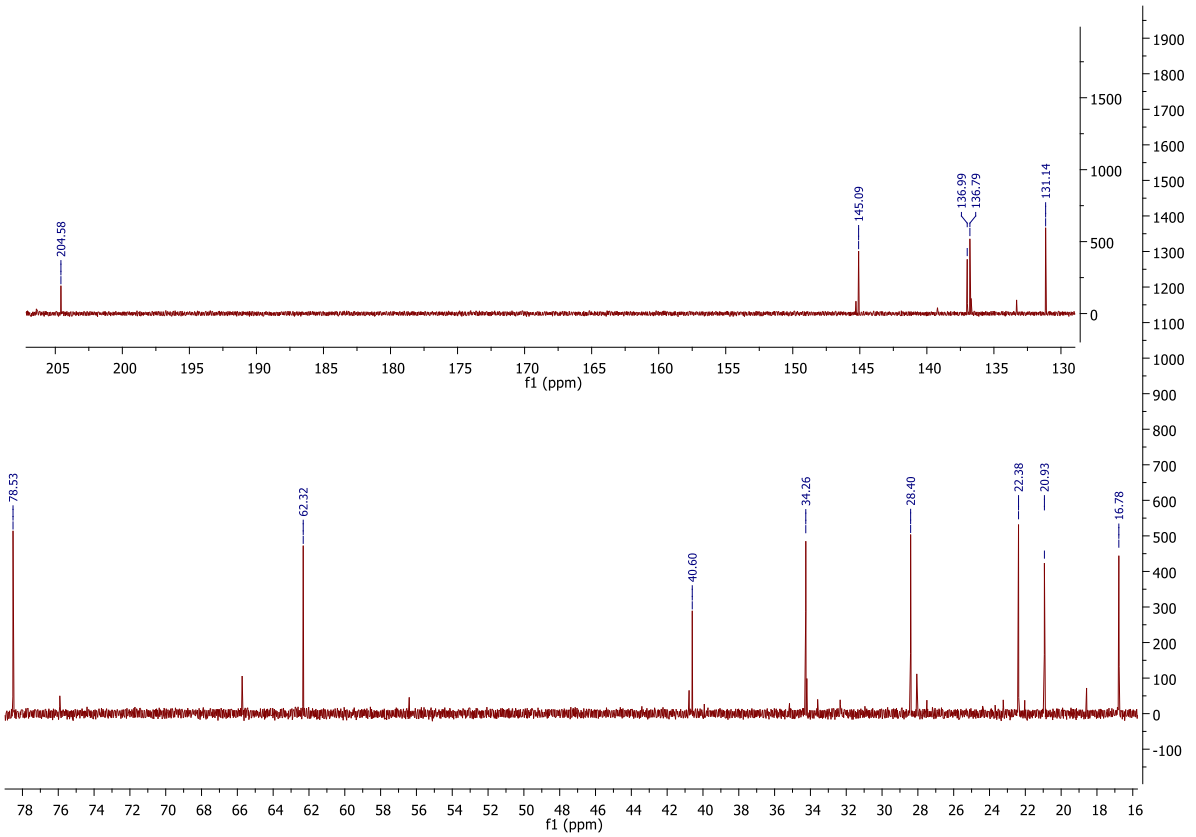

Figure A.17 (b): ^{13}C NMR of 2-hydroxy-δ-damascone in $CDCl_3$.

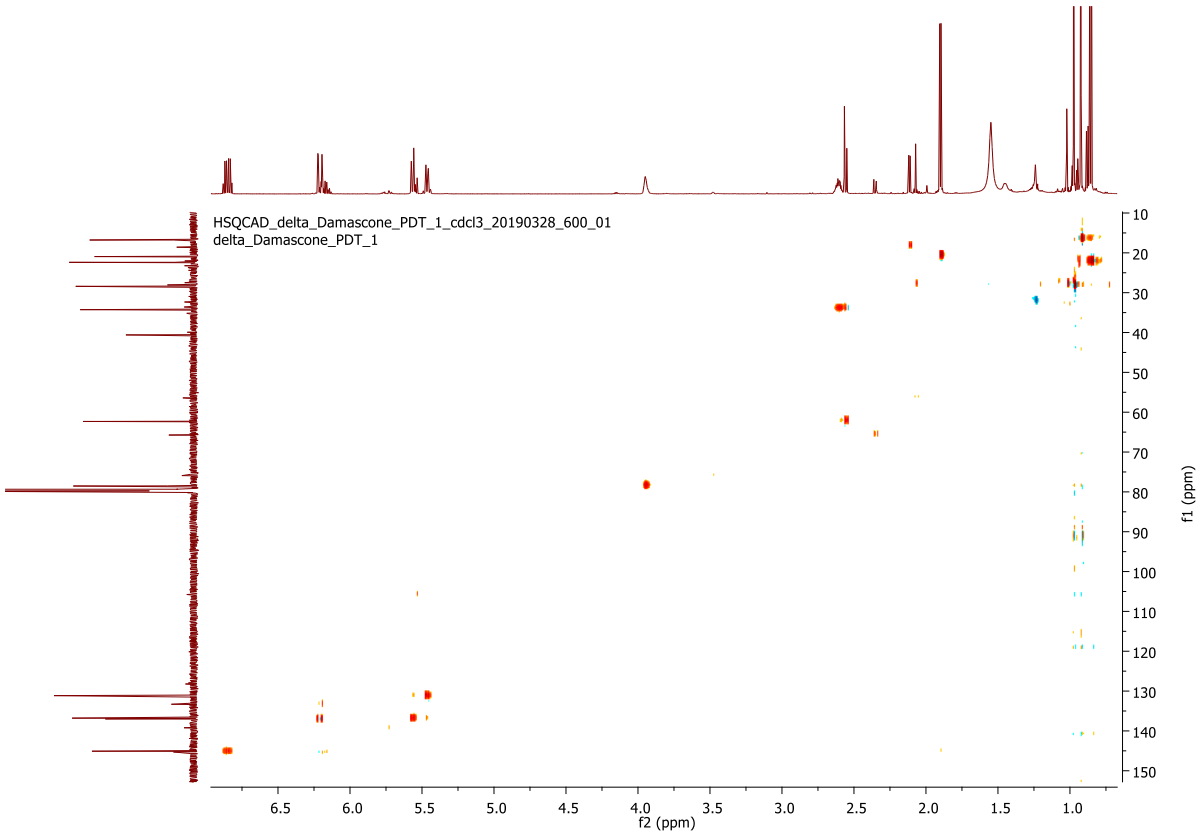

Figure A.17 (c): HSQC NMR of 2-hydroxy-δ-damascone in $CDCl_3$.

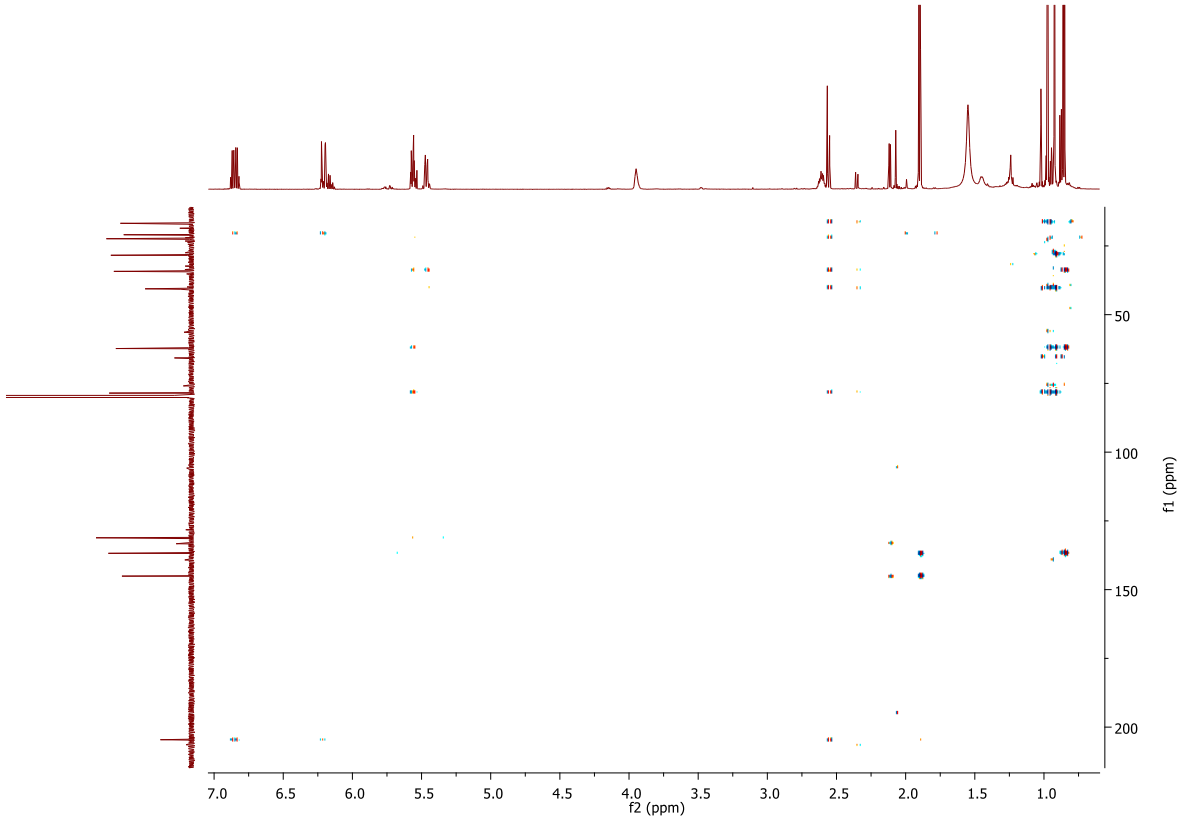

Figure A.17 (d): HMBC NMR of 2-hydroxy-δ-damascone in $CDCl_3$.

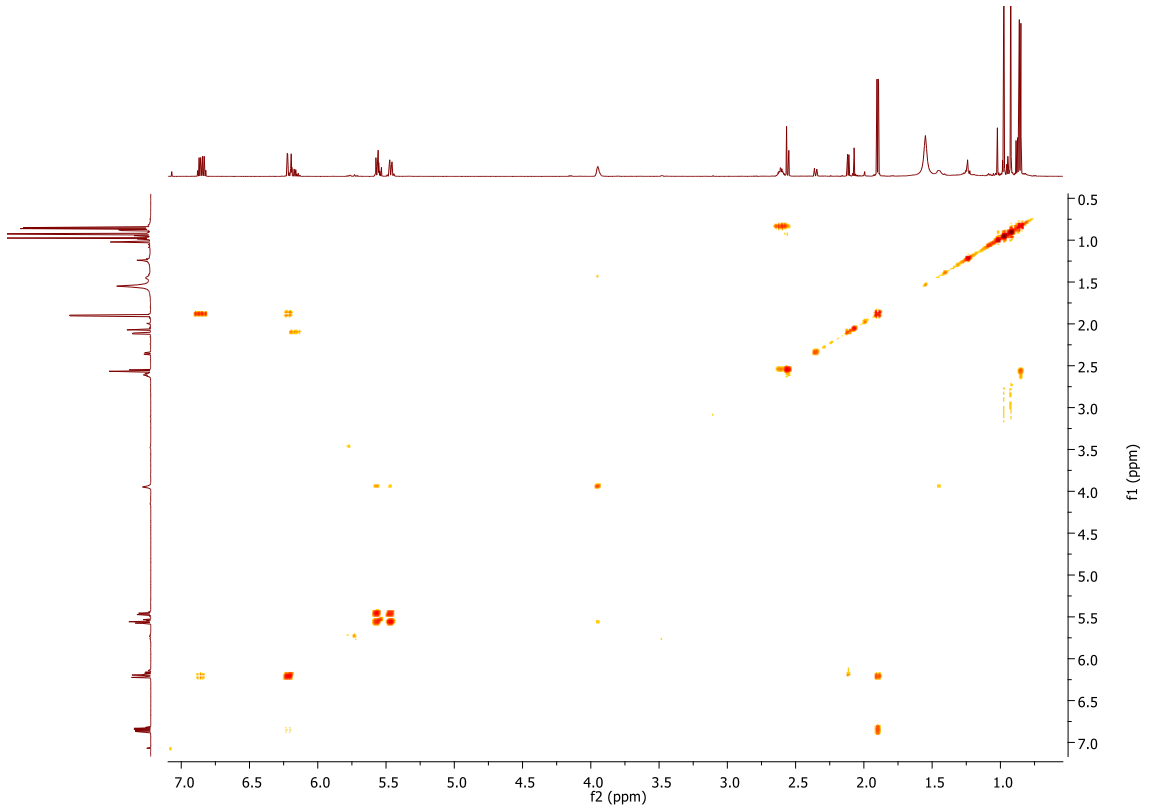

Figure A.17 (e): g-COSY NMR of 2-hydroxy-δ-damascone in $CDCl_3$.

Data for *cis*-3-hydroxy-α-ionol [109]:

^{1}H NMR (500 MHz, $CDCl_3$) δ 5.61 – 5.53 (m, 2H, H7, H4), 5.38 (dd, *J* = 15.3, 9.8 Hz, 1H, H8), 4.37 – 4.29 (m, 1H, H9), 4.24 (s, 1H, H3), 2.33 (d, *J* = 9.8 Hz, 1H, H6), 1.83 (dd, *J* = 13.2, 5.9 Hz, 1H, H2), 1.62 (s, 3H, H10), 1.36 (dd, *J* = 13.3, 6.7 Hz, 1H, H2), 1.29 (d, *J* = 6.4 Hz, 3H, H13), 1.01 (s, 3H, H11), 0.85 (s, 3H, H12). ^{13}C NMR (126 MHz, $CDCl_3$) δ 140.24 (C8), 140.05 (C5), 131.75 (C4), 127.32 (C7), 71.36 (C9), 68.47 (C3), 56.65 (C6), 47.06 (C2), 36.05 (C1), 32.03 (C13), 26.88 (C12), 26.28 (C11), 25.28 (C10).

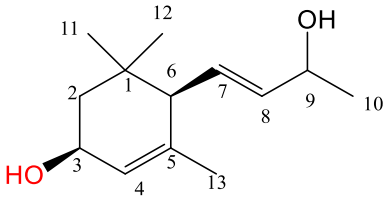

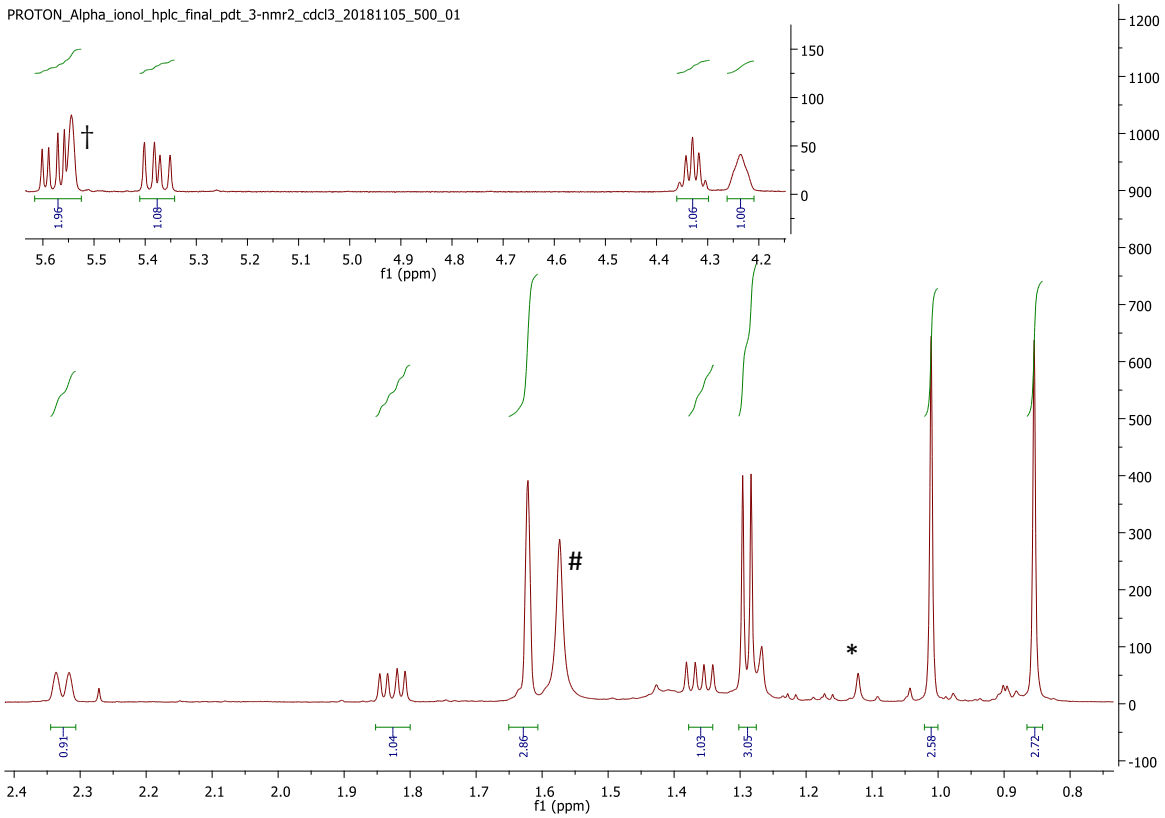

Figure A.18 (a): ^{1}H NMR of *cis*-3-hydroxy-α-ionol in $CDCl_3$. Impurity (*), H_2O (#). (†) Signal for H7 is partially visible at 5.61 ppm and partly hidden behind the signal for H4.

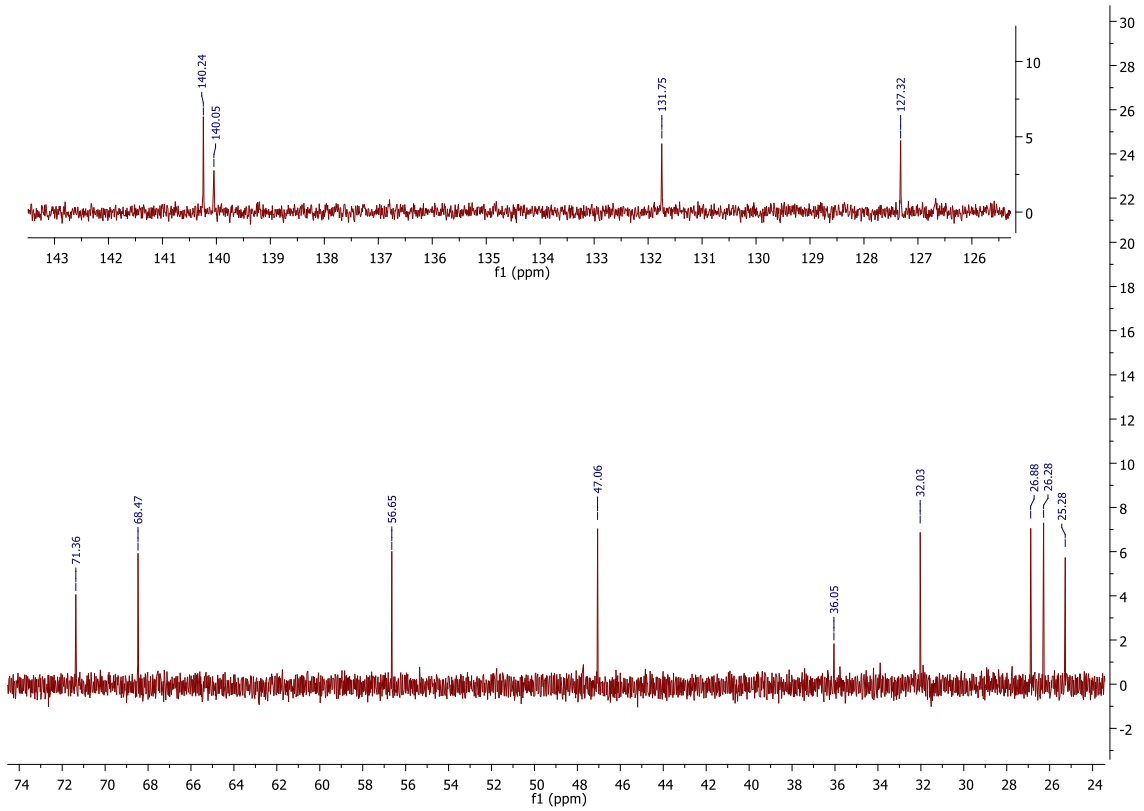

Figure A.18 (b): ^{13}C NMR of *cis*-3-hydroxy-α-ionol in $CDCl_3$.

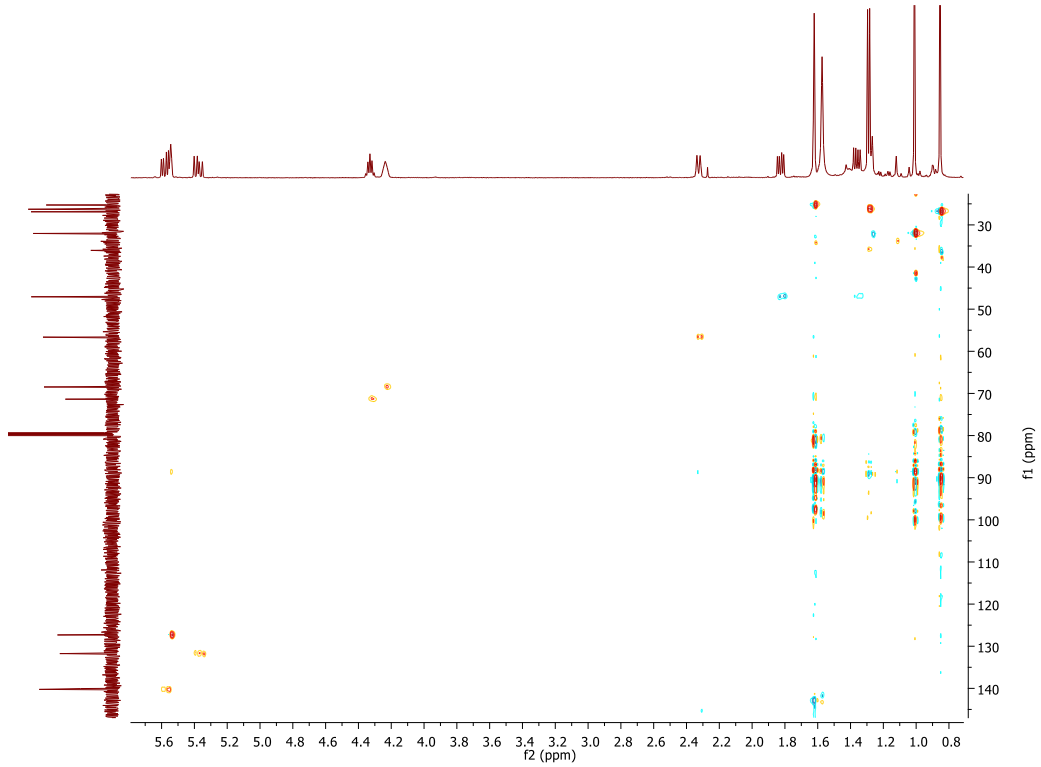

Figure A.18 (c): HSQC NMR of *cis*-3-hydroxy-α-ionol in $CDCl_3$.

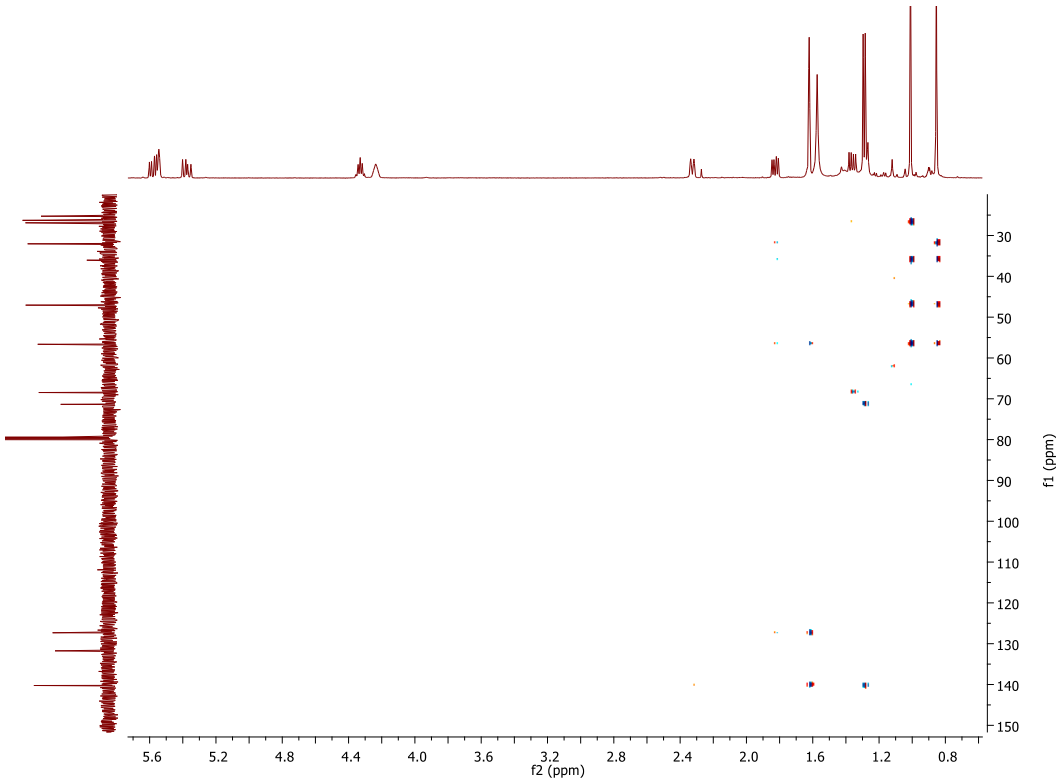

Figure A.18 (d): HMBC NMR of *cis*-3-hydroxy-α-ionol in $CDCl_3$.

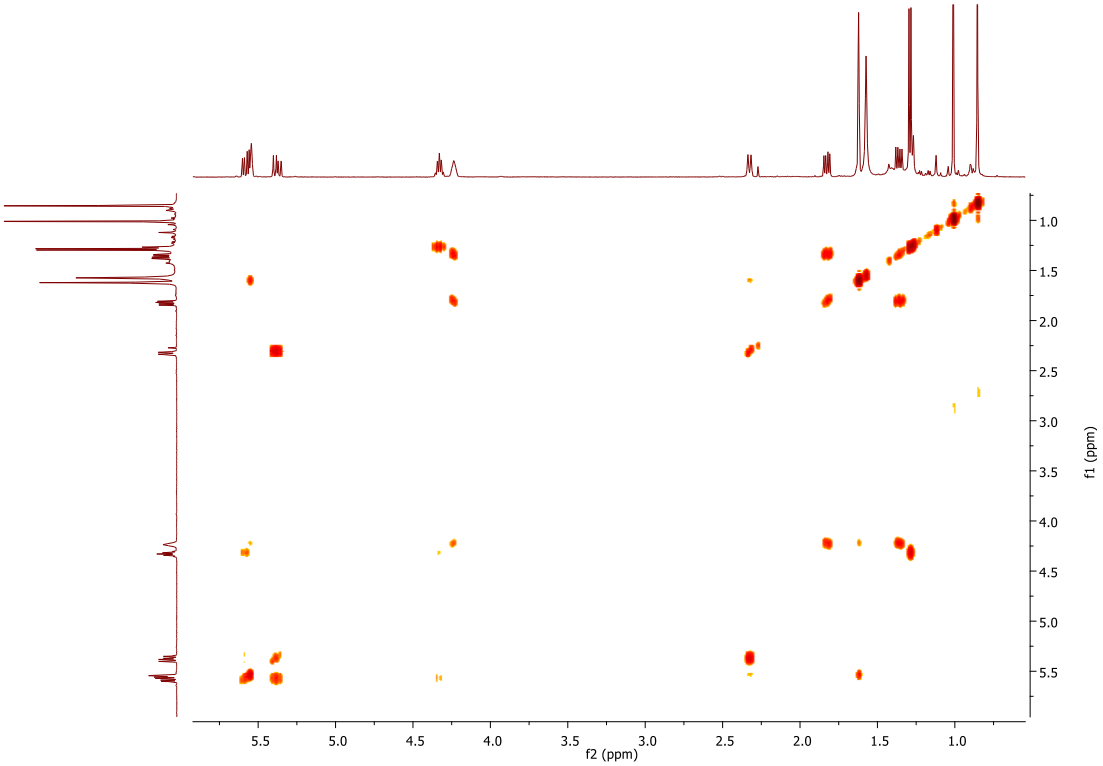

Figure A.18 (e): g-COSY NMR of *cis*-3-hydroxy-α-ionol in $CDCl_3$.

trans-3-hydroxy-α-ionol [109]:

^{1}H NMR (500 MHz, $CDCl_3$) δ 5.55 (dd, *J* = 6.1, 2.5 Hz, 1H, H4), 5.50 (d, *J* = 9.4 Hz, 2H, H8, H7), 4.32 (p, *J* = 6.6 Hz, 1H, H9), 4.25 – 4.19 (m, 1H, H3), 2.08 (d, *J* = 9.0 Hz, 1H, H6), 1.66 – 1.62 (m, *J* = 8.9 Hz, 4H, H2, H10), 1.36 (dd, *J* = 12.6, 9.8 Hz, 1H, H2), 1.31 – 1.27 (m, 3H, H13), 0.94 (s, 3H, H12), 0.86 (d, *J* = 10.5 Hz, 3H, H11). ^{13}C NMR (126 MHz, $CDCl_3$) δ 137.57 (C5), 136.45 (C8), 130.26 (C4), 124.77 (C7), 68.80 (C9), 66.72 (C3), 54.00 (C6), 40.85 (C2), 34.32 (C1), 29.07 (C13), 26.99 (C12), 23.61 (C11), 22.43 (C10).

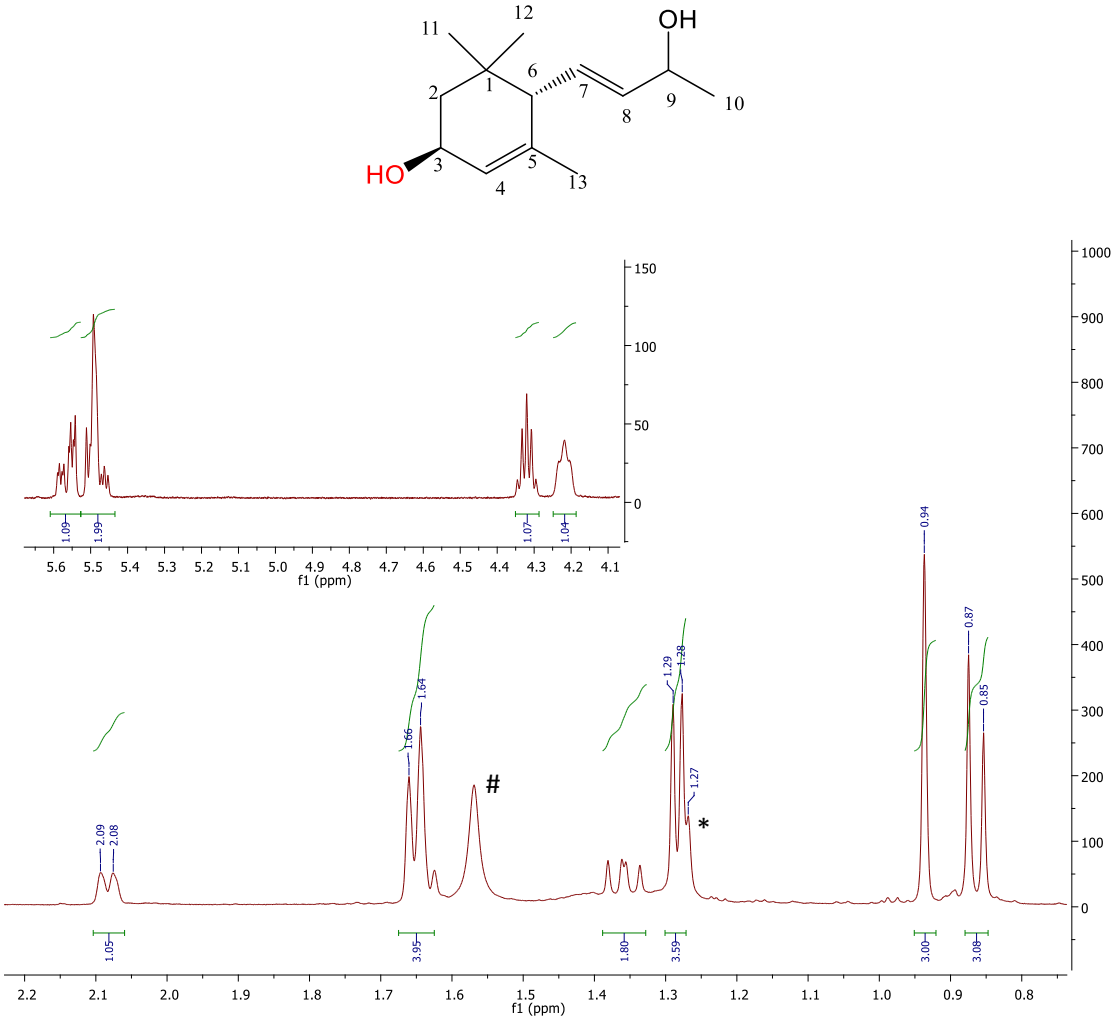

Figure A.19 (a): ^{1}H NMR of *trans*-3-hydroxy-α-ionol in $CDCl_3$. Impurity (*), H_2O (#). Signal for H7 is partially visible at 5.55 ppm and partly hidden behind the signal for H8. Signal for H2 is partly visible at 1.63 ppm and partly hidden behind the signal for H10. The signal for H11 is seen as a doublet in the ^{1}H NMR of substrate as well.

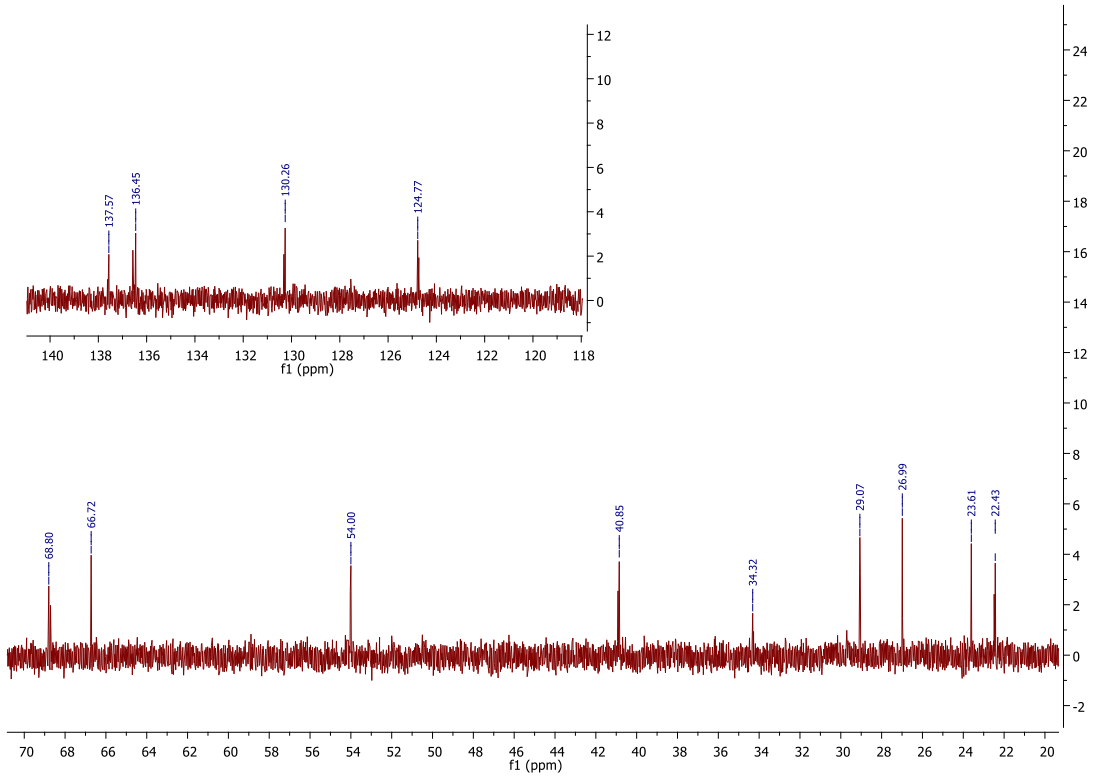

Figure A.19 (b): ^{13}C NMR of *trans*-3-hydroxy-α-ionol in $CDCl_3$, along with some impurities.

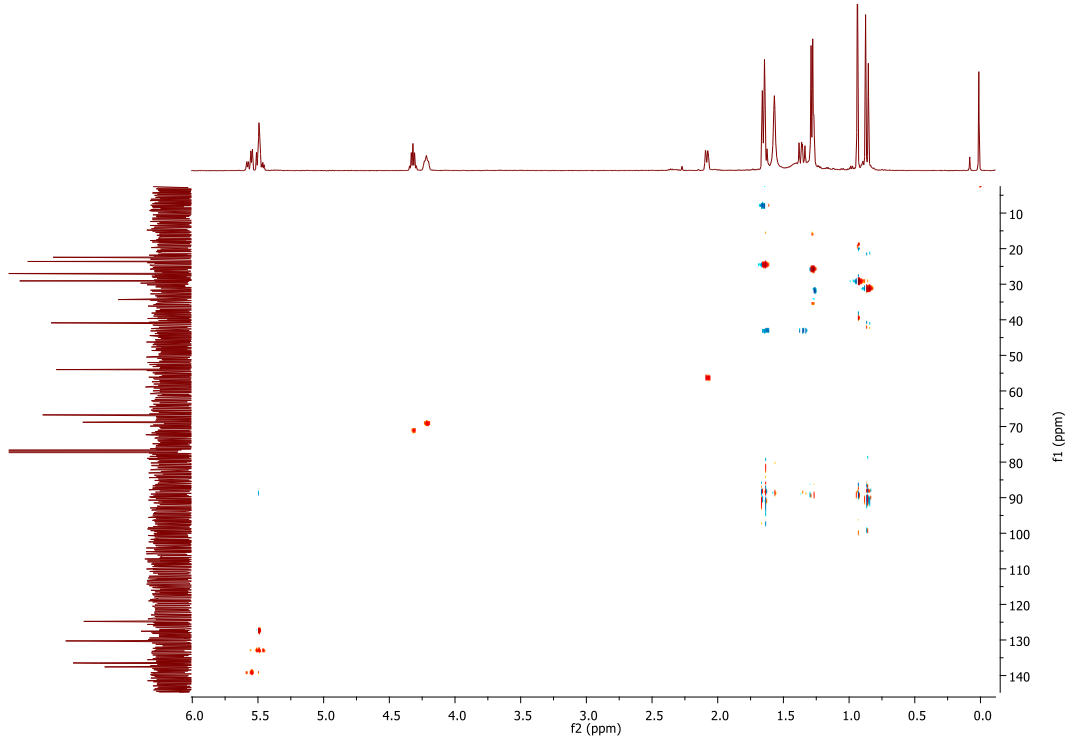

Figure A.19 (c): HSQC NMR of *trans*-3-hydroxy-α-ionol in $CDCl_3$.

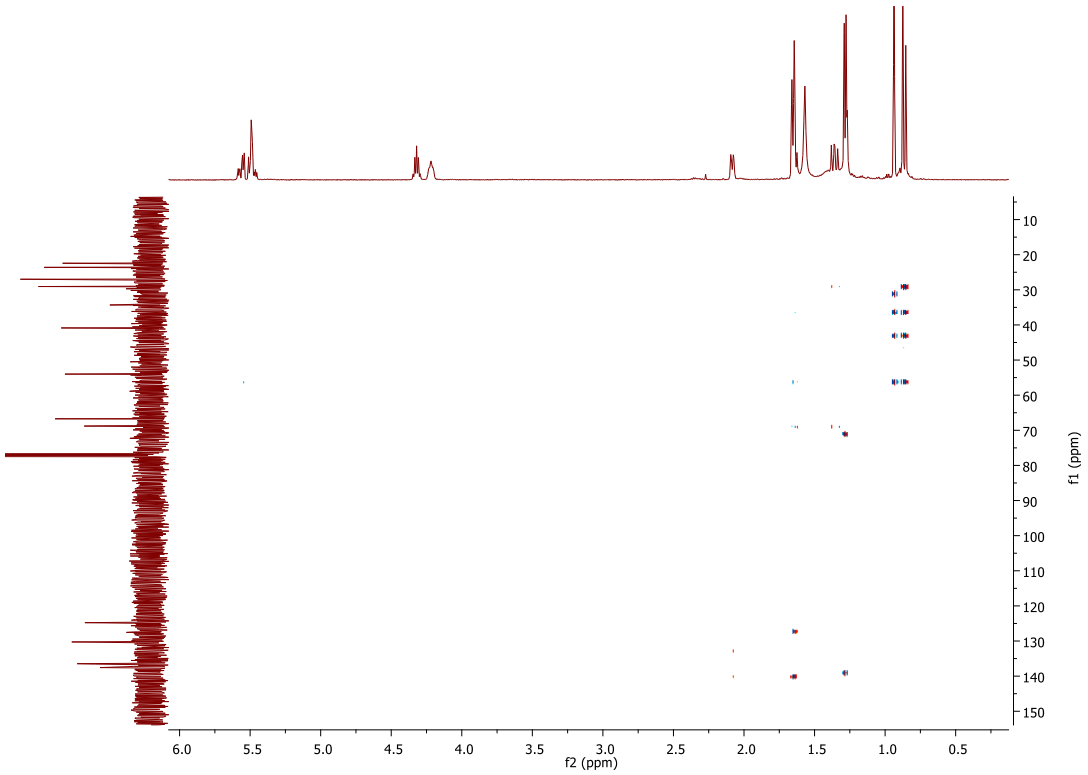

Figure A.19 (d): HMBC NMR of *trans*-3-hydroxy-α-ionol in $CDCl_3$.

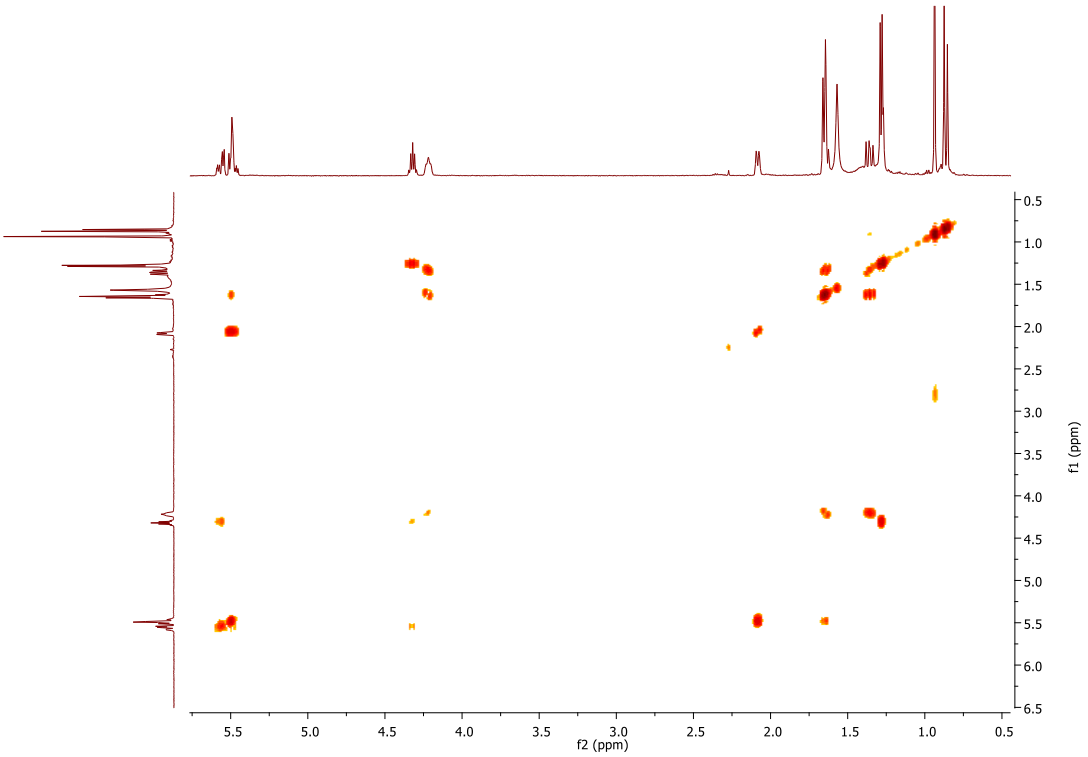

Figure A.19 (e): g-COSY NMR of *trans*-3-hydroxy-α-ionol in $CDCl_3$.

MS analysis of α-ionone substrate (m/z = 192.250 AMU)

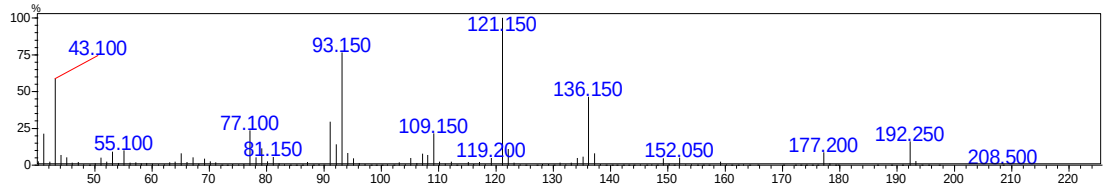

MS analysis of *trans*-3-hydroxy-α-ionone (m/z=208.250; Δm/z = +16 AMU)

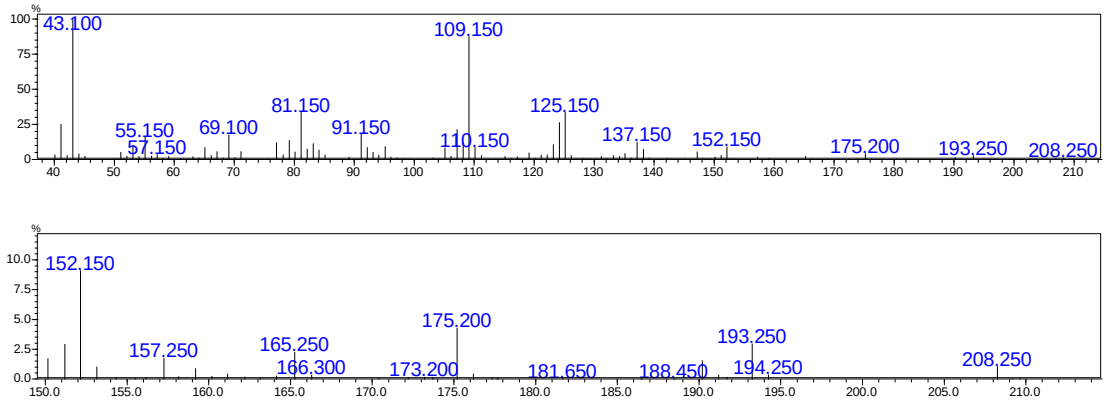

MS analysis of *cis*-3-hydroxy-α-ionone at (m/z=208.250 AMU; Δm/z = +16 AMU)

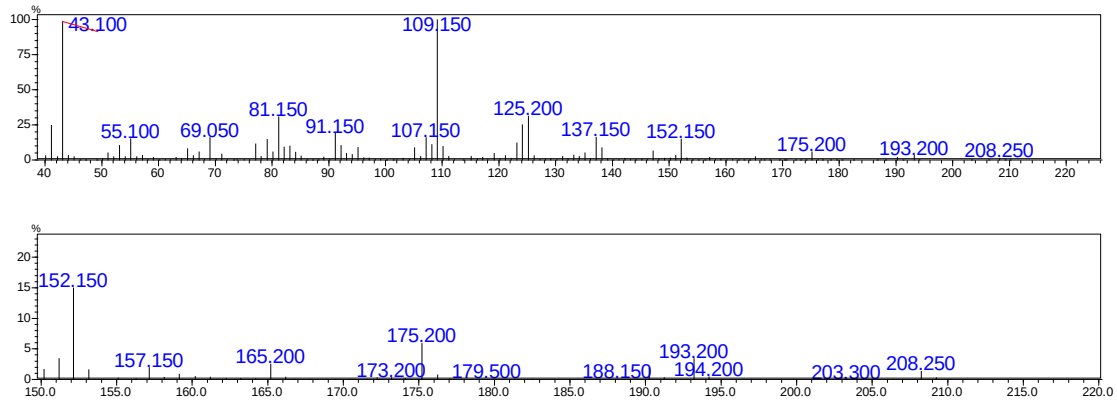

MS analysis of *trans*-3-oxo-α-ionone (m/z = 206.250 AMU; Δm/z = +14 AMU)

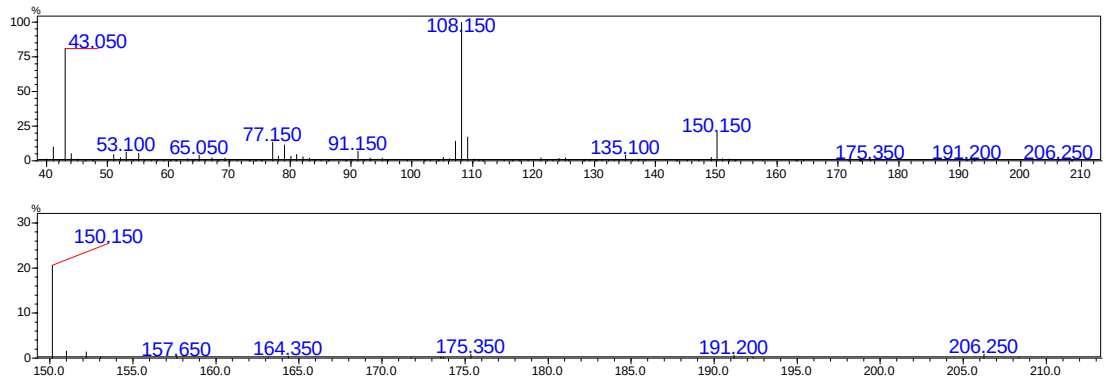

Figure A.20: MS data for the *In vitro* turnover of α-ionone with M82L-CYP101C1.

MS analysis of β-ionone substrate (m/z = 192.250 AMU)

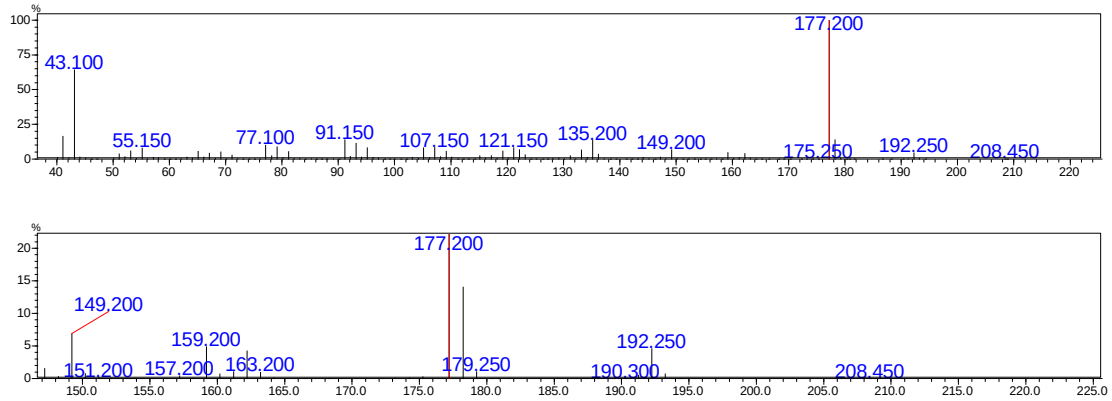

MS analysis of 4-hydroxy-β-ionone (m/z=208.250 AMU; Δm/z = +16 AMU)

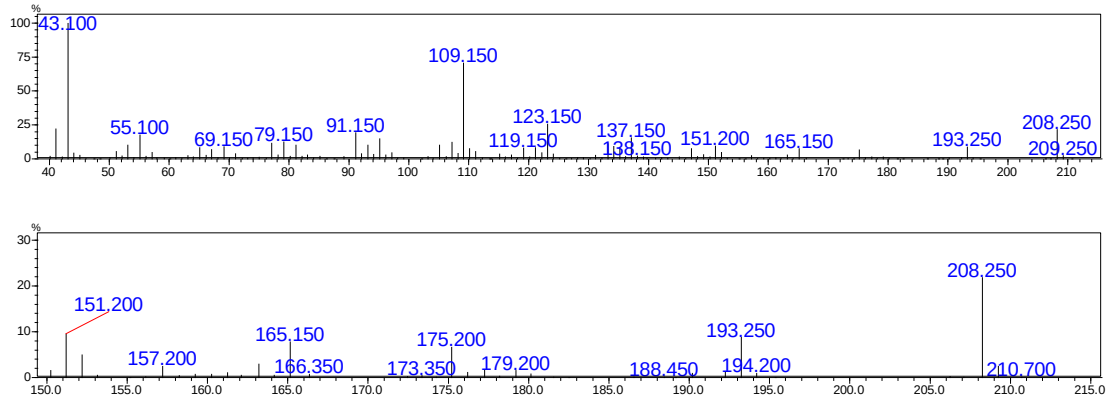

MS analysis of 3-hydroxy-β-ionone (m/z=208.200 AMU; Δm/z = +16 AMU)

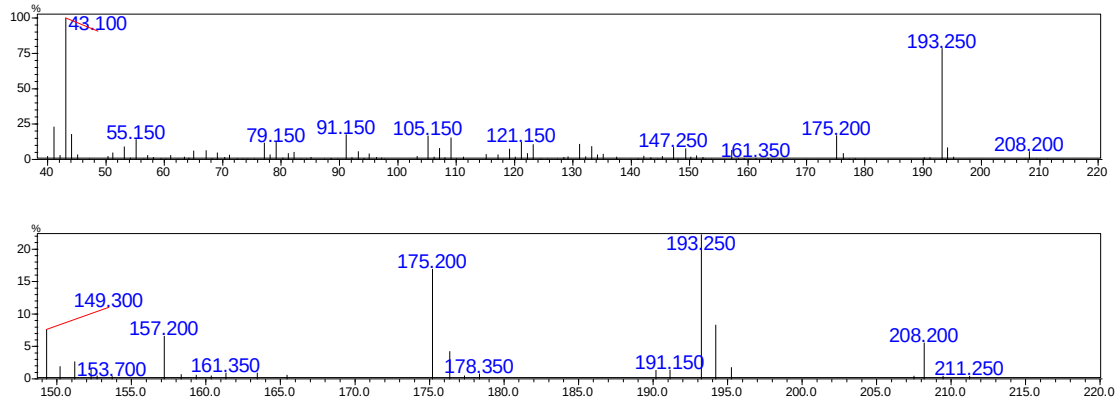

MS analysis of 3,4-dihydroxy-β-ionone** (m/z=206.000 AMU; Δm/z = +14 AMU)

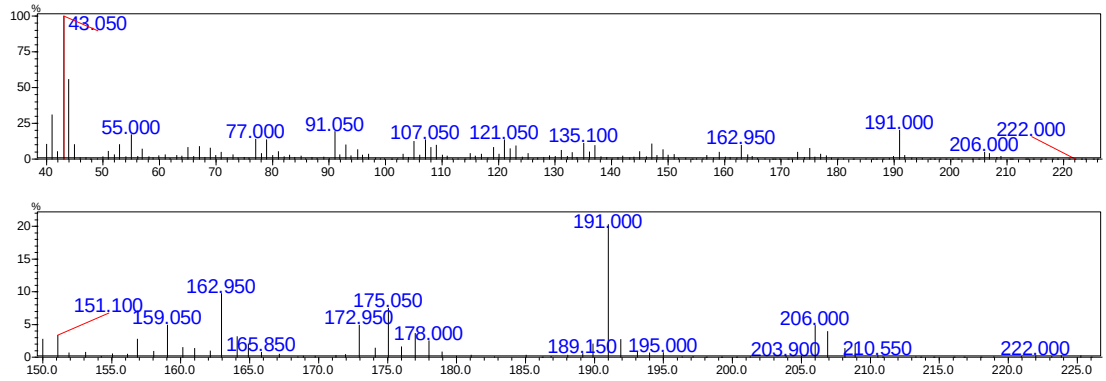

** The expected mass for this product is 224 AMU. The peak at 206.000 AMU suggests that there is a loss of 18 AMU, which signifies the loss of a H_2O molecule from the substrate. The retention time on GC and chemical shifts of the hydroxylated site in ^1H NMR confirms the product as 3,4-dihydroxy-β-ionone.

Figure A.21: MS data for the *In vitro* turnover of β-ionone with M82L-CYP101C1.

MS analysis of α-damascone substrate (m/z = 192.200 AMU)

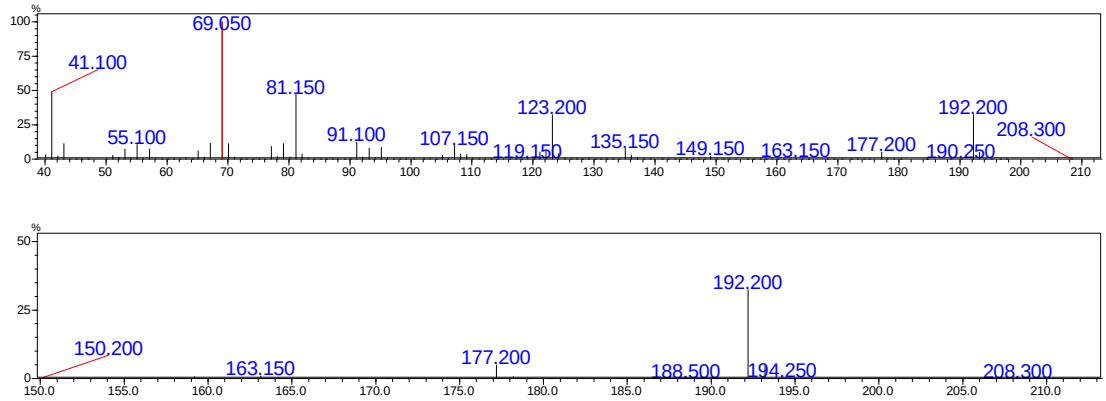

MS analysis of *cis*-3-hydroxy-α-damascone (m/z=208.200 AMU; Δm/z = +16 AMU)

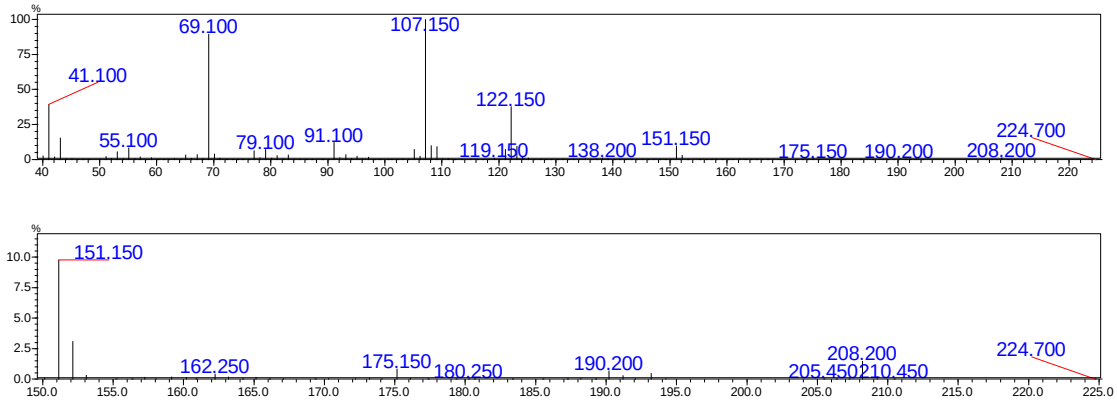

MS analysis of *trans*-3-hydroxy-α-damascone (m/z=208.200 AMU; Δm/z = +16 AMU)

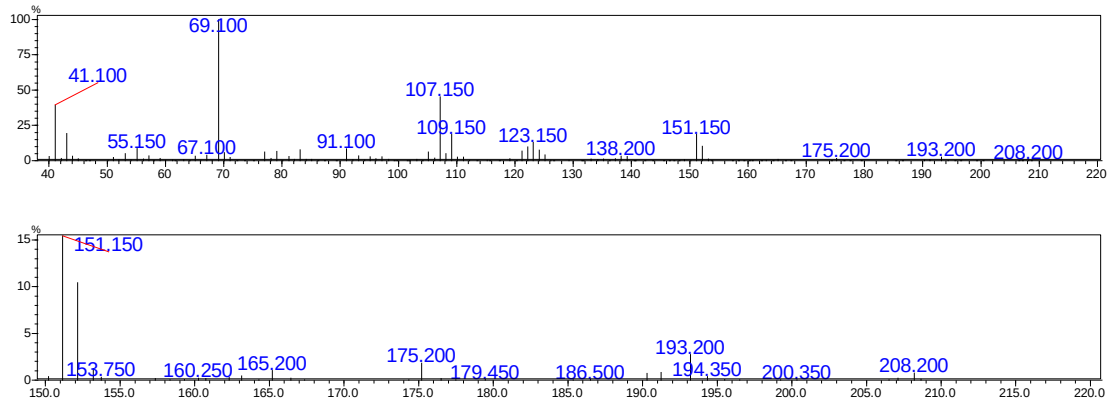

MS analysis of 3-oxo-α-damascone (m/z = 206.250 AMU; Δm/z = +14 AMU)

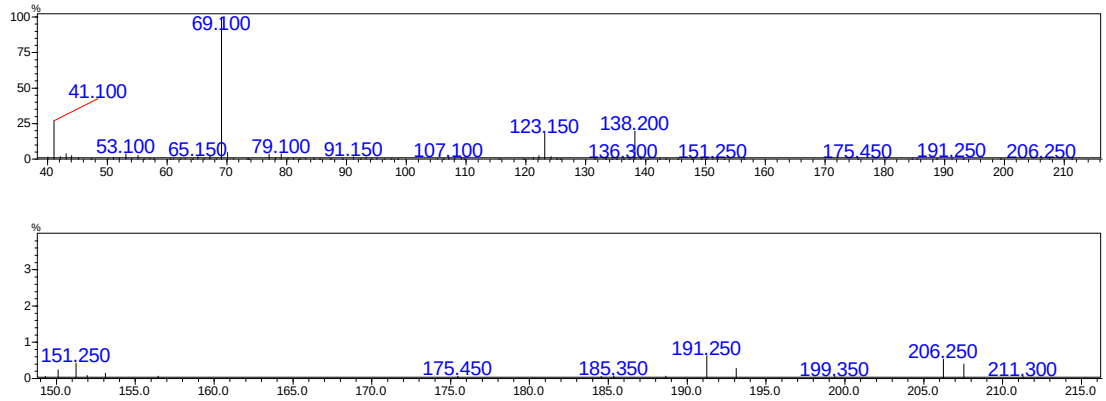

Figure A.22: GC-MS data for the *In vitro* turnover of α-damascone with M82L-CYP101C1

MS analysis of β-damascone substrate (m/z = 192.200 AMU)

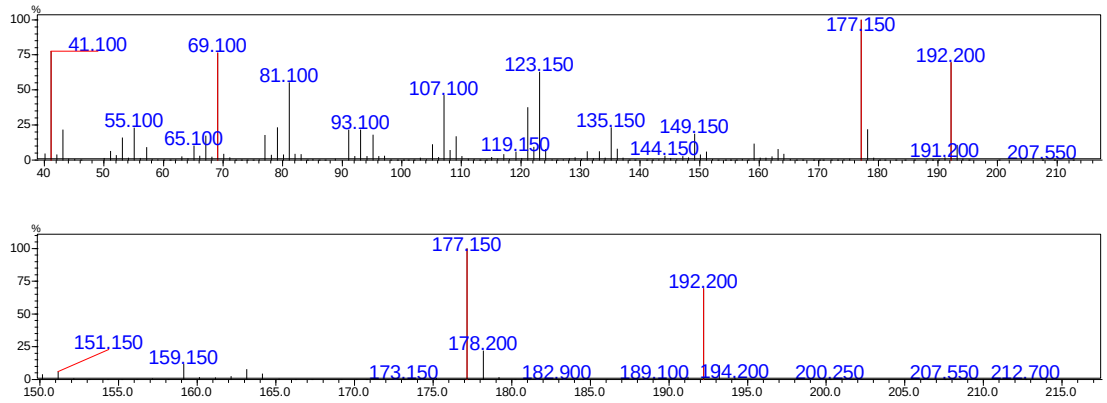

MS analysis of 4-hydroxy-β-damascone (m/z=208.05; Δm/z = +16 AMU)

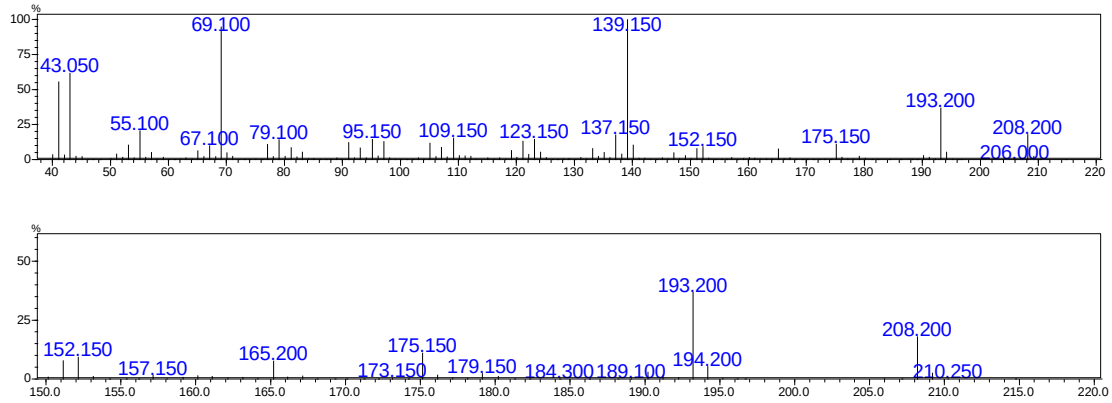

MS analysis of 3-hydroxy-β-damascone (m/z=208.05; Δm/z = +16 AMU)

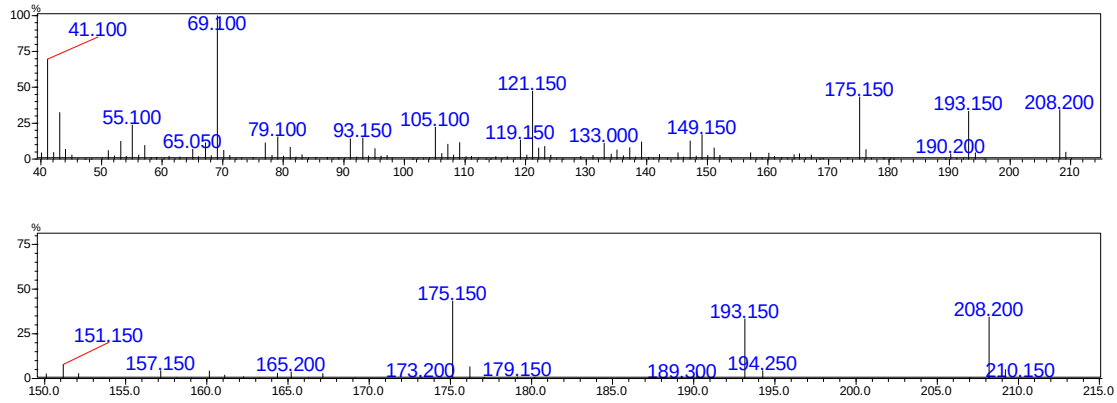

MS analysis of 3,4-dihydroxy-β-damascone** (m/z = 206.950 AMU; Δm/z = +14 AMU)

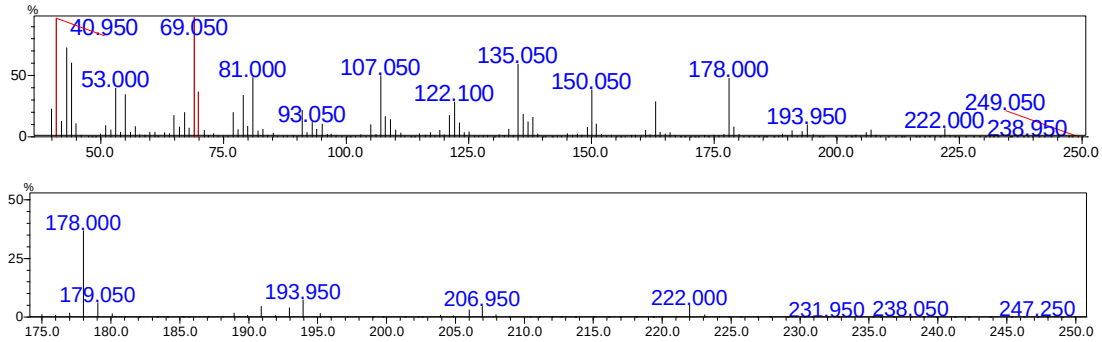

** The expected mass for this product is 224 AMU. The peak at 206.950 AMU suggests that there is a loss of 18 AMU, which signifies the loss of a H_2O molecule from the substrate. The retention time on GC confirms the product as 3,4-dihydroxy-β-damascone.

Figure A.23: GC-MS data for the *In vitro* turnover of β-damascone with M82L-CYP101C1.

MS analysis of δ-damascone substrate (m/z = 192.250 AMU)

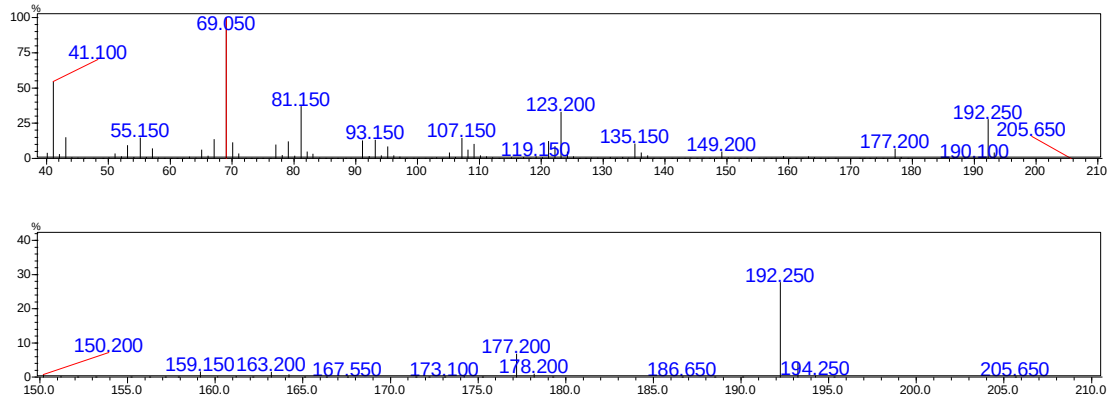

MS analysis of 3,4-epoxy-δ-damascone (m/z=208.200 AMU; Δm/z = +16 AMU)

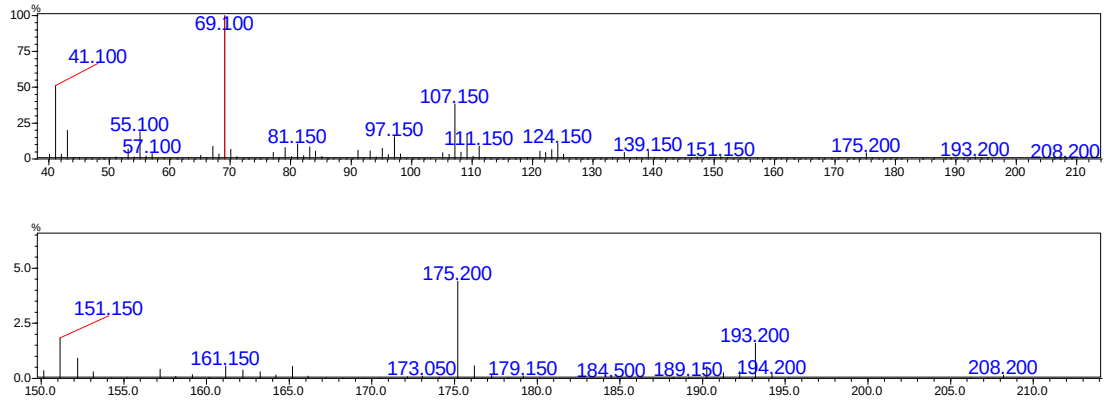

MS analysis of 2-hydroxy-δ-damascone (m/z=208.05; Δm/z = +16 AMU)

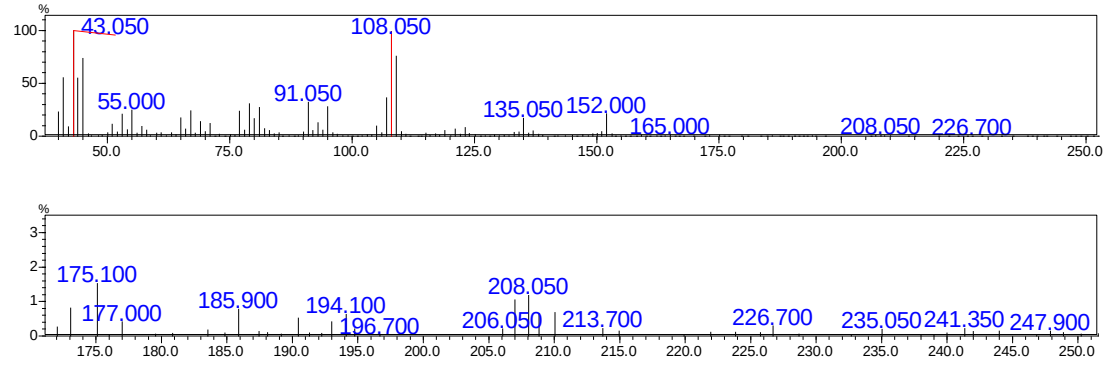

Figure A.24: GC-MS data for the *In vitro* turnover of δ-damascone with M82L-CYP101C1.

MS analysis of α-ionol substrate (m/z = 194.00 AMU)

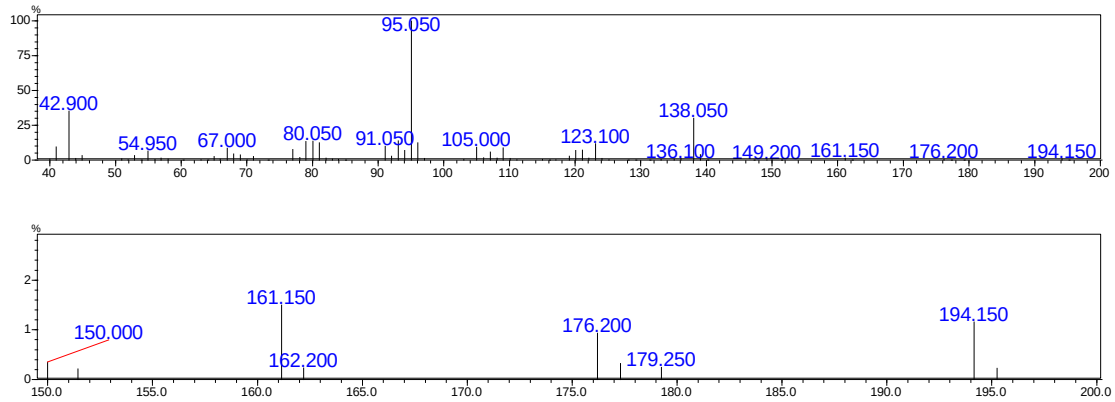

MS analysis of *cis*-3-hydroxy-α-ionol (m/z=210.650 AMU; Δm/z = +16 AMU)

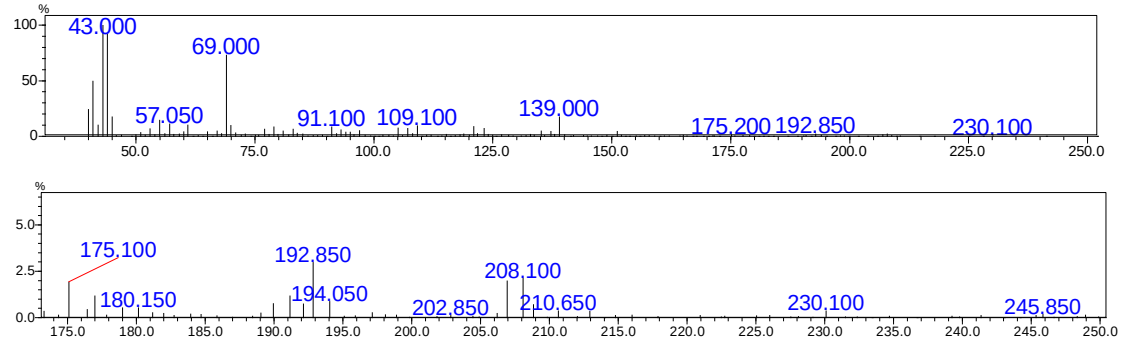

MS analysis of *trans*-3-hydroxy-α-ionol (m/z=210.200 AMU; Δm/z = +16 AMU)

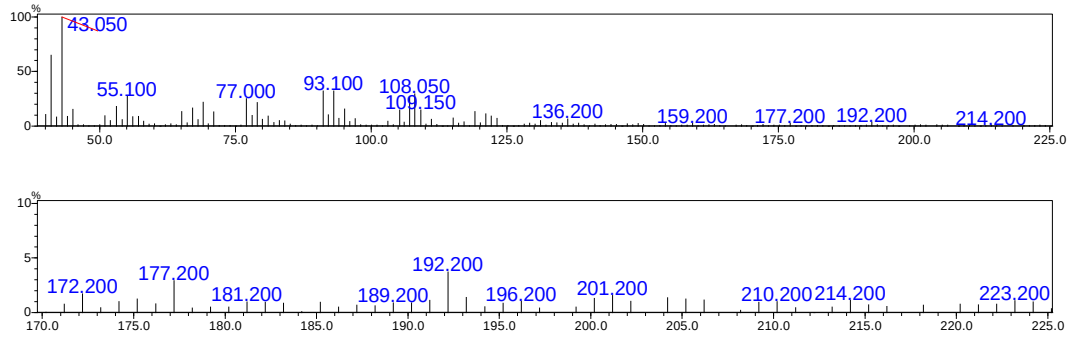

MS analysis of 3-oxo-α-ionol (m/z=208.100 AMU; Δm/z = +14 AMU)

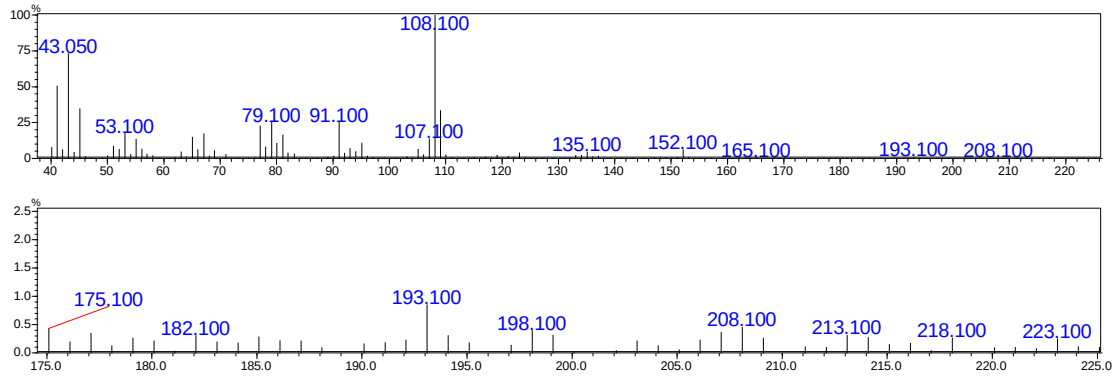

Figure A.25: GC-MS data for the *In vitro* turnover of α-ionol with M82L-CYP101C1.

MS analysis of β-ionol substrate (m/z = 194.100 AMU)

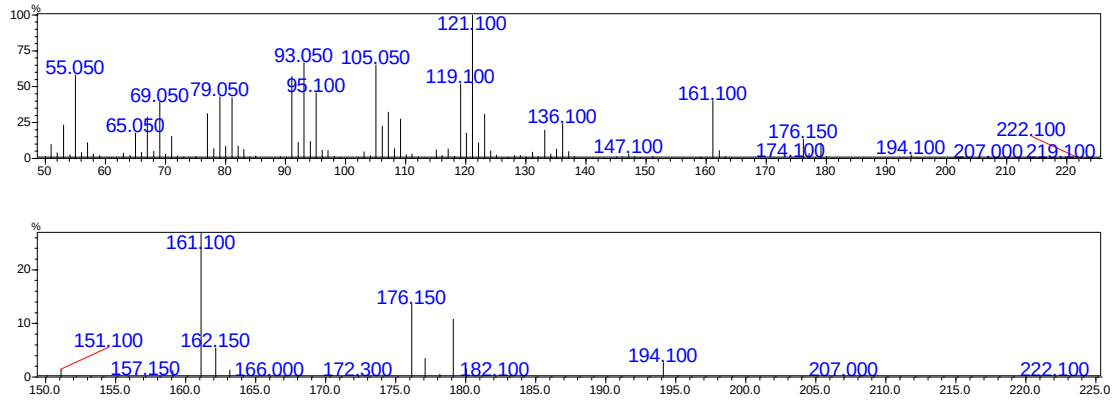

MS analysis of 4-hydroxy-β-ionol (m/z = 210.05AMU; Δm/z = +16 AMU)

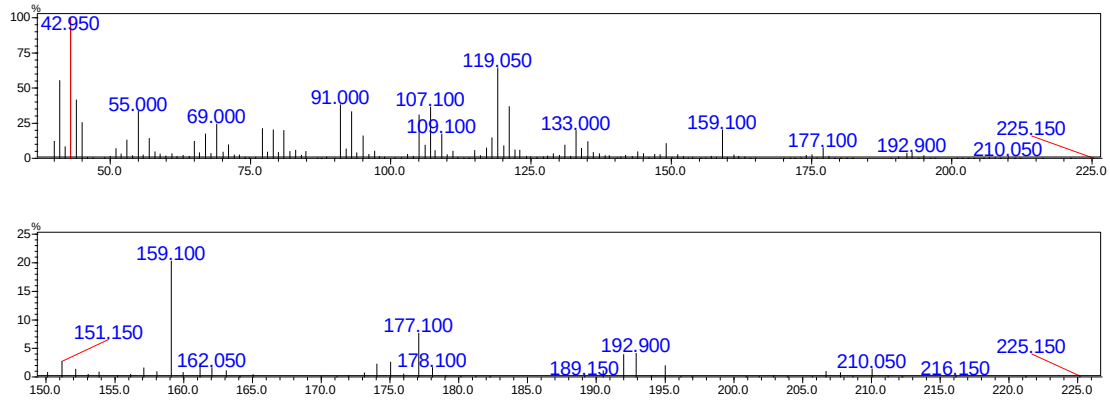

MS analysis of 3-hydroxy-β-ionol (m/z = 210.100 AMU; Δm/z = +16 AMU)

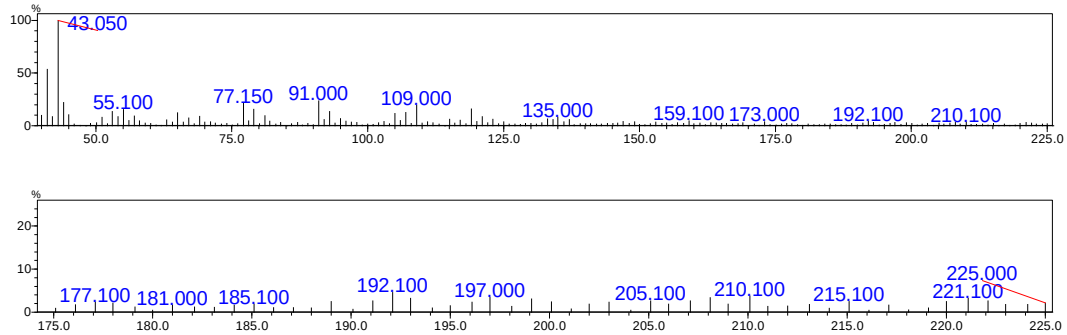

MS analysis of β-ionol product (m/z = 208.050 AMU; Δm/z = +14)

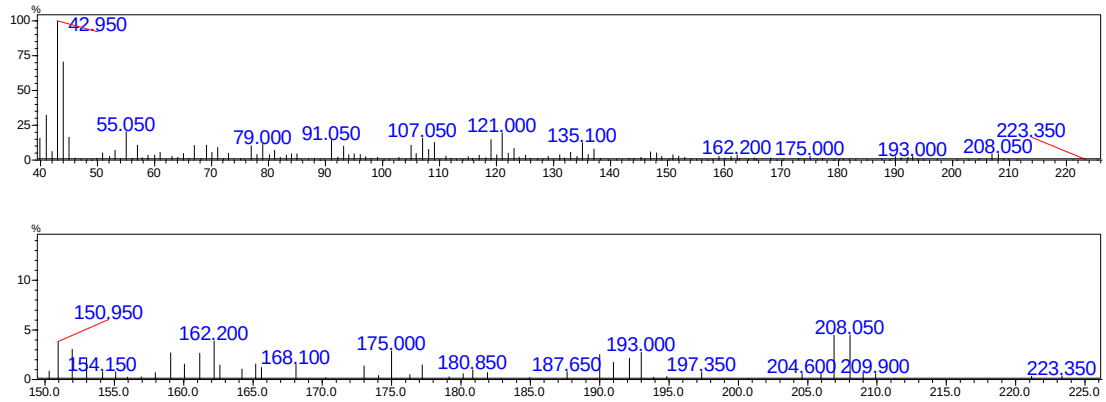

Figure A.26: GC-MS data for the *In vitro* turnover of β-ionol with M82L-CYP101C1.

GC-FID data for *in vivo* turnovers

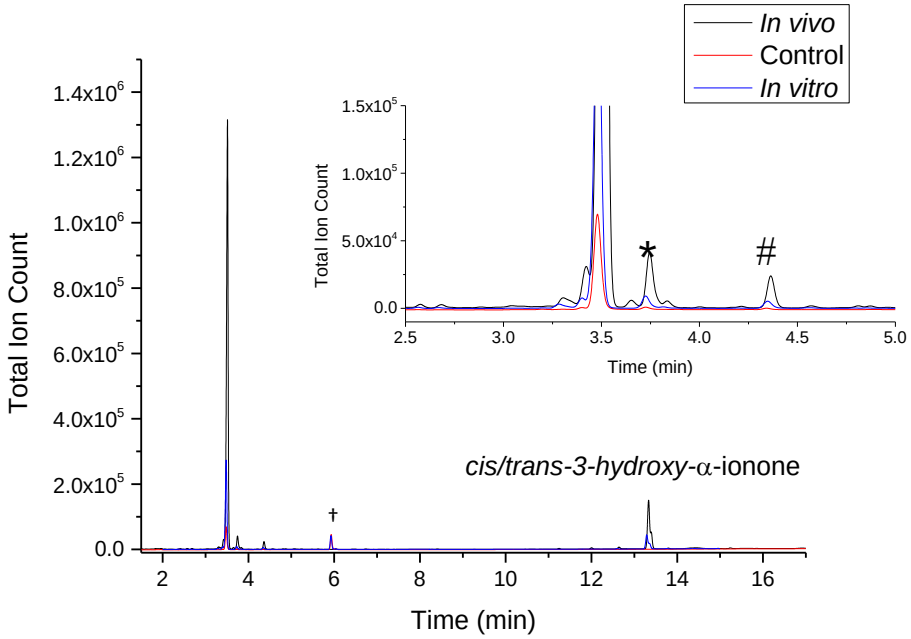

Figure A.27: GC-FID analysis of the *in vitro* turnover (blue) and *in vivo* turnover (black) of WT-CYP101C1 with α-ionone in comparison to substrate control (red). Internal standard (†), impurity of α-ionol (*), impurity of β-ionone (#).

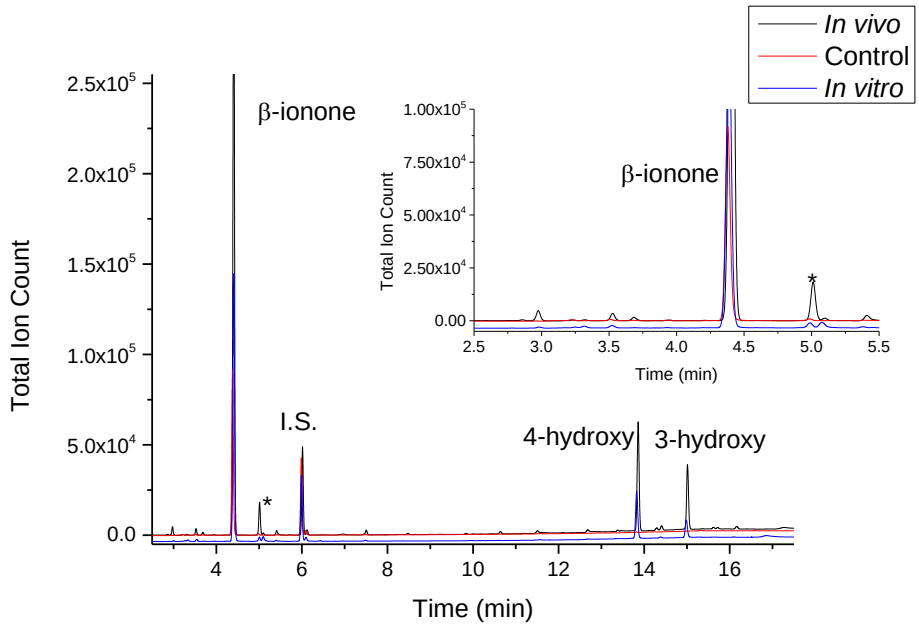

Figure A.28: GC-FID data for whole-cell (black) turnover of β-ionone with WT-CYP101C1 in comparison to substrate control (red) and *in vitro* turnover (blue) of β-ionone with WT-CYP101C1. Impurity from substrate or extraction (*), internal standard (I.S.).

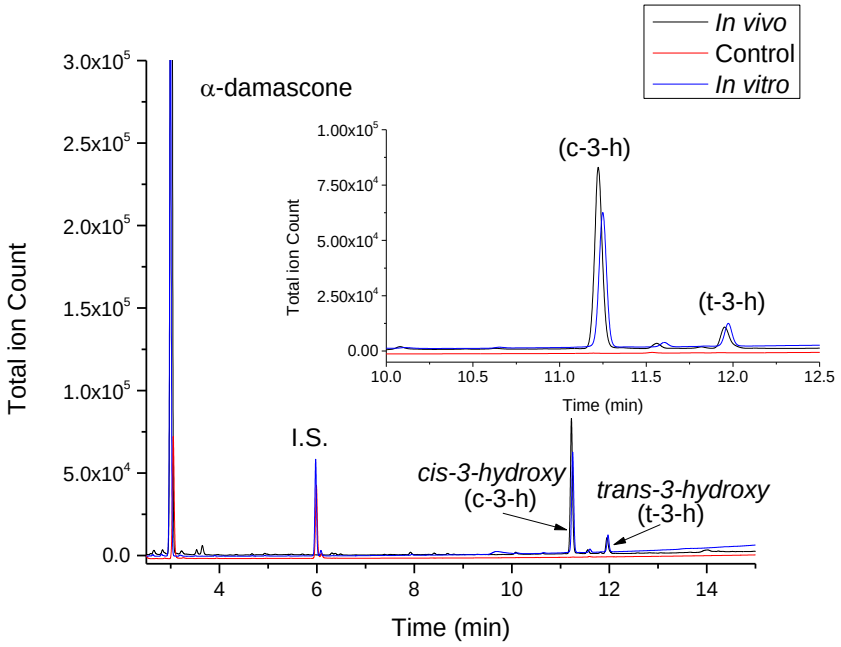

Figure A.29: GC-FID data for whole-cell (black) turnover of α-damascone with WT-CYP101C1 in comparison to substrate control (red) and *in vitro* turnover (blue) of α-damascone with WT-CYP101C1. Internal standard (I.S.).

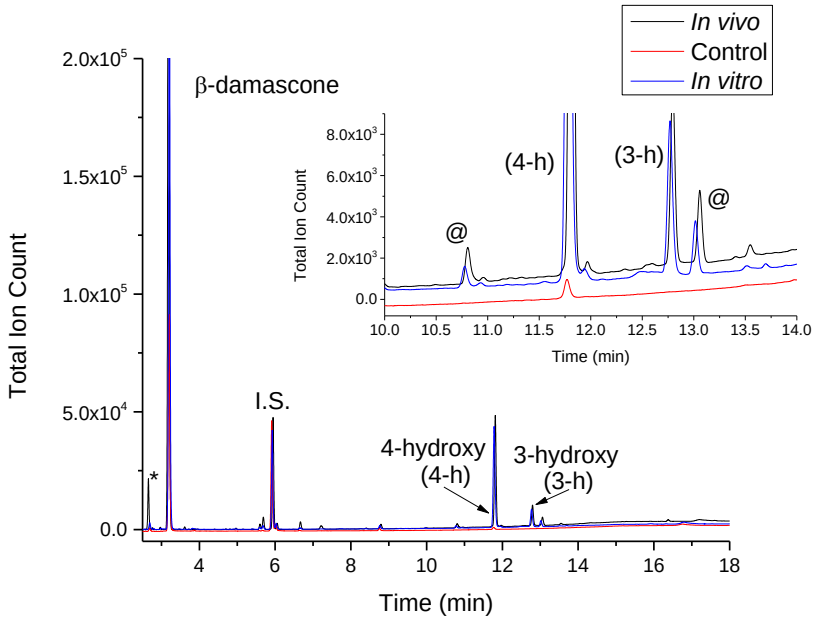

Figure A.30: GC-FID data for whole-cell (black) turnover of β-damascone with WT-CYP101C1 in comparison to substrate control (red) and *in vitro* turnover (blue) of β-damascone with WT-CYP101C1. Oxidation of impurity (#), unidentified product (@), impurity from substrate or extraction (*), Internal standard (I.S.).

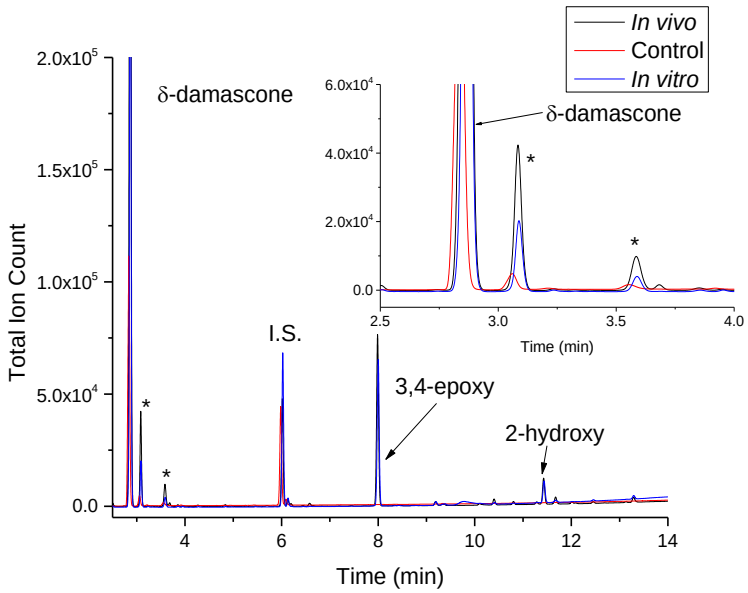

Figure A.31: GC-FID data for whole-cell (black) turnover of δ-damascone with WT-CYP101C1 in comparison to substrate control (red) and *in vitro* turnover (blue) of δ-damascone with WT-CYP101C1. Impurity from substrate or extraction (*), Internal standard (I.S.).

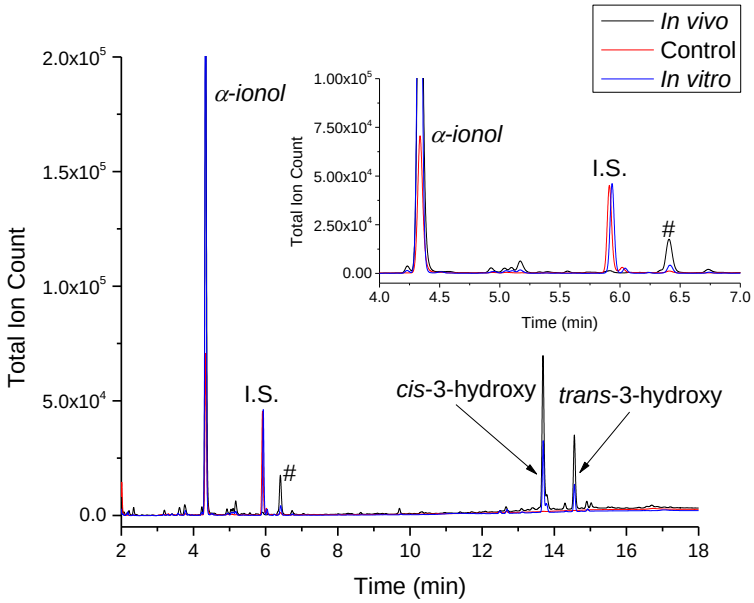

Figure A.32: GC-FID data for whole-cell (black) turnover of α-ionol with WT-CYP101C1 in comparison to substrate control (red) and *in vitro* turnover (blue) of α-ionol with WT-CYP101C1. Internal standard (I.S.), unidentified impurity (#).

Appendix-B (Data for Chapter-4)

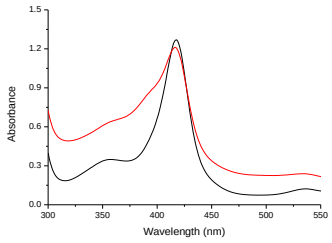

Undecanoic-δ -lactone

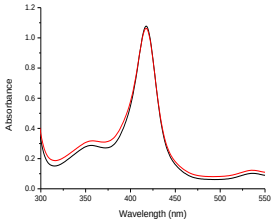

N-(*t*-butyl)decahydro isoquinone-3-carboxamide

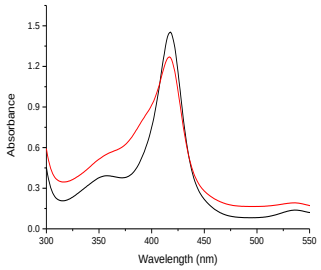

4-(*trans*-4-propylcyclohexyl) cyclohexanone

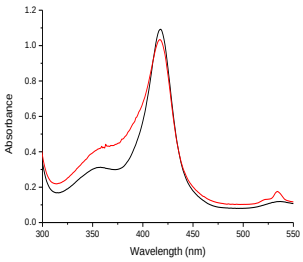

4-Heptyl cyclohexanone

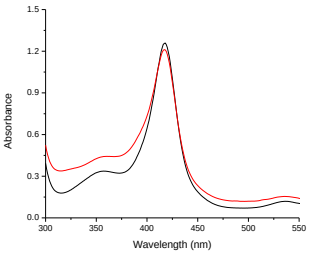

Homosalate

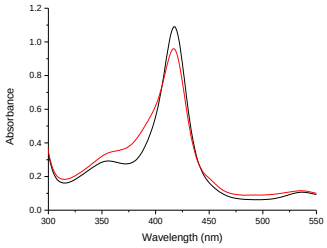

Icaridin

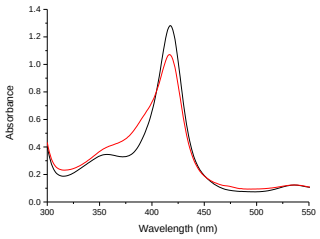

Octahydro-2H-chromen-2-one

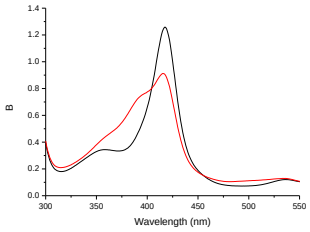

Parthenolide

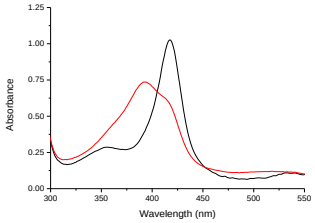

Cyclopentadecanone

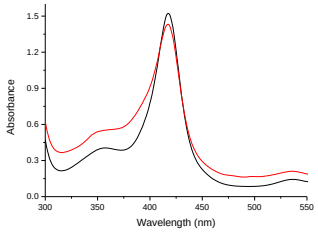

trans [4-butyl-1,1' bicyclohexyl]-4-one

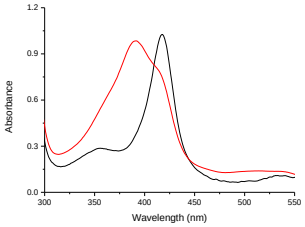

p-Tolyl acetate

Figure B.1: Spin state shift of selected substrates with CYP101B1.

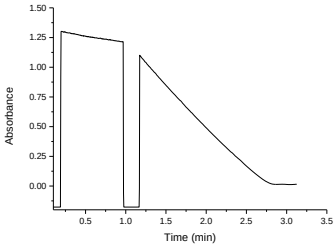

trans-1-Decalone

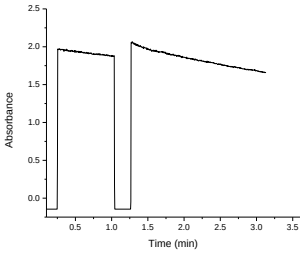

2-Cyclohexyl cyclohexanone

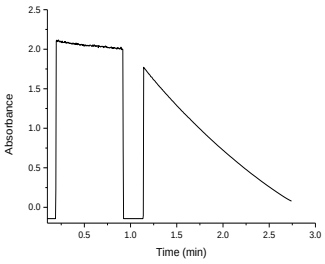

2-Decalone

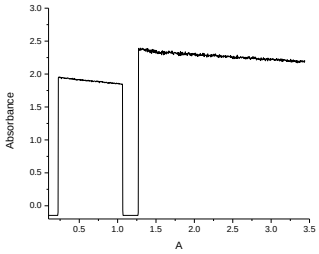

4-(*trans*-4-propylcyclohexyl) cyclohexanone

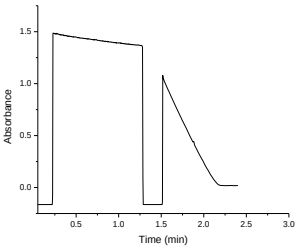

Dihydroactinidiolide

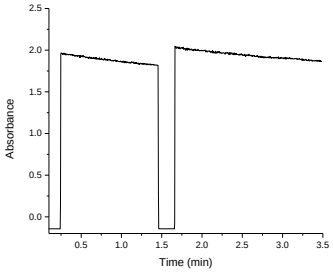

4-Heptyl cyclohexanone

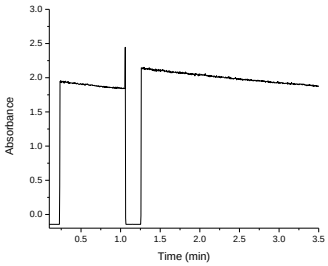

Homosalate

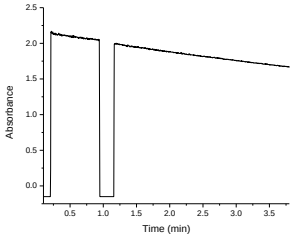

Icaridin

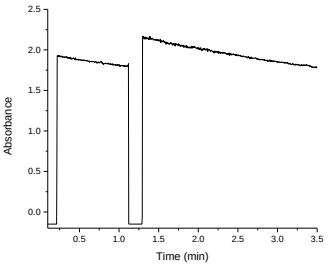

Muscone

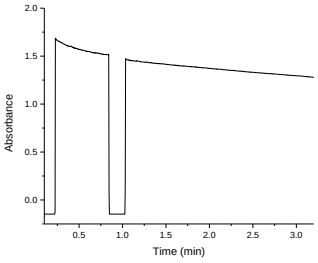

N(*t*-butyl)decahydro isoquinone-3-carboxamide

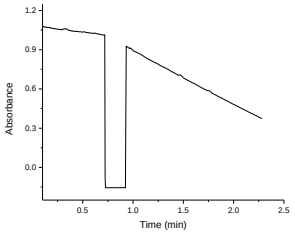

Octahydro-2H-Chromen-2-one

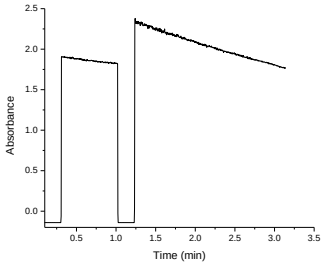

Cyclopentadecanone

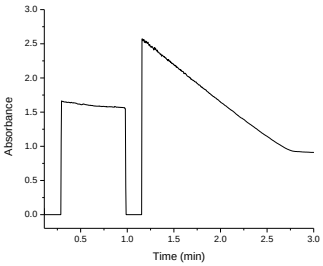

Oxacyclotridecan-2-one

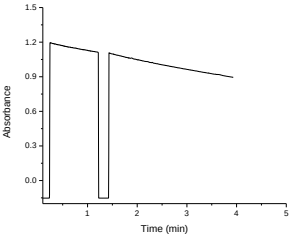

Parthenolide

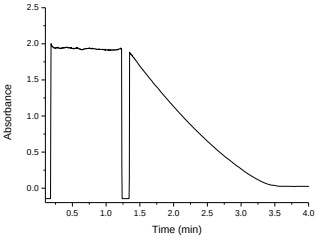

p-tolyl acetate

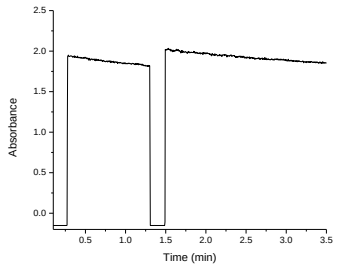

trans [4-butyl-1,1' bicyclohexyl]-4-one

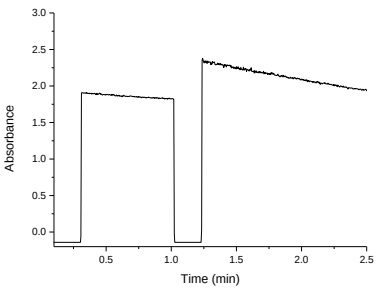

Cyclopentadecanone

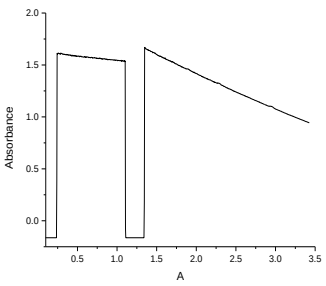

Undecanoic-δ-lactone

Figure B.2: *In vitro* turnover of selected substrate at 340nm with CYP101B1.

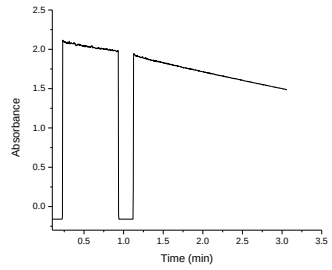

trans-1-Decalone

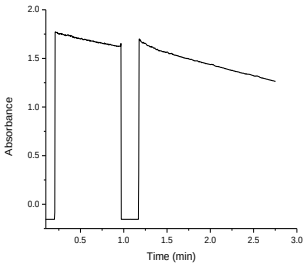

2-Cyclohexyl cyclohexanone

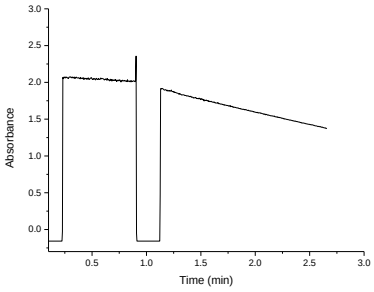

2-Decalone

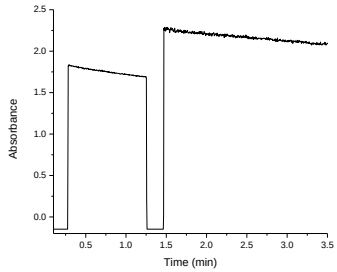

4-(*trans*-4-propylcyclohexyl) cyclohexanone

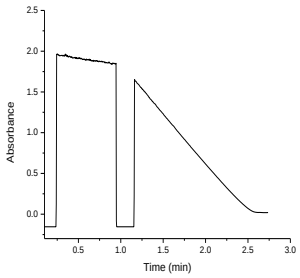

Dihydroactinidiolide

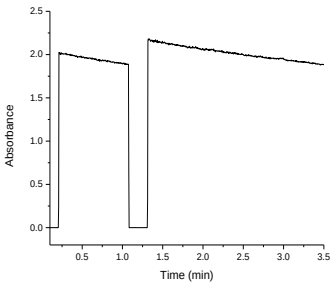

4-Heptyl cyclohexanone

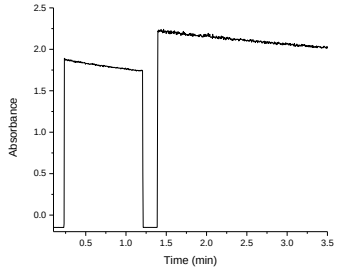

Homosalate

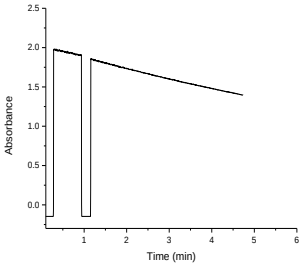

Icaridin

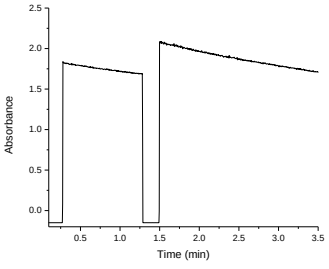

Muscone

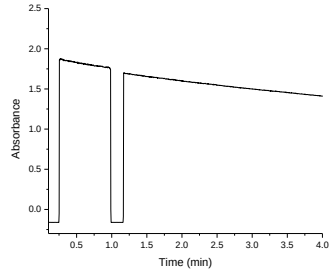

N(*t*-butyl)decahydro isoquinone-3-carboxamide

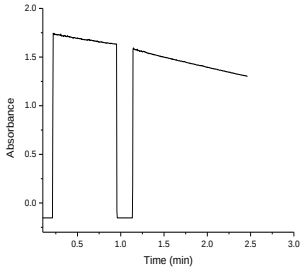

Octahydro-2H-Chromen-2-one

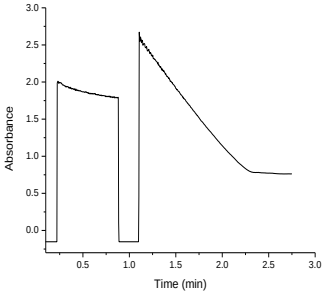

Oxacyclotridecan-2-one

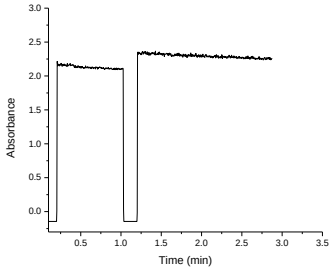

trans [4-butyl-1,1' bicyclohexyl]-4-one

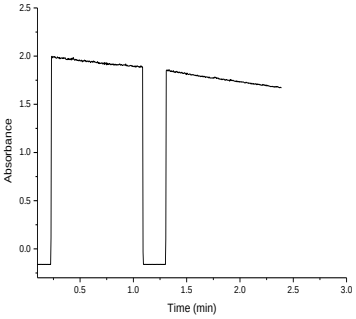

Parthenolide

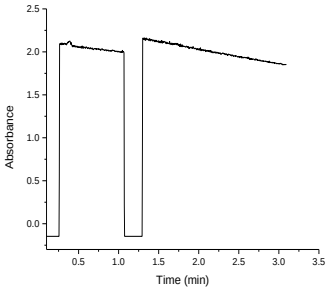

Undecanoic-δ-lactone

Figure B.3: *In vitro* turnover of selected substrate at 340nm with CYP101C1.

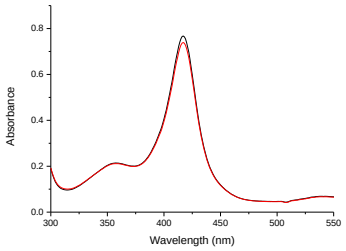

N(*t*-butyl)decahydro isoquinone-3-carboxamide

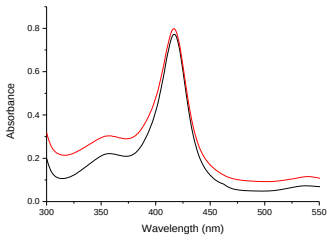

Undecanoic-δ-lactone

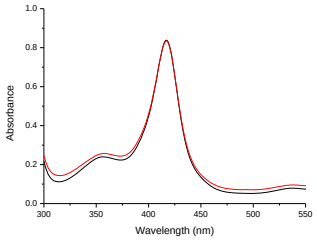

4-(*trans*-4-propylcyclohexyl) cyclohexanone

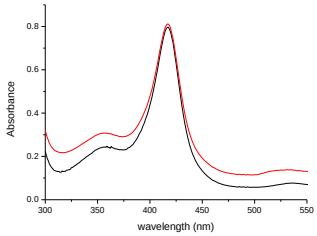

4-Heptylcyclohexanone

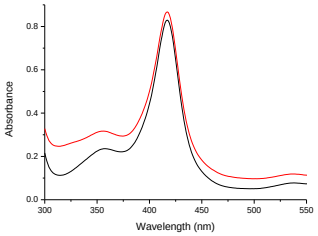

Homosalate

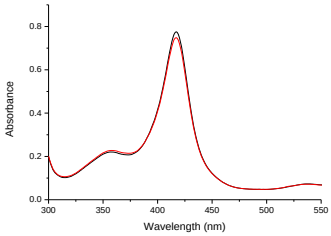

Icaridin

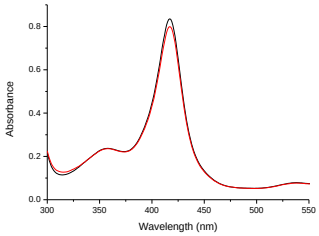

Octahydro-2H-chromen-2-one

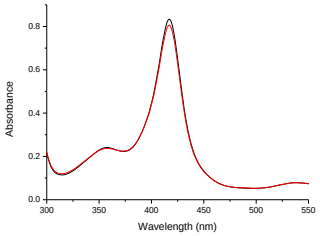

Parthenolide

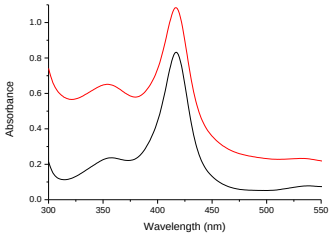

Plasmodione

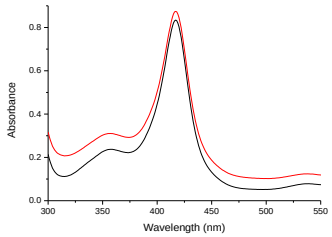

trans [4-butyl-1,1' bicyclohexyl]-4-one

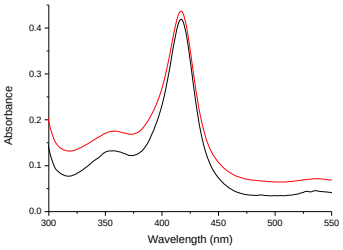

Cyclopentadecanone

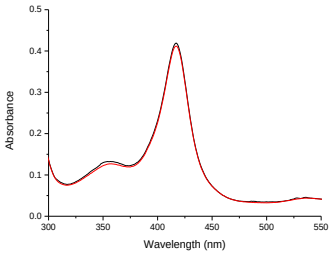

p-tolyl acetate

Figure B.4: Spin state shift of selected substrate with CYP101C1.

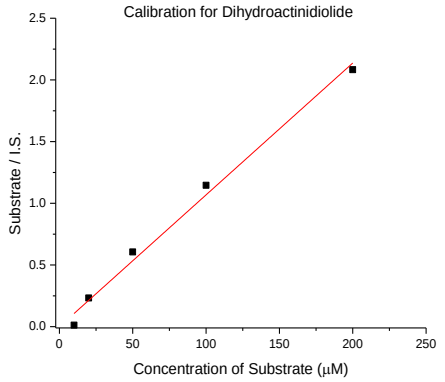

$R^2 = 0.9915$; m = 0.0107

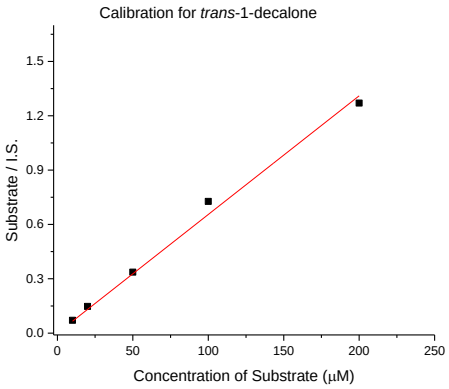

$R^2 = 0.996$; m= 0.0065

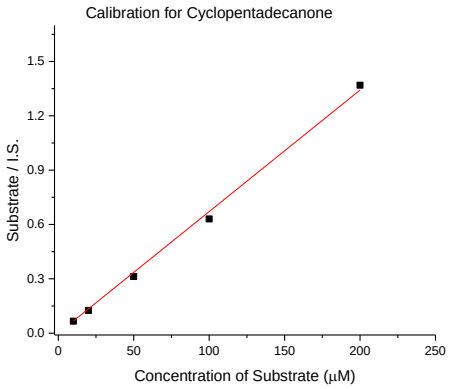

$R^2 = 0.998$; m = 0.0067

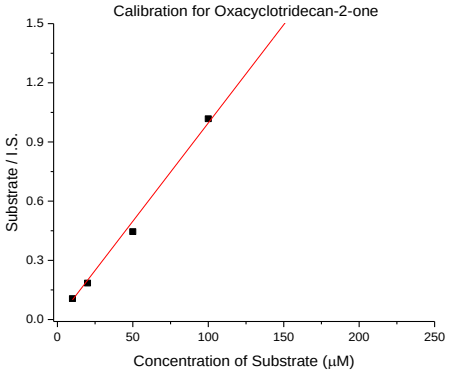

$R^2 = 0.9991$; m = 0.00996

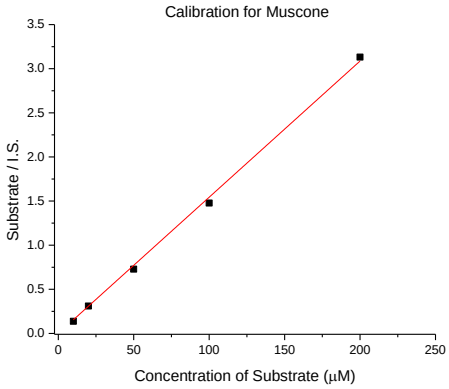

$R^2 = 0.999$; m = 0.0154

Figure B.5: Calibration data for selected substrates. The slope (m) of the calibration curve is used to determine the amount of metabolites generated in turnovers.

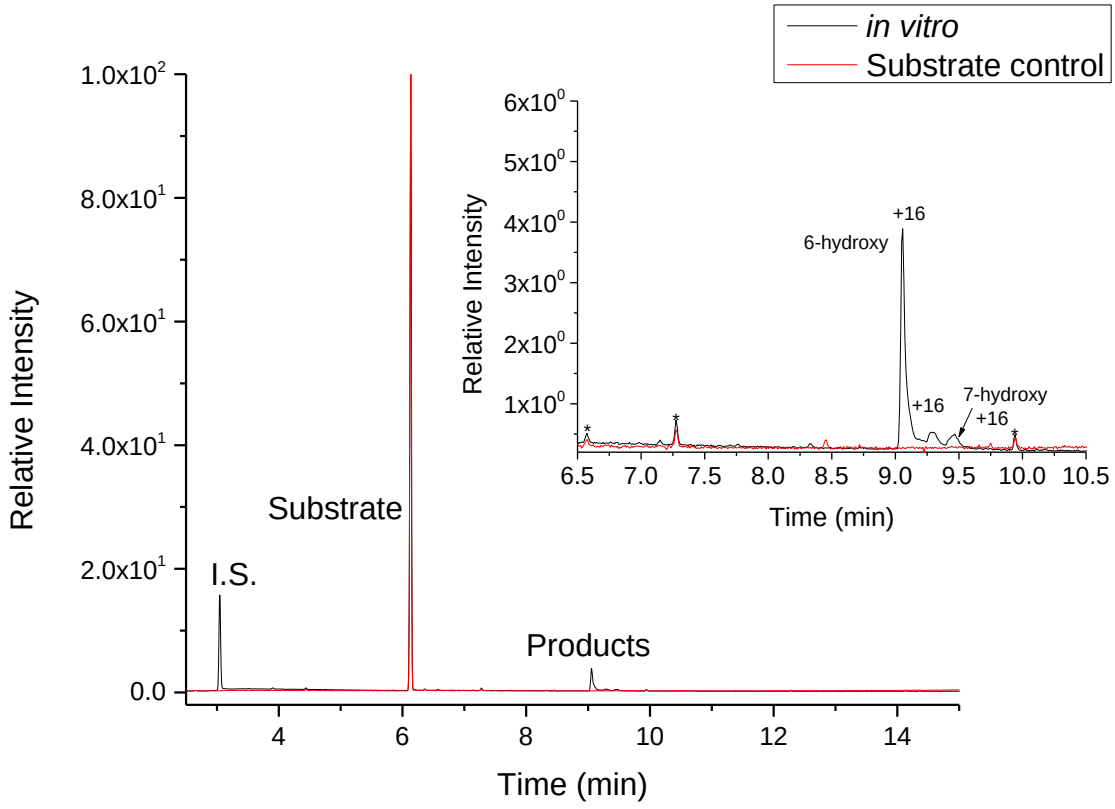

Figure B.6 (a): GCMS analysis of *In vitro* turnover of *trans*-1-decalone by CYP101B1 (black) with substrate control (red). Internal standard is marked as (I.S.). Impurities are marked as (*).

MS analysis of *trans*-1-Decalone substrate at t_R = 6.13 min (m/z = 152.1 AMU)

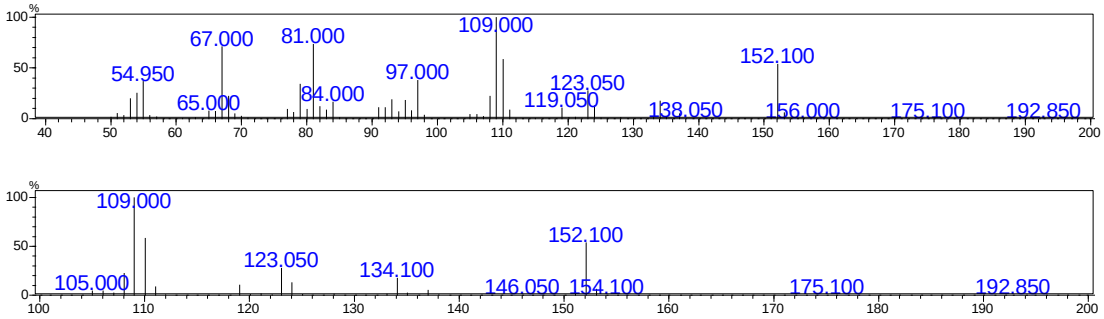

MS analysis of 6-hydroxy-*trans*-1-decalone (t_R = 9.06 min) (m/z = 168.050 AMU, Δm/z = + 16 AMU)

Reported m/z = 168.0, 150.0 and 97.1 [107].

Experimental m/z = 168.050, 150.050, 135.050, 121.050, 111.050, 97.000, 93.050, 81.000, 68.050, 67.000 and 54.950

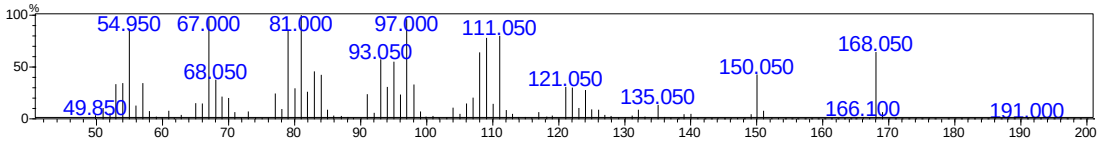

MS analysis of peak at t_R = 9.27 min of *in vitro* oxidation of *trans*-1-decalone by CYP101B1 (m/z = 168.150 AMU, Δm/z = + 16 AMU)

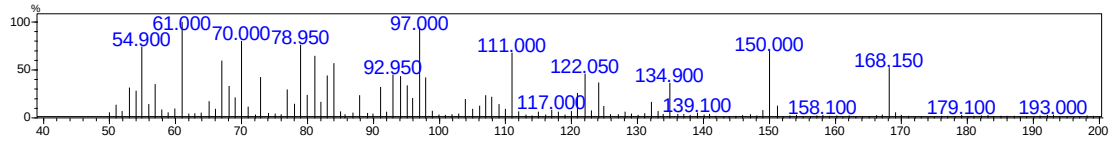

MS analysis of 7-hydroxy-*trans*-1-decalone (t_R = 9.46 min) (m/z = 168.000 AMU, Δm/z = + 16 AMU)

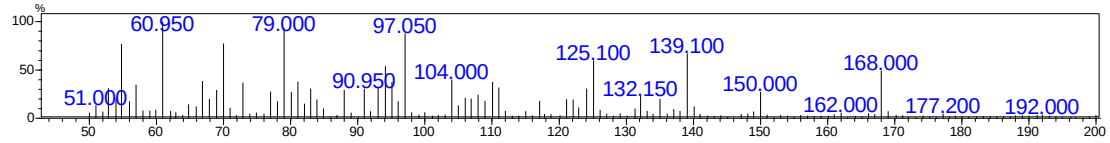

Figure B.6 (b): MS analysis of the substrate and oxidation metabolites generated in *in vitro* turnover of *trans*-1-decalone with CYP101B1.

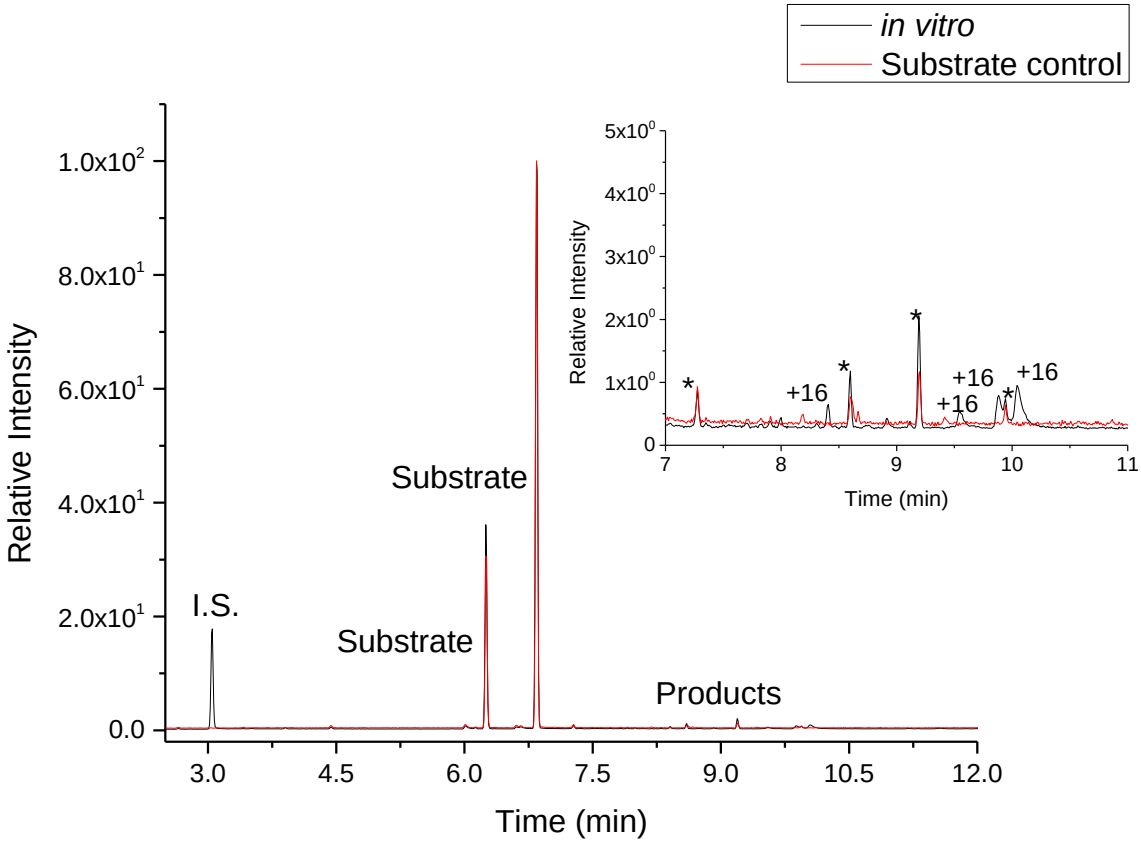

Figure B.7 (a): GCMS analysis of *In vitro* turnover of 2-decalone by CYP101B1 (black) with substrate control (red). Internal standard is marked as (I.S.). Impurities are marked as (*).

MS analysis of 2-decalone substrate at t_R = 6.25 (m/z = 152.1 AMU)

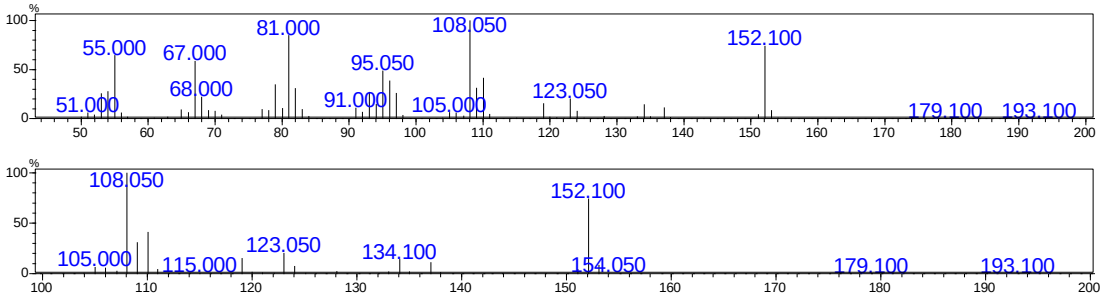

MS analysis of 2-decalone substrate at t_R = 6.85 min (m/z = 152.1 AMU)

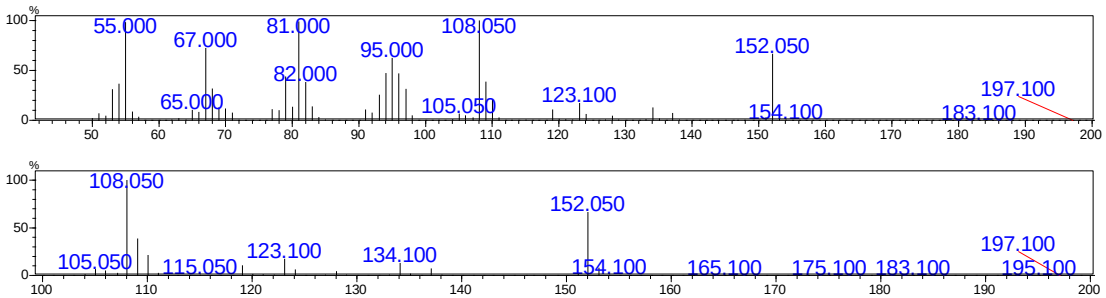

MS analysis of metabolite at t_R=8.40 min (m^+/z = 168.05 AMU; Δm/z = +16 AMU)

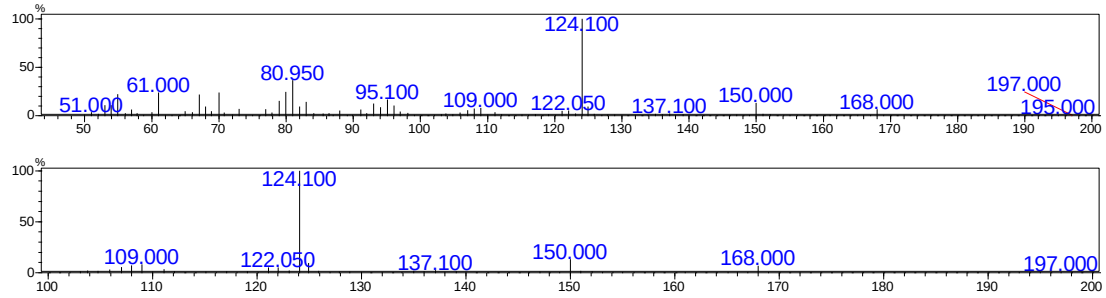

MS analysis of metabolite at t_R=9.53 min (m^+/z = 168.05 AMU; Δm/z = +16 AMU)

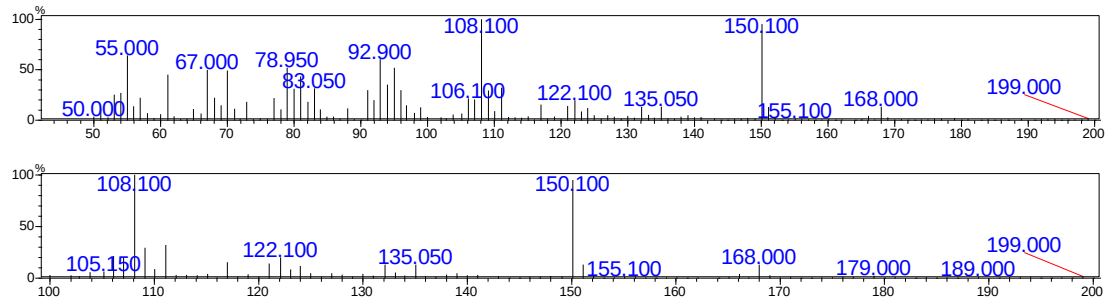

MS analysis of metabolite at t_R=9.86 min (m^+/z = 168.05 AMU; +16 AMU)

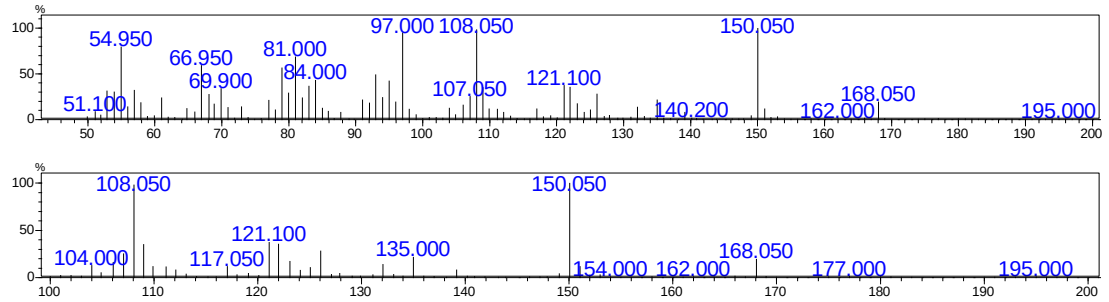

MS analysis of metabolite at t_R=10.02 min (m^+/z = 168.05 AMU; +16 AMU)

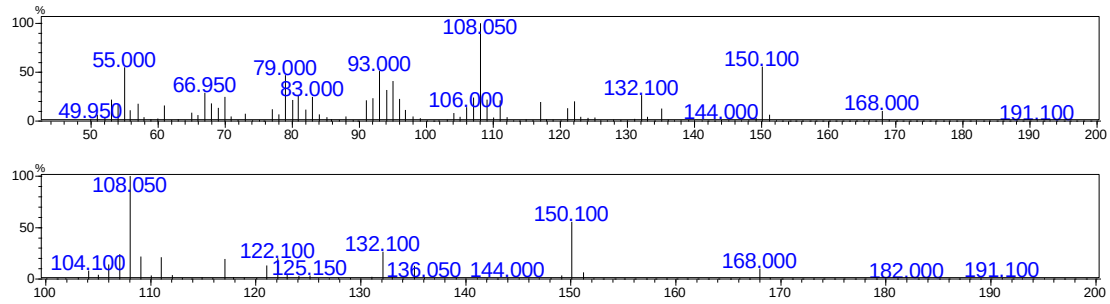

Figure B.7 (b): MS analysis of the substrate and oxidation metabolites generated in *in vitro* turnover of 2-decalone with CYP101B1.

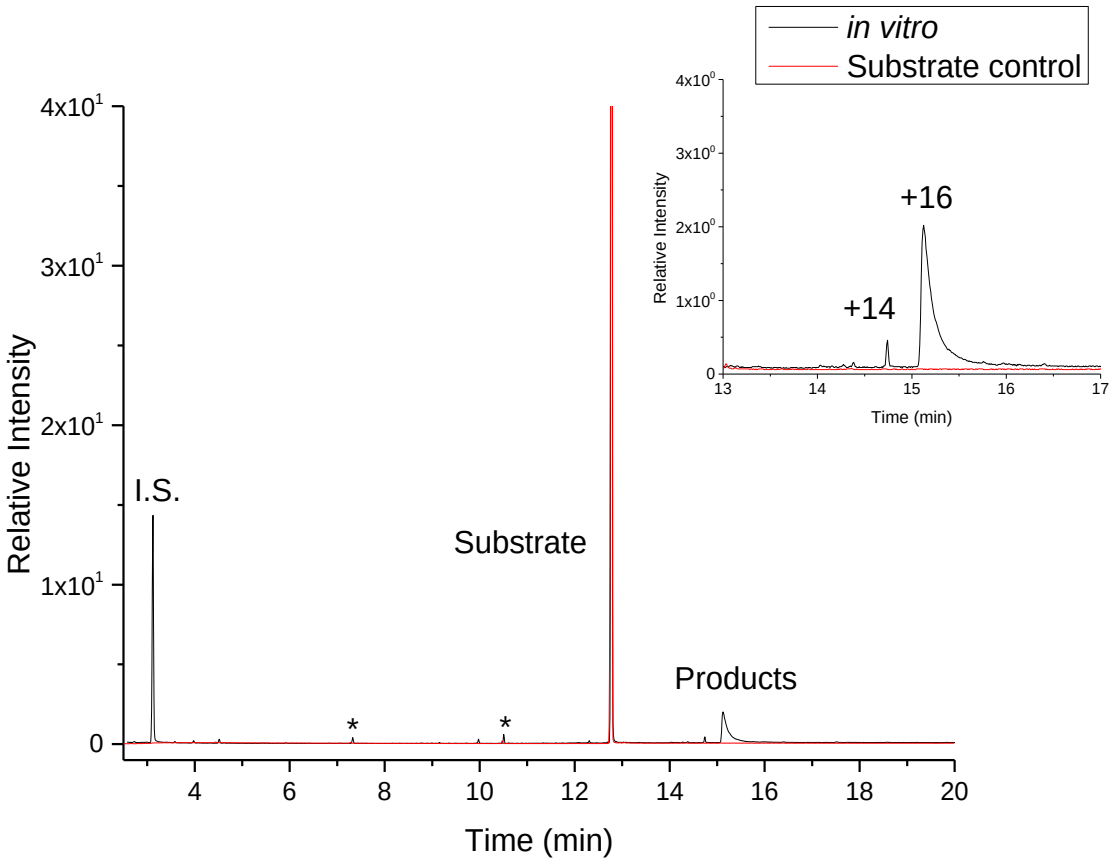

Figure B.8 (a): GCMS analysis of *In vitro* turnover of cyclopentadecanone by CYP101B1 (black) with substrate control (red). Internal standard is marked as (I.S.). Impurities are marked as (*).

MS analysis of cyclopentadecanone substrate at t_R = 12.7 min (m/z = 224.200 AMU)

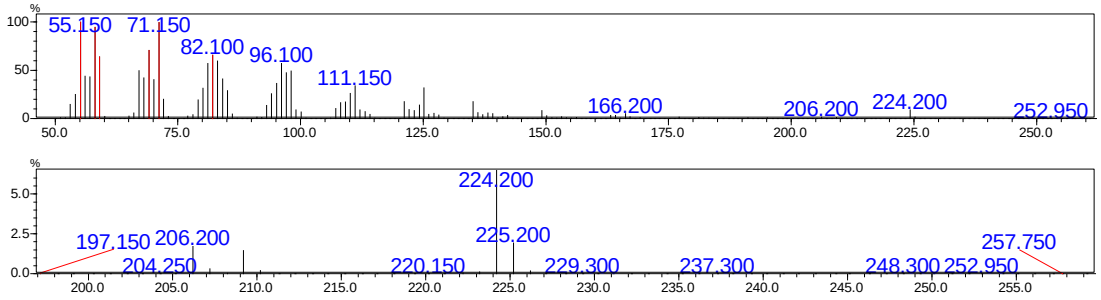

MS analysis 8-hydroxy-cyclopentadecanone peak at t_R = 15.08 min (m/z = 240.25 AMU, Δm/z = +16 AMU) [106]

Reported m/z = 240.2, 222.2, 207.2, 197.2, 179.2, 165.2, 151.1, 141.2, 127.1, 109.1, 95.1, 84.1, 81.1, 67.1, 55.1.

Experimental m/z = 240.25, 222.20, 207.05, 165.20, 151.1, 127.1, 109.15, 95.15, 81.10, 67.10, 55.05.

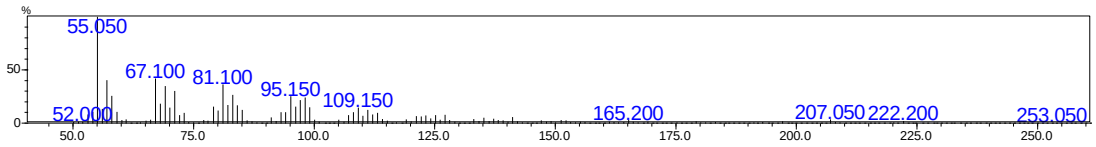

Zoomed in version:

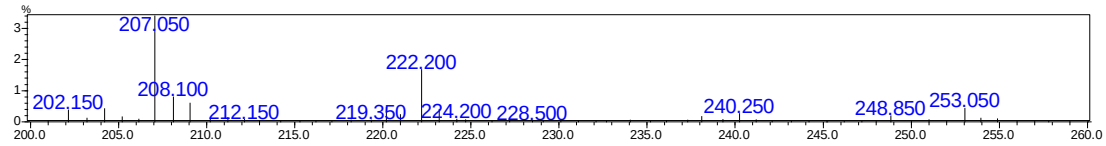

MS analysis of minor product (cyclopentadecane-1,8-dione) at t_R = 14.65 min (m/z = 238.3 AMU, Δm/z = +14 AMU)

Reported m/z = 238.2, 220.2, 207.25, 181.2, 125.15, 112.1, 111.15, 98.15, 84.15, 83.10, 69.10, 55.10 and 43.10 [106].

Experimental m/z = 238.30, 220.20, 207.00, 191.0, 149.15, 98.15, 83.10, 69.10, 55.10.

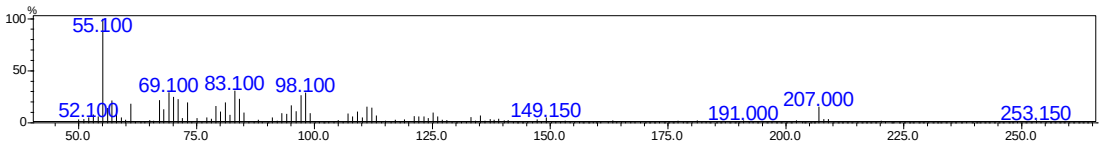

Zoomed in version:

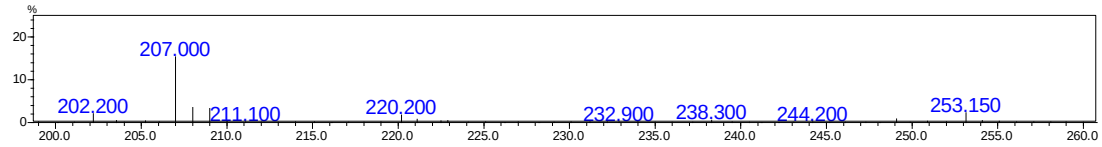

Figure B.8 (b): MS analysis of the substrate and oxidation metabolites generated in *in vitro* turnover of cyclopentadecanone with CYP101B1.

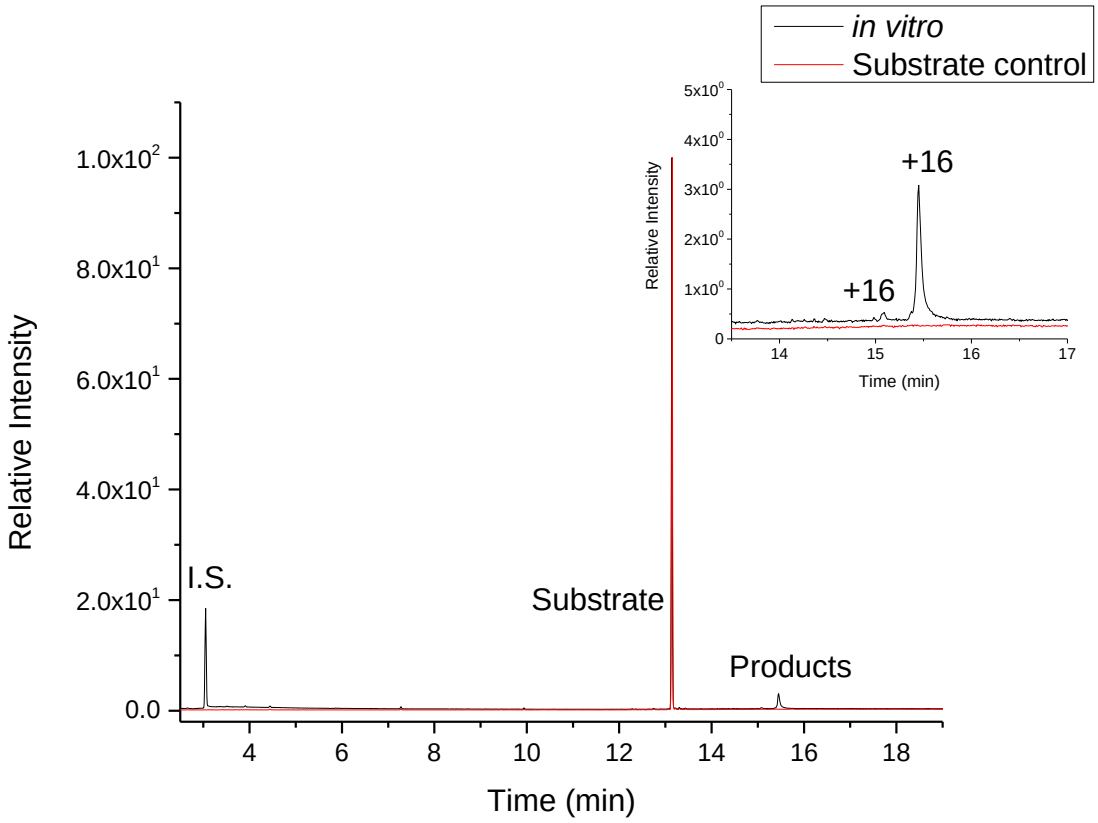

Figure B.9 (a): GCMS analysis of *In vitro* turnover of muscone by CYP101B1 (black) with substrate control (red). Internal standard is marked as (I.S.). Impurities are marked as (*).

MS analysis of muscone substrate at t_R = 13.12 min (m/z = 238.2 AMU).

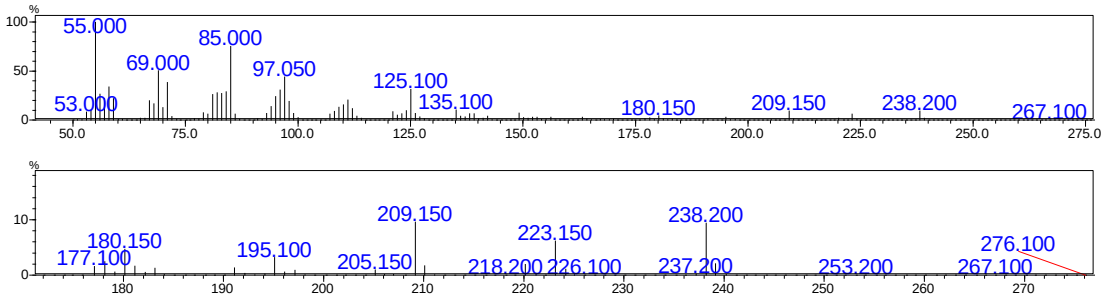

MS analysis of metabolite at t_R=15.09 min (m/z = 254 AMU; Δm/z = +16 AMU)

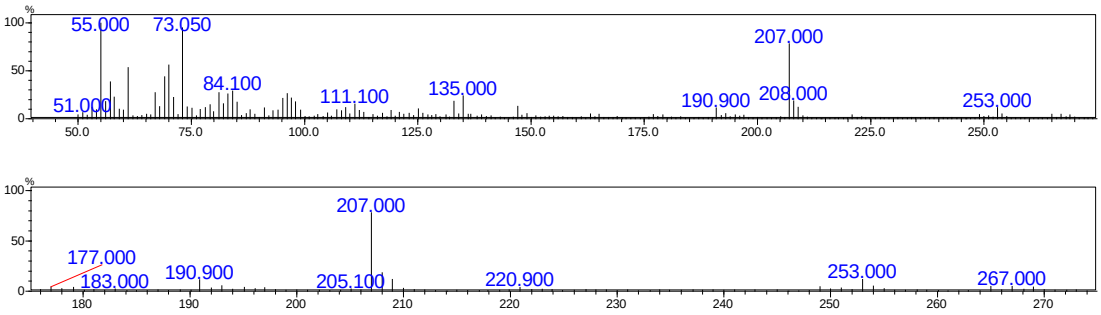

MS analysis of metabolite at t_R=15.45 min (m/z = 254 AMU; Δm/z = +16 AMU)

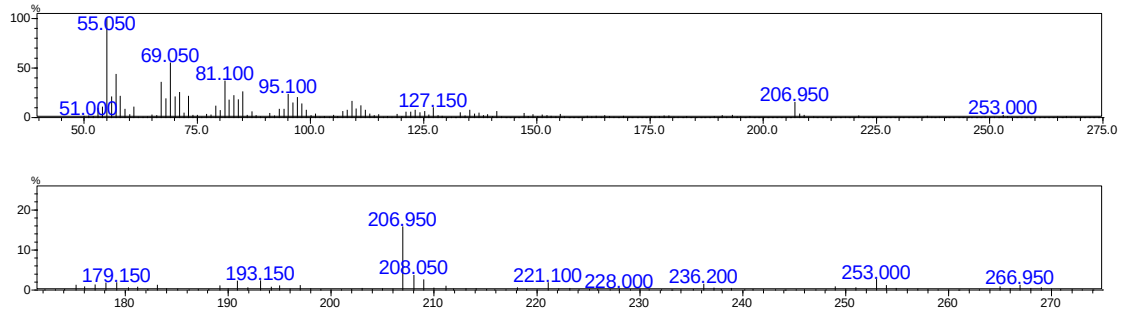

Figure B.9 (b): MS analysis of the substrate and oxidation metabolites generated in *in vitro* turnover of muscone with CYP101B1.

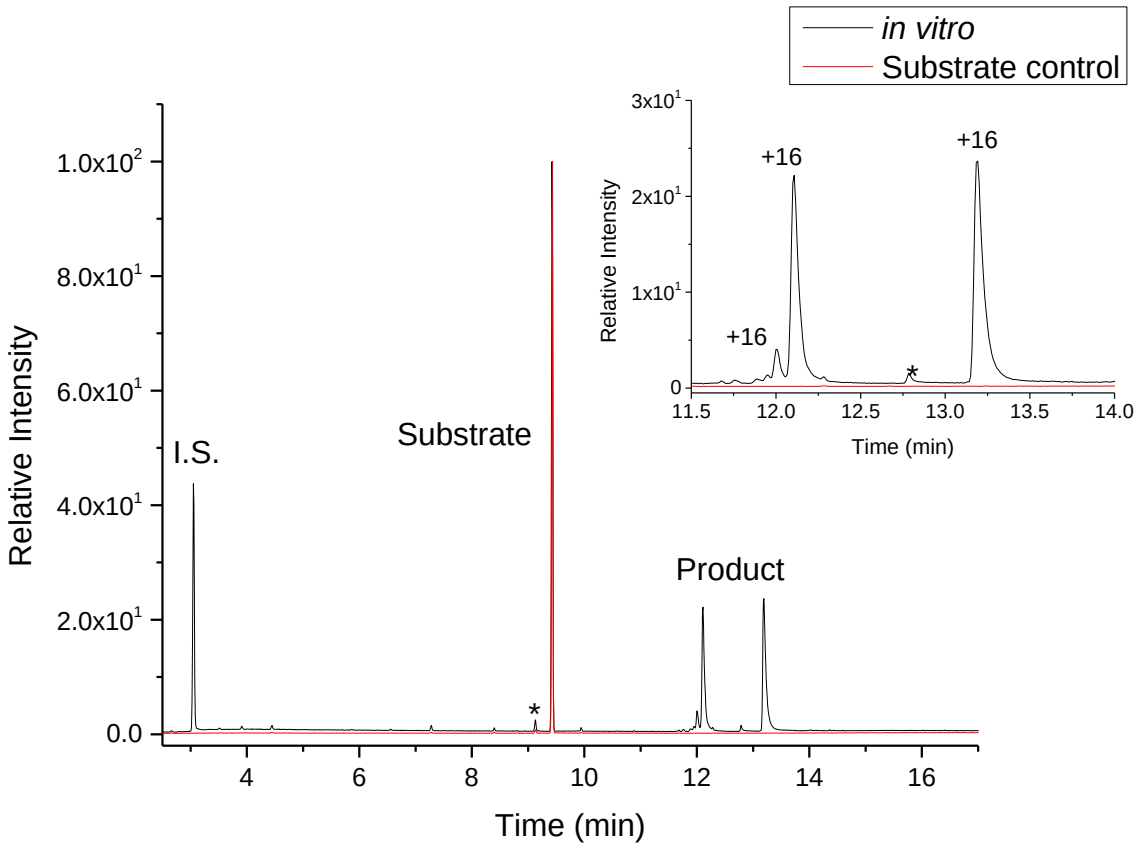

Figure B.10 (a): GCMS analysis of *In vitro* turnover of oxacyclotridecan-2-one by CYP101B1 (black) with substrate control (red). Internal standard is marked as (I.S.). Impurities are marked as (*).

MS analysis of oxacyclotridecan-2-one substrate at t_R = 9.40 min (m/z = 198.05 AMU)

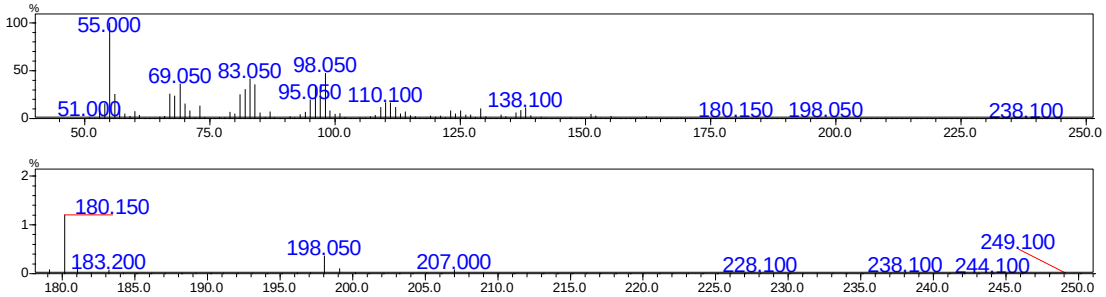

MS analysis of metabolite at t_R=11.99 min (m/z = 214.0 AMU; Δm/z = +16 AMU)

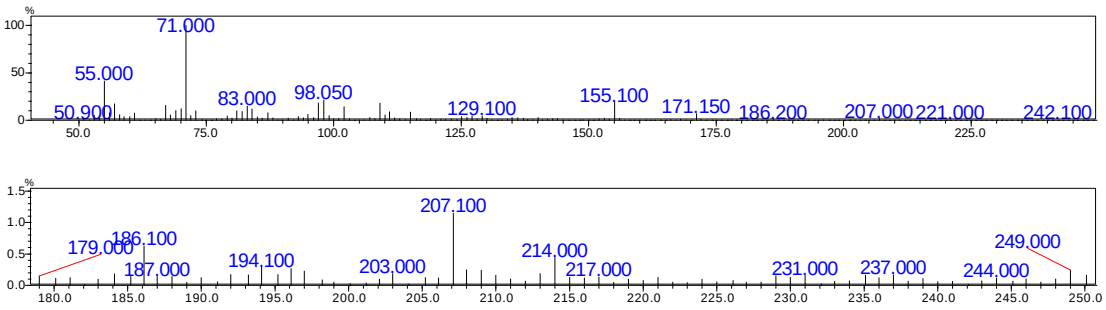

MS analysis of metabolite at t_R=12.10 min (m/z = 214 AMU; Δm/z = +16 AMU)

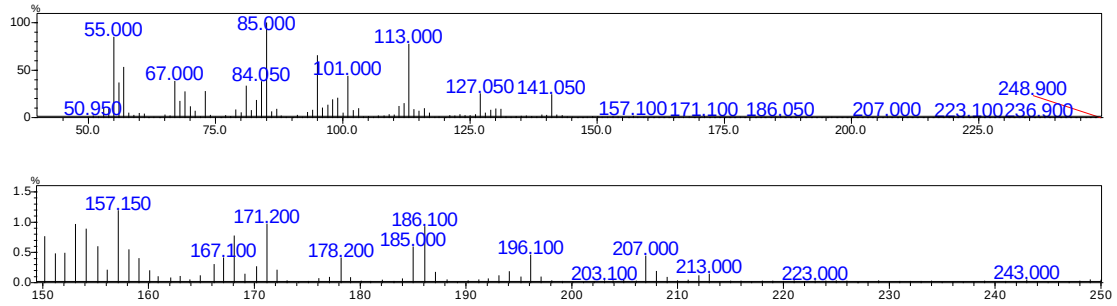

MS analysis of metabolite at t_R=13.18 (m^+/z = 214.1 AMU; Δm/z = +16 AMU)

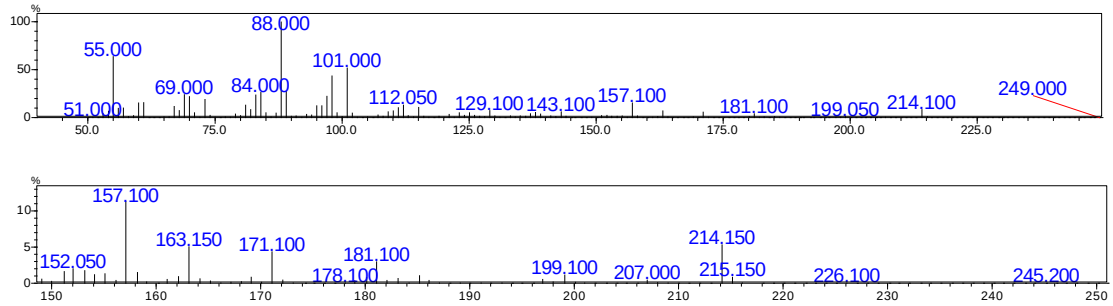

Figure B.10 (b): MS analysis of the substrate and oxidation metabolites generated in *in vitro* turnover of oxacyclotridecan-2-one with CYP101B1.

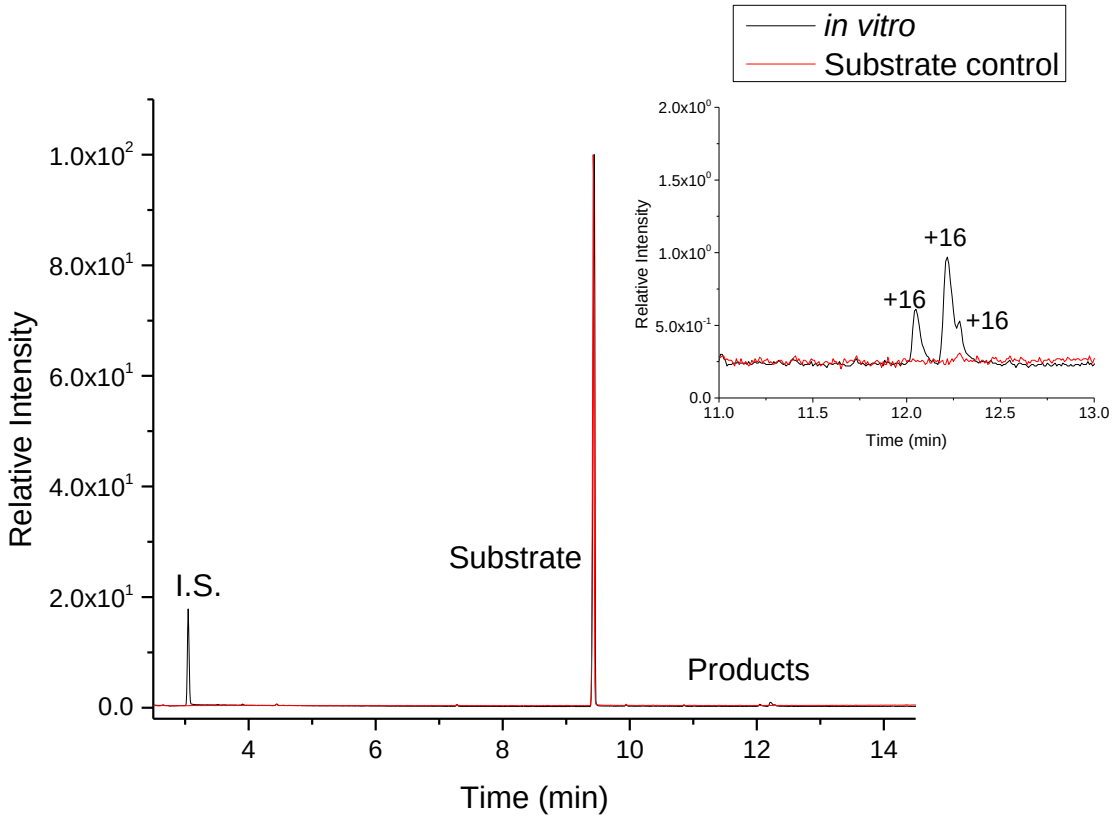

Figure B.11 (a): GCMS analysis of *In vitro* turnover of dihydroactinidiolide by CYP101B1 (black) with substrate control (red). Internal standard is marked as (I.S.). Impurities are marked as (*).

MS analysis of dihydroactinidiolide substrate at t_R = 9.41 min (m/z = 180.05 AMU)

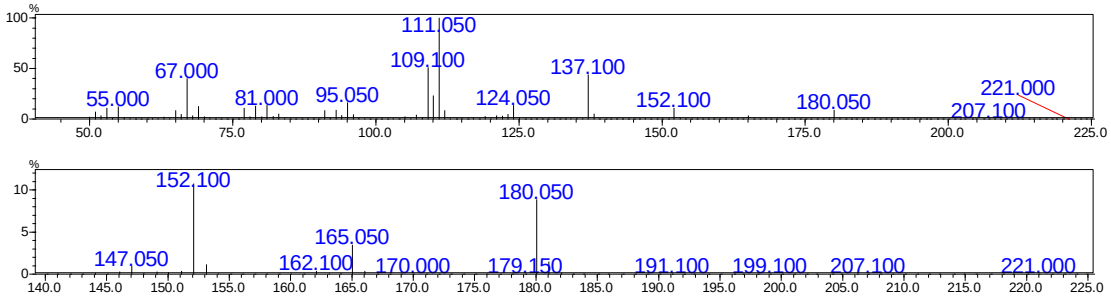

MS analysis of metabolite at t_R=12.04 min (m/z = 196.1 AMU; Δm/z = +16 AMU)

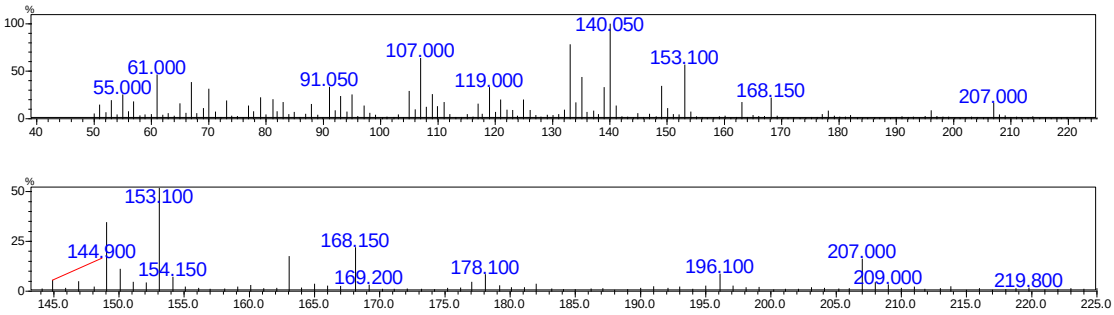

MS analysis of metabolite at t_R=12.21 min (m/z = 196.0 AMU; Δm/z = +16 AMU)

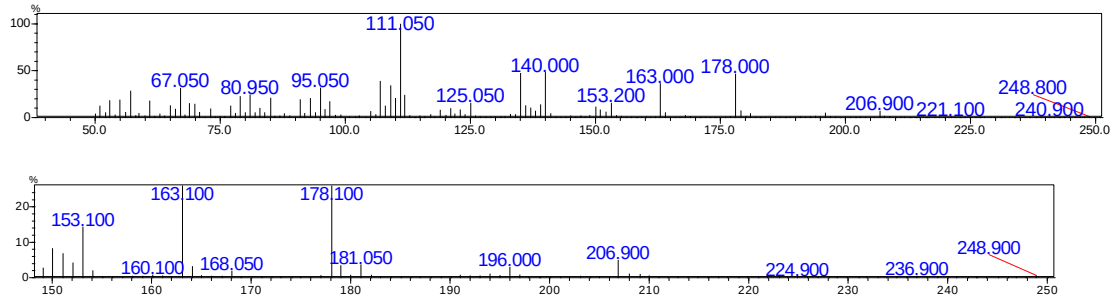

MS analysis of metabolite at t_R=12.28 min (m/z = 196.2 AMU; Δm/z = +16 AMU)

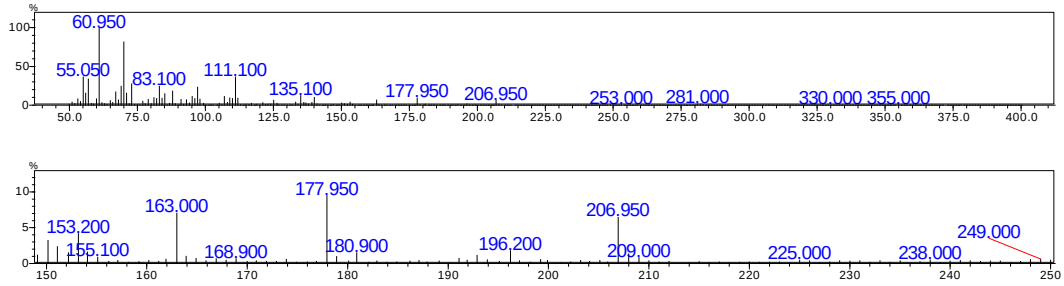

Figure B.11 (b): MS analysis of the substrate and oxidation metabolites generated in *in vitro* turnover of dihydroactinidiolide with CYP101B1.

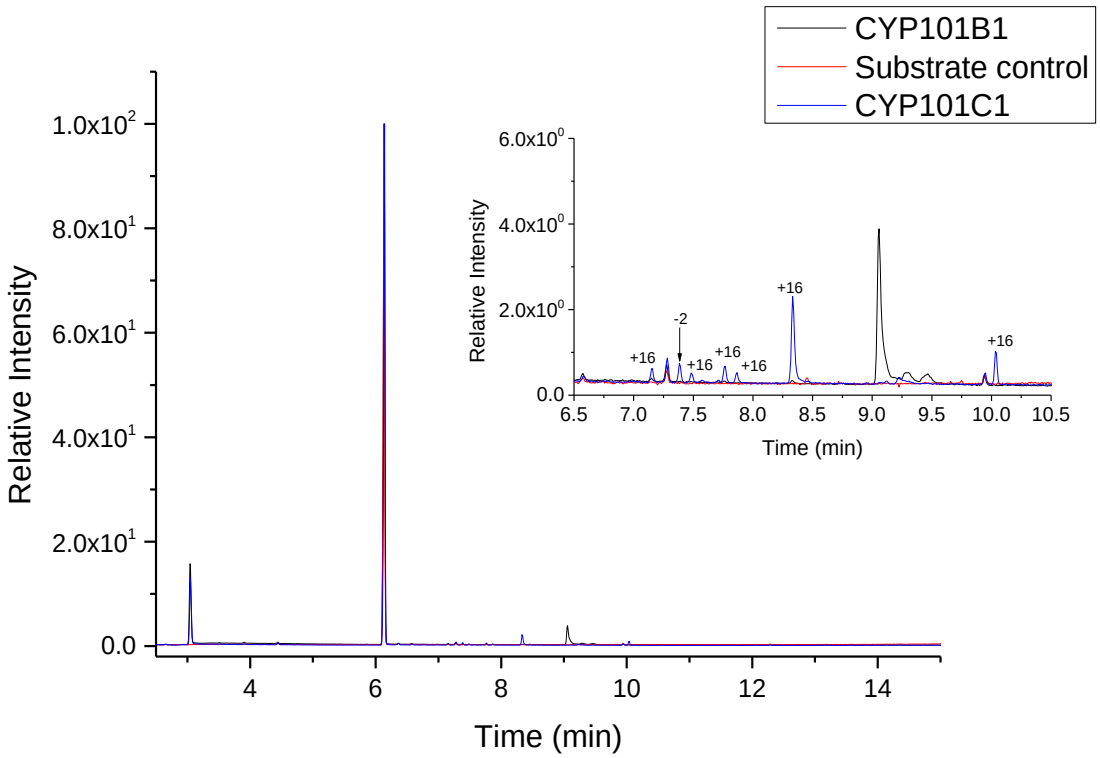

Figure B.12 (a): GCMS analysis of *In vitro* turnover of *trans*-1-decalone with CYP101C1 (blue) in comparison with substrate control (red) and CYP101B1 (black). Internal standard is marked as (I.S.). Impurities are marked as (*).

MS analysis of *trans*-1-decalone substrate at t_R = 6.12 min (m/z = 152.100 AMU)

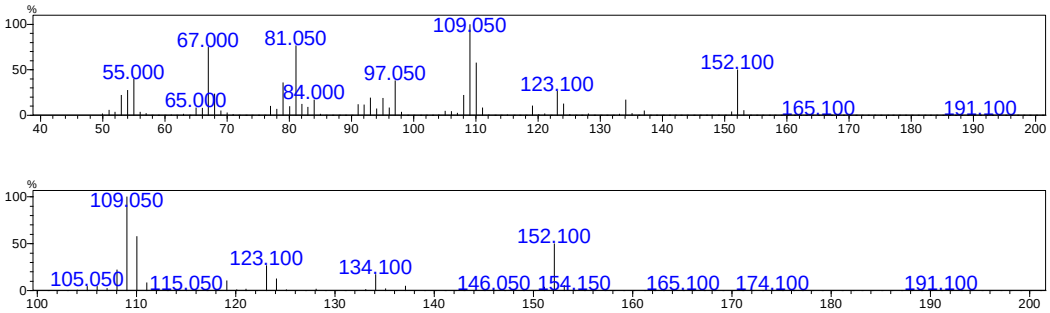

MS analysis of metabolite at t_R = 7.15 min (m/z = 168.05 AMU; Δm/z = +16 AMU)

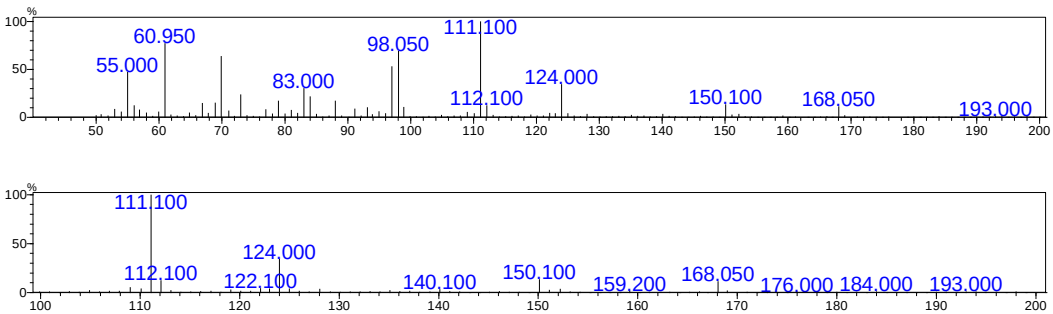

MS analysis of metabolite at t_R = 7.38 min (m/z = 150.150 AMU; Δm/z = -2 AMU)

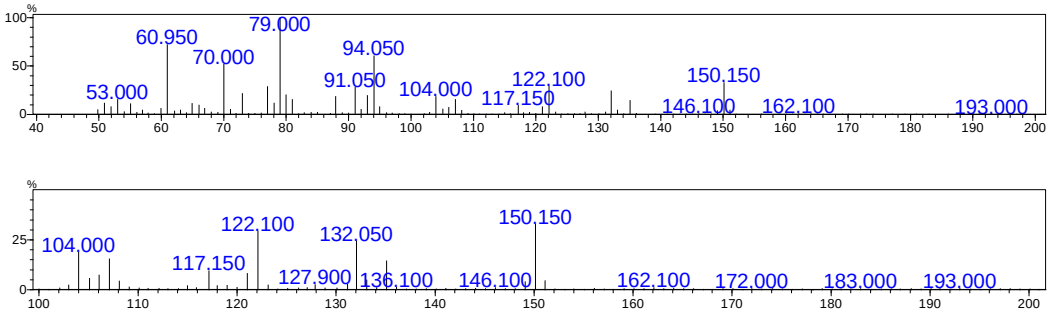

MS analysis of metabolite at t_R = 7.48 min (m/z = 167.900 AMU; Δm/z = +16 AMU)

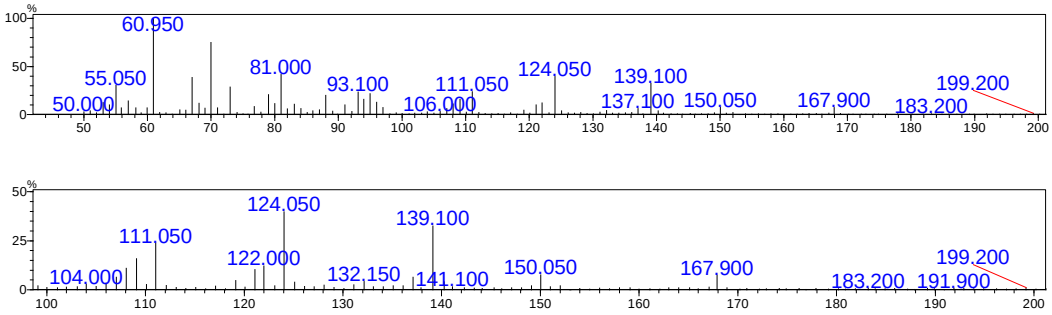

MS analysis of metabolite at t_R = 7.75 min (m/z = 168.050 AMU; Δm/z = +16 AMU)

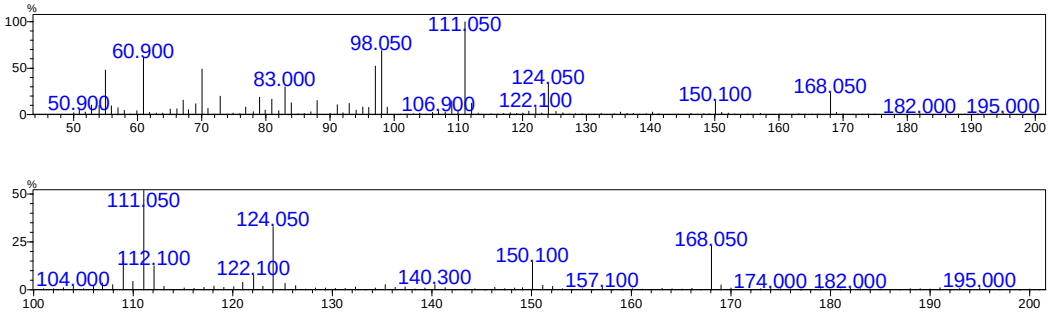

MS analysis of metabolite at t_R =7.86 min (m/z = 150.050 min; Δm/z = -2 AMU)

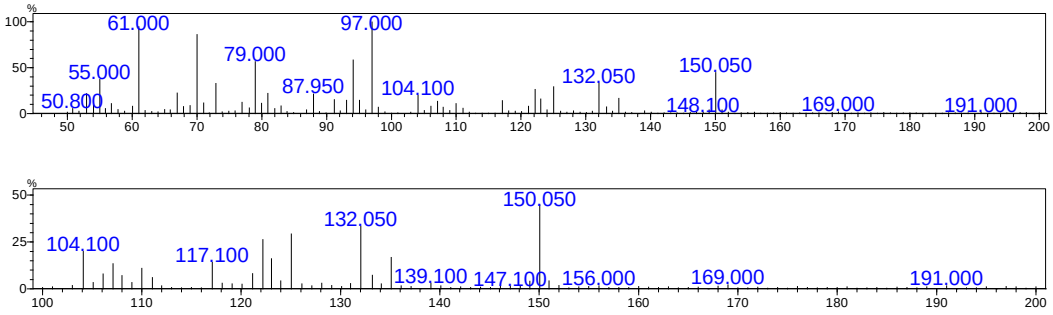

MS analysis of metabolite at t_R =8.34 min (m/z = 168.100; Δm/z = +16 AMU)

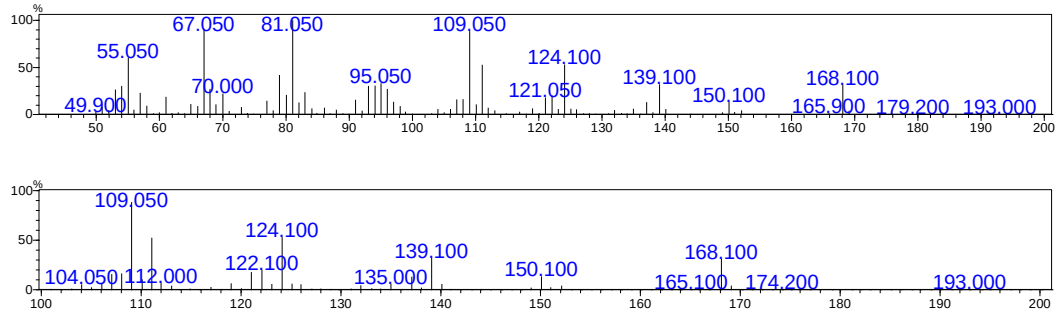

MS analysis of metabolite at t_R = 10.04 min (m/z = 167.100 AMU; Δm/z = +15 AMU)

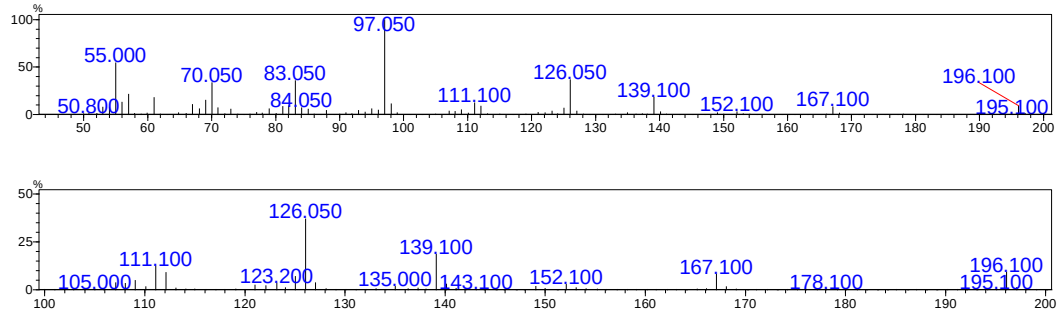

Figure B.12 (b): MS analysis of the substrate and oxidation metabolites generated in *in vitro* turnover of *trans*-1-decalone with CYP101C1.

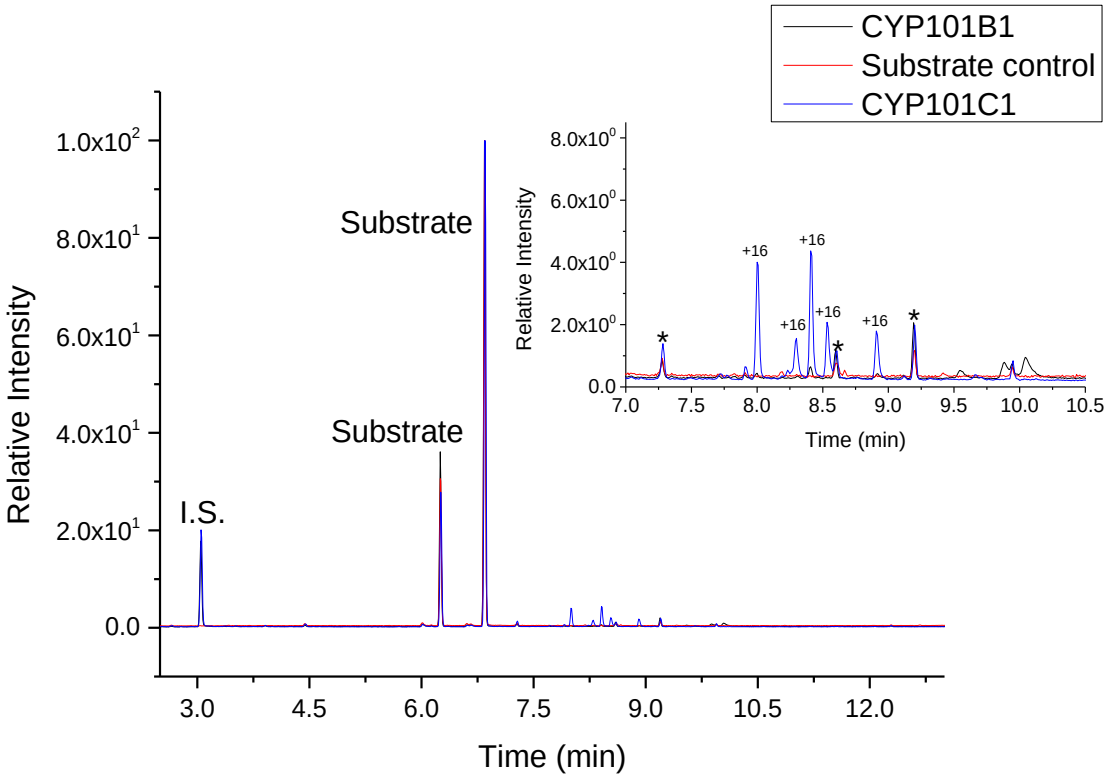

Figure B.13 (a): GCMS analysis of *In vitro* turnover of 2-decalone with CYP101C1 (blue) in comparison with substrate control (red) and CYP101B1 (black). Internal standard is marked as (I.S.). Impurities are marked as (*).

MS analysis of 2-decalone substrate at t_R = 6.25 min (m/z = 152.100 AMU)

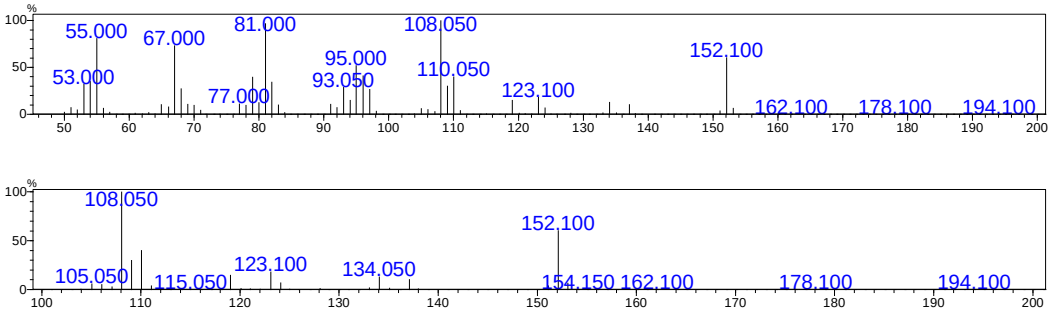

MS analysis of 2-decalone substrate at t_R = 6.85 min (m/z = 152.100 AMU)

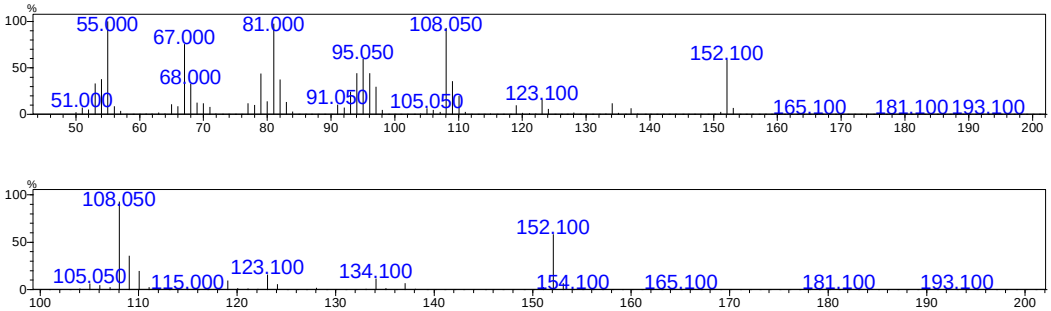

MS analysis of metabolite at t_R = 7.91 min (m/z = 150.100 AMU; Δm/z = -2 AMU)

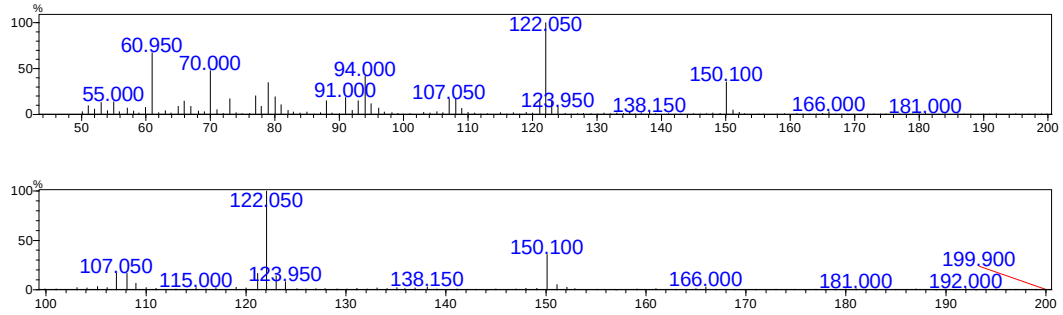

MS analysis of metabolite at t_R = 8.01 min (m/z = 168.050 AMU; Δm/z = +16 AMU)

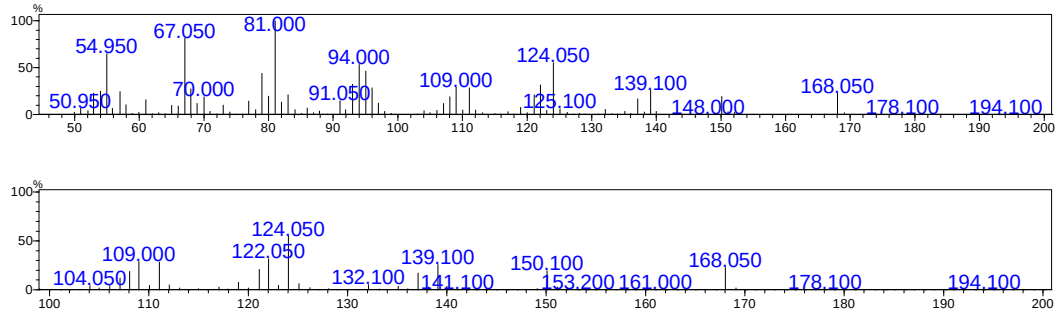

MS analysis of metabolite at t_R = 8.29 min (m/z = 168.100 AMU; Δm/z = +16 AMU)

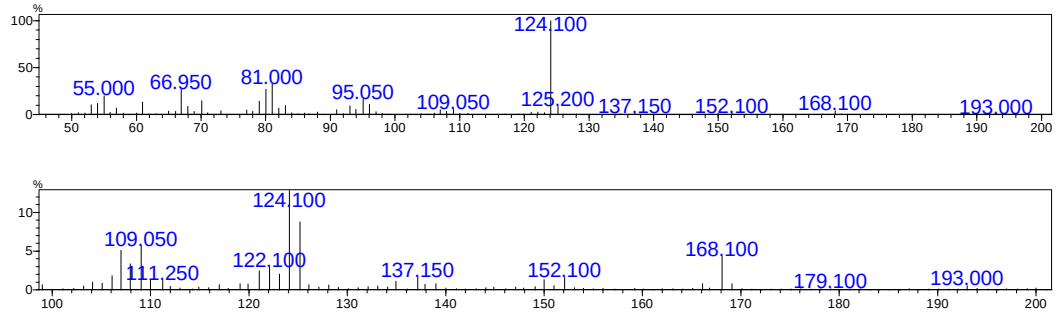

MS analysis of metabolite at t_R = 8.41 min (m/z = 168.050 AMU; Δm/z = +16 AMU)

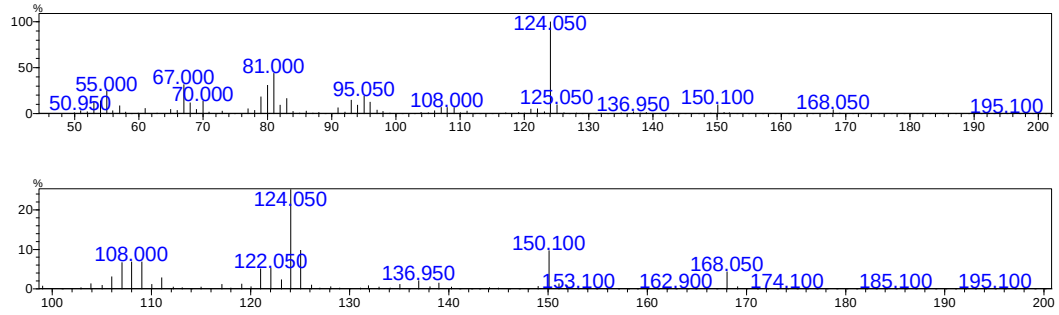

MS analysis of metabolite at t_R = 8.53 min (m/z = 168.050 AMU; Δm/z = +16 AMU)

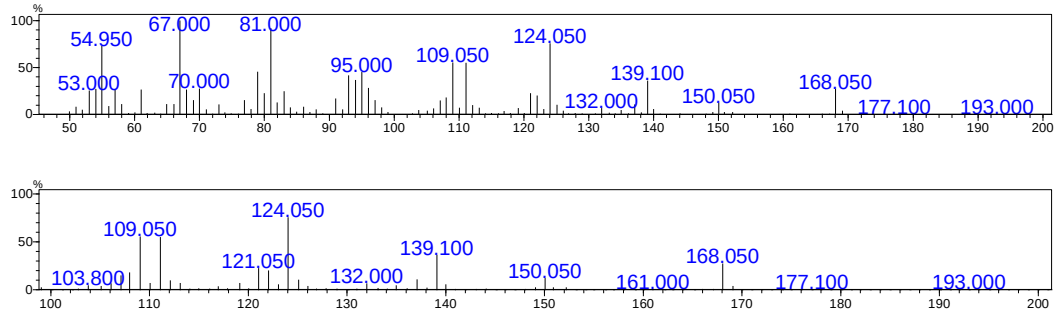

MS analysis of metabolite at t_R = 8.91 min (m/z = 168.050 AMU; Δm/z = +16 AMU)

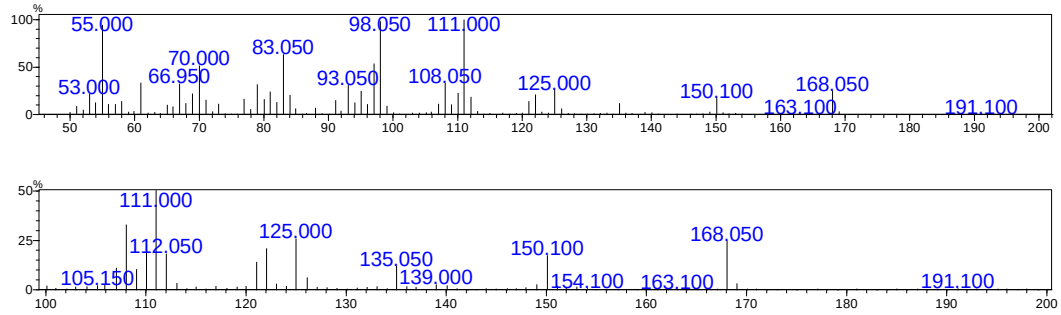

Figure B.13 (b): MS analysis of the substrate and oxidation metabolites generated in *in vitro* turnover of 2-decalone with CYP101C1.

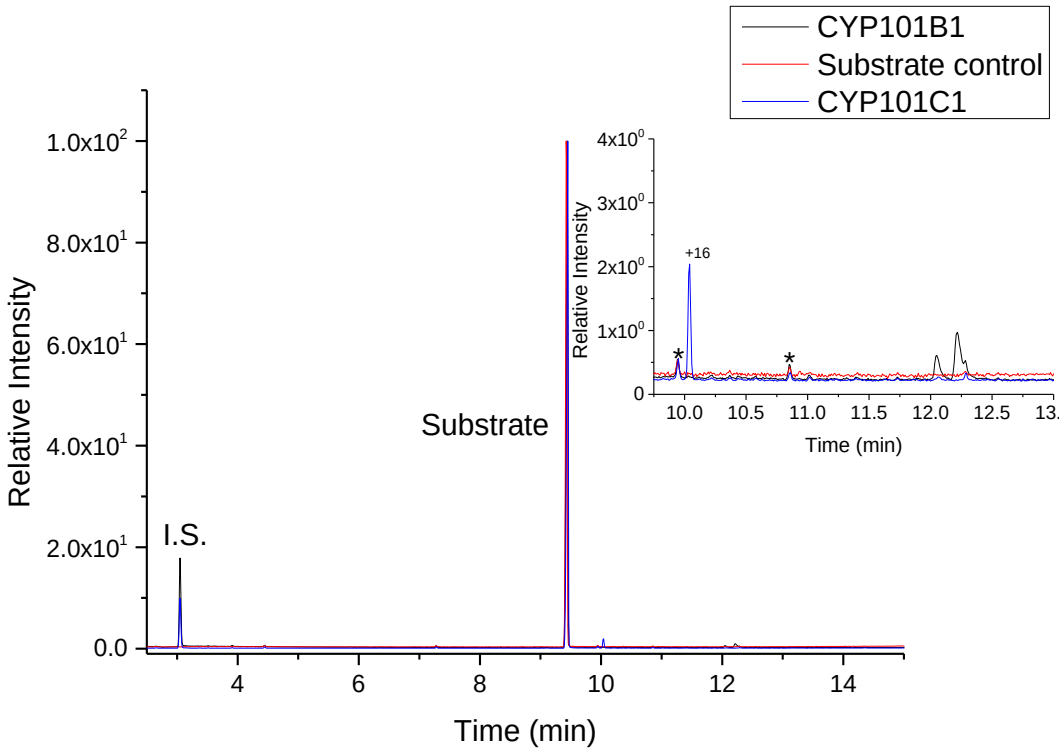

Figure B.14 (a): GCMS analysis of *In vitro* turnover of dihydroactinidiolide with CYP101C1 (blue) in comparison with substrate control (red) and CYP101B1 (black). Internal standard is marked as (I.S.). Impurities are marked as (*).

MS analysis of dihydroactinidiolide substrate at t_R = 9.45 min (m/z = 180 AMU)

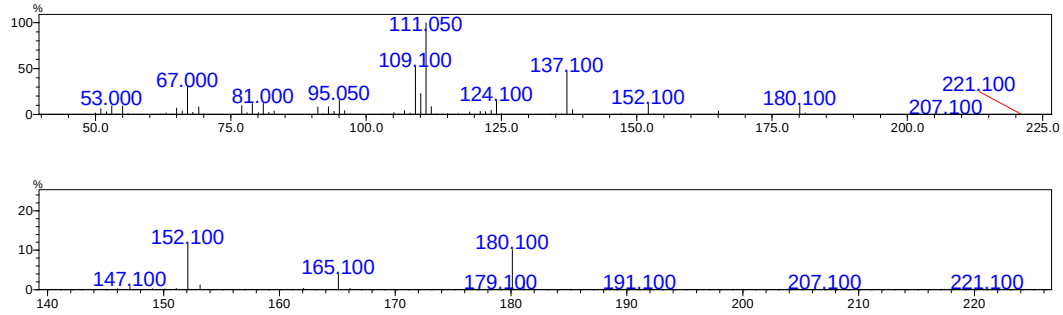

MS analysis of metabolite at t_R = 10.03 min (m/z = 196.200 AMU; Δm/z = +16 AMU)

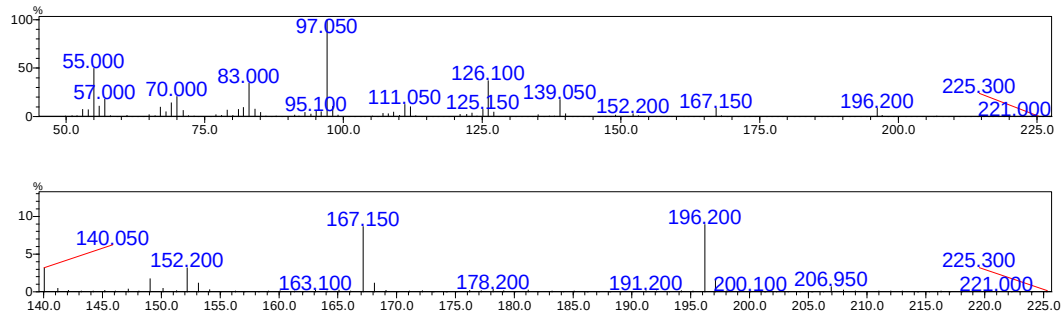

Figure B.14 (b): MS analysis of the substrate and oxidation metabolites generated in *in vitro* turnover of dihydroactinidiolide with CYP101C1.

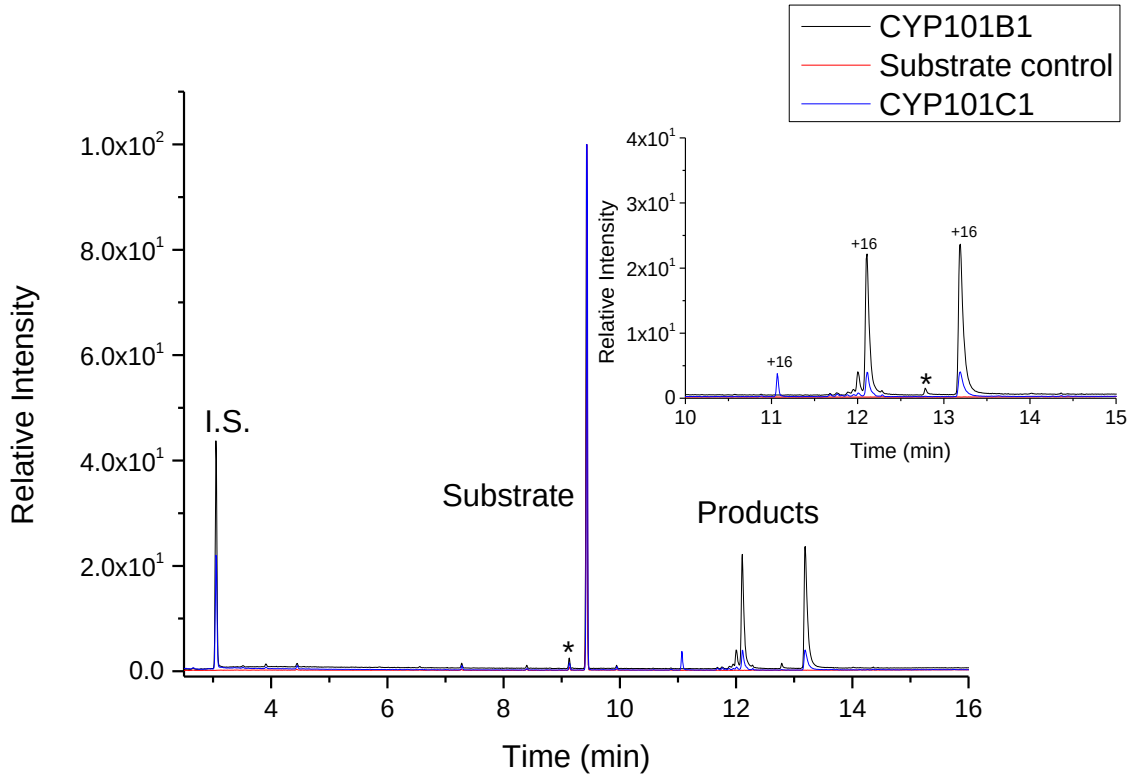

Figure B.15 (a): GCMS analysis of *In vitro* turnover of oxacyclotridecan-2-one with CYP101C1 (blue) in comparison with substrate control (red) and CYP101B1 (black). Internal standard is marked as (I.S.). Impurities are marked as (*).

MS analysis of oxacyclotridecan-2-one substrate at t_R = 9.43 min (m/z = 198.000 AMU)

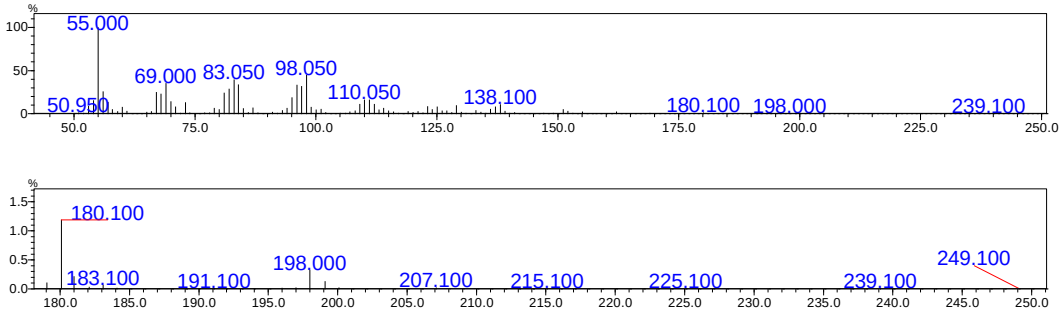

MS analysis of metabolite at t_R = 11.06 min (m/z = 213.900 AMU; Δm/z = +16 AMU)

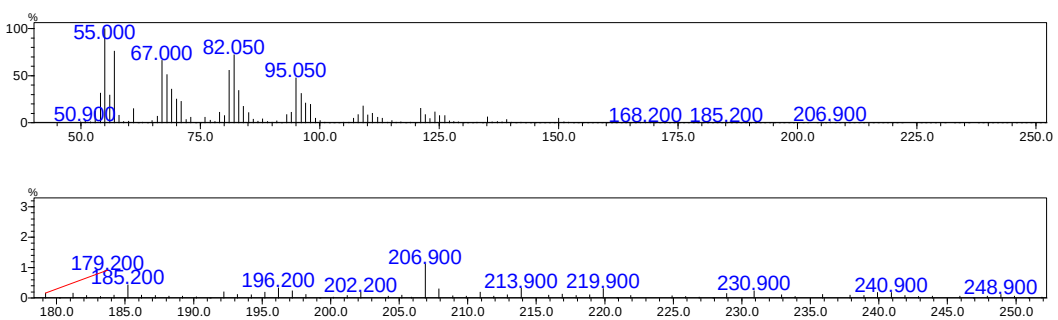

MS analysis of metabolite at t_R = 12.12 min (m/z = 212.900 AMU; Δm/z = +14 AMU)

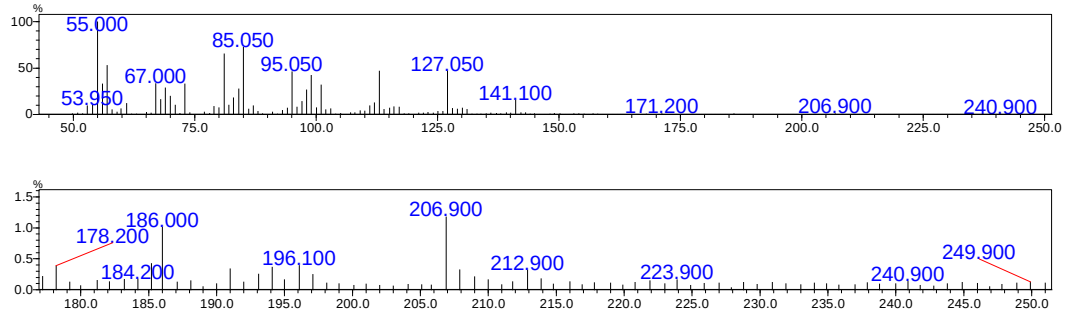

MS analysis of metabolite at t_R = 13.17 min (m/z = 214.200 AMU; Δm/z = +16 AMU)

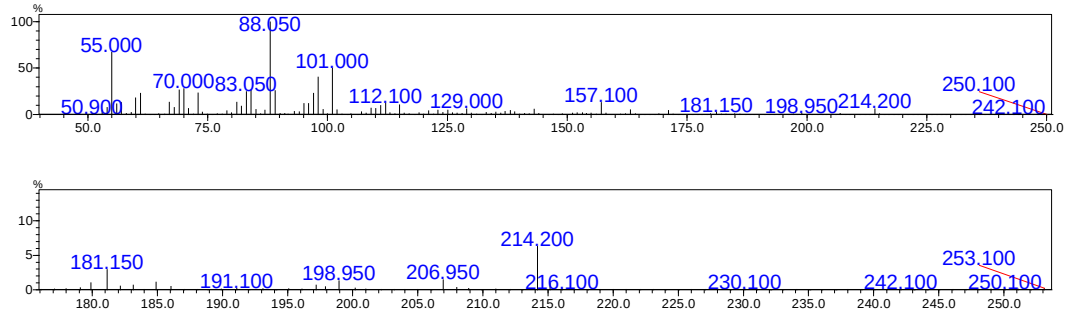

Figure B.15 (b): MS analysis of the substrate and oxidation metabolites generated in *in vitro* turnover of oxacyclotridecan-2-one with CYP101C1.

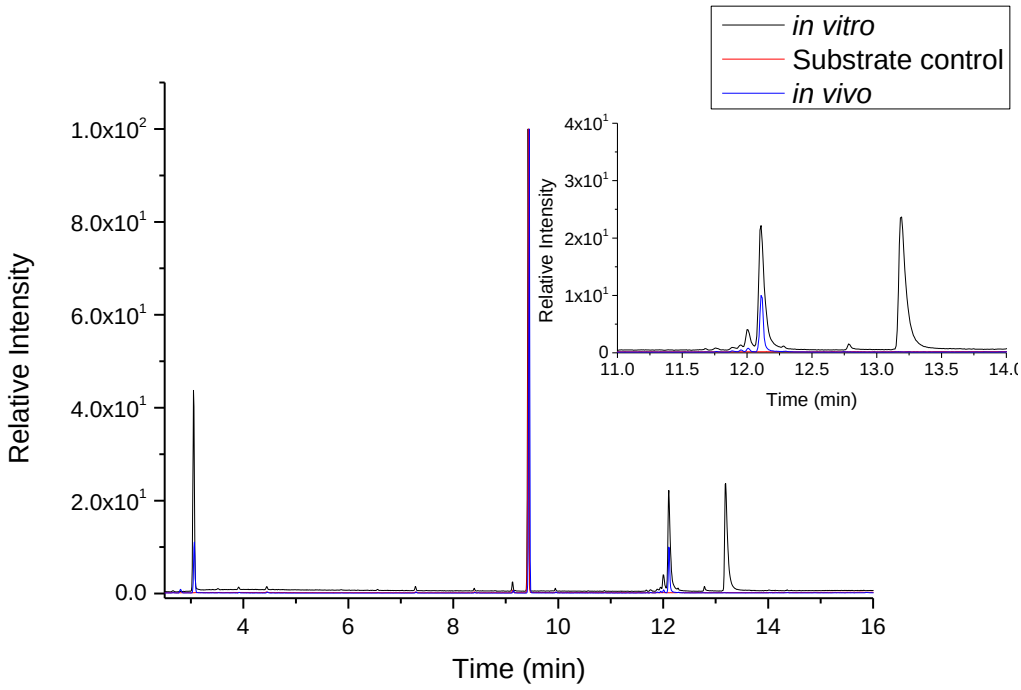

Figure B.16: GCMS analysis of whole-cell turnover of oxacyclotridecan-2-one with CYP101B1 (blue) in comparison with substrate control (red) and *in vitro* turnover by CYP101B1 (black).

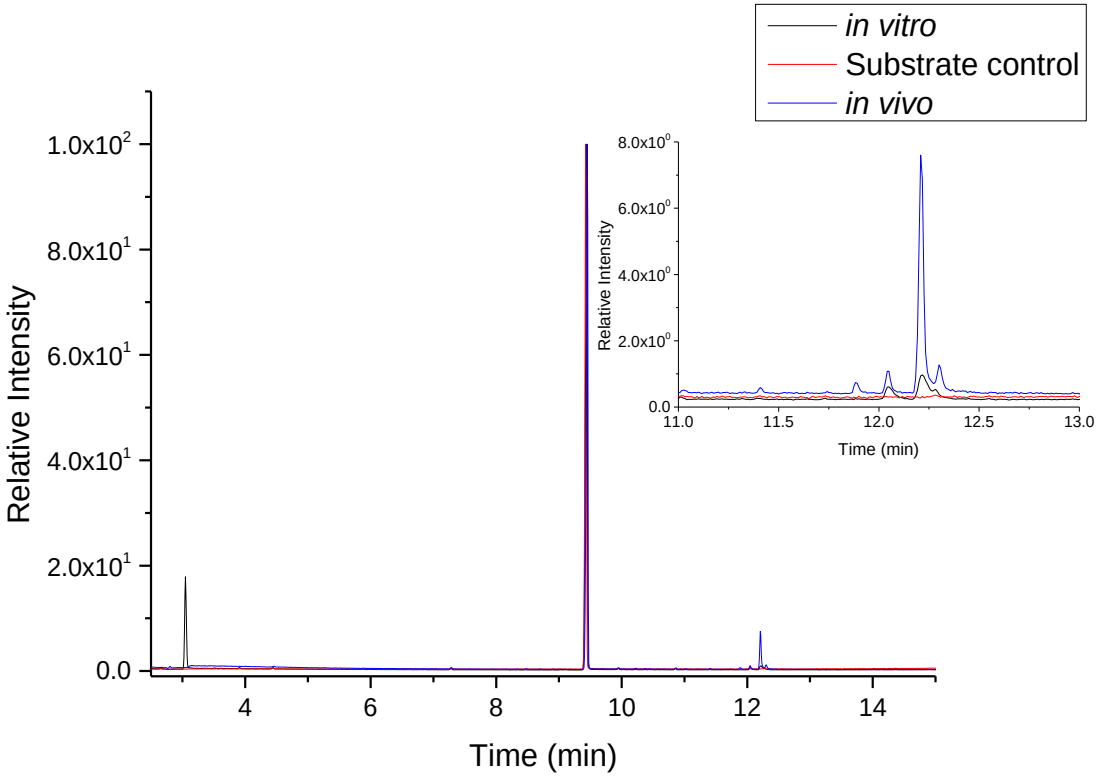

Figure B.17: GCMS analysis of whole-cell turnover of dihydroactinidiolide with CYP101B1 (blue) in comparison with substrate control (red) and *in vitro* turnover by CYP101B1 (black).

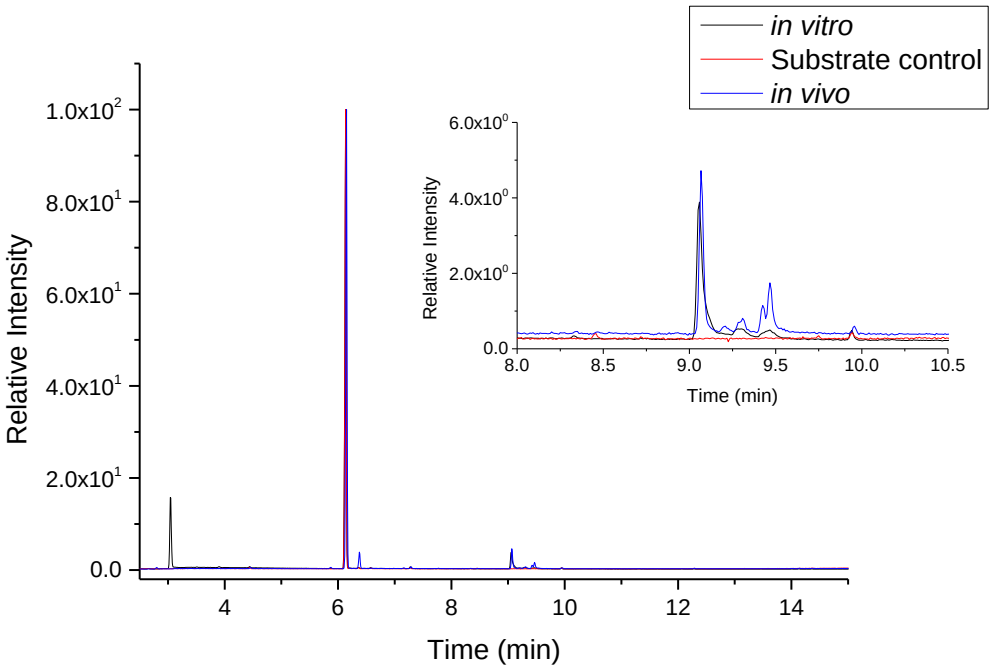

Figure B.18: GCMS analysis of whole-cell turnover of *trans*-1-decalone with CYP101B1 (blue) in comparison with substrate control (red) and *in vitro* turnover by CYP101B1 (black).

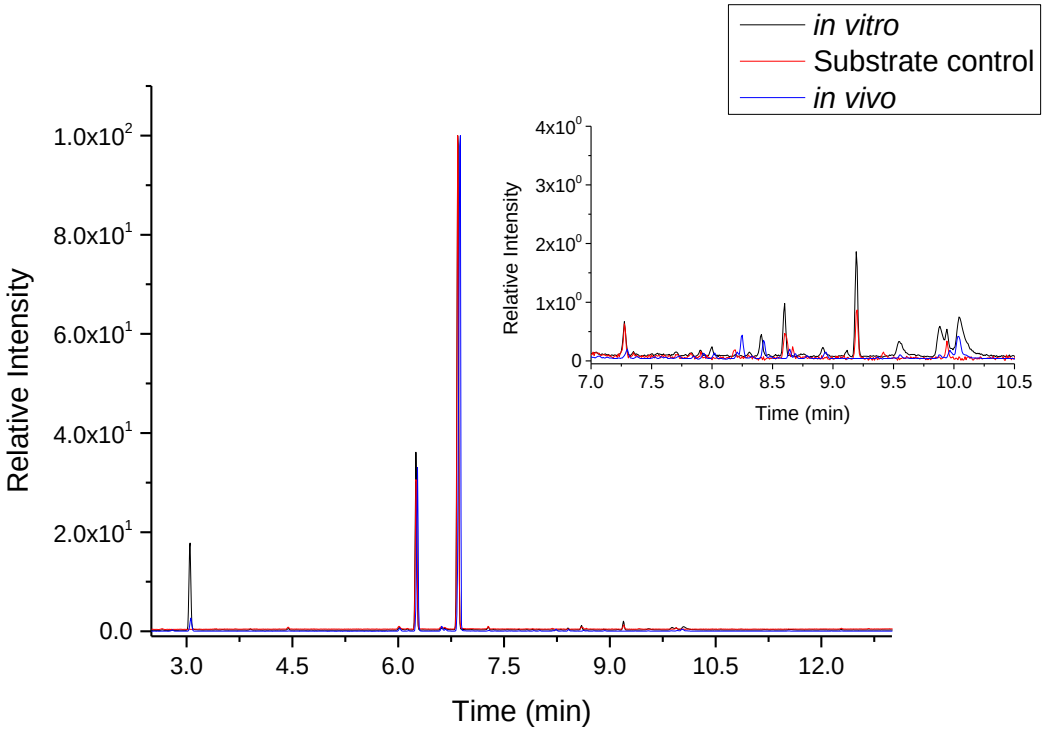

Figure B.19: GCMS analysis of whole-cell turnover of 2-decalone with CYP101B1 (blue) in comparison with substrate control (red) and *in vitro* turnover by CYP101B1 (black).

Cyclopentadecanone:

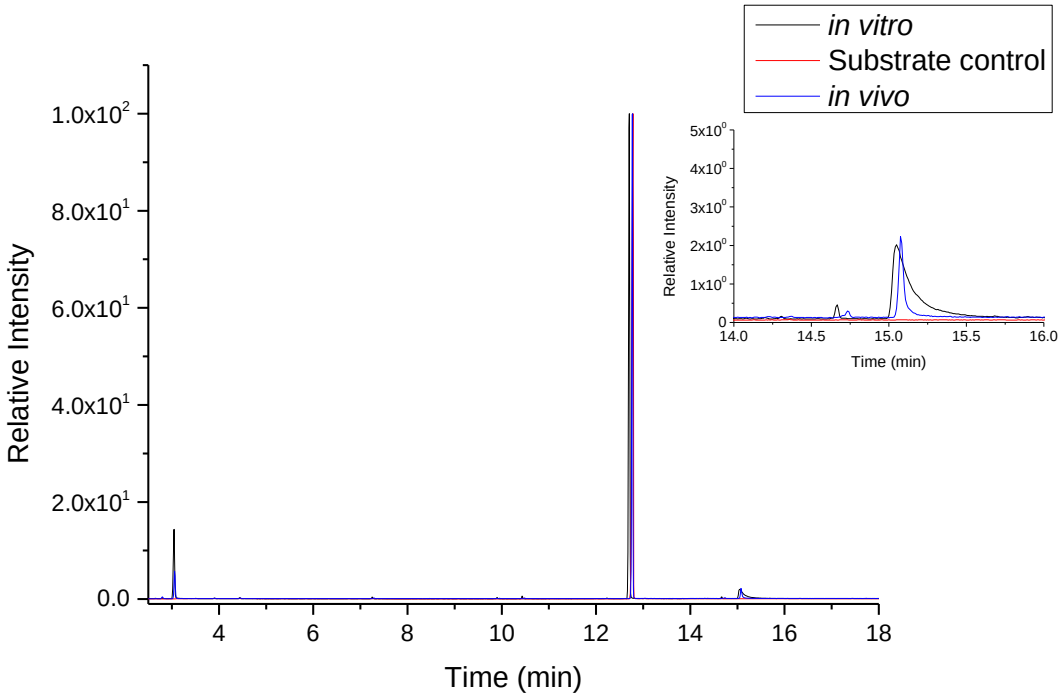

Figure B.20: GCMS analysis of whole-cell turnover of cyclopentadecanone with CYP101B1 (blue) in comparison with substrate control (red) and *in vitro* turnover by CYP101B1 (black).

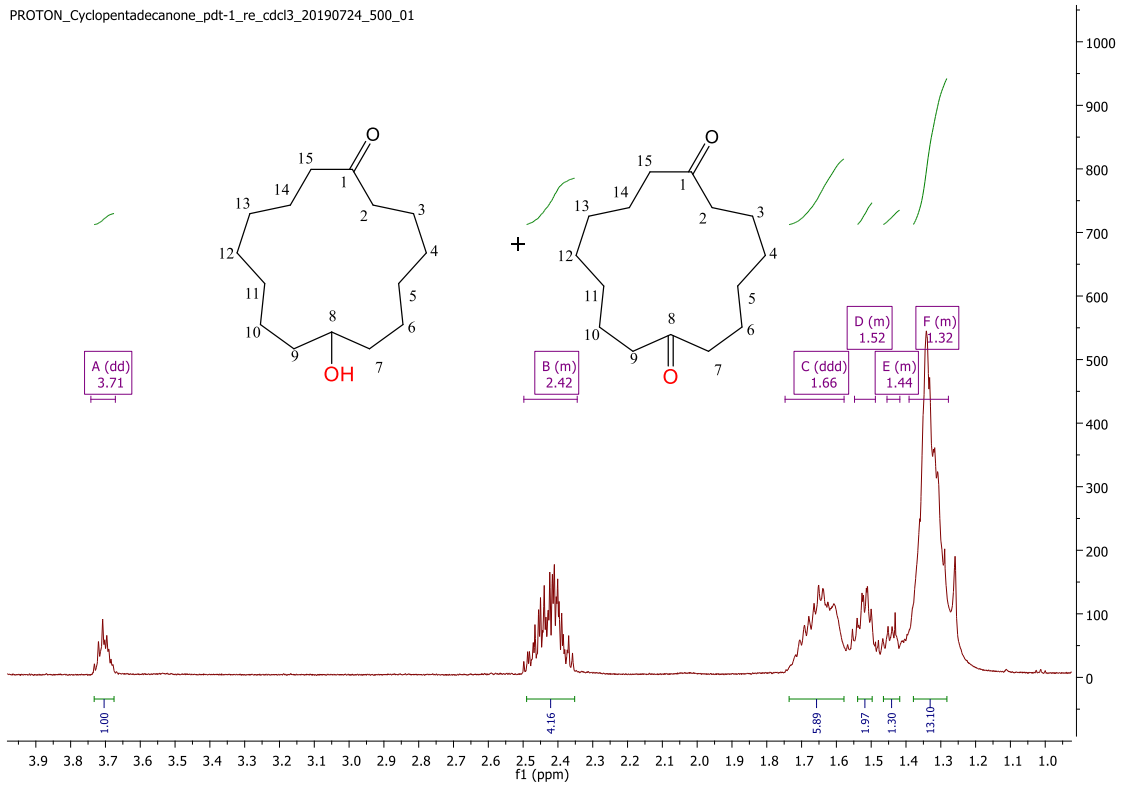

Figure B.21 (a): ^{1}H NMR data for product of Cyclopentadecanone in $CDCl_3$.

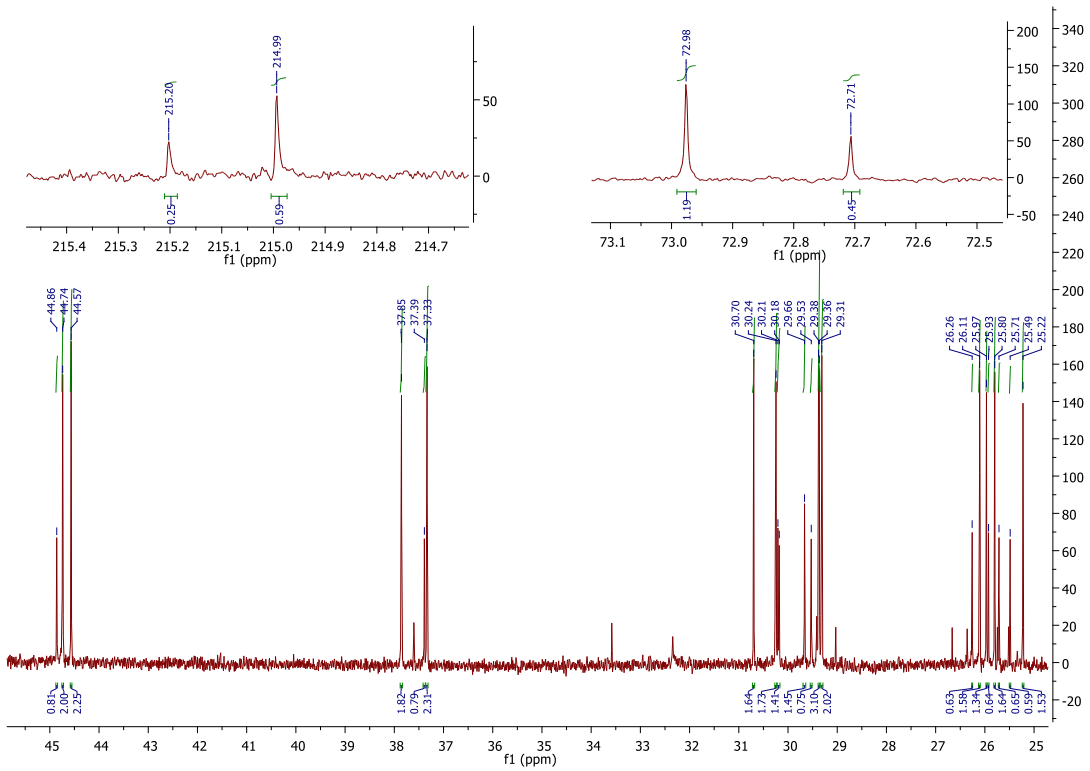

Figure B.21 (b): ^{13}C NMR data for product of Cyclopentadecanone in $CDCl_3$.

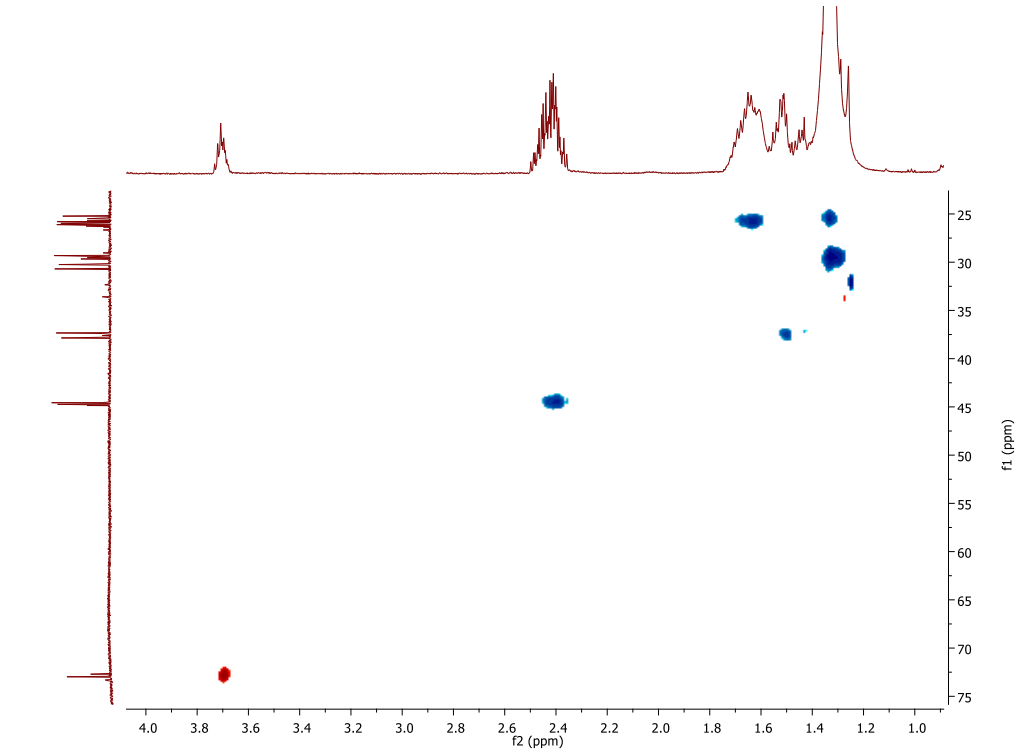

Figure B.21 (c): HSQC NMR data for product of Cyclopentadecanone in $CDCl_3$.

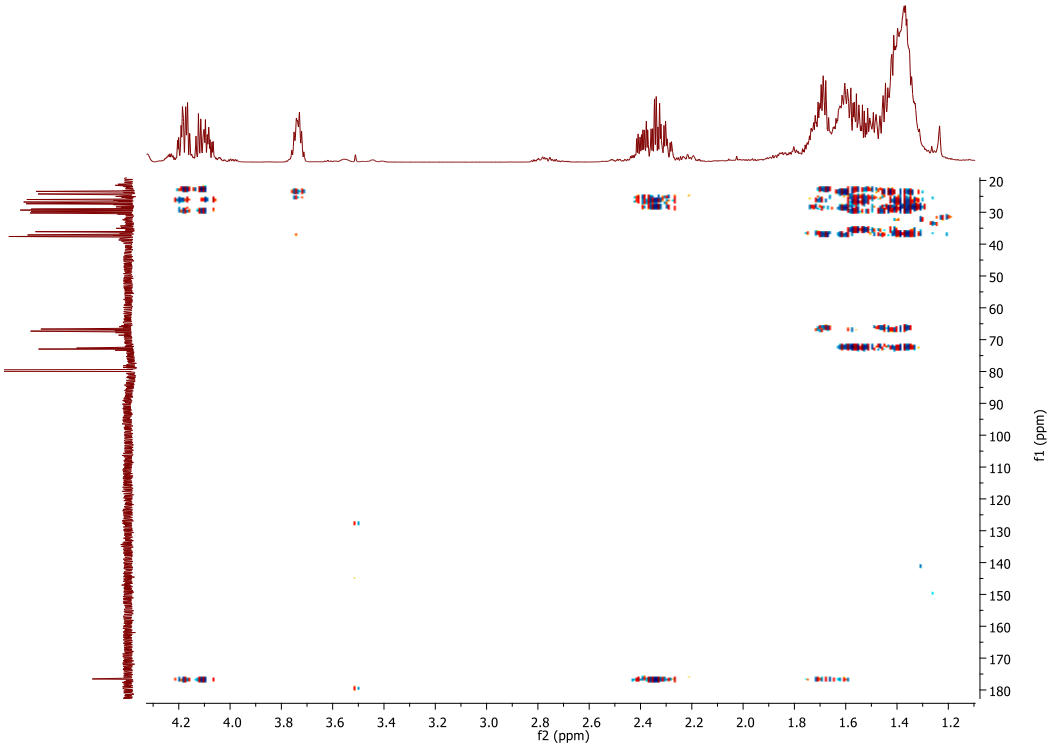

Figure B.21 (d): HMBC NMR data for product of Cyclopentadecanone in $CDCl_3$.

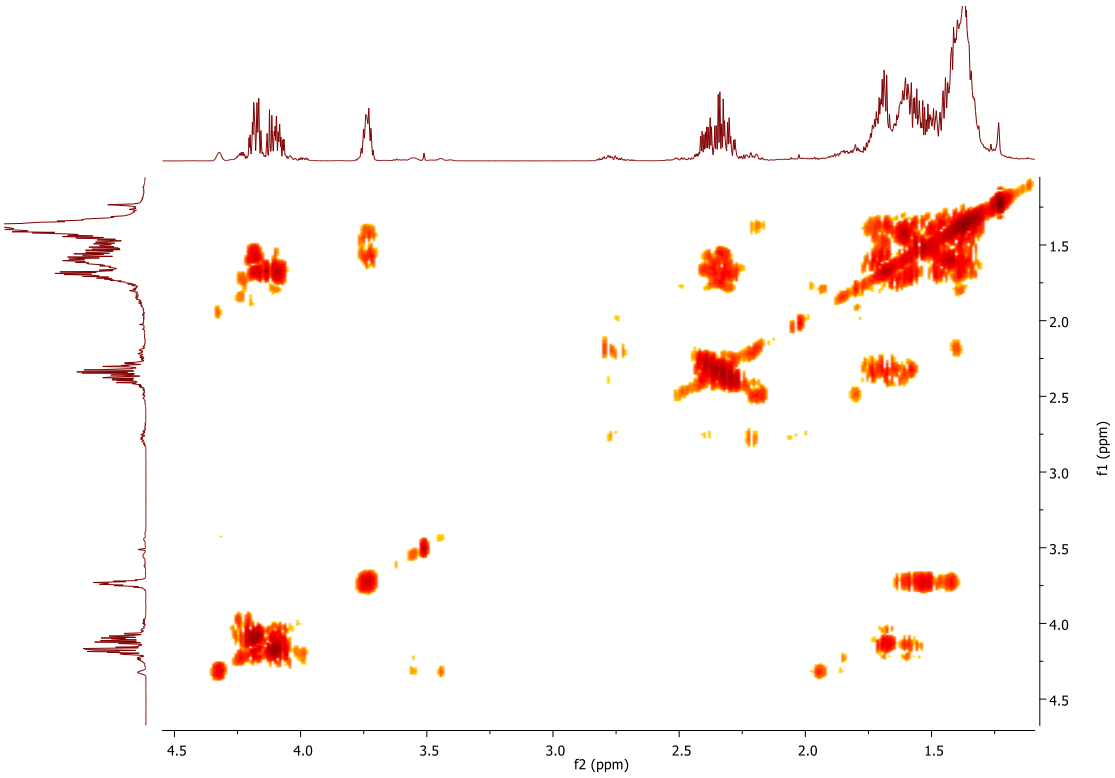

Figure B.21 (e): g-COSY NMR data for product of Cyclopentadecanone in $CDCl_3$.

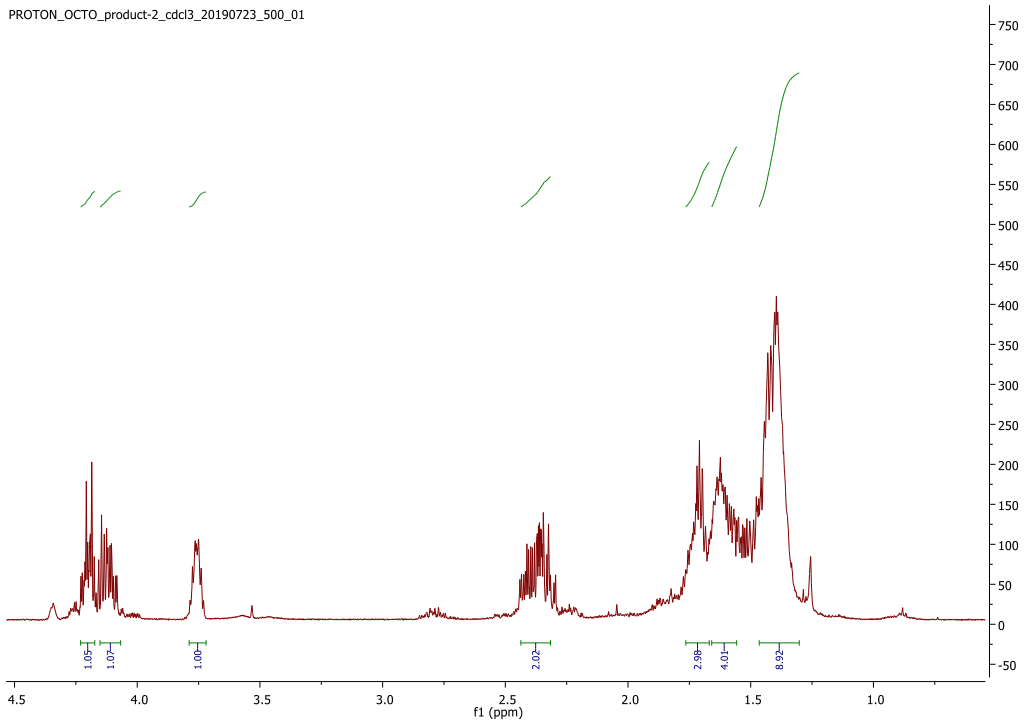

Figure B.22 (a): ^{1}H NMR of product for oxacyclotridecan-2-one in $CDCl_3$.

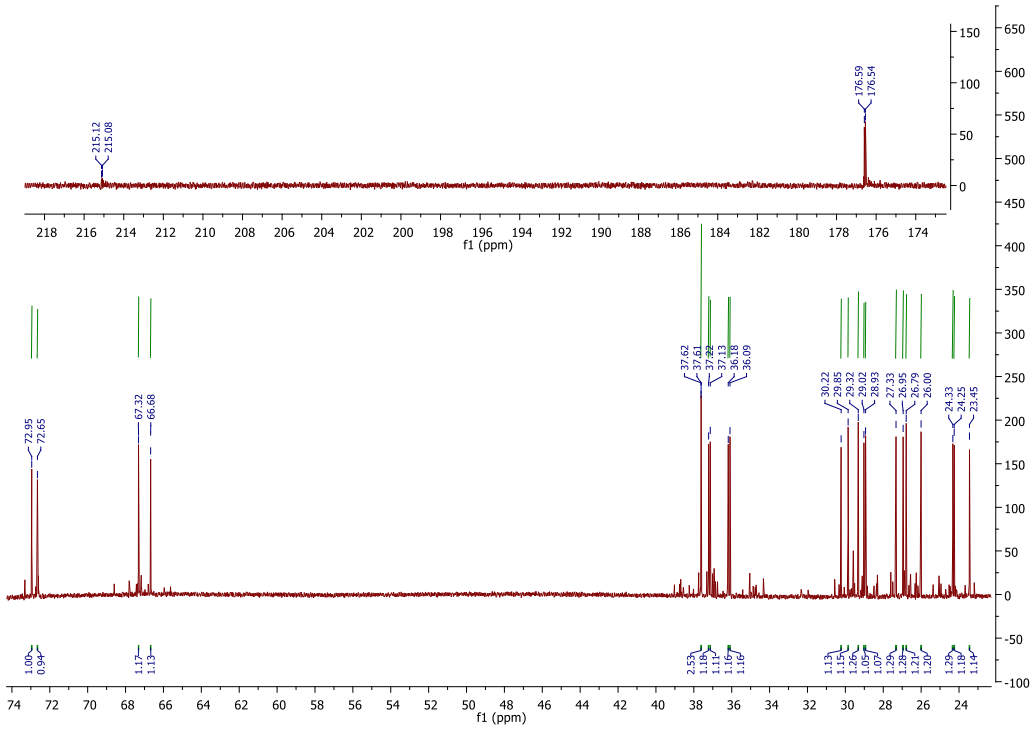

Figure B.22 (b):^{13}C NMR of product for oxacyclotridecan-2-one in $CDCl_3$.

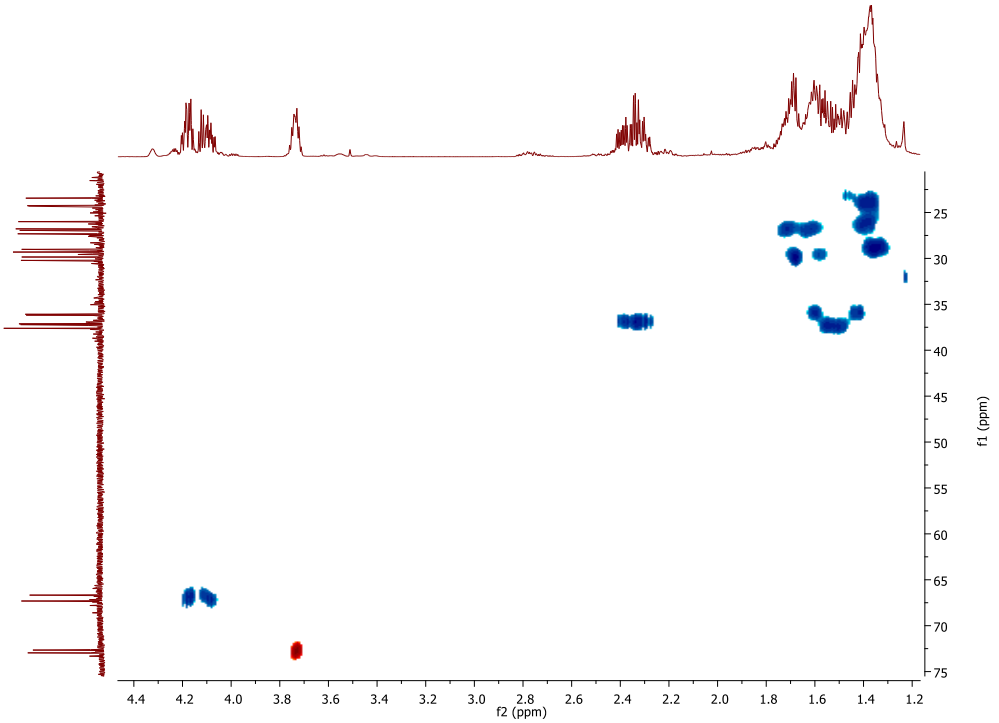

Figure B.22 (c): HSQC NMR of product for oxacyclotridecan-2-one in $CDCl_3$.

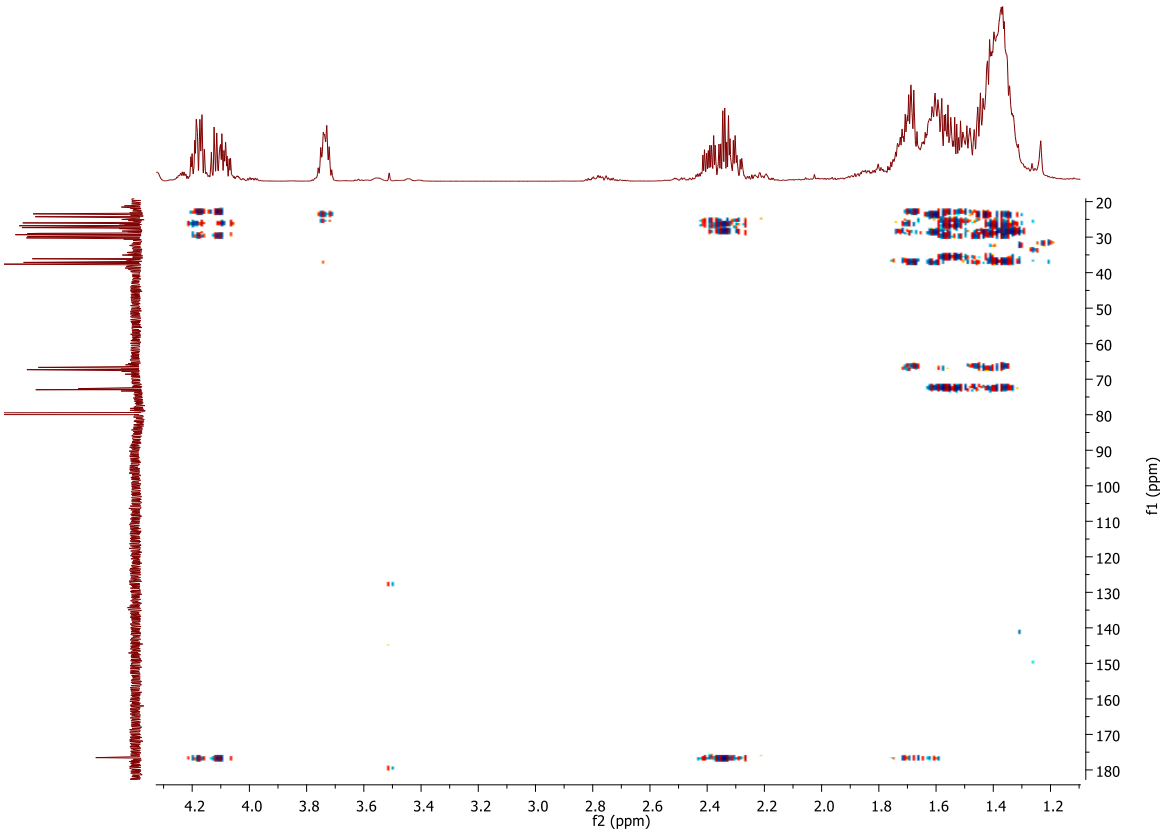

Figure B.22 (d): HMBC NMR of product for oxacyclotridecan-2-one in $CDCl_3$.

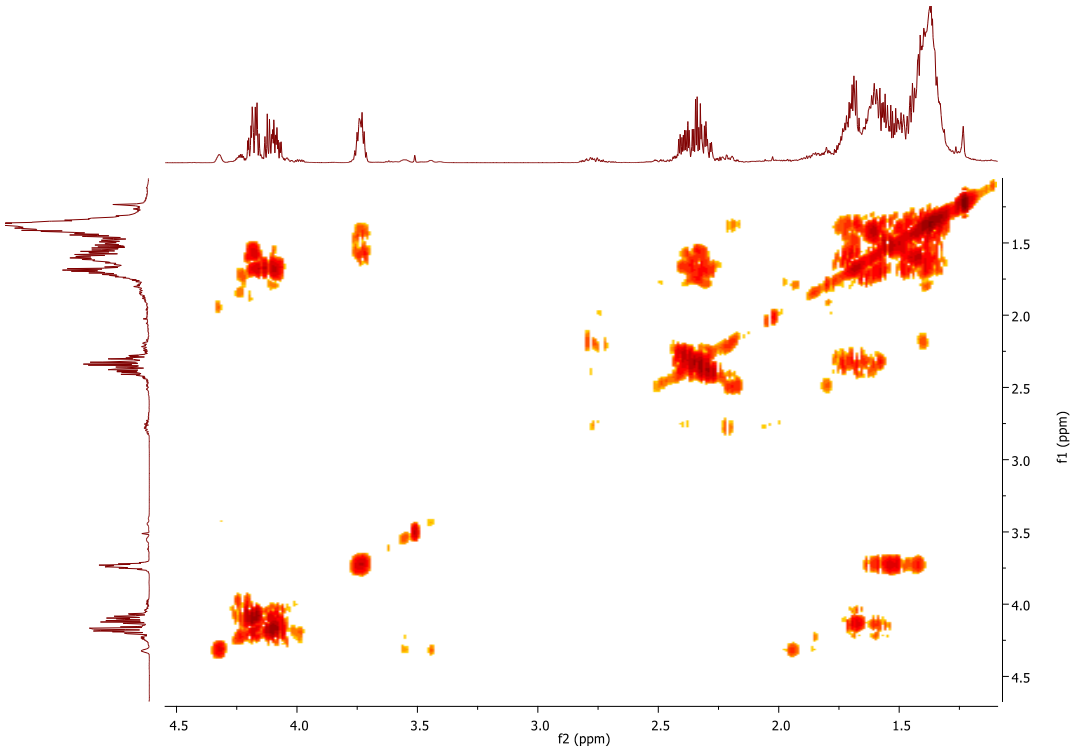

Figure B.22 (e): g-COSY NMR of product for oxacyclotridecan-2-one in $CDCl_3$.

6-hydroxy-dihydroactinidiolide: ^{1}H NMR (500 MHz, $CDCl_3$) δ 5.69 (s, 1H, H2), 4.32 (p, *J* = 3.48 Hz, 1H, H6), 2.46 (dt, *J* = 14.1, 2.6 Hz, 1H, H5), 1.97 (dt, *J* = 14.5, 2.58, 1H, H7), 1.80 – 1.76 (m, 4H, H5, H12), 1.53 (dd, *J* = 14.3, 3.6 Hz, 1H, H7), 1.47 (s, 3H, H10), 1.27 (s, 3H, H11). ^{13}C NMR (151 MHz, $CDCl_3$) δ 185.13 (C3), 174.57 (C1), 115.53 (C2), 89.37 (C4), 69.44 (C6), 49.94 (C7), 48.25 (C5), 38.58 (C4), 33.30 (C10), 29.64 (C12), 29.12 (C11).

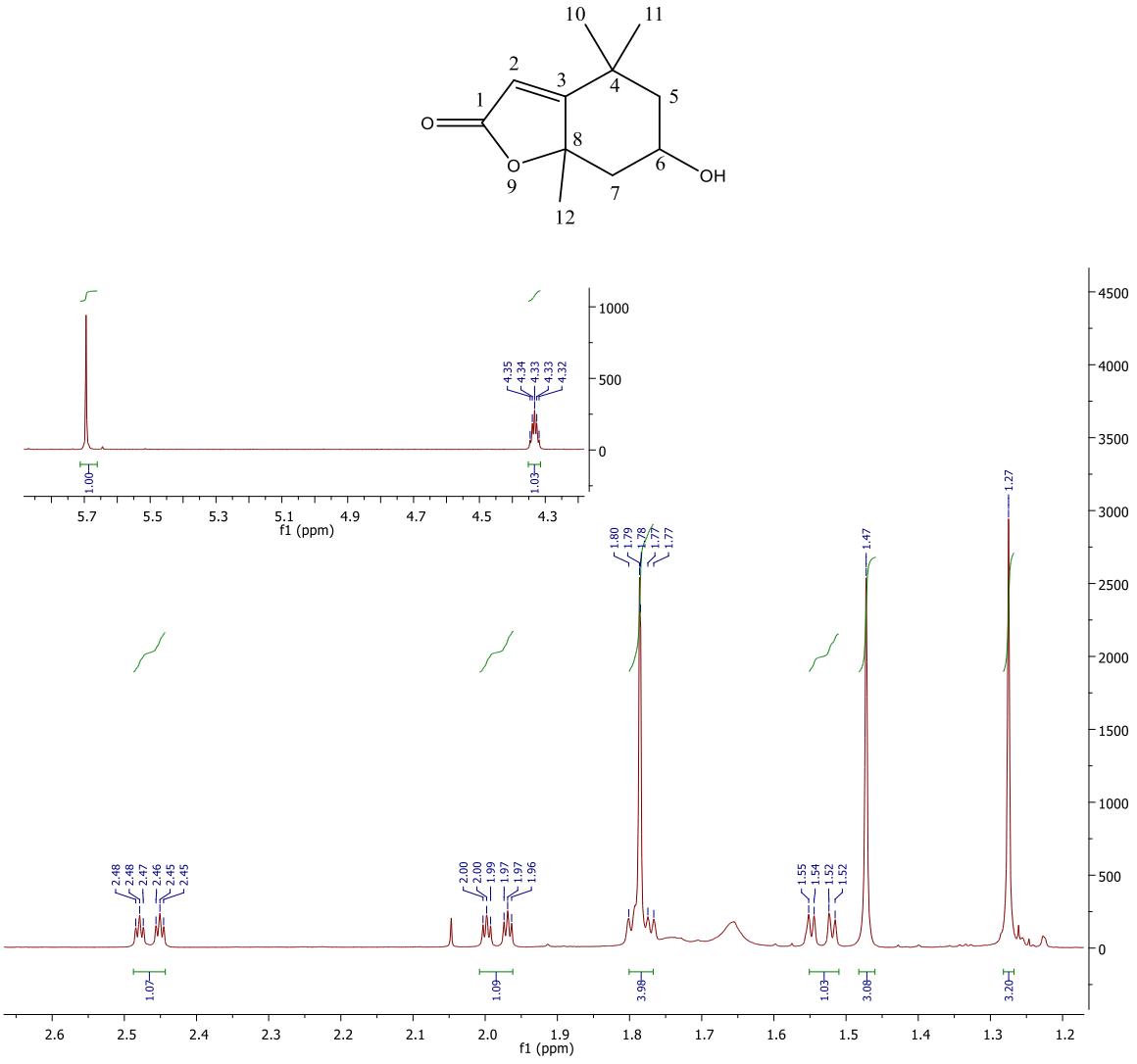

Figure B.23 (a): ^{1}H NMR for 6-hydroxy-dihydroactinidiolide in $CDCl_3$.

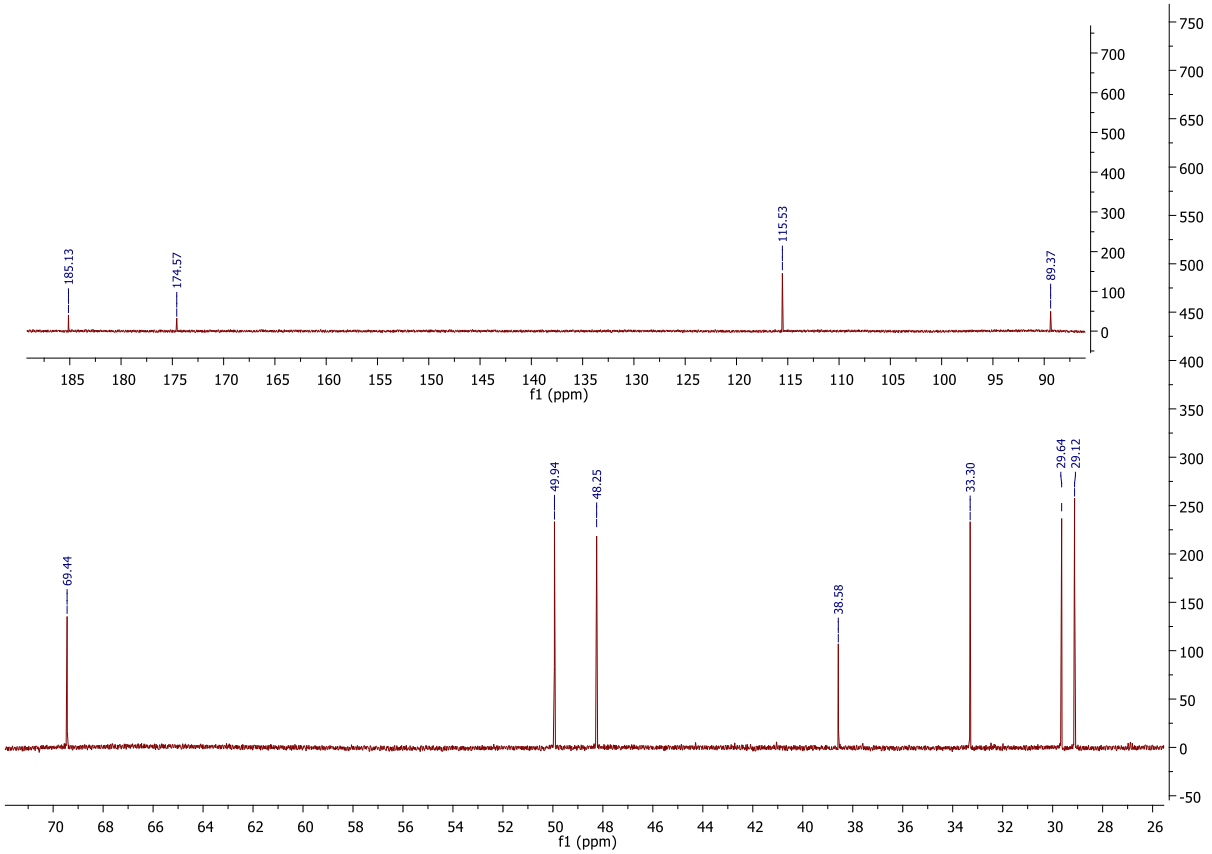

Figure B.23 (b): ^{13}C NMR for 6-hydroxy-dihydroactinidiolide in $CDCl_3$.

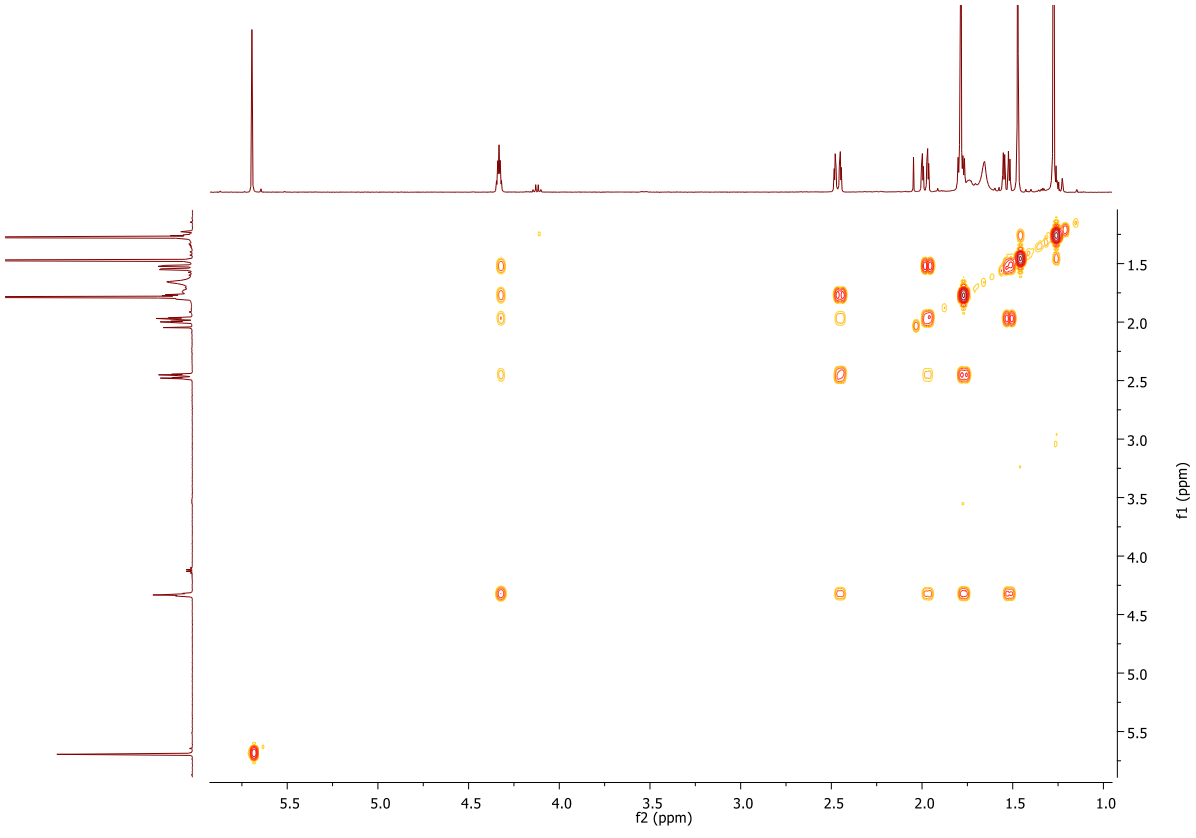

Figure B.23 (c): g-COSY NMR for 6-hydroxy-dihydroactinidiolide in $CDCl_3$

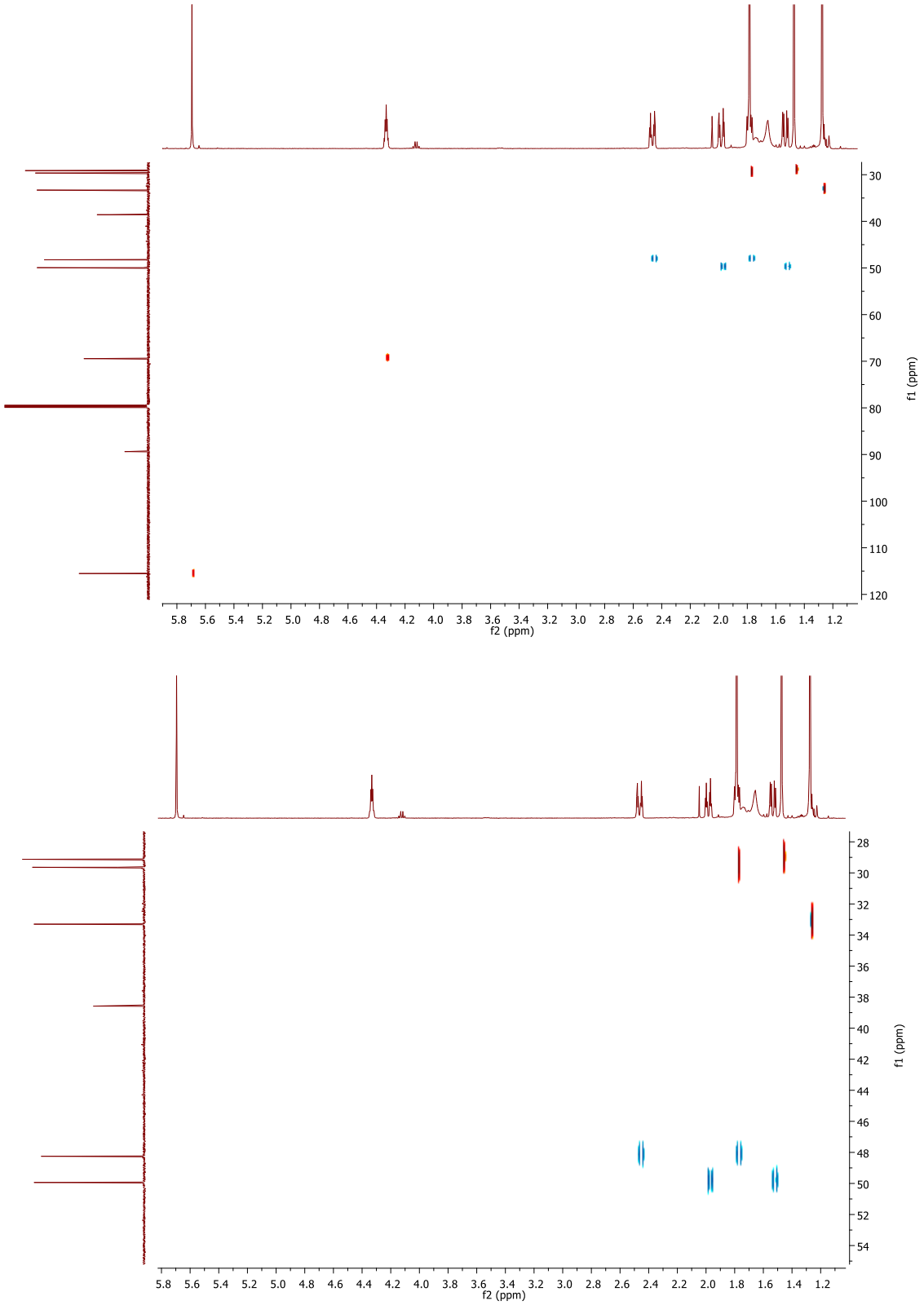

(Zoomed in)

Figure B.23 (d): HSQC NMR for 6-hydroxy-dihydroactinidiolide in $CDCl_3$.

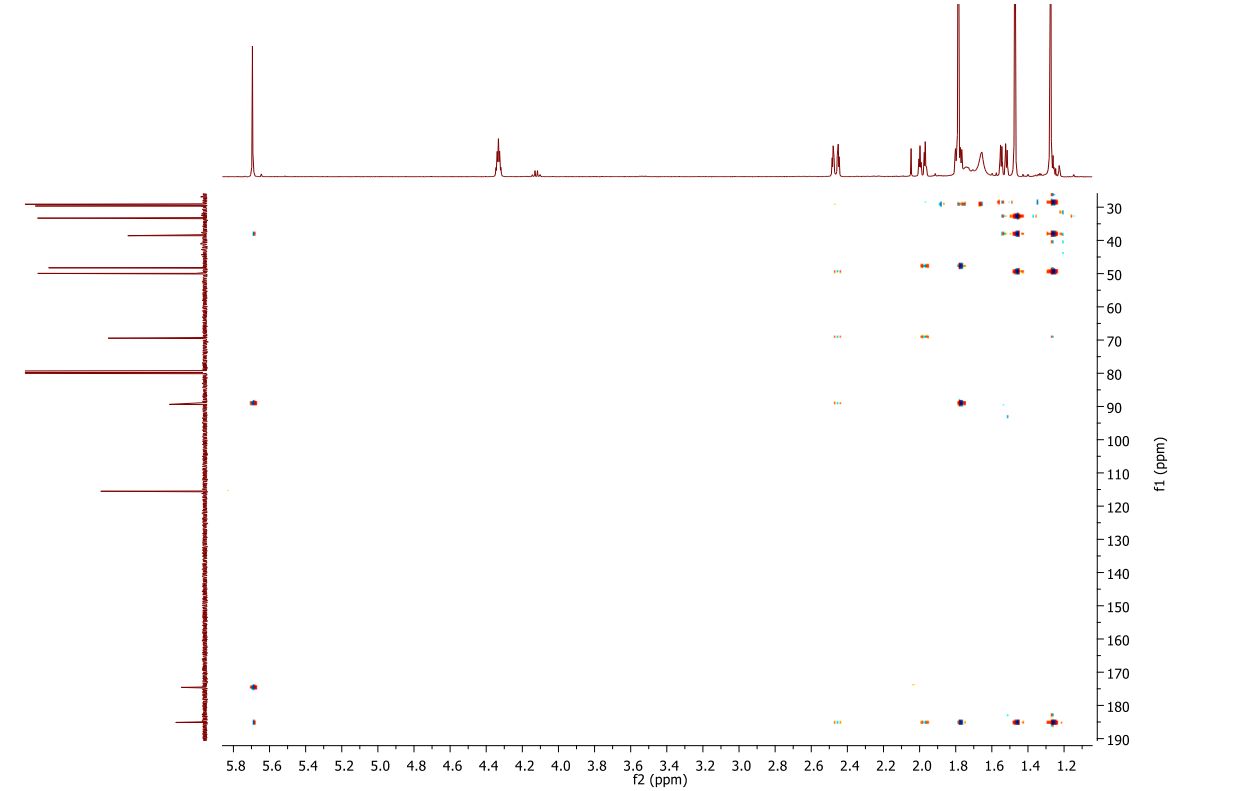

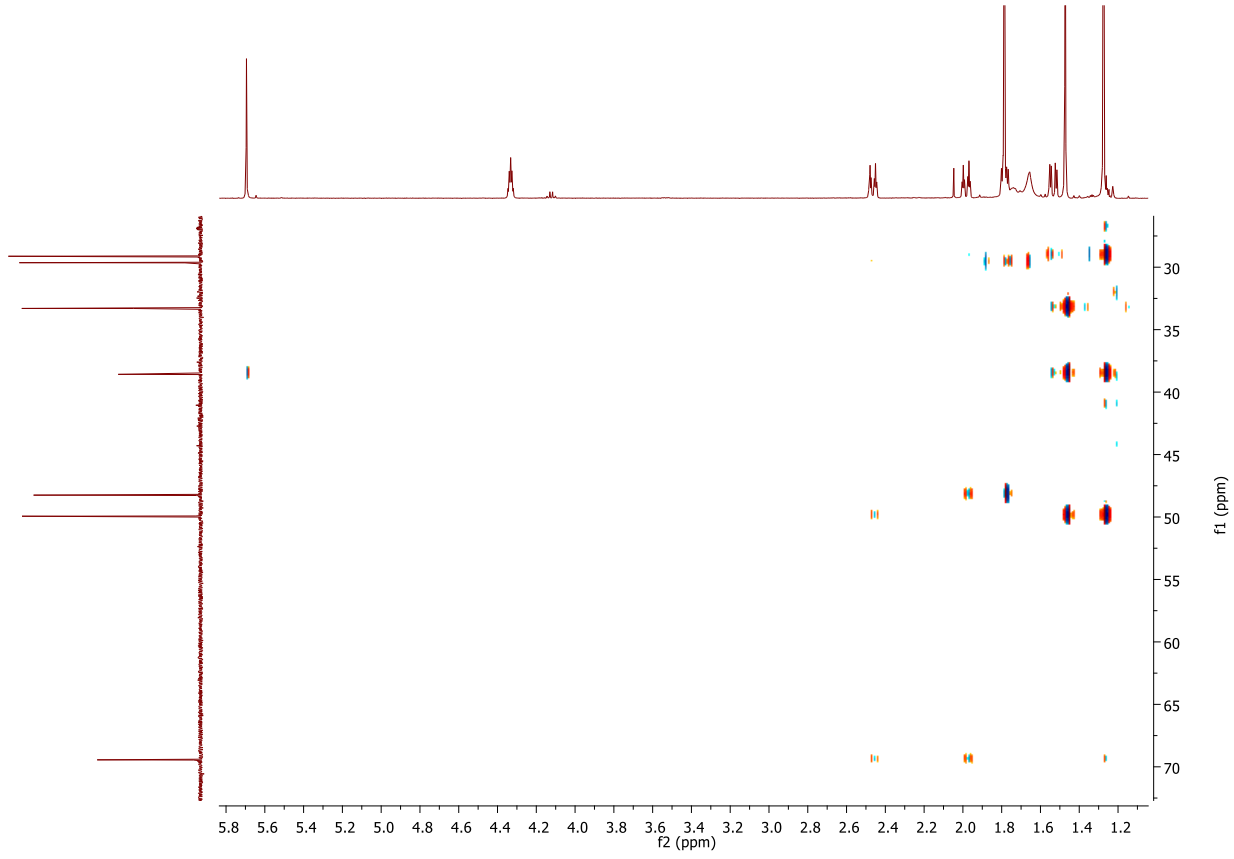

(Zoomed in)

Figure B.23 (e): HMBC NMR for 6-hydroxy-dihydroactinidiolide in $CDCl_3$.

7-hydroxy-*p*-tolyl acetate: ^{1}H NMR (500 MHz, $CDCl_3$) δ=7.38 (d, *J* = 8.4 Hz, 2H, H2, H6), 7.07 (d, *J* = 8.4 Hz, 2H, H3, H5), 4.68 (s, 2H, H7), 2.30 (s, 3H, H10). ^{13}C NMR (126 MHz, $CDCl_3$) δ 172.18(C9), 152.72(C4), 141.14(C1), 130.71(C2, C6), 124.32 (C3, C5), 67.40 (C7), 23.75 (C10).

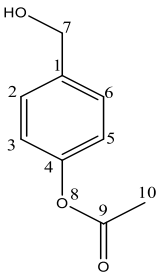

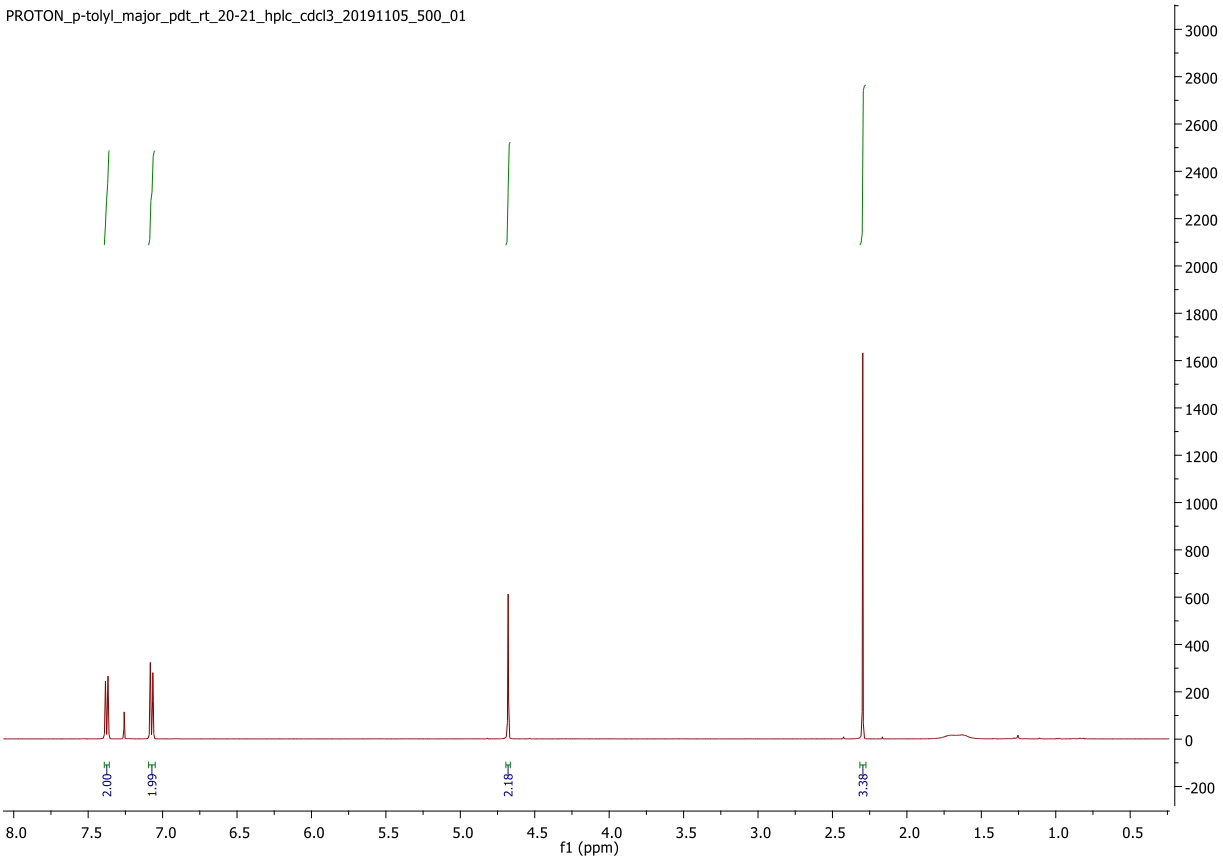

Figure B.24 (a): ^{1}H NMR for 7-hydroxy-*p*-tolyl acetate.

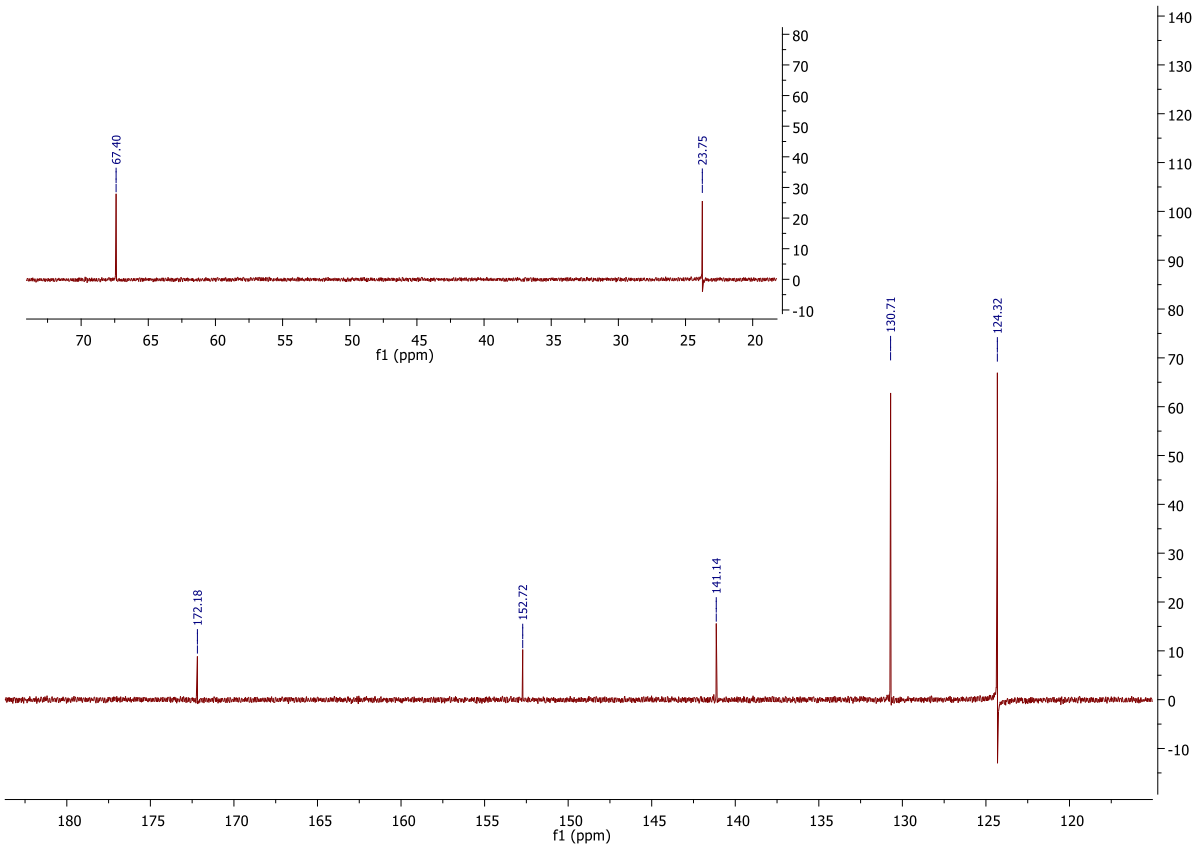

Figure B.24 (b): ^{13}C NMR for 7-hydroxy-*p*-tolyl acetate.

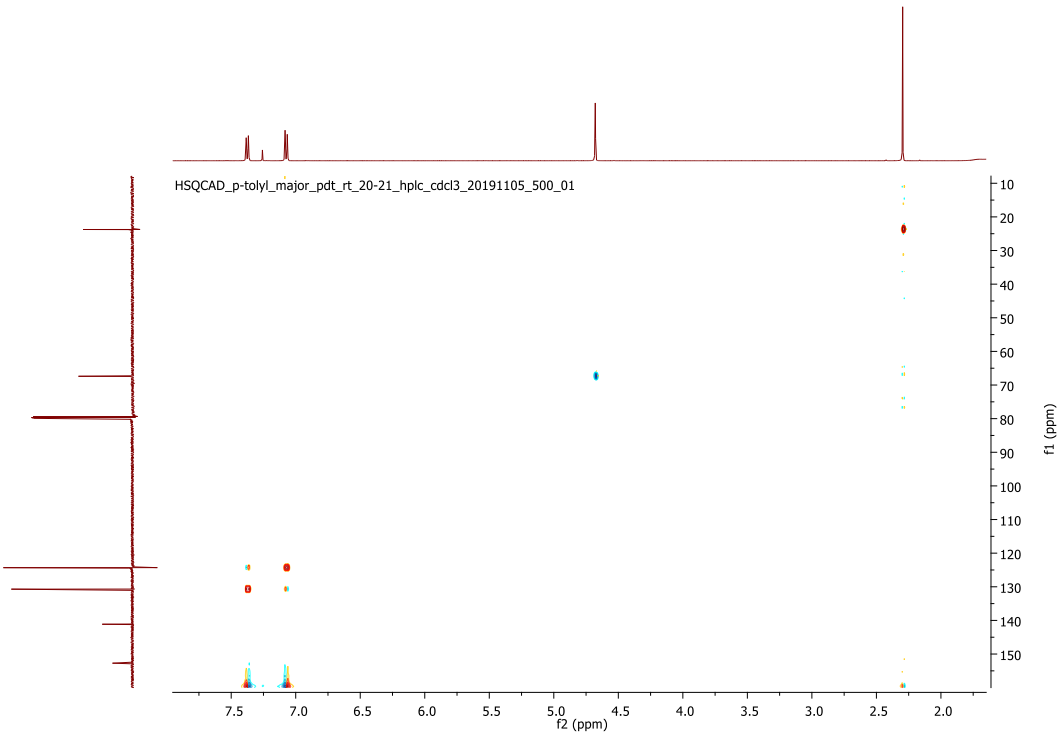

Figure B.24 (c): HSQC NMR for 7-hydroxy-*p*-tolyl acetate.

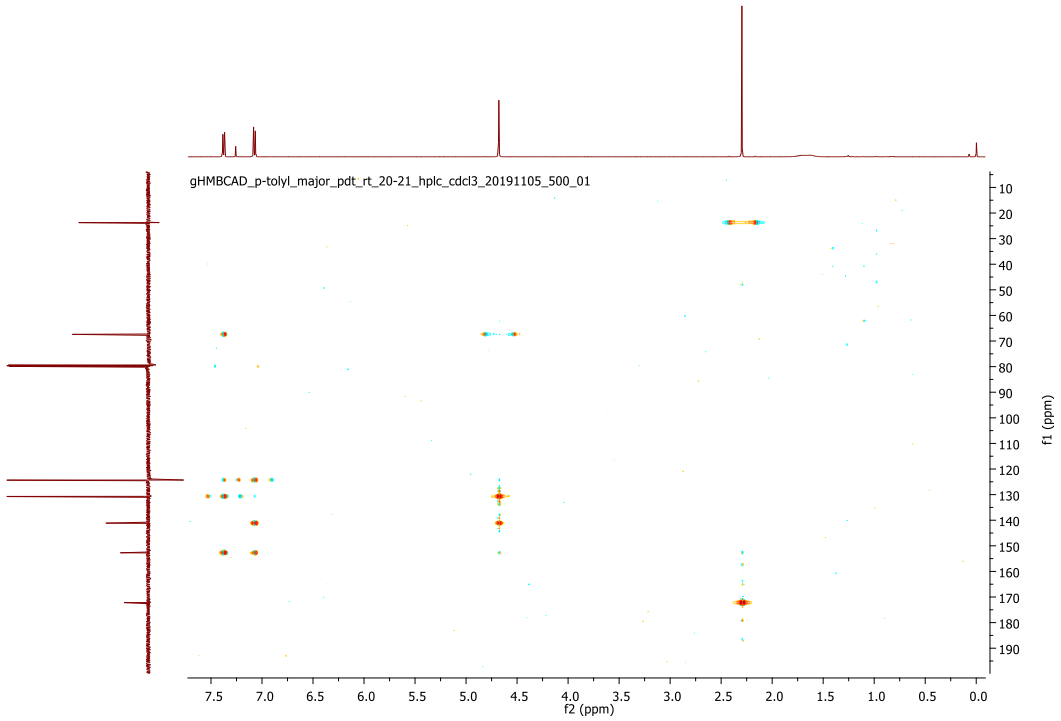

Figure B.24 (d): HMBC NMR for 7-hydroxy-*p*-tolyl acetate.

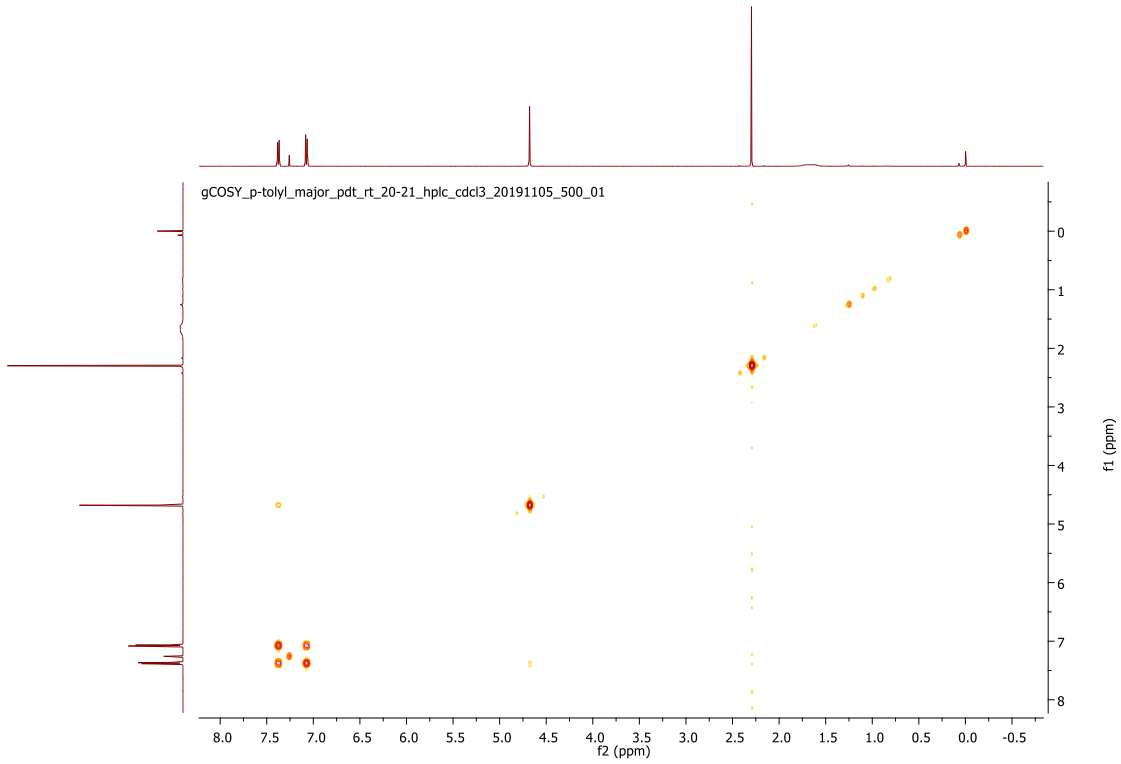

Figure B.24 (e): g-COSY NMR for 7-hydroxy-*p*-tolyl acetate.

6-hydroxy-*trans*-1-decalone:

^{1}H NMR (599 MHz, $CDCl_3$) δ 3.41 – 3.36 (m, *J* = 10.3, 4.2 Hz, 1H, H6), 2.40 – 2.29 (m, 3H, H2, H2, H9), 2.15 – 2.09 (m, 1H, H4), 2.04 – 1.99 (m, 1H, H10), 1.98 – 1.93 (m, 1H, H7), 1.89 – 1.84 (m, *J* = 8.5, 4.5 Hz, 1H, H8), 1.84 – 1.79 (m, *J* = 8.6, 6.2, 2.9 Hz, 1H, H3), 1.68 – 1.59 (m, 1H, H4), 1.40 – 1.32 (m, 2H, H5, H9), 1.27 – 1.19 (m, 3H, H3, H7, H8). 13C NMR (151 MHz, $CDCl_3$) δ 211.76 (C1), 75.07 (C6), 53.24 (C10), 51.61 (C5), 41.54 (C2), 35.17 (C7), 28.21 (C9), 26.02 (C4), 24.58 (C8), 22.70 (C3).

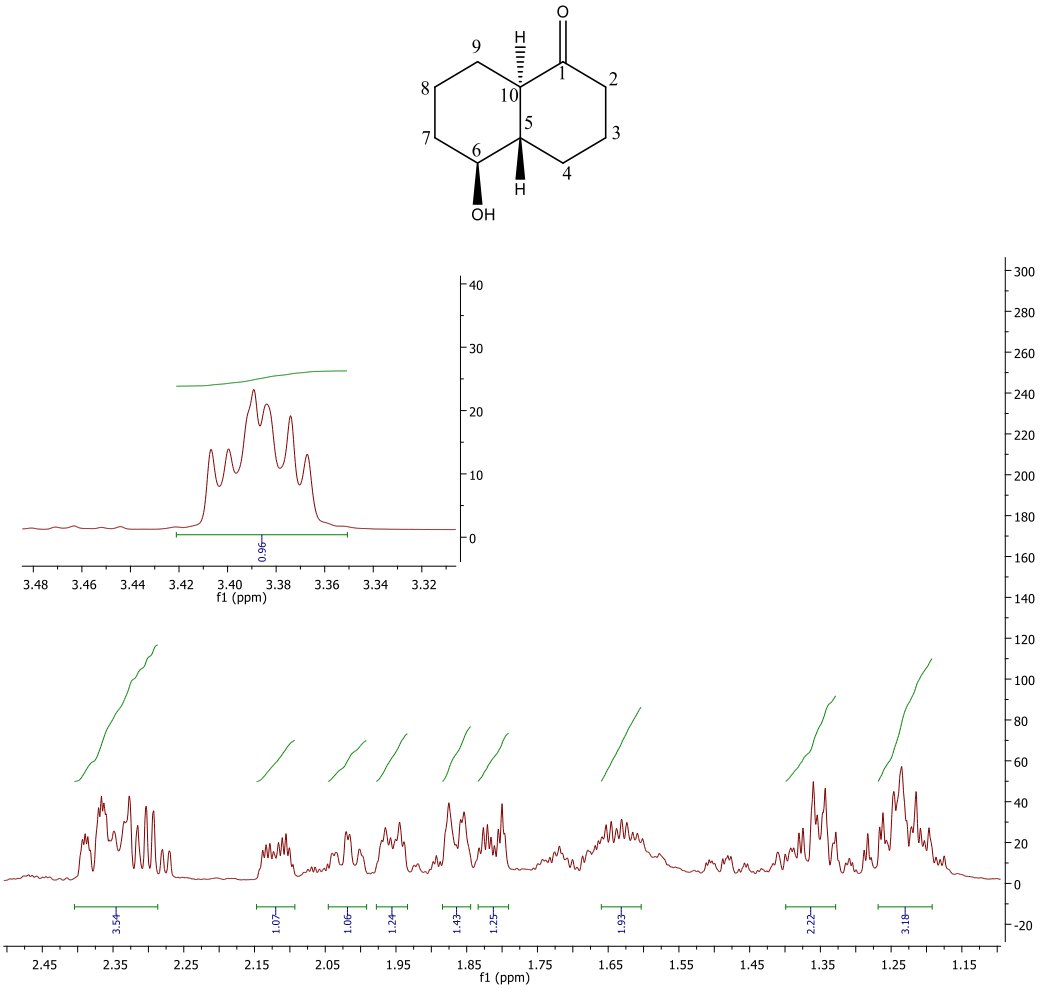

Figure B.25 (a): ^{1}H NMR for 6-hydroxy-*trans*-1-decalone.

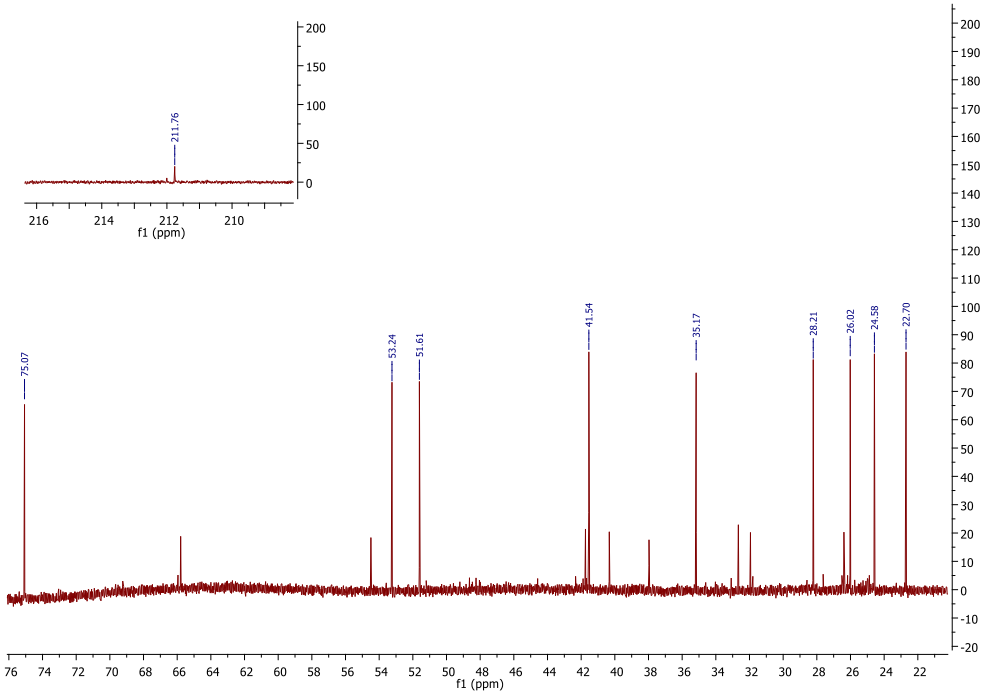

Figure B.25 (b): ^{13}C NMR for 6-hydroxy-*trans*-1-decalone in $CDCl_3$

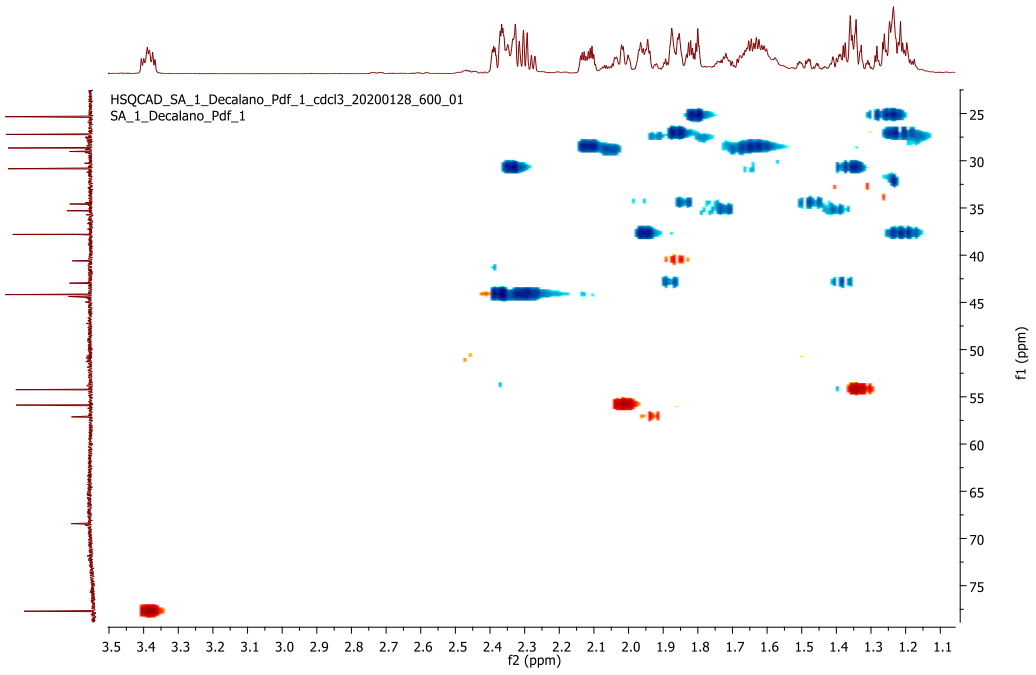

Figure B.25 (c): HSQC NMR for 6-hydroxy-*trans*-1-decalone in $CDCl_3$.

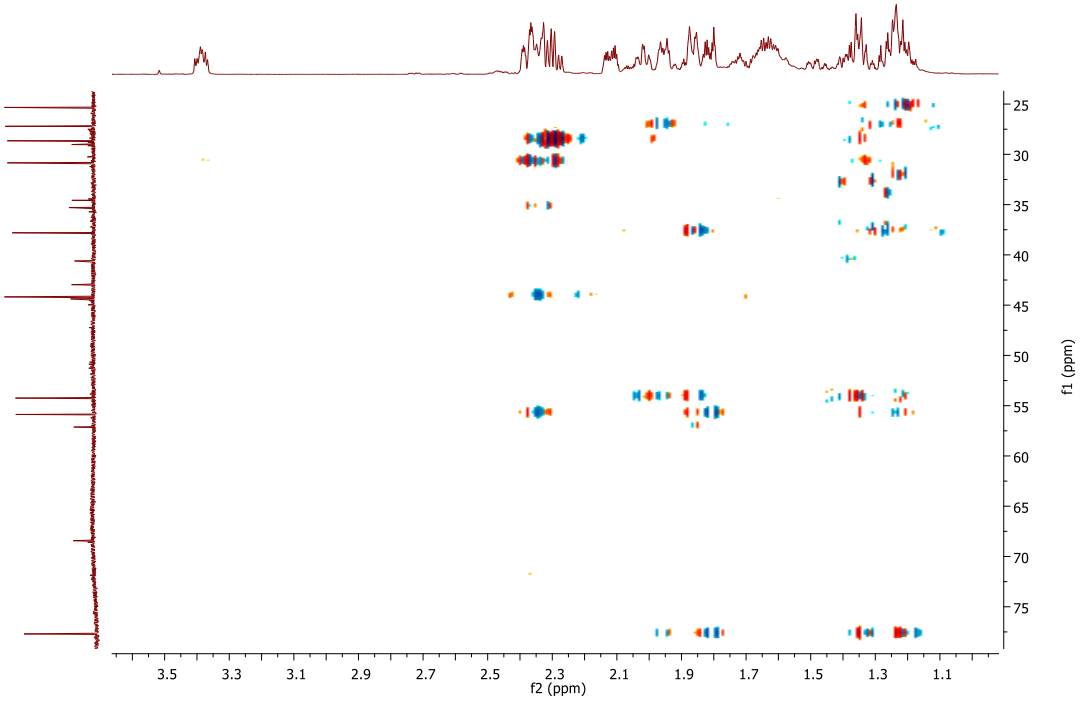

Figure B.25 (d): HMBC NMR for 6-hydroxy-*trans*-1-decalone in $CDCl_3$.

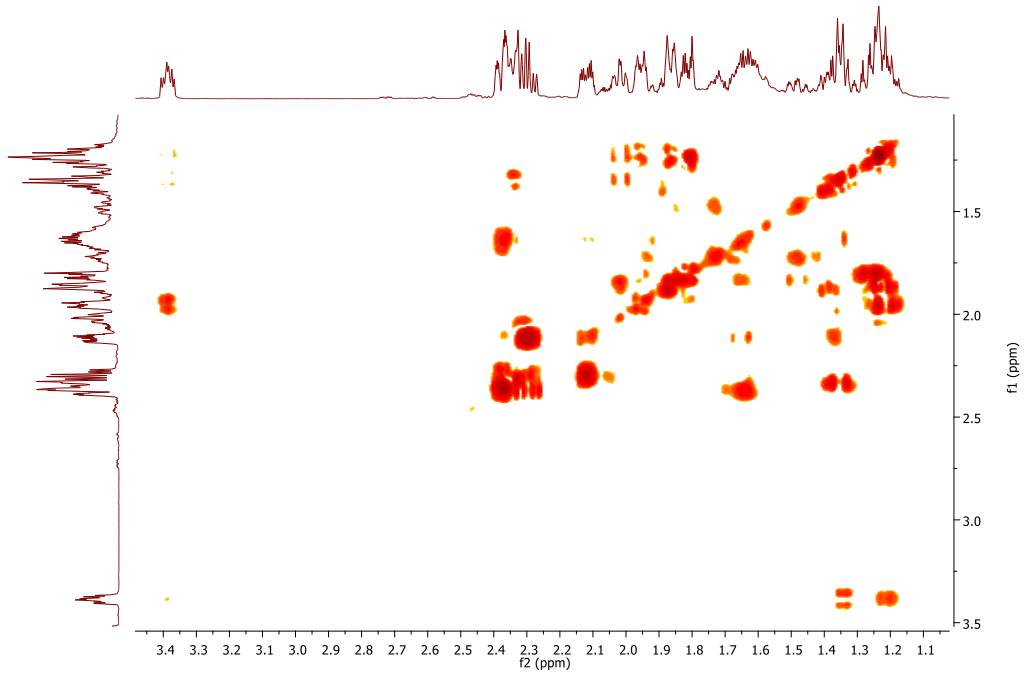

Figure B.25 (e): g-COSY NMR for 6-hydroxy-*trans*-1-decalone in $CDCl_3$.

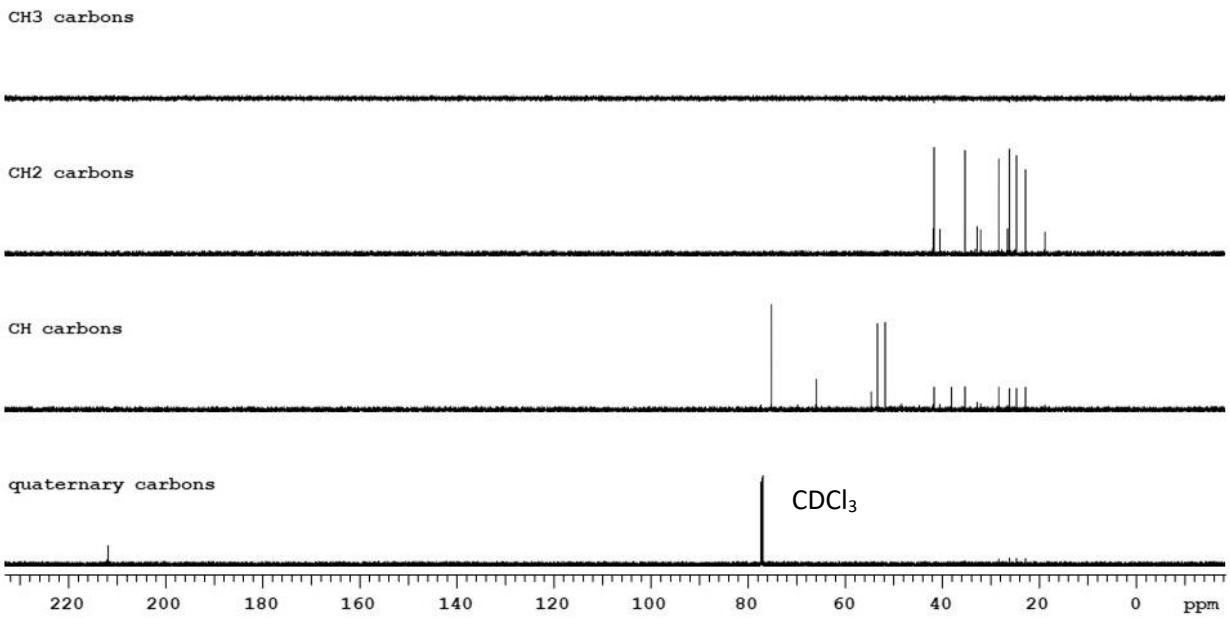

Figure B.25 (f): DEPT NMR for 6-hydroxy-*trans*-1-decalone in $CDCl_3$. This shows the 6 CH2 carbons (C2, C7, C9, C4, C8 and C3) and 3 CH carbons (C5, C6 and C10).

7-hydroxy-*trans*-1-decalone: ^{1}H NMR:

^{1}H NMR (500 MHz, $CDCl_3$) δ 3.60 (ddd, *J* = 11.8, 9.2, 5.3 Hz, 1H, H7), 2.42 – 2.36 (m, 1H, H2), 2.30 (ddd, *J* = 13.7, 6.3, 1.2 Hz, 1H, H2), 2.23 – 2.17 (m, 1H, H6), 2.10 – 2.03 (m, 1H, H3), 2.02 – 1.97 (m, 2H, H4, H10), 1.85 (ddd, *J* = 13.5, 8.6, 4.4 Hz, 2H, H8/H9), 1.67 (dt, *J* = 13.0, 4.0 Hz, 1H, H3), 1.42 – 1.31 (m, 2H, H5, H8/H9), 1.28 – 1.20 (m, 4H, H4, H6, H8/H9). ^{13}C NMR (126 MHz, $CDCl_3$) δ 211.06 (C1), 70.49 (C7), 52.87 (C10), 43.81 (C5), 41.35 (C2), 34.86 (C4), 34.58 (C6), 32.26 (C9/C8), 32.17 (C9/C8), 26.31 (C3).

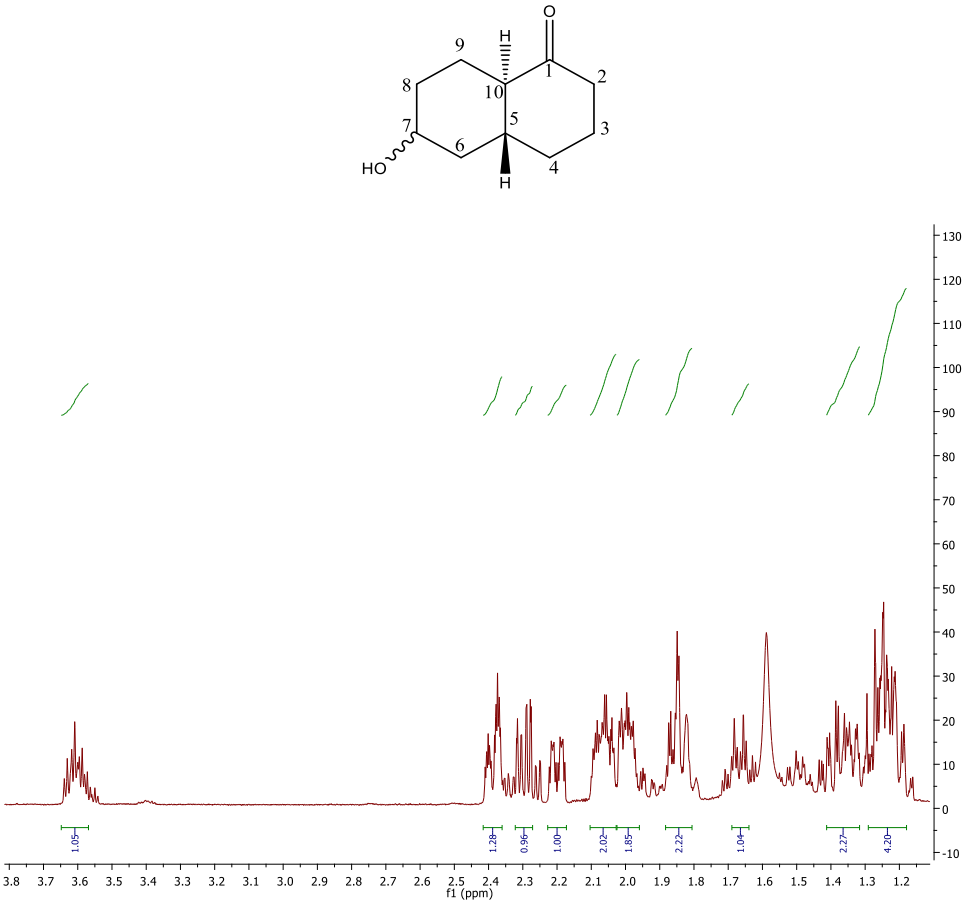

Figure B.26 (a): ^{1}H NMR for 7-hydroxy-*trans*-1-decalone in $CDCl_3$.

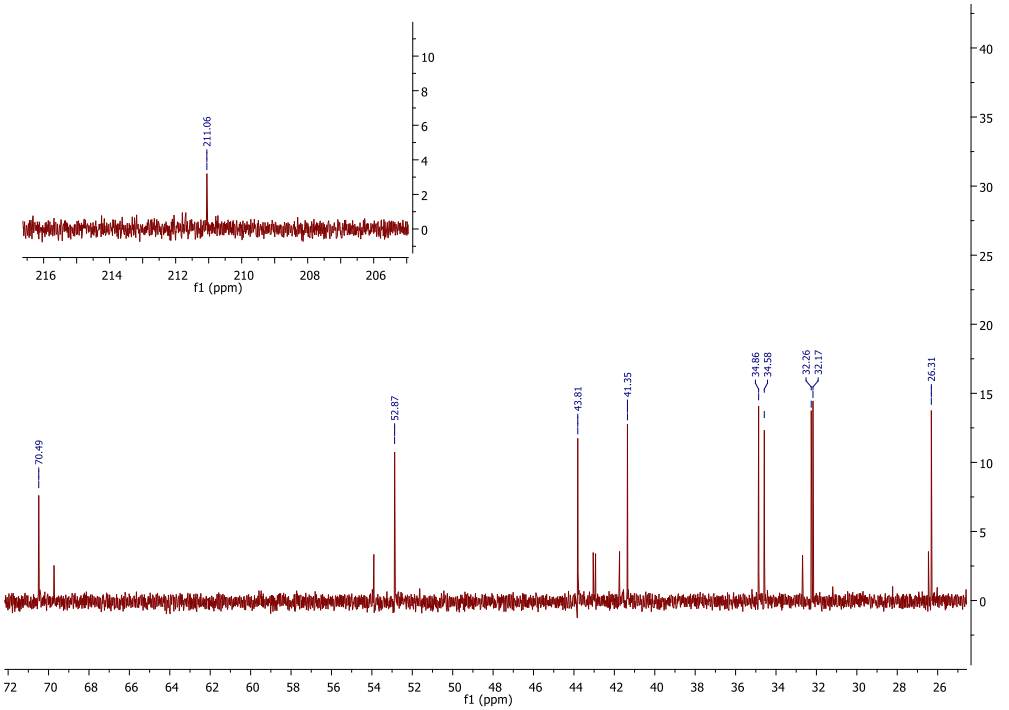

Figure B.26 (b): ^{13}C NMR for 7-hydroxy-*trans*-1-decalone in $CDCl_3$.

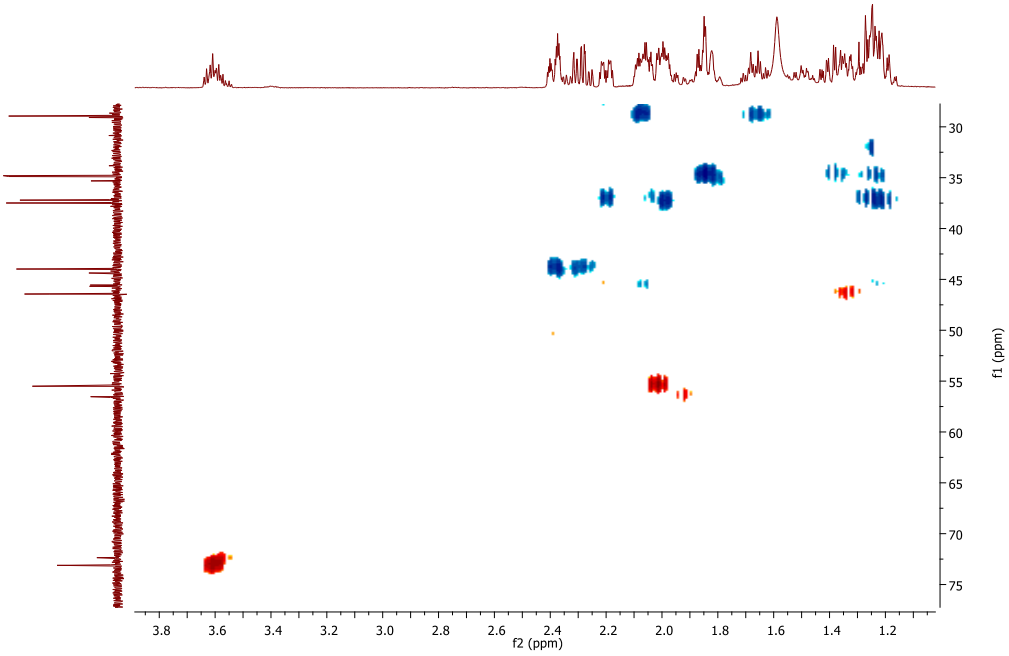

Figure B.26 (c): HSQC NMR for 7-hydroxy-*trans*-1-decalone in $CDCl_3$.

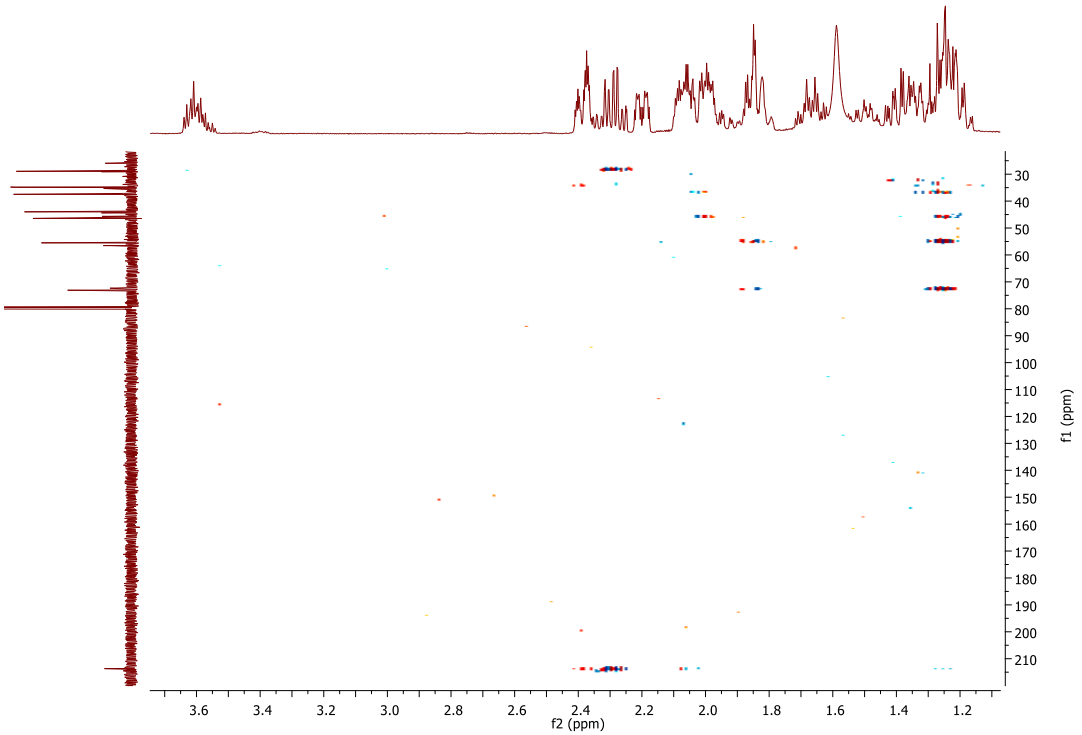

Figure B.26 (d): HMBC NMR for 7-hydroxy-*trans*-1-decalone in $CDCl_3$.

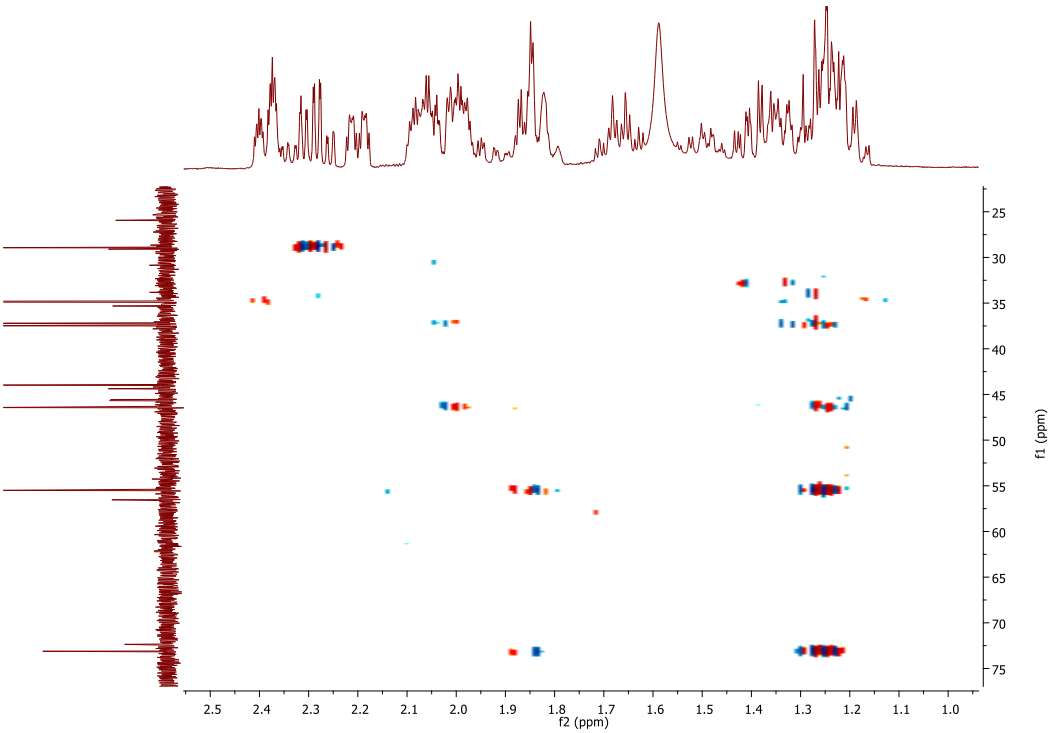

Figure B.26 (e): HMBC NMR for 7-hydroxy-*trans*-1-decalone in $CDCl_3$.

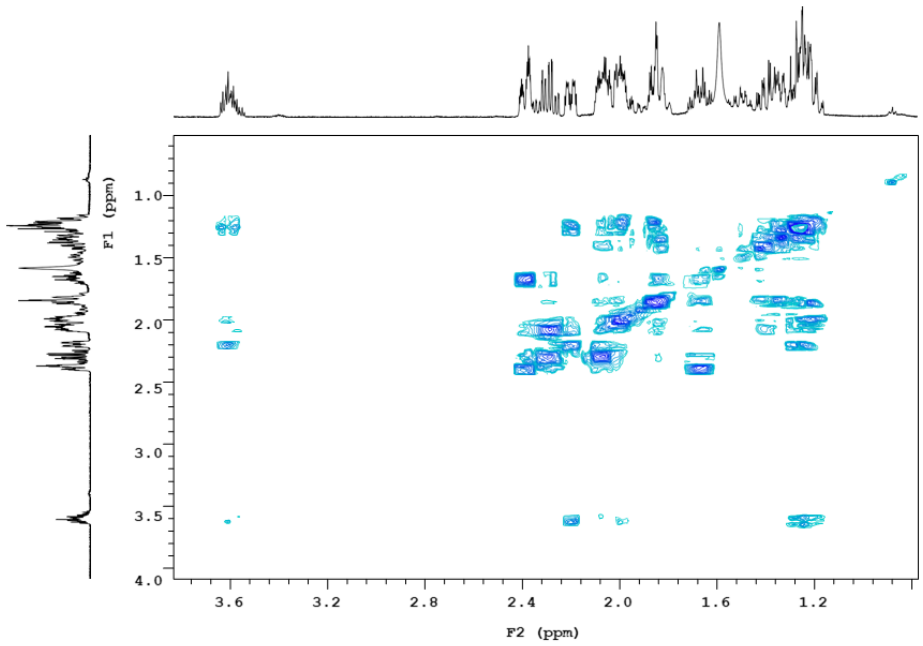

Figure B.26 (f): g-COSY NMR for 7-hydroxy-*trans*-1-decalone in $CDCl_3$.

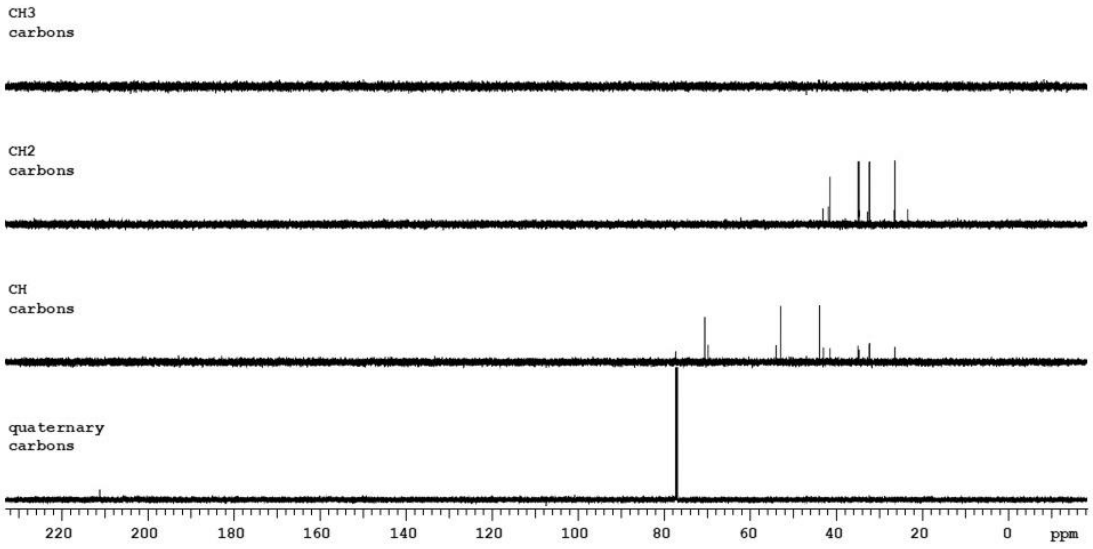

Figure B.26 (g): DEPT NMR for 7-hydroxy-*trans*-1-decalone in $CDCl_3$. This shows the 6 CH2 carbons (C2, C6, C9, C4, C8 and C3) and 3 CH carbons (C5, C7 and C10).